



Dissertation

Defects in Two - Dimensional Crystals

ausgeführt zum Zwecke der Erlangung des akademischen Grades eines
Doktors der Naturwissenschaften (Dr. rer. nat.)

unter der Anleitung von Prof. Dr. **Florian Libisch**
Institut für Theoretische Physik, TU Wien, Wien, Österreich

eingereicht an der Technischen Universität Wien, Fakultät für Physik

von

Dipl.-Ing. **Christoph Schattauer**
Matr.Nr.: 01228718

Gutachter: Prof. Dr. rer. nat. **Ludger Wirtz**
Département Physique et sciences des matériaux
Université du Luxembourg
Luxemburg

Gutachter: Priv. Doz. Dr. techn. **Robert Stadler**
Institut für Theoretische Physik
TU Wien
Vienna, Austria

Wien, Februar 2023

*The health of the eye seems to demand a horizon.
We are never tired, so long as we can see far enough.*

RALPH WALDO EMERSON

Declaration

This work was supported by the doctoral colleges *Solids4Fun* W1243-N16 funded by the FWF and *TU-D* funded by TU Wien as well as FWF DACH project I3827-N36 and COST action CA18234. Furthermore, I acknowledge support as a recipient of a DOC fellowship of the Austrian Academy of Sciences. Numerical support was provided by the Vienna Scientific Cluster (VSC).

Affidavit

I declare in lieu of oath, that I wrote this thesis and performed the associated research myself, using only literature cited in this volume. If text passages from sources are used literally, they are marked as such. I confirm that this work is original and has not been submitted elsewhere for any examination, nor is it currently under consideration for a thesis elsewhere. I acknowledge that the submitted work will be checked electronically-technically using suitable and state-of-the-art means (plagiarism detection software). Firstly, this ensures that the submitted work was prepared according to the high-quality standards within the applicable rules to ensure good scientific practice “Code of Conduct” at the TU Wien. Secondly, a comparison with other student theses avoids violations of my personal copyright.

I certify that the printing of this thesis is subject to confirmation by the board of examiners.

Deutsche Kurzfassung

Zweidimensionale Kristalle, die aus schwach (Van der Waals) gekoppelten, geschichteten Materialien herausgelöst werden, eröffnen die Möglichkeit, 2D-Materialien sowohl theoretisch als auch experimentell zu untersuchen. Ihre im Vergleich zu herkömmlichen “3D-Materialien” unterschiedlichen elektronischen, optischen und mechanischen Eigenschaften, die sie zu erstklassigen Kandidaten für künftige Anwendungen in der Informationstechnologie machen, stoßen auf reges Forschungsinteresse. Aufgrund des maximalen Verhältnisses von Oberfläche zu Volumen dieser Systeme ist es auch möglich, die Eigenschaften dieser Materialien durch externe Maßnahmen zu beeinflussen. Diese äußeren Einflüsse können von elektrostatischen Gates, die eine präzise Ladungskontrolle und Stromsteuerung ermöglichen, bis hin zu einer weiteren Schicht eines anderen 2D-Materials reichen, die je nach der genauen relativen Ausrichtung zur ersten Schicht zu einer neuartigen Moiréphysik auf verschiedenen Längenskalen führt.

Eine weitere Quelle für die Veränderung von Materialeigenschaften - wenn auch eine historisch unerwünschte - sind Gitterfehler und Defekte. Die außerordentliche Vielseitigkeit und Beeinflussbarkeit niedrig-dimensionaler Werkstoffe macht sie auch anfälliger für Veränderungen, die durch Fehler in ihrer kristallinen Struktur verursacht werden. Obwohl die Probenvorbereitung und damit die Kontrolle über das Auftreten dieser Defekte seit der Entdeckung dieser niedrig-dimensionalen Systeme erheblich verbessert wurde, ist das Verständnis des Einflusses solcher Defekte nach wie vor ein entscheidender Faktor für die Entwicklung von Materialien mit gewünschten Eigenschaften.

Diese Arbeit zielt darauf ab, die theoretische Modellierung solcher Systeme mit Defekten voranzutreiben, und untersucht mehrere Beispiele, bei denen Defekte nicht nur Fehler in der Kristallstruktur sind, sondern auch die Möglichkeit bieten, sowohl optische als auch elektronische Eigenschaften aktiv in wünschenswertere Konfigurationen zu ändern. Ich wende Modelle unterschiedlicher Komplexität an, um experimentelle Daten von Photolumineszenz-, Rastertunnel- und elektronischen Transportmessungen in Systemen zu verstehen und zu erklären, deren Eigenschaften entweder durch Gitterdefekte oder elektrostatische Gates verändert werden. Neben verschiedenen spannenden Möglichkeiten, experimentelle Daten theoretisch zu untermauern, untersuche ich auch einige Systeme von einem rein theoretischen Standpunkt aus und versuche, Anreize für die experimentelle Umsetzung zu schaffen. Die Modellierung dieser Systeme beinhaltet oft Multi-Skalen-ansätze, bei denen numerisch teure, aber genaue Methoden (z.B. Dichtefunktionaltheorie für Defekt-Superzellen) in ein erfolgreiches Zusammenspiel mit groß-skaliigen Methoden (z.B. Tight-Binding für elektronischen Transport) gebracht werden müssen, die die Simulation von

Millionen von Atomen (d.h. vergleichbar mit experimentell zugänglichen Längenskalen) ermöglichen.

Trotz der Tatsache, dass die Qualität der Übereinstimmung zwischen gemessenen und simulierten Daten nicht immer eine monotone Funktion der Modellierungskomplexität und des Aufwands ist, versuche ich auch die Generierung von ab-initio abgeleiteten Defektparametrisierungen anzuzeigen. Zu diesem Zweck implementiere ich einen modernen maschinellen Lernalgorithmus, der versucht, die hervorragenden, aber aufwendigen Standard-Defektmodellierungsmethoden zu umgehen. Darüber hinaus wende ich modernste numerische Algorithmen an, die in Zusammenarbeit mit Florian Libisch und seinen früheren Doktoranden entwickelt wurden, um den elektronischen Transport in Moiré-Strukturen von zweischichtigem Graphen (tBLG) und hexagonalem Bornitrid (hBN) zu untersuchen.

Abstract

Two dimensional crystals — exfoliated from weakly (Van der Waals) coupled layered materials — open the possibility of studying 2D materials both theoretically and experimentally. Their differences in electronic, optical and mechanical properties when compared to conventional “3D materials” makes them prime candidates for future application in information technology, attracting considerable interest. Due to the maximal surface to bulk ratio of these systems it is also possible to tailor the characteristics of these materials via external measures. These can range from electrostatic gates enabling precise charge localization and current control, all the way to a sheet of another 2D material, which depending on the precise relative orientation with respect to the first layer results in novel moiré physics.

Another source of altering material properties — albeit a historically undesirable one — are lattice imperfections and defects. In this regard the outstanding versatility and influenceability of low dimensional materials also renders them more susceptible to changes caused by flaws within their crystalline structure. While sample preparation and thus control over the occurrence of these imperfections has undergone vast improvements since the discovery of these low-dimensional systems, understanding the influence of such defects remains a vital ingredient to tailoring materials with desired properties.

This thesis aims at advancing the theoretical modeling of such modified systems and studies several examples where defects are not only flaws in the crystal structure but present opportunities to actively change both optical and electronic properties to more desirable configurations. I apply models of varying complexity to help understand and explain experimental data of photoluminescence, scanning tunneling and electronic transport measurements in systems with characteristics altered by either lattice defects or electrostatic gates. Apart from several exciting opportunities to provide theoretical support to experimental data I also study some systems from a purely theoretical aspect and try to provide incentive for experimental realization. Modeling these systems often involves multi-scale approaches where numerically expensive but accurate methods (e.g. density functional theory for defect super cells) need to be brought into a successful interplay with large scale methods (e.g tight-binding for electronic transport) that allow for the simulation of millions of atoms (i.e. comparable to experimentally accessible length scales).

Although the quality of agreement between measured and simulated data is not always a monotonous function of modeling complexity and effort I also try to address the generation of ab-initio derived defect parametrizations. To this extent I implement a modern machine learning algorithm that tries to circumvent the excellent but cumbersome standard defect modeling methods. Furthermore I also apply state-of-art numerical algorithms developed in a

group effort with Florian Libisch and his preceding PhD students to study electronic transport in twisted moiré structures of bilayer graphene (tBLG) and hexagonal boron nitride (hBN).

List of publications

Graphene quantum dot states near defects

C. Schattauer, L. Linhart, T. Fabian, T. Jawecki and F. Libisch.
Phys. Rev. B 102, 155430 (2020)

Machine Learning Sparse Tight-Binding Parameters for Defects

C. Schattauer, M. Todorovic, K. Ghosh, P. Rinke, F. Libisch.
npj Comput Mater 8, 116 (2022)

Strain control of hybridization between dark and localized excitons in a 2D semiconductor

P. Hernández López, S. Heeg, C. Schattauer, S. Kovalchuk, A. Kumar, D. J. Bock, J. N. Kirchhof, B. Höfer, K. Greben, D. Yagodkin, L. Linhart, F. Libisch, K. I. Bolotin

Nat. Comm. **13**, 7691 (2022)

Mapping quantum Hall edge states in graphene by scanning tunneling microscopy

T. Johnsen, C. Schattauer, S. Samaddar, A. Weston, M. Hamer, R. Gorbachev, F. Libisch, M. Morgenstern.
submitted to PRX (2023)

Composite super-moiré lattices in hBN commensurate twisted bilayer graphene

A. Rothstein, C. Schattauer, R. Dolleman, S. Trelenkamp, F. Lentz, K. Watanabe, T. Taniguchi, D. M. Kennes, F. Libisch, B. Beschoten, C. Stampfer

in preparation (2023)

Spin valves based on bilayer graphene quantum point contacts

E. Icking, C. Volk, L. Banszerus, C. Schattauer, K. Watanabe, T. Taniguchi, F. Libisch, B. Beschoten, C. Stampfer

in preparation (2023)

Acronyms

AC	armchair
AI	artificial intelligence
BI	band insulator
BLG	bilayer graphene
BZ	Brillouin zone
CGTO	contracted Gaussian-type orbitals
CI	correlated insulator
CNN	convolutional neural network
CSL	coincidence site lattice
DFT	density functional theory
DL	deep learning
GGA	generalized gradient approximation
GLD	gradient-less descent
GPR	Gaussian process regression
GQDs	graphene quantum dots
LCAO	linear combination of atomic orbitals
LDA	local density approximation
ML	machine learning
MLP	multilayer perceptron
MLWF	maximally localized Wannier functions
PAO	pseudo-atomic orbitals
PL	photoluminescence
PW	plane waves
QDOT	quantum dot
QH	quantum Hall
SK	Slater-Koster
SLG	single layer graphene
SQUID	superconducting quantum interference device
STM	scanning tunneling microscopy
STS	scanning tunneling spectroscopy
TB	tight-binding
tBLG	twisted bilayer graphene
TIQD	tip-induced quantum dot
TMDs	Transition metal dichalcogenides
ZZ	zig-zag

Contents

1	Introduction	1
I	Theory	5
2	2D crystals & lattice defects	6
2.1	Graphene	6
2.1.1	$k \cdot p$ Hamiltonian	8
2.2	Transition metal dichalcogenides	11
2.2.1	Tungsten diselenide WSe ₂	11
2.3	Crystal lattice defects	12
2.4	Moiré systems	15
3	Methods of solid state physics	17
3.1	Bloch's theorem	17
3.2	Density functional theory	17
3.3	Tight-binding	20
3.3.1	Example: tight-binding models for the p _z bands in graphene	21
3.4	Quantum transport	23
3.4.1	Green's functions	23
3.4.2	Infinite waveguides and the recursive Green's function method	23
3.5	Maximally localized Wannier functions	25
3.5.1	Example: MLWF of WSe ₂	26
4	Machine learning concepts	28
4.1	Neural networks	29
4.1.1	Network training & model fitting	31
4.1.2	Regularization	34
4.1.3	Convolutional neural networks	35
4.2	Gaussian Process Regression	37
4.2.1	Multivariate Gaussian	37
4.2.2	Gaussian Process	40
II	Application	43
5	Manipulating Quantum dots through lattice defects	44
5.1	Smoothly confined quantum dots in graphene	45
5.2	Model	46
5.3	Tunable Valley Splittings	51
5.4	Transition Dynamics	56

5.5 Conclusion	59
6 Defect parametrization via Machine Learning	60
6.1 Ab-initio modeling of defect super cells	60
6.2 Tight binding model	61
6.3 Inverse band structure problem	65
6.4 Algorithm comparison	66
6.4.1 Gradient-less descent	67
6.4.2 Bayesian optimization	68
6.4.3 Neural network models	71
6.5 Machine learning workflow	72
6.5.1 Data set generation	72
6.5.2 Training	73
6.5.3 Models for sparse parametrizations	75
6.6 Benchmarks	76
6.6.1 Band structure / LDOS	77
6.6.2 Electronic Transport	80
6.6.3 GQD spectra	81
6.7 Machine learning discrete Slater-Koster maps for a selenium di-vacancy in WSe ₂	83
6.8 Conclusion	87
7 Two particle spectra of bilayer graphene quantum dots	90
7.1 Introduction	90
7.2 Model and numerical trickery	91
7.3 Conclusion	96
8 Photoluminescence in strained WSe₂	97
8.1 Introduction	97
8.2 Experimental Photoluminescence of strained WSe ₂	99
8.2.1 Decoupling doping- and strain-induced effects	101
8.3 Modeling hybridization on the single particle level	102
8.4 Transition matrix elements of defect supercells	106
8.5 Comparison to experimental data	108
8.6 Other possible contributions to PL intensity of the suspended WSe ₂ system	109
8.7 Temperature dependent data	111
8.8 Conclusion	113
9 Grain boundaries as valley filters	115
9.1 TB models for symmetric line defects	116
9.2 Valley filtering via symmetry	117
9.3 Transport geometry	118
9.4 Valley polarization and bound defect states	121
9.5 Conclusion	124
10 Mapping quantum Hall edge states in graphene	125
10.1 Introduction	125
10.2 Experimental Observations	126
10.3 Rescaled TB model	129

10.4 Quantum dot states in single layer graphene (revisited)	130
10.5 Poisson calculations for the potential of TIQD and PN junction	132
10.6 From 1D Poisson to 2D Tight binding	136
10.7 Understanding STM measurements via LDOS maps	137
10.8 Conclusion	143
11 Quantum Hall conductivity of graphene-hBN moirés	144
11.1 Technicalities	144
11.1.1 A realistic moiré TB Hamiltonian	144
11.1.2 Efficient band structure calculations on dense \mathbf{k} -grids	146
11.2 From bandstructure to quantum Hall conductivity	147
11.3 Outlook	151
12 Composite super-moiré lattices in twisted bilayer graphene on hexagonal boron nitride	152
12.1 Introduction	152
12.2 Modelling two moiré superlattices in concert	153
12.3 Device characterization and band gap asymmetries	155
12.4 Magnetotransport simulations	158
12.5 Conclusion	160
13 Summary	161
Appendices	165
A Band structure reconstruction for the sparse ML models	168
B Sample fabrication and measurement details	172
C Valley character of QDOT states in SLG	177
D LDOS maps of the QDOT - PN system	179
E Charging lines in scanning tunneling spectroscopy	189
F Strain influence on the branching features	194
G Magnetotransport in a composite moiré system	196
Bibliography	223

Chapter 1

Introduction

“The scientist is not a person who gives the right answers, he is one who asks the right questions.”

C. Levi-Strauss

Imperfections are at the heart of what makes life interesting and exciting. They add character and charm to otherwise mundane objects. Without flaws, life would be boring and dull. In the context of materials science this certainly seems debatable and the answer depends on whether you talk to a frustrated PhD student that tries to measure a fragile effect in an unclean sample or a professor in theoretical solid state physics that vigorously insists on the importance of disorder to explain something as impressive as the integer quantum Hall effect. Occasionally, modern science and engineering even has us go out of our way to diminish the symmetries of an otherwise immaculate crystal structure of electronic devices to improve their desired properties (e.g. strain engineering [1–5]).

While process control in conventional, silicon based technologies — the workhorse of modern electronics design — is unparalleled in the fabrication of defect-free single crystals, novel materials in the early stages of their development often cannot be produced to the same quality standards. One subclass of prominent new materials are so called two-dimensional materials (layered crystals which can be thinned down to a monolayer). Starting with graphene (an atomically thin layer of graphite) in 2004 [6], research efforts towards the isolation of other 2D crystals [7] has brought forward a whole zoo of low dimensional materials ranging from metals, semi-metals, semiconductors to insulators. Apart from interesting physical effects emerging from their low dimensionality (e.g. linear dispersion, modified screening properties or spin-valley-locking in TMDs) these layered materials — by definition almost entirely made up of surface — are prone to modification by controlling their immediate surroundings (e.g. application of electromagnetic fields or substrate interaction). Continuous improvements in sample quality and measurement accuracy [8] has allowed the experimental realization of impressive achievements such as probing the multiplet structure of precisely controlled BLG quantum dots [9], single photon emitters in TMDs [10] or unconventional superconductivity in magic-angle tBLG [11], observation of a fractional quantum Hall effect in graphene [12, 13]. This recent amount of exceptional experimental data beckons theorists to advance and improve their predictive tools for both qualitative and quantitative analysis.

Furthermore, these 2D materials become especially interesting — albeit evermore challenging to describe from a theoretical perspective — if their intrinsic tuneability is employed for device manipulation. This internal modification may correspond to a change in twist angle of a bilayer system or the introduction of local lattice defects and generally require multi-scale approaches to allow theory comparable to experimental data. Over time the community established more or less two approaches to model the influence of defects on experimentally accessible systems. While a fairly straightforward description such as creating a vacancy via omission of an atomic site in an otherwise unrelaxed lattice (nevertheless to some extent also employed throughout this thesis) that lives entirely on the tight-binding level of theory tends to come short in terms of quantitative analysis, high-quality ab-initio derived tight-binding parametrizations that can be embedded into a model of much larger, pristine structures tend to be elusive and cumbersome in their extraction. Obviously, the latter models are much better candidates for experimental comparison. The interdependent analysis of both quantitative and qualitative agreement with measurements will guide us through most of this thesis.

This thesis is structured in two parts: Part I introduces the foundations of concepts in solid state theory and machine learning and Part II contains various projects and applications.

Prominent 2D materials and crystal structures studied throughout this work are introduced in Chapter 2. We present the electronic structure of the pristine systems and briefly outline different types of lattice defects.

Chapter 3 introduces the work horse solid-state-theories *tight-binding* and *density functional theory*. We discuss fundamental concepts and glimpse at computational aspects.

Chapter 4 gives a general introduction into machine learning aspects. In the grand scheme of this discipline our chapter only scratches the surface yet provides enough background for the algorithms encountered in Chapter 6. We give a concise definition of the discipline and follow with descriptions of neural network architectures and their “inner workings”. We conclude this chapter as well as Part I with describing Gaussian process regression and hope to convey not only the abstract concept but also its immense usefulness for modern optimization problems.

Part II opens with Chapter 5, where we explore the influence of several lattice defects of single layer graphene on the energy spectra of nearby edge-free quantum dots. In the presence of a strong magnetic field the electrical field of a scanning tunneling microscopy tip can localize electrons in graphene [14]. In theory, traversal of isolated lattice defects allows for controlled lifting of the valley degeneracy and could even induce controlled transitions between quantum dot levels.

Chapter 6 documents the joint efforts with the group of P. Rinke at the Aalto University to establish a machine learning based algorithm that efficiently extracts high-quality tight-binding parametrizations of defects in graphene and WSe₂ systems. We find that neural networks that learn a mapping between band structure data and a minimal set of hopping

parameters can, to some extent, provide an alternative route that does not rely on maximally localized Wannier functions.

In Chapter 7 we implement a Hartree-Fock algorithm to try to explain experimental data on the two-particle spectra of bilayer graphene quantum dots from the group of C. Stampfer at the RWTH Aachen. Our model re-diagonalizes a bare Coulomb kernel in basis states of a $\mathbf{k} \cdot \mathbf{p}$ Hamiltonian for Bernal stacked bilayer graphene in cylindrical coordinates.

Chapter 8 reports on a joint project with the group of S. Heeg at the Universität zu Berlin. We find signatures of hybridization of defect related states in WSe_2 that lead to resonances in photoluminescence measurements. We carefully disentangle doping and strain influences of the electrostatic based straining setup.

In Chapter 9 we study the valley filtering properties of grain boundaries in single layer graphene. We review simple symmetry arguments provided of [15] in the context of ab-initio derived parametrizations of periodic line defects in conjunction with first rate, 10th-nearest neighbour bulk descriptions.

Chapter 10 dissects scanning tunneling microscopy measurements of the group of M. Morgenstern at the RWTH Aachen. We study Landau quantized, single-layer graphene in strong perpendicular magnetic fields. Careful estimation of relevant parameters from experimental data followed by Poisson simulations of the electrostatic potential of a back gate induced p-n-junction culminates in large scale tight-binding simulations that accurately explain experimental features.

Chapter 11 discusses our efforts to calculate quantum Hall conductivities of graphene-hBN moiré systems from ab-initio derived real space tight-binding models. We employ highly efficient algorithms to produce finely sampled band structures. Employing Stréda's formula allows us to obtain the Hall conductivity within band gaps but is inappropriate for comparisons with experimental data.

Lastly we study magnetotransport through a system of composite moiré super lattices in Chapter 12. Together with our experimental collaborators from the group of C. Stampfer at the RWTH Aachen we find additional Landau fan features at non-integer fillings and pinpoint their origin to an additional moiré lattice with one of the hBN layers used for encapsulation.

Part I

Theory

Chapter 2

2D crystals & lattice defects

“In physics, you don’t have to go around making trouble for yourself - nature does it for you.”

F. Wilczek

Materials science is typically interested in understanding, modeling and possibly predicting the physical (or chemical) properties of materials. Early research was mostly interested to explain these traits based on what a particular substance was made of (i.e. atom type and bonding character). It took some time to understand that the fundamental properties of matter also depend on its size: electrical conductivity, chemical reactivity and even light matter interaction need not necessarily be identical if some of the materials dimensions approach the nano scale (i.e. anywhere between the atomic scale of a few Å and up to a few hundred nanometers). Once the thickness of a material gets negligible we can effectively speak of a two dimensional material.

The first two dimensional crystal (i.e. a structure with long range periodic order in only two dimensions) that was successfully extracted in experiment was graphene, a single atomic layer of graphite (honeycomb carbon lattice) [6, 16]. This discovery has since sparked an entire research field that includes a zoo of different 2D materials [17, 18]. What follows is a brief introduction to a small subset of these materials (the ones relevant to the projects in this thesis).

2.1 Graphene

Graphene [19] is a single atomic layer of graphite (a highly lamellar allotrope of carbon). The four valence electrons of each carbon atom ($[He]2s^22p^2$) hybridize into 3 sp^2 orbitals (in-plane σ bonds) and a single p_z orbital (protected from hybridization by mirror symmetry, assuming a perfectly flat hexagonal lattice). The unit cell of this lattice holds two carbon atoms (henceforth addressed as “A” and “B”) at $(0,0)^T$ and $a \cdot (0, 1/\sqrt{3})^T$ respectively.

Given the lattice constant $a = 2.46\text{\AA}$, a unit cell (see Fig. 2.1) can be spanned by the following real space lattice vectors:

$$\mathbf{a}_1 = \begin{pmatrix} a \\ 0 \end{pmatrix} \quad \mathbf{a}_2 = \begin{pmatrix} -a/2 \\ \sqrt{3}a/2 \end{pmatrix} \quad (2.1)$$

The diatomic basis of entirely indistinguishable carbon atoms introduces the sublattice degree of freedom (i.e graphene is made of two interwoven triangular lattices) which also has implications in reciprocal space. The reciprocal lattice vectors read:

$$\mathbf{G}_1 = \frac{2\pi}{\sqrt{3}a} \begin{pmatrix} \sqrt{3} \\ 1 \end{pmatrix} \quad \mathbf{G}_2 = \frac{4\pi}{\sqrt{3}a} \begin{pmatrix} 0 \\ 1 \end{pmatrix} \quad (2.2)$$

The 1st Brillouin zone of graphene is again hexagonal and includes several high-symmetry points (see Table 2.1). The most prominent points (K and K') are known as Dirac points and mark the reciprocal positions where conduction and valence band of graphene touch and build the gapless Dirac cone structure (see Fig. 2.1e).

Γ	$\begin{pmatrix} 0 \\ 0 \end{pmatrix}$	D_{6h}
K	$\frac{4\pi}{3a} \begin{pmatrix} 1 \\ 0 \end{pmatrix}$	D_{3h}
K'	-K	D_{3h}
M	$\frac{\pi}{\sqrt{3}a} \begin{pmatrix} \sqrt{3} \\ 1 \end{pmatrix}$	C_2

Tab. 2.1: Name, coordinates and symmetry groups (Schönflies notation) for the high symmetry points of the hexagonal lattice in reciprocal space.

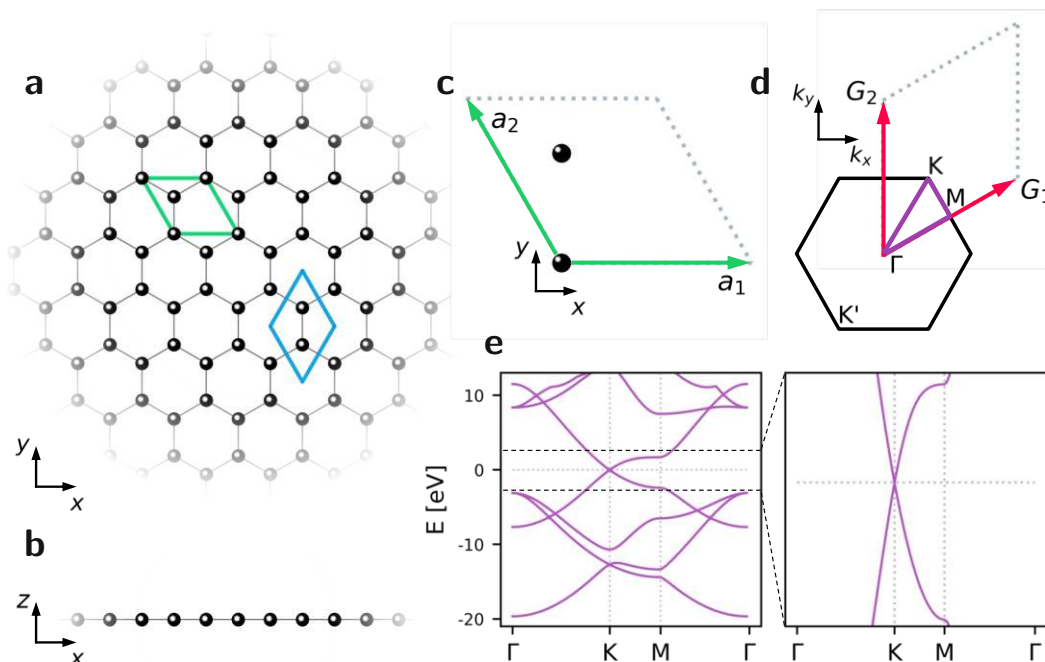


Fig. 2.1: Schematic honeycomb lattice of graphene (black carbon atoms with grey bonds) in **a** x, y plane (including the Wigner Seitz cell - blue rhombus) and **b** x, z plane. **c** Unit cell employed throughout this thesis (see also **a**). **d** Reciprocal unit cell spanned by \mathbf{G}_1 and \mathbf{G}_2 . The black hexagon represents the 1st Brillouin zone of graphene. High symmetry points of the hexagonal lattice including the k-point path for the band structure plots are indicated. **e** Band structure of single layer graphene (computed along the path shown in **d**) including zoom-in of the Dirac cone close to the Fermi energy.

K and K' are referred to as valleys and are intimately connected to the real space sublattice symmetry. The dispersion in their vicinity is linear and mimics the solution of a massless Dirac equation in ultra-relativistic quantum mechanics [20, 21]. Vanishing density of states at the Fermi level (which for undoped graphene coincides with the Dirac point) together with the lack of a real band gap classifies graphene as a peculiar *semi metal* somewhere in between semiconductor and metal.

The additional valley degree of freedom compared to conventional electronics materials (such as GaAs [22]) in combination with the linear dispersion relation give rise to many unique electronic properties of graphene (see [19, 23] for an in-depth introduction).

Graphene also exhibits high deformability allowing for elastic strains of up to 15% [24]. The valley degree of freedom with its two minima positioned in opposite corners of the Brillouin zone allows for the emergence of effective pseudo gauge fields in the presence of large wavelength deformations [25–28]. However, while isotropic and uniaxial strain only generate a pseudo-electric field [29] triaxial strain offers the prospect of inducing strong and uniform pseudo-magnetic fields in the order of several Tesla. It is worth noting that deformations locally change the interatomic distances and therefore in some configurations affect hopping amplitudes in a way that manifests in a gauge field that manipulates electron similar to a magnetic field. Naturally, pseudo-fields generated from these “artificial” vector potentials do not break time-reversal symmetry. Controlled introduction of mechanical strain [30–32] thus offers an alternative approach of altering electronic properties of graphene. Conversely, strain that is unintentionally introduced during the fabrication process may alter the electronic structure in an undesired way.

2.1.1 $\mathbf{k} \cdot \mathbf{p}$ Hamiltonian

Somewhat preemptively to Section 3.3 I choose to simply introduce the Dirac Hamiltonian as an approximative description for single layer graphene in the vicinity of the two inequivalent valleys $\tau = \pm 1$ (representing K and K' points respectively) at this point (instead of deriving it as a linearization of the full tight binding Hamiltonian of graphene, see [19]).

Single layer graphene To first order in momentum the gapless double cone-like band structure of single layer graphene may be described in terms of a massless Dirac Hamiltonian:

$$H_\tau = v_f \begin{bmatrix} 0 & \tau p_x - i p_y \\ \tau p_x + i p_y & 0 \end{bmatrix} \quad (2.3)$$

The solutions to $H\psi = E\psi$ are then of the following form:

$$E_{\tau,\pm} = \pm v_f |\mathbf{p}| \quad \psi_\pm = \frac{1}{\sqrt{2}} \left(\begin{array}{c} 1 \\ \pm e^{i\tau\phi} \end{array} \right) e^{\frac{i\mathbf{p}\cdot\mathbf{r}}{\hbar}} \quad (2.4)$$

where \pm refers to conduction and valence band respectively and $\phi = \arctan(p_y/p_x)$. The spinor components refer to the two sublattice sites

in the real space unit cell (and is rightfully referred to as pseudo spin). The off diagonal parts of Eq. (2.3) can be coupled via a mass term with opposite signs for each sublattice (i.e. $(m_A - m_B)/2\sigma_z = m\sigma_z$) which effectively opens a band gap in the dispersion, $E = \pm\sqrt{v_f^2|\mathbf{p}|^2 + m^2}$. It is worth noting that on their own the two variations of Eq. (2.3) (i.e. the two valleys $\tau = \pm 1$) break both parity and time reversal symmetry but restore them when combined (both parity and time reversal map the valleys onto each other).

Bilayer graphene Stacking two graphene layers results in a bilayer system (experimentally distinguishable via e.g. Raman spectroscopy [33]) with parabolic dispersion and a field-tunable band gap. The degrees of freedom for this stacking (x shift, y shift, relative angle) can generate rich physics in the form of moiré structures [34]. Bernal stacking (see Fig. 2.2) describes two perfectly aligned but slightly shifted sheets such that the sublattice sites A_2 and B_1 (two sublattices in each layer, i.e. A_1, B_1, A_2, B_2) are vertically aligned (*dimer site*).

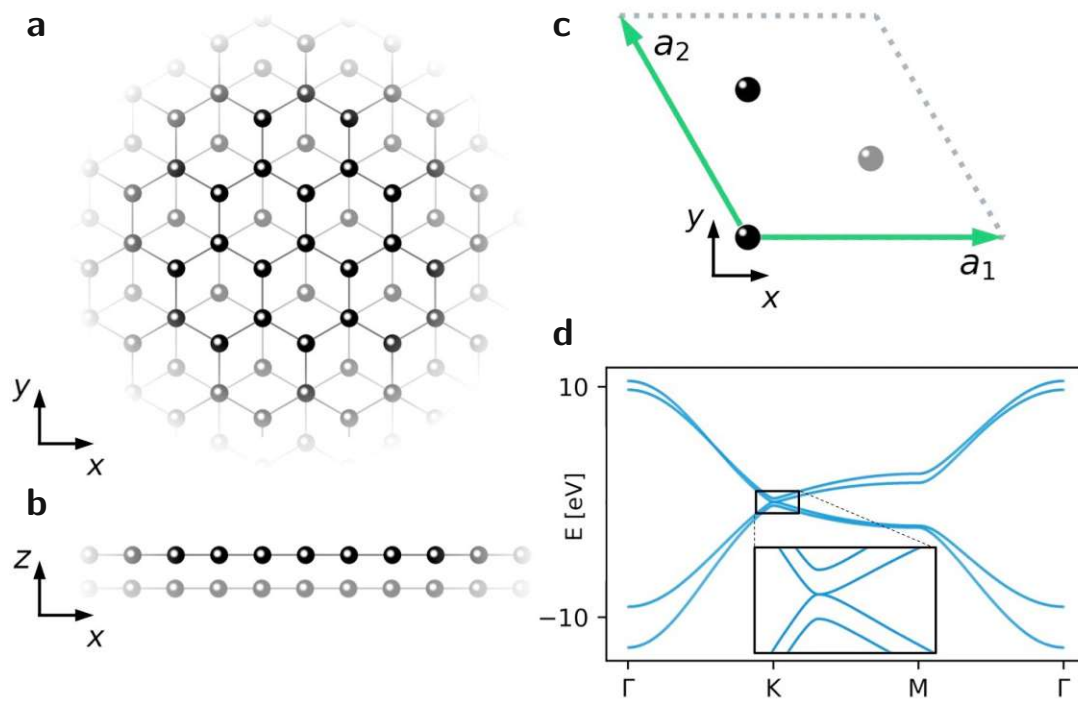


Fig. 2.2: Schematic structure of Bernal stacked bilayer graphene (bottom layer slightly opaque) in **a** x,y plane and **b** x,z plane. **c** Unit cell with 4 atoms (two of them congruent in z view). **d** Bandstructure along Γ KM Γ including zoom-in close to the Fermi energy highlighting the now quadratic dispersion.

An approximative but still reasonable model for the bilayer system is given by two single layer Dirac Hamiltonians and an interlayer coupling γ_1 at the dimer site:

$$H_\tau = v_f \begin{bmatrix} 0 & \tau p_x - ip_y & 0 & 0 \\ \tau p_x + ip_y & 0 & \frac{\gamma_1}{v_f} & 0 \\ 0 & \frac{\gamma_1}{v_f} & 0 & \tau p_x - ip_y \\ 0 & 0 & \tau p_x + ip_y & 0 \end{bmatrix} \quad (2.5)$$

where we now use a four component wave function basis of the form $\Psi = (\psi_A, \psi_B, \psi_{A'}, \psi_{B'})^T$. Inserting the second and third row of $H\Psi = E\Psi$ into one another:

$$\psi_{A'} = \frac{E^2}{\gamma_1^2} \psi_{A'} - \frac{E^2 v_f}{\gamma_1^2} (\tau p_x - ip_y) \psi_{B'} - \frac{v_f}{\gamma_1} (\tau p_x + ip_y) \psi_A \quad (2.6)$$

$$\psi_B = \frac{E^2}{\gamma_1^2} \psi_B - \frac{E^2 v_f}{\gamma_1^2} (\tau p_x + ip_y) \psi_A - \frac{v_f}{\gamma_1} (\tau p_x - ip_y) \psi_{B'} \quad (2.7)$$

and plugging them into the first and last row respectively, yields an effective low energy equation for the non-dimer sites:

$$E_\tau \begin{pmatrix} \psi_A \\ \psi_{B'} \end{pmatrix} = -\frac{v_f}{\gamma_1} \begin{bmatrix} 0 & (\tau p_x - ip_y)^2 \\ (\tau p_x + ip_y)^2 & 0 \end{bmatrix} \begin{pmatrix} \psi_A \\ \psi_{B'} \end{pmatrix} \quad (2.8)$$

Solutions then take the form:

$$E_{\tau,\pm} = \pm \frac{v_f}{\gamma_1} |\mathbf{p}|^2 \quad \psi_\pm = \frac{1}{\sqrt{2}} \begin{pmatrix} 1 \\ \mp e^{i2\tau\phi} \end{pmatrix} e^{\frac{i\mathbf{p}\cdot\mathbf{r}}{\hbar}} \quad (2.9)$$

describing parabolic bands near the K/K' points.

Bilayer graphene provides another highly useful property in the form of displacement-field induced band gap opening [35–37]. A strong enough perpendicular electric field introduces a potential difference Δ between top and bottom layer of bilayer graphene,

$$H_\tau = \frac{v_f^2}{\gamma_1} \begin{bmatrix} \frac{\Delta}{2} & (\tau p_x - ip_y)^2 \\ (\tau p_x + ip_y)^2 & -\frac{\Delta}{2} \end{bmatrix} \quad (2.10)$$

which in turn leads to an energy spectrum of

$$E_{\tau,\pm} = \pm \sqrt{\frac{\mathbf{p}^4}{\gamma_1 v_f^4} + \frac{\Delta^2}{4}} \quad (2.11)$$

for the low-energy two-band model. We have thus opened a band gap of roughly Δ . Solving the full four-band model numerically only adds a small correction to this result. Voltages accessible in experiment can therefore open band gaps on the order of up to 40 meV. In practice this allows one to electrostatically define quantum point contacts and localize electrons in bilayer graphene quantum dots in a way that preserves valley information (in contrast to physical patterning). Closer inspection reveals that such a displacement field effectively upends the quadratic dispersion and for strong enough fields introduces three mini-valleys per Dirac cone [38].

Interestingly, introducing a mass term $\propto \sigma_z$ in sublattice space that causes a potential difference between the trigonal sublattices within one graphene layer also opens a band gap. While such a configuration cannot be exploited experimentally theorists often employ this approach in numerical calculations as a robust method to avoid edge states [39].

2.2 Transition metal dichalcogenides

Transition metal dichalcogenides (TMDs) represent a family of 2D materials commonly made up of one transition metal atom (molybdenum Mo or tungsten W) and two chalcogen atoms (sulfur S, selenium Se or tellurium Te). Similar to graphite their bulk form is a van der Waals stack of individual three atom thick layers (metal sandwiched between chalcogen atoms, see Fig. 2.4). The electronic structure of the metal and chalcogen are typically well described by d orbitals and p orbitals respectively [40, 41]. I will briefly introduce WSe₂ and point out general aspects as well as differences to the other TMDs whenever relevant.

2.2.1 Tungsten diselenide WSe₂

The unit cell of tungsten diselenide ($\mathbf{a}_1 = (\mathbf{a}, 0)^T, \mathbf{a}_2 = (-\mathbf{a}/2, \sqrt{3}\mathbf{a}/2)^T$) is hexagonal and features three atoms ($1 \times W, 2 \times Se$) positioned at $\mathbf{r}_W = (0, 0, 0)^T$ and $\mathbf{r}_{Se} = (0, \mathbf{a}/\sqrt{3}, \pm\bar{z})^T$ with lattice constant $\mathbf{a} = 3.32 \text{ \AA}$ and layer separation $\bar{z} = 1.67 \text{ \AA}$ (see Fig. 2.4). TMDs are a good example for the change of properties (e.g. phonon frequencies [47]) when transitioning from bulk (i.e. several layers) to the mono layer [48, 49]: Bulk TMDs are generally indirect band gap semiconductors (see Table 2.2) with valence band maxima at Γ and conduction band minima at K/K' (or $Q = \bar{\Gamma}K/2$). This changes when removing the neighboring layers (and thus the interlayer coupling mediated for the most part by the chalcogen atoms) and the new valence band maximum is shifted to K/K' . However, for WSe₂ there is some evidence that the nature of the monolayer band gap may remain indirect (minimal gap ΔE_{KQ} [50]). Semi-local density functional theory [51] is known to heavily underestimate the quasiparticle band gap of TMDs (see also Table 2.2). This shortcoming is of little consequence for the character of the involved states and can (for most investigations) be fixed by scissor operators (i.e. a rigid shift of the conduction bands without altering their wave functions [52]) which can increase the band gap to some experimentally verified value. The position of the conduction band minima in reciprocal

TMD	exp. [eV]	DFT ^b [eV]
MoS ₂	2.5 ^a	1.59
MoSe ₂	2.18 ^c	1.34
WS ₂	2.14 ^d	1.58
WSe ₂	2.51 ^e	1.27

Tab. 2.2: Measured and calculated band gaps (ΔE_{KK}) for prominent TMDs. ^a[42], ^b[43], ^c[44], ^d[45], ^e[46]

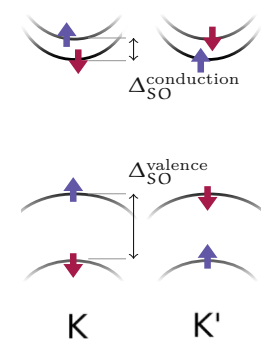


Fig. 2.3: Illustration of the spin-valley texture of WSe₂ in K and K'.

space is also heavily influenced by strain [53]. This becomes immediately relevant in Chapter 8.

The electronic band gap in TMDs is furthermore substantially renormalized by massive exciton binding energies (several hundred meV, [54, 55]). An effect ascribed to the strongly suppressed screening mechanisms in 2D materials [56]. The different types of TMDs all lack inversion symmetry which in combination with heavy metal cores ($\Delta_{SO} \propto Z^4$ with atomic $Z = 74(W)$ or $Z = 42(Mo)$) manifests large spin-orbit coupling. $\Delta_{SO}^{\text{valence}}$ gets up $\approx 500\text{meV}$ whereas $\Delta_{SO}^{\text{conduction}}$ remains on the order of a few meV. The sign of this spin splitting depends on the constituents of the TMD (opposite in valence and conduction band for Mo or identical for W, see Fig. 2.3). The spin splitting in the conduction band is maximal at the Q point (an important point in reciprocal space for possibly indirect relaxation processes in TMDs, albeit not a high symmetry point of the lattice). As non-centrosymmetric materials TMDs exhibit non trivial spin texture with opposite spin orientations in the K and K' valleys (see Fig. 2.4). This interrelation of spin and valley degree of freedom (*spin-valley locking* [57]) allows for both valley- and spin-selective excitation (*circular dichroism* [58]) and enables long lived spin and valley accumulations [59].

2.3 Crystal lattice defects

A perfect crystal is an idealization. There is no such thing in nature. A pristine crystalline structure, while it may indeed be preferred energetically, is in the limit of low temperatures (atoms are relatively immobile in solids⁰¹) difficult to achieve since eliminating whatever imperfections are introduced into the crystal during its growth, processing or use is unlikely. These defects come in a plethora of different variations and can among other criteria be categorized via concepts of topological homotopy [60].

point defects do not extend in any space dimension. They typically involve a few atoms at most, are historically called *centers* and can be specified via Kröger-Vink notation [61]. *Intrinsic point defects* do not introduce foreign atomic species into the crystal and thus only rearrange or add/remove indigenous atoms (e.g. vacancies, self-interstitials, anti-sites, topological defects, ...) while *extrinsic* or *impurity defects* add or substitute lattice sites via foreign atoms (e.g. impurity interstitial, add-atoms, substitutional centers, ...).

line defects are linear defects that extend in one dimension and can to some extent be described via gauge theories [62]. The constituents of this category also depend on the dimensionality of the material in question: Three dimensional crystals may feature edge and screw dislocations caused by premature termination of a plain of atoms or partial in-plane shifts of lattice planes. Those are defined via a *Burgers vector* [63]. Studying two-dimensional materials also introduces grain boundaries into this category.

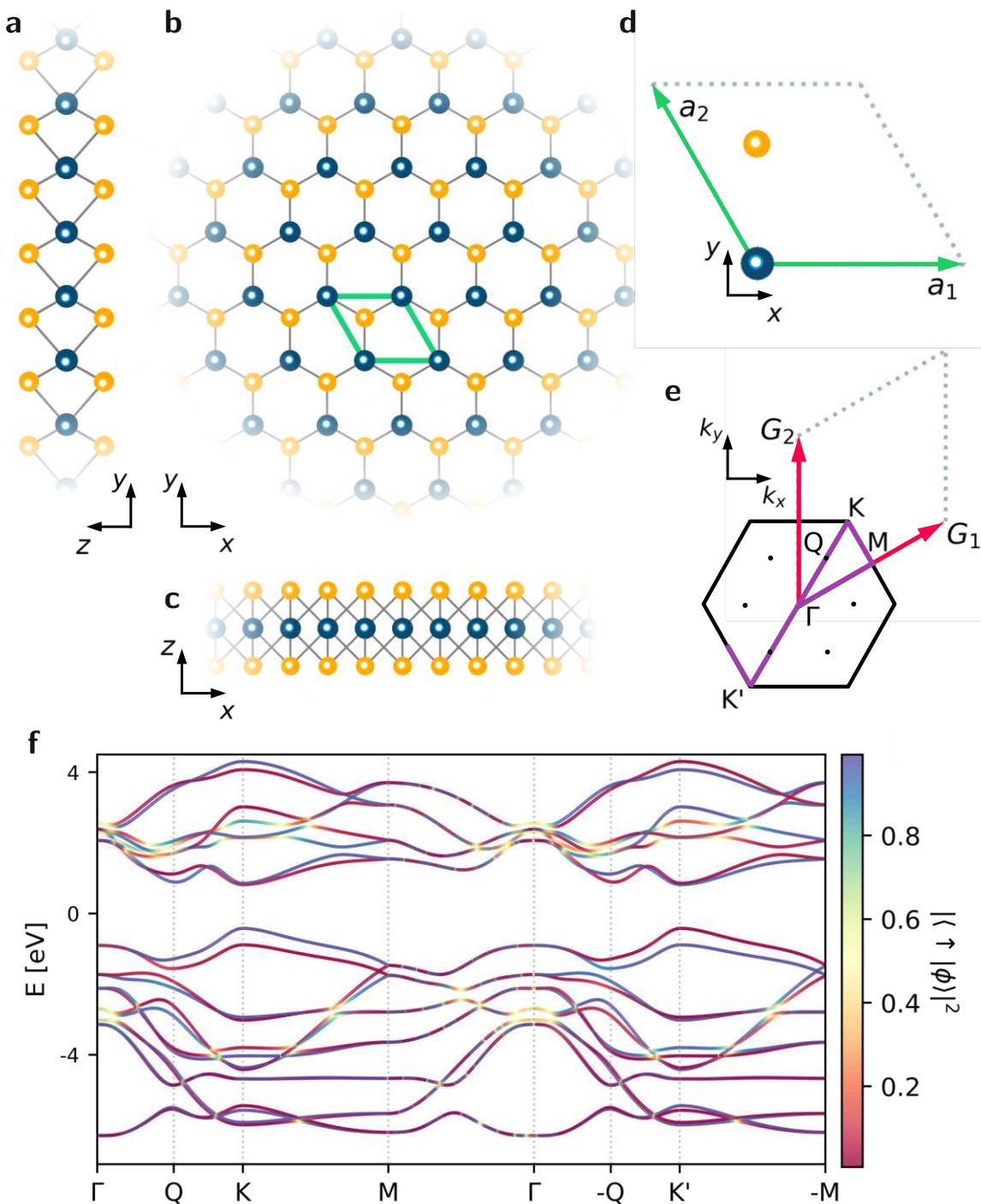


Fig. 2.4: Schematic lattice of tungsten-diselenide (WSe_2) (blue tungsten atoms and orange selen atoms, bonds indicated in grey) in **a** z, y plane **b** x, y plane and **c** x, z plane. **d** Unit cell employed throughout this thesis (see also **b**). **e** Reciprocal unit cell spanned by \mathbf{G}_1 and \mathbf{G}_2 . The black hexagon represents the 1st Brillouin zone of WSe_2 . High symmetry points of the lattice including the k -point path for the band structure plots are indicated. **f** Band structure of WSe_2 (computed along the path shown in **e**). Colorscale indicates spin character of the respective band in k -space.

planar defects extend in two dimensions and include: grain boundaries (of three dimensional materials), phase boundaries, stacking faults and many more. Interfacial defects typically separate regions of the material that have different crystal structures and or crystallographic orientations.

bulk defects are necessarily confined by planar defects and may take form as voids (whole cavities of vacant lattice sites), pores, impurity clusters and generally any form of conglomeration of point-, line- or planar-defects. These defects generally occur on a much larger scale than microscopic imperfections.

Continuous improvement in the fabrication and preparation of two-dimensional crystal structures [64, 65] has lead to excellent sample qualities with low defect densities and high mobilities. To some extent it is also possible to purposefully re-introduce certain defects in a controlled manner to influence material properties via defect engineering [66, 67]. These processes typically involves irradiation with either photons or high-energy particles. Depending on defect formation energies and temperature it is also possible for defects to migrate (possibly with a preference along certain crystallographic directions) and rearrange into other configurations (e.g. two vacancies transitioning into a di-vacancy).

The presence of lattice defects may introduce non-dispersive defect levels into the band structure. These flat bands typically correspond to electronic states localized in the real space vicinity of a point defect. Depending on the local chemical structure of the defect (e.g. dangling bonds, different coordination numbers) these defect levels may emerge at energies well inside the band gap. Such configurations are referred to as *deep* defect levels and tend to bind charge carriers much more strongly. Due to their high ionization energies deep levels contribute very little to the free charge carriers. Defects that introduce these deep levels (also called *traps* or *recombination centers*) can be both desirable (e.g. switching devices that can exploit these recombination centers to quickly remove minority carriers [68, 69]) and a nuisance (e.g. reducing efficiency of photovoltaic cells).

Another, oftentimes more interesting configuration is if such a flat defect band emerges close to a band edge (≈ 0.1 eV energy separation allows for thermal ionization). Ionization energies can often be described by modified hydrogen models. These states are referred to as *donor* or *acceptor* depending on whether they are close to the conduction or valence bands respectively. Shallow defects drastically alter electronic or optical properties in 2D semiconductors such as gapped bilayer graphene or TMDs. One such example would be vacancy defects in WSe₂ that are theorized to host donor bound excitons and act as single photon emission centers. This topic is also explored in Chapter 8.

⁰¹ “Solids always feel quite frosty.”, Prof. Reissner while deriving expressions for the Debye temperature in *solid state theory I*.

2.4 Moiré systems

Bilayer systems of 2D materials can generate superordinate periodicity if certain conditions are met. Aligned *Hetero-bilayers*, stacks of two different 2D materials, with slightly different lattice constants can display long-range periodic patterns to form so-called *moiré* super cells [70]. These patterns usually consist of a large number of primitive unit cells of the constituent materials and thus introduces a new, much larger length scale into the system. Bilayers of the same materials, *homo-bilayers*, can also display moiré patterns if the individual layers are slightly rotated with respect to each other.

While homo-bilayers with hexagonal symmetry show quasi-periodic structures for all angles, perfect periodicity is only obtained for so-called commensurable twist angles $\theta_{\text{comm.}}$ [71, 72],

$$\cos(\theta_{\text{comm.}}) = \frac{3m^2 + 3mr + \frac{r^2}{2}}{3m^2 + 3mr + r^2} \quad \text{with } m, r \in \mathbb{N} \quad (2.12)$$

The new, generally larger moiré unit cell (see Fig. 2.5) is then (up to shifts of origin) obtained via

$$\begin{pmatrix} A_1 \\ A_2 \end{pmatrix} = \begin{bmatrix} m+r & m \\ 2m+r & -(m+r) \end{bmatrix} \begin{pmatrix} a_1 \\ a_2 \end{pmatrix} \quad (2.13)$$

While for sufficiently large m, r the commensurable angles seem densely ranked (not in the mathematical sense), in reality lattice relaxation has to be taken into account. Obviously, this reconstruction is twist-angle dependent and will render some configurations energetically more stable than others. This (apart from many other obstacles a theorist knows little about) makes precise adjustment of bilayer twist angles experimentally quite challenging [73–75].

Hetero-bilayers with marginally different lattice constants a, a' (e.g. graphene/hBN) also generate moiré patterns for vanishing twist angle. The new lattice periodicity λ then depends on lattice constant mismatch $\epsilon = \frac{a'}{a} - 1$ as well as the twist angle θ [76]:

$$\lambda = \frac{a(1+\epsilon)}{\sqrt{\epsilon^2 + 2(1+\epsilon)(1-\cos(\theta))}} \quad (2.14)$$

Unfortunately moiré effects often become relevant when the supercell size (number of atoms in moiré unit cell $\propto 1/\theta^2$) is already too large for density functional theory [77, 78]. While there exist works of computationally demanding supercell DFT calculations [72, 79–82], L. Linhart (a PhD predecessor in our group) has implemented ab-initio derived tight-binding models [83, 84] based on sampling the local stacking configuration in large moiré cells and mapping to small untwisted DFT calculations (see Chapter 11 for details). It is also worth noting that in stacked systems consisting of

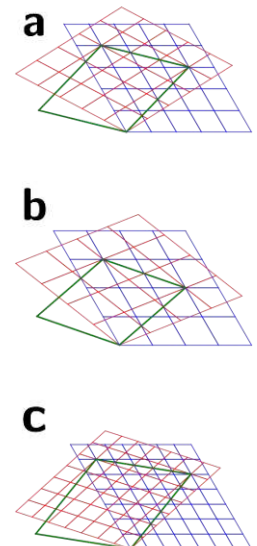


Fig. 2.5: Illustration of commensurable moiré unit cells (green) for twisted bilayers (top layer - red, bottom layer - blue) for
a $m=1, r=2$ ($\theta \approx 32^\circ$)
b $m=1, r=1$ ($\theta \approx 21^\circ$)
c $m=1, r=4$ ($\theta \approx 42^\circ$)

more than two layers one may form competing moiré lattices at more than one interface. These concurring structures would then in theory again form an even larger super moiré lattice. Depending on their relative energy scales one of the moiré subsystems may dominate physical properties. Chapter 12 discusses the appearance of two competing moiré lattices in hBN/tBLG stacks in the context of magnetotransport measurements

Chapter 3

Methods of solid state physics

“In the beginning there was nothing, which exploded.”

T. Pratchett

3.1 Bloch's theorem

We can describe crystalline systems (systems with long-range periodic order) via a Hamiltonian \hat{H} that includes a potential \hat{V} which respects the periodicity of the lattice:

$$\hat{V}(\mathbf{r}) = \hat{V}\left(\mathbf{r} + \underbrace{\sum_{i=1}^3 \lambda_i \mathbf{a}_i}_{\mathbf{t}}\right) \quad \text{with} \quad \lambda_1, \lambda_2, \lambda_3 \in \mathbb{Z} \quad (3.1)$$

with lattice vectors \mathbf{a}_i (see for example Fig. 2.1) and \mathbf{t} a general translation along these real space lattice vectors. The density $n(\mathbf{r}) = |\langle \psi | \mathbf{r} \rangle|^2$ has to respect the same periodicity while the wavefunction, itself not a physical observable, only needs to be periodic up to a uni-modular phase factor:

$$\psi_{\mathbf{k}}(\mathbf{r} + \mathbf{t}) = e^{i\mathbf{k} \cdot \mathbf{t}} \psi_{\mathbf{k}}(\mathbf{r}) \quad (3.2)$$

Furthermore we can separate the wavefunction into a lattice periodic part $u_{\mathbf{k}}(\mathbf{r}) = u_{\mathbf{k}}(\mathbf{r} + \mathbf{t})$ (i.e. meaningfully defined only within the unit cell) and a phase factor (Bloch phase) $\psi_{\mathbf{k}}(\mathbf{r}) = e^{i\mathbf{k} \cdot \mathbf{r}} u_{\mathbf{k}}(\mathbf{r})$. This insight by Felix Bloch [85] has since been exploited in many computational implementations and is a workhorse theorem in solid state physics.

3.2 Density functional theory

In computational materials science few methods are applied as frequently as density functional theory (DFT) to understand and predict the electronic structure of condensed matter. Not unlike Thomas-Fermi theory [86, 87] but first formulated by Hohenberg and Kohn [88, 89] DFT is a versatile quantum mechanical theory that solves the scaling problem of the many-body Schrödinger equation by choosing the electron density $n(\mathbf{r})$ as its key variable.

The Hohenberg-Kohn theorems (somewhat generalized [90–92] from their initial formulation) constitute the basis for this theory:

- I) Both the external potential $V_{\text{ext}}(\mathbf{r})$ and the total energy E are unique functionals of the ground state density $n(\mathbf{r})$ (typically proven via *reductio ad absurdum*).
- II) $E[n]$ is minimal as $n(\mathbf{r})$ approaches the exact ground state density.

This energy functional is of the form:

$$E[n] = T_{\text{ni}}[n] + \underbrace{E_V[n]}_{\int V_{\text{ext}}(\mathbf{r}) n(\mathbf{r}) d\mathbf{r}} + \underbrace{E_{\text{Hartree}}[n]}_{\frac{e^2}{2} \iint \frac{n(\mathbf{r}) n(\mathbf{r}')}{|\mathbf{r} - \mathbf{r}'|} d\mathbf{r} d\mathbf{r}'} + \underbrace{E_{xc}[n]}_{E_x[n] + E_c[n]} \quad (3.3)$$

and includes the kinetic energy $T_s[n]$ (of a non-interacting system with identical density), the external potential contribution $E_V[n]$ as well as the Hartree term $E_{\text{Hartree}}[n]$ on an exact level. Furthermore it contains contributions that are not known exactly and thus constitute a form of approximation. These terms are collected into an exchange-correlation functional $E_{xc}[n]$ that is also defined with deceptive simplicity by the above equation as the difference between the exact functional and the sum of T_{ni} and E_{Hartree} . It is common practice to further subdivide this term into correlation $E_c[n]$ and exchange $E_x[n]$ contributions. While the latter is defined as the Hartree-Fock exchange energy functional, the correlation part is then defined as the difference between the exact functional and the Hartree-Fock approximation to the exact functional. Both exchange and correlation can be properly treated with diagrammatic techniques in many-body theory (which leaves the realm of mean-field theories such as DFT and therefore the scope of this thesis). Improving the available approximations for $E_{xc}[n]$ is still an active field of research [93, 94]. Simple and yet surprisingly accurate approximations are semi-local functionals that only depend on the electronic density $n(\mathbf{r})$ (local density approximation (LDA) [51, 95]) and/or its gradient $\nabla n(\mathbf{r})$ (generalized gradient approximation (GGA)) where respecting the exchange-correlation-hole sum rule proved vital for error cancellation [96].

Variational minimization of the total energy functional Eq. (3.3), $\delta E[n]/\delta n = 0$ yields the Kohn-Sham equations,

$$n(\mathbf{r}) = \sum_{i=1}^N f_i |\phi_i(\mathbf{r})|^2 \quad (3.4)$$

$$\left[-\frac{\hbar^2 \nabla^2}{2m} + \underbrace{V_{\text{eff}}(n(\mathbf{r}), \mathbf{r})}_{V_{\text{ext}} + \frac{\delta E_{\text{Hartree}}[n]}{\delta n} + \frac{\delta E_{xc}[n]}{\delta n}} \right] \phi_i(\mathbf{r}) = \varepsilon_i \phi_i(\mathbf{r}) \quad (3.5)$$

which, while deceptively similar to Schrödinger-like equations, are typically solved self-consistently (mind their non linearity due to $V_{\text{eff}}(n(\mathbf{r}), \mathbf{r})$). In this formulation of DFT we have opted to solve for wave functions ϕ_i (Kohn Sham orbitals) to generate an electronic density from (according to the occupation function f_i). While the resulting scaling of $\mathcal{O}(N^3)$ (with N the total number of electrons) limits DFT to systems no larger than

roughly several hundred atoms it is often preferable over direct functional minimization of $E[n]$ (orbital free DFT) since the treatment of the kinetic energy contributions become far less accurate with only the density as a working variable [97].

In order to solve the non-linear eigenvalue equations Eq. (3.5) numerically it is customary to expand our solution in a suitable set of basis functions $\{\Phi_i\}$. There are two main types of basis sets with fundamentally different properties: localized pseudo-atomic orbitals (PAO) and delocalized plane waves (PW) and lots of subcategories of the former. PW basis sets consist of so called *augmented plane waves* truncated at a certain energy cut-off that thus also controls the resolution of the real-space grid. In order to reduce the necessary basis set size the system under consideration is typically divided into active and spectator electrons with the latter efficiently replaced by additional pseudo potentials (non-local potential terms that enforce the Pauli exclusion of the now absent core levels). PW basis sets are equally applicable to molecules or solids and display convenient convergence properties. Most modern localized basis sets are some variation of contracted Gaussian-type orbitals (CGTO) ($\Phi_{abc}^{\text{CGTO}}(x, y, z) = \mathcal{N} \sum_i^n c_i x^a y^b z^c e^{-\zeta_i r^2}$) which are superpositions (to better approximate cusps) of atom-centered Gaussians. The basis set size is determined by choosing a number of basis functions per atomic orbital (*minimal, double-zeta, triple-zeta, ...*) as well as the number of polarization functions (mixtures of different angular momenta). These basis sets can be efficiently used in all-electron calculations (including core states), need to be tweaked for molecular or solids calculations, exhibit more complex convergence behavior (basis set superposition errors) and can be post-processed [98] to be optimized for various applications.

DFT is a well developed tool to investigate ground state properties but does a priori not provide insight into the response of systems to changes in external parameters. However, the Hohenberg-Kohn theorems introduce the total energy as a functional of the density while concealing its parametric dependence on some external quantity λ (e.g. position of nucleii, unit cell volume, ...). For any given set of these external parameters standard DFT as introduced above suffices for determining the ground state. In order to study the influence of these parameters we will generally require at least a first order derivate $dE/d\lambda$. For the practical purpose of this thesis we will be interested in atomic forces (e.g. geometry relaxation for defect structures). Starting from a full Hamiltonian that includes both the electronic and ionic degrees of freedom (i.e. $H_{e+I} = T_e + V_{e-e} + T_I + V_{I-I} + V_{I-e}$) we can employ a Born-Oppenheimer product ansatz (e.g. $|\Psi_{\{R_m\}, \{r_n\}}\rangle := |X_{\{R_m\}}\rangle \cdot |\Theta_{\{R_m\}, \{r_n\}}\rangle$) and drop terms proportional to the mass ratio of electron and nucleus. Assuming the electronic system reacts adiabatically to ionic changes it would suffice to minimize $V_{I-I} + E(\{R_m\})$ to find the equilibrium of atomic positions. $E(\{R_m\})$ is the potential energy surface that encodes the energy contributions of the electronic system for the ionic system and is readily replaceable with the parametric energy functional of DFT $E_{\{R_m\}}[n]$. Lastly

the Hellman-Feynman theorem allows us to replace the total with a partial derivative, yielding our atomic forces as:

$$\mathbf{f}_m = -\frac{\partial(V_{I-I} + V_{ext})}{\partial \mathbf{R}_m} \quad (3.6)$$

We mention that modern DFT codes also add so called *Pulay force* corrections [99] to the Hellman-Feynman forces that arise due to incompleteness of the basis set. These corrections become especially important when the basis set explicitly depends on the ionic positions (i.e. localized basis sets).

So in order to relax atomic positions in a given solid we have to adhere to the twofold self-consistent process of 1) calculating the electronic ground state for a fixed ionic configuration 2) update atomic positions according to \mathbf{f}_m and repeat 1) and 2) until all atomic forces are below a predefined threshold.

Unless specified otherwise, all DFT calculations in this thesis are (depending on the choice of basis) either performed in the Vienna ab-initio simulation package (VASP [100–103] with a plane wave basis set) or GPAW [104–106] (Gaussian type basis sets) with the Perdew-Burke-Enzersdorf exchange-correlation functional [107].

3.3 Tight-binding

The tight-binding (TB) formalism [108–110] constitutes an approximation of the single-particle Schrödinger equation that projects it onto a set of tightly bound (i.e. well localized) orbitals ϕ_α . The motivation for this approximation is splitting the potential term $\hat{V}(\mathbf{r})$ of the Hamiltonian \hat{H} into that of an isolated atom $V^{\text{atom}}(\mathbf{r})$ plus a (presumably) small term $V^{\text{lattice}}(\mathbf{r})$ that accounts for the surrounding periodic lattice of atoms in a solid. The eigenfunctions of the isolated atom $[-\hbar^2 \nabla^2 / (2m) + V^{\text{atom}}(\mathbf{r})] \phi_\alpha = \varepsilon_\alpha \phi_\alpha$ then provide a natural basis that is usually referred to as a linear combination of atomic orbitals (LCAO) basis set. The Bloch wave functions of a solid can then be expanded in this basis as

$$\chi_{\alpha,\mathbf{k}}(\mathbf{r}) = \frac{1}{\sqrt{N}} \sum_c e^{i\mathbf{k} \cdot \mathbf{R}_{\alpha,c}} \phi_\alpha(\mathbf{r} - \mathbf{R}_{\alpha,c}) \quad (3.7)$$

without violating the periodicity condition Eq. (3.2). $\mathbf{R}_{\alpha,c}$ points to the α^{th} orbital (out of n_o orbitals in the unit cell) in the c^{th} periodic unit cell. The electronic wavefunction in the solid is then made up of several of these Bloch states corresponding to the same \mathbf{k} (crystal momentum \mathbf{k} is a good quantum number in periodic lattices):

$$\Psi_{\beta,\mathbf{k}}(\mathbf{r}) = \sum_\alpha b_{\beta,\alpha}(\mathbf{k}) \chi_{\alpha,\mathbf{k}}(\mathbf{r}) \quad (3.8)$$

With this there are n_o different energy bands in the system, with energies $E_\beta = \langle \Psi_\beta | \hat{H} | \Psi_\beta \rangle / \langle \Psi_\beta | \Psi_\beta \rangle$. The numerator evaluates to:

$$\begin{aligned}
\langle \Psi_\beta | \hat{H} | \Psi_\beta \rangle &= \frac{1}{N} \sum_{\alpha, c, \delta, c'} b_{\beta, \alpha}^* b_{\beta, \delta} e^{ik \cdot (R_{\delta, c} - R_{\alpha, c'})} \langle \phi_\alpha(r - R_{\alpha, c'}) | \hat{H} | \phi_\delta(r - R_{\delta, c}) \rangle = \\
&= \sum_{\alpha, c, \delta} b_{\beta, \alpha}^* b_{\beta, \delta} e^{ik \cdot (R_c + R_\delta - R_\alpha)} \langle \phi_\alpha(r) | \hat{H} | \phi_\delta(r - R_{\delta, c}) \rangle = \\
&= \underbrace{\sum_{\alpha, \delta} b_{\beta, \alpha}^* b_{\beta, \delta} \langle \phi_\alpha(r) | \hat{H}^{(0)} | \phi_\delta(r) \rangle}_{E_\beta^{(0)} \langle \psi_\beta | \psi_\beta \rangle} + \\
&\quad \underbrace{\sum_{\alpha} |b_{\beta, \alpha}|^2 \langle \phi_\alpha(r) | V^{\text{lattice}}(r) | \phi_\alpha(r) \rangle}_{o_\alpha} + \\
&\quad \underbrace{\sum_{\alpha, \delta, c \neq 0} b_{\beta, \alpha}^* b_{\beta, \delta} e^{ik \cdot (R_{\delta, c} - R_\alpha)} \langle \phi_\alpha(r) | V^{\text{lattice}}(r) | \phi_\delta(r - R_{\delta, c}) \rangle}_{\gamma_{\alpha \delta}^c} \quad (3.9)
\end{aligned}$$

where we used translational invariance between the first two lines and identified the individual terms $E_\beta^{(0)}$ as the (\mathbf{k} -independent) energy contributions of the isolated atom, o_α the onsite term (i.e. the correction due to the presence of the other atoms in the lattice) and $\gamma_{\alpha \delta}^c$ the hopping amplitude between orbital α and orbital δ situated in unit cell c . The hopping integral $\gamma_{\alpha \delta}^c(R_{\delta, c})$ generally decreases exponentially with the inter orbital distance. Therefore all the summations will only have to take a finite number of neighbouring sites into account. The number of orbitals per atomic site can — depending on the material under investigation — often be restricted to some outer shell eigenfunctions of the atomic Hamiltonian.

Finally we arrive at the energy dispersion of the β^{th} band,

$$E_{\beta, k} = E_\beta^{(0)} + \frac{\sum_\alpha |b_{\beta, \alpha}|^2 o_\alpha + \sum_{\alpha, \delta, c \neq 0} b_{\beta, \alpha}^* b_{\beta, \delta} \gamma_{\alpha \delta}(R_c) e^{ik \cdot (R_{\delta, c} - R_\alpha)}}{1 + \sum_{\alpha, \delta, c \neq 0} b_{\beta, \alpha}^* b_{\beta, \delta} \eta_{\alpha \delta}(R_c) e^{ik \cdot (R_{\delta, c} - R_\alpha)}} \quad (3.10)$$

where the second term in the denominator, $\eta_{\alpha \delta}(R_c) = \langle \phi_\alpha(r) | \phi_\delta(r - R_{\delta, c}) \rangle$, accounts for corrections of the norm $\langle \psi_\beta | \psi_\beta \rangle$ caused by finite overlaps between orbitals on different sites.

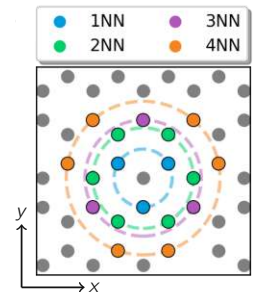


Fig. 3.1: Sketch of the NN neighbour sites in the graphene lattice.

3.3.1 Example: tight-binding models for the p_z bands in graphene

There are a plethora of valid TB parametrizations for single layer graphene (SLG) [19, 111]. Here I briefly introduce TB models generated via maximally localized Wannier functions (MLWF) [112] (which are employed throughout this thesis) for the π bands of graphene. These models include varying numbers of neighbour interactions (NN= 3, 5, 10) (see Fig. 3.1). We include two orbitals per unit cell (one p_z orbital per carbon atom) represented by orthogonal, well-localized basis functions, i.e the overlap matrix S in the generalized eigenvalue problem

$$\mathbf{H}\mathbf{b}_\beta = E_\beta \mathbf{S}\mathbf{b}_\beta \quad (3.11)$$

reduces to the identity $\mathbb{1}_2$ in this case ($\mathbf{b}_\beta = (b_{\beta,1}, b_{\beta,2})^T$ is the vector of expansion coefficients).

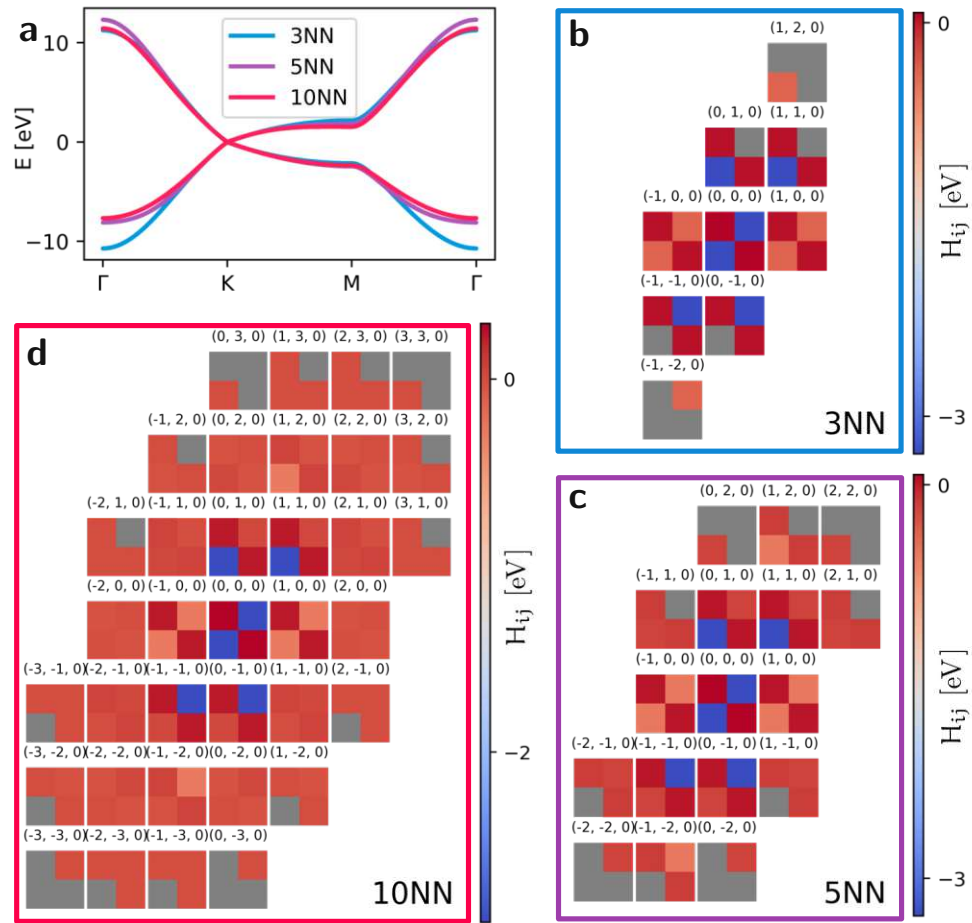


Fig. 3.2: a p_z bands of graphene calculated from TB models with different numbers of neighbour interactions. b, c, d Periodic Hamiltonians $H^{(\lambda_1, \lambda_2, 0)}$ for TB models of SLG with 3, 5 and 10 NN interactions respectively with labels for $(\lambda_1, \lambda_2, 0)$.

If the unit cell is large enough (i.e. it consists of $n \times n$ minimal unit cells) the Hamiltonian matrix of that system $H^{(n \times n)}$ is banded and includes on-site elements s_i on the diagonal and up to NN hopping term $\gamma_{ij}^{(NN)}$ on the minor diagonals.

$$H^{(n \times n)} = \begin{bmatrix} s_0 & \gamma_{01} & \gamma_{02} & 0 & & \\ \gamma_{01}^\dagger & s_1 & \gamma_{12} & \gamma_{13} & 0 & \\ \gamma_{02}^\dagger & \gamma_{12}^\dagger & s_2 & \gamma_{23} & \ddots & \\ 0 & \gamma_{13}^\dagger & \gamma_{23}^\dagger & \ddots & \ddots & \ddots \\ & 0 & \ddots & \ddots & \ddots & \ddots \\ & & & \ddots & \ddots & s_{2n^2} \end{bmatrix} \quad (3.12)$$

Since we deal with a periodic system compartmentalized into minimal unit cells (see Fig. 3.3) we have a whole set of periodic Hamiltonian matrices (of size 2×2). The periodic Hamiltonian matrices $H^{(\lambda_1, \lambda_2, \lambda_3=0)}$ determine the interaction of sites in the original cell $(0, 0, 0)$ with sites in the periodic image of the cell $(\lambda_1, \lambda_2, 0)$ translated along a linear combination of lattice vectors $\{\lambda_1 \cdot \mathbf{a}_1, \lambda_2 \cdot \mathbf{a}_2, 0\}$. The range of the indices $\lambda_1, \lambda_2, \lambda_3$ depends on the range of non-zero interactions between periodically shifted unit cells and thus on the number of neighbours any which orbital shares a finite hopping amplitude with (see Fig. 3.2).

3.4 Quantum transport

We will give a very concise introduction to quantized transport in the context of Landauer-Büttiker theory [113] and the tight-binding framework. Seeing as this formalism is not a major part of my work I will only introduce the basics (even though this discipline is a specialty of our group) and refer to theses of colleagues [114–116] for a thorough introduction.

3.4.1 Green's functions

Green's functions are a vital and widely applied concept throughout physics and engineering [117]. They represent integral kernels and are used to solve equations involving a differential operator \mathcal{L} :

$$\mathcal{L}(q)r(q) = x(q) \quad \mathcal{L}G(q, q') = \delta(q - q') \quad (3.13)$$

$$\rightarrow r(q) = \int G(q, q')x(q')dq' \quad (3.14)$$

where the *response* r to an *excitation* x of a system in this context is computed via the Green's function $G \propto \mathcal{L}^{-1}$ (i.e. something resembling the inverse of the differential operator). Hamiltonian systems in quantum mechanics allow for a clever introduction of an energy dependent Green's function,

$$\hat{G}(E) := \lim_{\epsilon \rightarrow 0} (\hat{H} - E \pm \epsilon) \quad (3.15)$$

where ϵ avoids issues at the eigen energies of the system and the direction of the limit approach defines *retarded* and *advanced* Green's function respectively.

3.4.2 Infinite waveguides and the recursive Green's function method

The total Hamiltonian of an infinite lead of repeated building blocks reads,

$$\hat{H} = \begin{bmatrix} \hat{H}_0 & \hat{L}_I & 0 & \dots & \\ \hat{R}_I & \hat{H}_0 & \hat{L}_I & 0 & \dots \\ 0 & \hat{R}_I & \hat{H}_0 & \hat{L}_I & 0 \\ \vdots & 0 & \hat{R}_I & \ddots & \ddots \end{bmatrix} \quad (3.16)$$

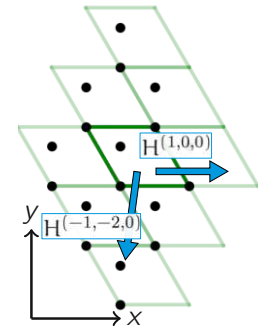


Fig. 3.3: Sketch of the periodic neighbour unit cells in graphene.

where blocks described by \hat{H}_0 are coupled via interaction Hamiltonians $\hat{R}_I = \hat{L}_I^\dagger$. Enforcing Bloch's theorem via $\psi = (\dots, e^{-ik\Delta_x}\eta, \eta, e^{ik\Delta_x}\eta, \dots)^T$ we can solve the eigenvalue problem $H\psi = E\psi$ of the form,

$$\left(\hat{H}_0 + e^{ik\Delta_x} \hat{H}_I^{(L)} + e^{-ik\Delta_x} \hat{H}_I^{(R)} \right) \eta = E\eta \quad (3.17)$$

by casting it into a space of double the size via the introduction of $\zeta = e^{ik\Delta_x}\eta$,

$$\begin{bmatrix} \hat{H}_0 - E & \hat{R}_I \\ 1 & 0 \end{bmatrix} \begin{pmatrix} \zeta \\ \eta \end{pmatrix} = e^{ik\Delta_x} \begin{bmatrix} -\hat{L}_I & 0 \\ 0 & 1 \end{bmatrix} \begin{pmatrix} \zeta \\ \eta \end{pmatrix} \quad (3.18)$$

The $2N$ (twice the transversal system size) eigenvectors and eigenvalues E_n of this generalized problem represent left- and right-moving lead modes of the system identified via the sign of their group velocity,

$$v_G^{(n)} = \frac{1}{\hbar} \frac{\partial E_n}{\partial k} = i\Delta x \langle \eta_n | e^{ik\Delta_x} \hat{L}_I - e^{-ik\Delta_x} \hat{R}_I | \eta_n \rangle \quad (3.19)$$

Solutions of a square lattice with parabolic dispersion in the continuum limit take the form $\sin(k_y y)$ with quantized $k_y = n\pi/W$ (with W the width of the transversal y direction). Depending on the energy, the factor $e^{ik\Delta_x}$ determines whether a solution propagates in x ($-x$) direction (i.e. $k_x \in \mathcal{R}$) or exponentially decays (i.e. $\text{Im}(k_x) \neq 0$).

The Green's function for such an infinite lead can be expressed in the basis of left (right) moving Bloch states $|\eta^l\rangle$ ($|\eta^r\rangle$) as,

$$G(x, x') = \mathcal{N} \left(\sum_n |\eta^l\rangle e^{ik\Delta x} \langle \eta^l | \Theta(x - x') + \sum_n |\eta^r\rangle e^{-ik\Delta x} \langle \eta^r | \Theta(x' - x) \right) \quad (3.20)$$

with Heaviside function Θ and normalization constant \mathcal{N} .

The recursive Green's function formalism [115, 116] presents an elegant algorithm for computing the total Green's function of a scattering geometry connected to two semi-infinite leads. By virtually cutting the entire region into smaller building blocks we can invert the smaller regions individually and then recombine them for the full Green's function. This is achieved via Dyson's equation [118] which incorporates perturbations into Green's functions. For example, the Green's function of a half infinite lead extending to the left, $G^L(x, x')$ follows

$$G^L = G^S + G^S \hat{R}_I G^L \hat{L}_I G^L \quad (3.21)$$

where we exploit the idea that adding a single slice (described by G^S) to half an infinite lead again yields half an infinite lead. This kind of equations allow us to both dissect a larger section into smaller ones as well as recombine them later on. The strategy of the overall algorithm would be to identify building blocks of the scattering structure corresponding to different transversal width. Then for all widths encountered:

- I) solve the eigen problem Eq. (3.18) for an infinite lead,
- II) express the half-infinite lead Green's function G^L in the freshly acquired basis of Bloch states,

- III) extract the Green's function of a rectangle G^\square (a finite-length section of the respective half-infinite lead),
- IV) then re-assemble the solutions to acquire the total Green's function G^{tot} and
- V) obtain transmission- t_{mn} and reflection-coefficients r_{mn} (i.e. the scattering matrix) by sandwiching the total Green's function between eigenstates of infinite leads.

Finally, Landauer-Büttiker theory [119] lets us compute the conductance by summing over squares of transmission coefficients ($\sum_m \sum_n |t_{mn}|^2$) and multiplying by twice (spin) the conductance quantum e^2/h .

3.5 Maximally localized Wannier functions

TB models need not necessarily employ atomic orbitals but can be formulated with any reasonably localized set of basis functions. As alluded to in Section 3.2, ab-initio electronic structure calculations are often solved in terms of Bloch states (e.g. VASP). The formalism of Wannier functions [120] provides an elegant bridge between highly accurate DFT calculations and large scale TB models. The m^{th} Wannier function $|\mathbf{R}, m\rangle$ in a unit cell pointed to by \mathbf{R} is a non-unique Fourier transform of a mixture of Bloch states $|n, k\rangle$:

$$|\mathbf{R}, m\rangle = \frac{V}{(2\pi)^3} \int e^{-ik \cdot \mathbf{R}} \sum_n U_{mn}(\mathbf{k}) |n, \mathbf{k}\rangle d\mathbf{k} \quad (3.22)$$

where $U_{mn}(\mathbf{k})$ represents a unitary mixing of Bloch states. The resulting generalized Wannier functions will vary in their localization. One can try to find a set of maximally localized Wannier functions (MLWF) by tweaking $U_{mn}(\mathbf{k})$ to minimize one of many localization criteria [121–123]. In this thesis we adhere to minimizing the spread functional Ω (the sum of quadratic spreads of the Wannier probability density) defined by Vanderbilt and Marzari [124]:

$$\Omega := \sum_n \left[\underbrace{\langle \hat{\mathbf{r}}^2 \rangle_n}_{\langle 0, n | \hat{\mathbf{r}} | 0, n \rangle} - \underbrace{\langle \hat{\mathbf{r}} \rangle_n^2}_{\langle 0, n | \hat{\mathbf{r}}^2 | 0, n \rangle} \right] \quad (3.23)$$

Successfully minimizing this spread functional (e.g. via steepest descend) guarantees some important properties of the resulting MLWFs: 1) they are unique, 2) exponentially localized and 3) are typically found to be real as long as time reversal symmetry is not broken in the system under consideration (i.e. systems without spin-orbit coupling).

If this transformation of Bloch states into Wannier orbitals incorporates more energy bands than target MLWFs at some region in the Brillouin zone (BZ) (e.g. energy bands of a different orbital character crossing through the ones we are interested in modelling) one has to perform an appropriate *disentangling* step. We pick energy ranges to build up N-dimensional sub Hilbert spaces $\mathcal{H}(\mathbf{k})$ (i.e. an *outer energy window* that includes possible Bloch states as well as an *inner energy window* the states in which are

guaranteed to be used). This optimal subspace selection is again based on the spread functional Eq. (3.23) which can be decomposed into two terms:

$$\Omega = \underbrace{\sum_n \left[\langle \mathbf{r}^2 \rangle_n - \sum_{\mathbf{R}, m} |\langle \mathbf{R}, m | \hat{\mathbf{r}} | \mathbf{0}, n \rangle|^2 \right]}_{\Omega_i} + \underbrace{\sum_n \sum_{\mathbf{R}, m \neq \mathbf{0}, n} |\langle \mathbf{R}, m | \hat{\mathbf{r}} | \mathbf{0}, n \rangle|^2}_{\Omega_g} \quad (3.24)$$

with the first (Ω_i) measuring the k-space dispersion of the band-projection operator and the latter (Ω_g) quantifying the degree to which the Wannier functions fail to be eigenfunctions of the projected position operators. Ω_i does not depend on $U_{mn}(\mathbf{k})$ which means the computation of MLWFs can be decomposed into 1) minimizing Ω_i via subspace selection and 2) subsequently finding the optimal mixing of the selected Bloch states. Physically Ω_i measures the similarity of the selected states across the BZ in terms of the subspace mismatch between adjacent k-points:

$$\Omega_i = N \sum_{\mathbf{k}, \mathbf{b}} w_b \sum_m^N \left[1 - \sum_n |\langle n, \mathbf{k} | m, \mathbf{k} + \mathbf{b} \rangle|^2 \right] \quad (3.25)$$

with \mathbf{b} connecting neighbouring k-points \mathbf{k} , N some normalization and w_b weight factors introduced by the discrete derivatives with respect to \mathbf{k} used in evaluating the position operator elements in Eq. (3.24), $\langle \mathbf{R}, m | \hat{\mathbf{r}} | \mathbf{0}, n \rangle = iV/(2\pi)^3 \int e^{i\mathbf{k} \cdot \mathbf{R}} \langle m, \mathbf{k} | \nabla_{\mathbf{k}} | n, \mathbf{k} \rangle d\mathbf{k}$. Depending on the desired number of Wannier functions (i.e. the number of orbitals in the unit cell) this non-convex, high-dimensional minimization problem benefits immensely from sensible initial guesses. To this extent it is often a good idea to start by projecting Bloch states onto LCAO orbitals. Nonetheless, finding a high-quality Wannier parametrization requires both chemical intuition and tenacity for several trial and error cycles. Chapter 6 of this thesis explores ways to circumvent the Wannier transformation altogether by invoking machine learning techniques to extract highly accurate parametrizations with merely band energies and geometry information as inputs.

Throughout this thesis all MLWF are calculated with the Wannier90 code package [125] using the VASP2Wannier interface. The next section provides a brief discussion for Wannier models of WSe₂ (used in Chapter 8).

3.5.1 Example: MLWF of WSe₂

Starting with a non-collinear, plane wave based DFT calculation (including spin orbit coupling) we employ the vasp2wannier interface to produce a TB parametrization of pristine WSe₂. The Wannier model includes 22 orbitals (11 per spin component) and omits the bands below -12eV (see Fig. 3.5d). Disentanglement proves fairly straightforward with the most of the desired bands isolated in energy. We use p_x, p_y and p_z orbitals as initial projections for the selenium sites and d-orbitals for m = 0, 1, 2 (i.e. d_{z²}, d_{xz}, d_{xy}, d_{x²-y²}, d_{xy}) for the tungsten atoms.

The semi-local DFT calculation (PBE) heavily underestimate the band gap to about 1.3eV [43]. The bands around the HOMO-LUMO gaps are to a large extent made of tungsten d-orbitals while the orbitals character of the

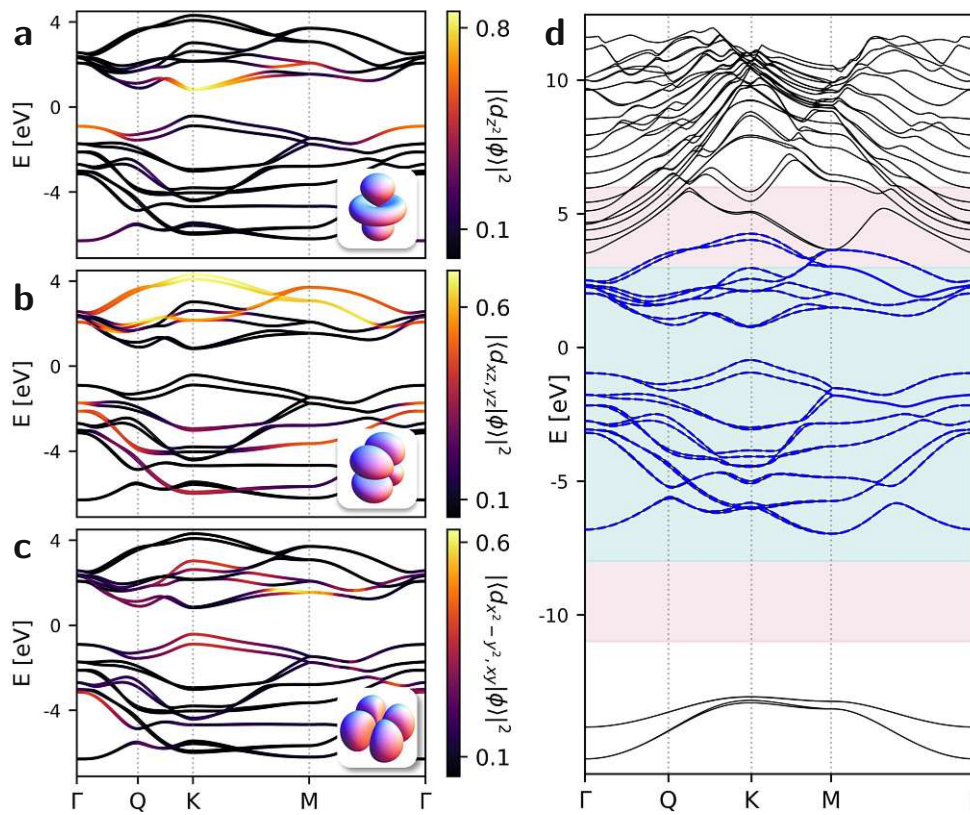


Fig. 3.5: Wannier band structure of pristine WSe₂ with color scale indicating the contribution of the different d-type orbitals (**a** - d_{z^2} , **b** - $d_{xz,yz}$, **c** - $d_{x^2-y^2,xy}$) of W. Insets represent schematics of the corresponding spherical harmonics. **d** DFT band structure (solid black lines) of pristine WSe₂ with Wannier band structure on top (dashed blue lines). Shaded regions represent energy windows (inner - green, outer - red) for the disentanglement process of wannier90.

lower valence bands ($E < -1.7\text{eV}$) is dominated by the selenium p-orbitals (see Fig. 3.4). In terms of spherical harmonics the valence band around K is dominated by d_{xy} and $d_{x^2-y^2}$ (50%) and transitions to d_{z^2} at Γ . The conduction band is mostly made up of d_{z^2} at the K point and features a pronounced character change to the $m = 2$ d-orbitals at M.

Chapter 4

Machine learning concepts

“But I don’t want to go among mad people.”

Alice

“Oh, you can’t help that. We’re all mad here.”

Cheshire Cat

The recent rise in popularity of so-called machine learning methods provides a plethora of novel approaches for optimization and automation tasks. These methods come with individual benefits as well as drawbacks and the torrent of acronyms and keywords can seem daunting at first. This section is by no means a complete introduction to the topic and highly motivated readers are encouraged to take their pick among [126–129]. I will give a concise and vastly incomplete introduction to the concepts relevant for my work.

Let us start by charting out the machine learning landscape. The common catchphrases artificial intelligence (AI), machine learning (ML) and deep learning (DL) are best introduced as a kind of matryoshka doll with AI spanning the largest conceptual space of *trying to automate tasks or activities that would usually involve human supervision or action* [130]. This most vaguely defined discipline thus also encompasses all hard-coded *if* bifurcations and virtually any kind of code that has a useful purpose. If we choose to omit algorithms with hard-coded procedures and only focus

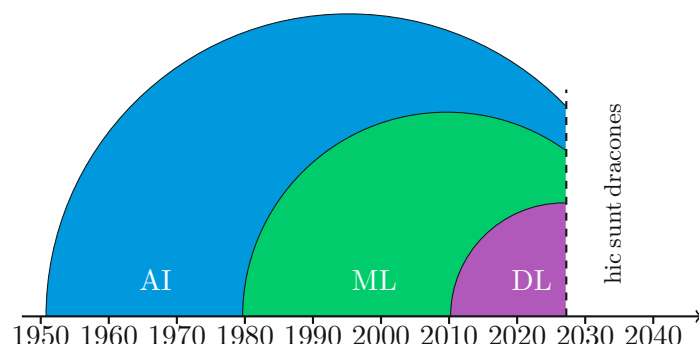


Fig. 4.1: Schematic ML time line.

on those that “learn” their purpose by observing data, we arrive at the subdiscipline of machine learning. These algorithms undergo training (i.e. establishing correlations between inputs and outputs of a general data set) and thus formulate their own “rules” to process future data. Machine learning can therefore be viewed as a technology that mines knowledge from data. The a priori vaguely determined act of learning itself is best defined by Mitchell [131]: “an algorithm learns if its performance measure P improves with experience E for a given task T ”. Therefore things learn if they change in a way that allows them to perform better in the future (in our daily language we often use “training” to designate a kind of mindless or mundane learning which seems much more fitting here). The experience E obviously represents a dataset with lots of examples (i.e. data points) that are either labeled (typically via human assistance → *supervised learning*) or unlabeled (*unsupervised learning*). The most common tasks T can be categorized into:

classification computing $f : \mathbb{R}^n \rightarrow \{1, \dots, k\}$ that maps data $x \in \mathbb{R}^n$ to a “category” in $\{1, \dots, k\}$
(e.g. image processing, face recognition)



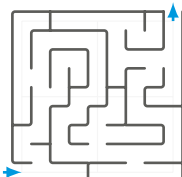
regression predict a real-valued variable $f(x')$ given a pattern $\{x_i, y_i\}_{i=1, \dots, N}$ with $f : \mathbb{R}^n \rightarrow \mathbb{R}$ and $x_i \in \mathbb{R}^n, y_i \in \mathbb{R}$
(e.g. algorithmic trading, ...)



density estimation estimate a density $p : \mathbb{R}^n \rightarrow \mathbb{R}_+$ that can be interpreted as a probability distribution on the example space.
(e.g. automatic generative models)



reinforcement learning a virtual agent within an environment takes actions such that their mutual influence maximizes a cumulative reward.
(e.g. AI in games [132, 133], autonomous driving,...)



Deep learning is again a subcategory to machine learning that involves so called neural network models that generate their decision or approximation power by successively applying seemingly simple but non-linear transformations to their input and repeatedly do so within a layered setup (deep then refers to a large number of these layers).

Before diving into more specific machine learning algorithms I would like to mention that the threshold of getting started with machine learning is continuously lowered by many excellent and highly usable open source implementations of the most frequently used algorithms in packages such as scikit-learn [134], PyTorch [135] or TensorFlow [136].

Fig. 4.2: Explanatory sketches for the different types of tasks.

4.1 Neural networks

Neural networks, or rather artificial neural networks, are interconnected arrays of basic modules that to some extent imitate the functions of brain

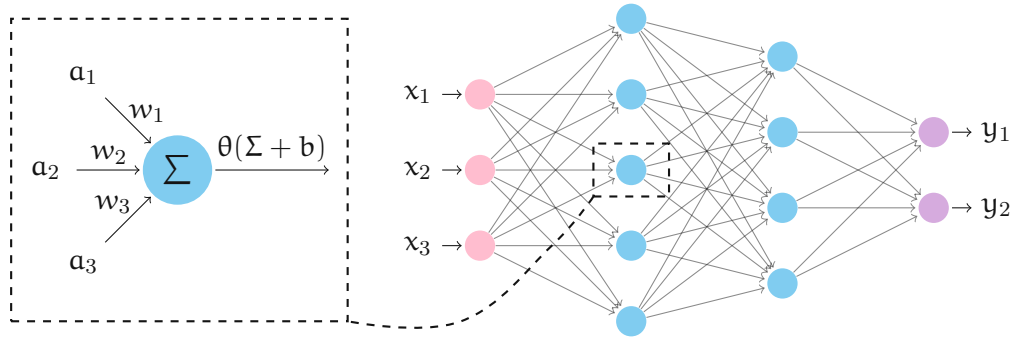


Fig. 4.3: Schematic layout of a simple fully-connected feed-forward neural network layout with two hidden layers (associated neurons in blue) that processes three input values (pink input neurons) to a result stored in two output neurons (purple). Inset to the left sketches an artificial neuron with inputs a_i , weights w_i , bias b and activation function θ .

nerve cells in living organisms [137]. These computational models aim to allow data processing akin to the human brain which typically consists of several 100 billion of *neurons* the communication of which occurs via impulse-like electrical signals mediated by the *synapses*. A *neuron* is densely connected to its peers and will thus receive numerous input signals. It then “decides” whether to output (or “fire”) a signal of its own depending on the type (excitatory or inhibitory) and magnitude of its incoming stimuli [138].

The fundamental building block of neural networks (the artificial neuron) stems from models such as the *threshold logic unit* [137] by McCulloch and Pitts in 1943 or the *perceptron* [139] of Rosenblatt in 1958. The inability of these early models to learn the XOR logic gate [140] (a non linear separable problem) led to a stagnant field of research until Rumelhart et. al. started to rekindle the mindfulness to these models by successful application of *back propagation* [141] in 1968. Followed by Hornik’s *universal approximation theorem* [142] and the advent of efficient GPU computing the architectures of deep neural networks became feasible. This created one of the most prominent research area in recent years the success of which tentatively culminated in superhuman performance in games of Go and Chess [132, 143] as well as impressive breakthroughs in protein folding [144, 145].

$$a_i^{(l)} = \theta \left(\sum_{j=0}^{n_n^{(l-1)}} w_{ij}^{(l)} a_j^{(l-1)} + b_i^{(l)} \right) \quad \text{with } l \in [1, L] \quad (4.1)$$

The artificial neurons of modern day neural networks still work fundamentally similar to these pioneering approaches: A neuron processes an arbitrary but fixed amount of input activations $a_i^{(l-1)} \forall i \in [0, n_n^{(l-1)} - 1]$ (coming from a previous layer $l - 1$) by feeding the sum of all these weighted (weight $w_{ij}^{(l)} \in \mathbb{R}$ connects neurons j in layer $l - 1$ to neuron i in layer l) inputs plus a neuron specific bias $b_i^{(l)} \in \mathbb{R}$ into a non-linear activation function θ (see Eq. (4.1) and Fig. 4.3). While the possible choices of this activation function are numerous (Fig. 4.4), even barring the historically outdated ones, and not necessarily identical for the different layers, the concatenation of these relatively simple but non-linear functions creates an immense plasticity

for the neural network to approximate a seemingly arbitrarily complicated function $F_w : \mathbf{x} \in \mathbb{R}^{n_n^{(0)}} \rightarrow \mathbf{y} \in \mathbb{R}^{n_n^{(L)}}$. This adaptability is then exploited during training (see Section 4.1.1) where both weights w and biases b of all neurons represent tunable parameters of the model. The universal approximation theorem [142] in principle guarantees that a fully connected neural network with a single hidden layer can approximate any compactly supported, continuous function to arbitrary accuracy. However, it does not provide a constructive prescription on the finite but presumably quite large number of neurons in this shallow network. Thus in practice one often employs “deep” (more hidden layers) but “leaner” (less neurons per layer) networks to great success. If all neurons in the previous layer are connected to all neurons in the following one the network is termed fully-connected (otherwise called convolutional network). The absence of loop structures for these connections classifies a network as feed-forward (otherwise termed recurrent network). I will mostly discuss fully connected feed-forward networks and briefly introduce the specifics of convolutional neural networks (see Section 4.1.3). Apart from this crude classification of different network architectures it is worth noting that the topic of architecture search makes up a research field on its own [146–149].

4.1.1 Network training & model fitting

So far we have introduced neural networks as general parametric (potentially highly non-linear) functions. The total number d of the so called trainable parameters (weights and biases) of wide or deep networks can become immense ($d > 10^6$ is nothing out of the ordinary), especially so for fully-connected networks (Eq. (4.2)):

$$d = \sum_{l=1}^L n_n^{(l)} (1 + n_n^{(l-1)}) \quad (4.2)$$

Determining the “correct” choice of these internal parameters for a given task is done during “training”. This typically involves a sufficiently large set of training examples (the training set S_t) and a set of validation examples (validation set S_v). Furthermore one needs to be able to quantify the network’s performance. This is of course dependent on the task at hand but generally encompasses a so called loss function: $\mathcal{L} : \mathbb{R}^{n_n^{(L)}} \times \mathbb{R}^{n_n^{(L)}} \rightarrow \mathbb{R}$. Equipped with such a loss function we can immediately evaluate how far off-target the model prediction $F_w(\mathbf{x})$ is in relation to the desired output (the “truth”) \mathbf{y} for a given input-output pair (\mathbf{x}, \mathbf{y}) in our data set. A loss function can be highly customized and may also involve derived quantities (see Table 4.1 for some common examples). Training a model thus constitutes minimizing this loss function averaged over all available pairs in the training set:

$$\min_w \langle \mathcal{L}(F_w(\mathbf{x}), \mathbf{y}) \rangle_{(\mathbf{x}, \mathbf{y}) \in S_t} \quad (4.3)$$

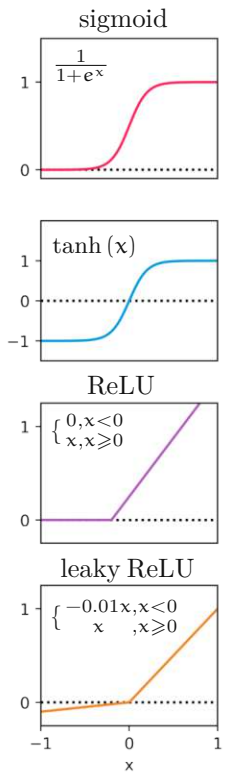


Fig. 4.4: Typical activation functions $\theta(x)$.

regression	mean squared error
	$\ \mathbf{y} - F_w(\mathbf{x})\ ^2$
classification	mean absolute error
	$\ \mathbf{y} - F_w(\mathbf{x})\ $
	categorical crossentropy
	$-\sum_i y_i \ln(F_w(\mathbf{x}))$

Tab. 4.1: Common loss functions \mathcal{L} in regression and classification problems.

Apart from the issue of efficiently implementing this minimization in practice we have a priori no way to be sure if the network will succeed to grasp the desired underlying patterns in our data. In other words, will the network still predict meaningful when presented with inputs that it has not seen during training? In this context we desire that the model can “generalize” well enough to both effectively interpolate between known training samples as well as extrapolate beyond them in a universal manner. After all, a network lacking this property would be hardly more than an unnecessarily sophisticated look-up table for its training data. In order to evaluate model performance both during and after training (how else would we define a meaningful stop criterion for the fitting process) it is customary to split all available data into disjunct training and validation sets. A very thorough assessment method (among other methods such as *bootstrapping* or *leave-p-out validation*) is *k-fold cross validation* which involves splitting the total data in k subsets $\mathcal{S}^{(i)} \forall i \in [1, k]$ before training k different models by employing $k - 1$ of those subsets as training data $\mathcal{S}_t^{(i)}$ and the remaining subset as validation data $\mathcal{S}_v^{(i)}$ before finally assessing the performance via the validation error averaged over the k different models (i.e. $1/k \sum_{i=1}^k \mathcal{L}(F_w(\mathbf{x}), \mathbf{y}) \rangle_{(\mathbf{x}, \mathbf{y}) \in \mathcal{S}_v^{(i)}}$).

Training (i.e. the minimization problem introduced in Eq. (4.3)) is, despite its high dimensionality d , usually already well handled by seemingly simple optimization algorithms such as gradient descent. The new weights w' are generated via:

$$w' = w - \alpha \nabla_w \bar{\mathcal{L}}_w \quad (4.4)$$

where $\alpha \in \mathbb{R}^+$ is the learning rate of the system and $\bar{\mathcal{L}}_w$ denotes the loss function evaluated using the old weights and averaged over a batch \mathcal{B} (i.e. subset) of data points:

$$\bar{\mathcal{L}}_w = \frac{1}{\mathcal{B}} \sum_{(\mathbf{x}, \mathbf{y}) \in \mathcal{B}} \mathcal{L}(F_w(\mathbf{x}), \mathbf{y}) \quad (4.5)$$

The batch size (i.e. the cardinality of \mathcal{B}) can range from 1 (*stochastic gradient descent* - update weights after processing one data point) up to the full size of the training set. Iterating over the full training set is called an *epoch*. Both batch size and learning rate are so called *hyper parameters* that are not derived through training. However these parameters can heavily influence efficiency and effectiveness of the training process.

Backpropagation refers to computing the gradient in weight space necessary to execute an update of all the weights in a neural network. This aptly termed process utilizes that a forward pass through our network (i.e. evaluating $F_w(\mathbf{x})$) is merely a concatenation of (while non-linear) analytically known activation functions. One can thus calculate derivatives of F_w with respect to any weight via the chain rule. The necessary equations to update all the weights can be elegantly formulated as simple matrix multiplications. The approximation error a priori only accessible at the output layer can thus be efficiently “back propagated” from layer L to $L - 1$ (and so forth)

using linear algebra. Writing \mathcal{L} as concisely as possible while highlighting the nesting of its (in general) vector valued arguments:

$$\underbrace{\mathcal{L} \left(f_1^{(L)} \underbrace{\left(f_1^{(L-1)}(\dots), \dots, f_{n_n}^{(L-1)}(\dots) \right)}_{\substack{\text{outputs of the neurons in layer } L-1 \\ \text{connected to neuron 1 in the last layer } L}}, \dots, f_{n_n}^{(L)}(\dots); \underbrace{y_1, \dots, y_{n_n^{(L)}}}_{\text{truth}} \right)}_{\text{prediction (output of last network layer)}} \quad (4.6)$$

using short hand notation $f_k^{(l)} = \sum_m w_{km}^{(l)} a_m^{(l-1)} = \sum_m w_{km}^{(l)} \theta(f_m^{(l-1)})$ we find the back propagation of the loss information as

$$\frac{\partial \mathcal{L}}{\partial f_k^{(L-1)}} = \sum_m \frac{\partial \mathcal{L}}{\partial f_m^{(L)}} \frac{\partial f_m^{(L)}}{\partial f_k^{(L-1)}} = \theta'(f_k^{(l-1)}) \sum_m w_{mk} \frac{\partial \mathcal{L}}{\partial f_m^{(L)}}. \quad (4.7)$$

Recursive application of Eq. (4.7) can thus evaluate

$$\frac{\partial \mathcal{L}}{\partial w_{ji}^{(l)}} = \frac{\partial \mathcal{L}}{\partial f_j^{(l)}} \frac{\partial f_j^{(l)}}{\partial w_{ji}^{(l)}} = \frac{\partial \mathcal{L}}{\partial f_j^{(l)}} a_i^{(l)} \quad (4.8)$$

in all hidden layers l (regardless of network topology) and therefore update all weights according to Eq. (4.5). The suitability of GPU computation for this formulation of network training is at part responsible for the emergence of the deep learning field.

Despite the apparent elegance of this back propagation update there is the possibility that some of the gradients that are being multiplied together along the way will vanish or diverge. While the first (e.g. gradient of $\tanh(x)$ becomes very small for extreme arguments) could cut sections of our network off the training process altogether while the latter would lead to highly unstable weight updates. These issues while ever more prevalent in deeper architectures can be easily mitigated by I) employing well behaved activation functions (e.g. ReLU), II) appropriately initializing the weights and biases [150] and III) standardizing the activations on-the-fly after each layer to zero mean and unit variance (*batch normalization* [151]).

Modern back propagation algorithms [152] employ (among many other technical ingenuities) adaptive learning rates and “momentum” (i.e. an exponential moving average over past gradients) for the weight updates to accelerate minimization in smooth sections of the loss function while maintaining stability in highly structured regions.

The prescribed training routine is not to be run in perpetuity but requires a halting criterion. While choices for this criterion are in no way unique it is customary to monitor the validation loss throughout the training and halt once this loss does not improve over a handful of epochs. Since each weight update will only allow for minor improvements in overall network performance one typically trains for many epochs before the model can utilize its full predictive power.

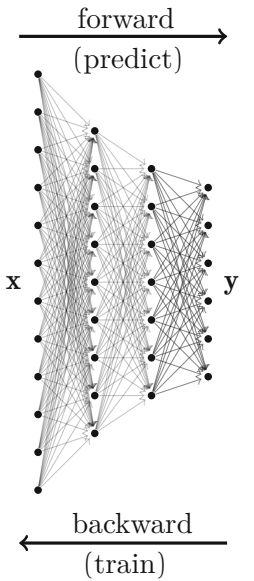


Fig. 4.5: Information flow schematic in neural networks.

4.1.2 Regularization

Regularization usually refers to adapting an ill-posed optimization task by adding additional penalties to the objective function. In the context of deep learning it typically controls the bias-variance trade-off (i.e. how well the model can generalize) when fitting a model.

The massive complexity of deep neural network architectures will (if not impeded) lead to a model that works almost perfectly on the training data. However, this behavior needs not necessarily transfer to unseen data (validation set). This constitutes a typical case of *overfitting* (similar problems arise in simple regression tasks when least-squares fitting data points of a scalar function $f(x)$ with a high order polynomial). In such scenarios the network is well capable of learning underlying patterns in the data but unfortunately picks up the features specific to the provided training data instead of the more general patterns we would rather have it learn. While such a deficiency is at heart a sampling issue of the available training data (i.e. the best way to mitigate overfitting, even though very academic, is to simply provide the network with more diverse data) one typically adapts hyperparameters and introduces various penalizing effects to the model as a countermeasure. The other extreme would be a network that is far too simple (imagine a very shallow network with few trainable parameters) to capture the intricate pattern of our data. In this case the model only partially manages to learn the desired input-output mapping and behaves too generic to be of real use (*underfitting*).

During a typical training process a reasonably complicated neural network model typically transitions between an underfitting state (i.e. the model initially has not learned a lot from the data) to an overfitting status (at some point the model prevalently customizes to the training data). This usually reflects in a trough-like structure for the validation loss. Initially both training and validation loss decrease. The training loss will continue to decrease (or converge) as training progresses while the validation loss reaches a minimal value before starting to increase again once overfitting sets in (see Fig. 4.6). With regularization one can typically achieve better performance than simply halting the training at the minimal validation loss.

Apart from simply reducing the model complexity (e.g. network with fewer layers) there are various approaches to introduce regularization to a model:

Weight regularization [153, 154] makes it more costly for the model to hold large weights by adding a penalty term to the loss function,

$$\mathcal{L} = \mathcal{L}_0 + \eta \mathcal{L}_{\text{reg}}. \quad (4.9)$$

Common penalty terms \mathcal{L}_{reg} are either L1 ($\|\mathbf{w}\|_1 = \sum_i |w_i|$) or L2 norms ($\|\mathbf{w}\|_2 = \sqrt{\sum_i |w_i|^2}$) of the total weight vector. L2 regularization limits model complexity but can never really enforce a weight w_i to exactly zero while L1 additionally performs some feature selection by setting some weights exactly zero. The hyperparameter η serves to regulate the magnitude of regularization.

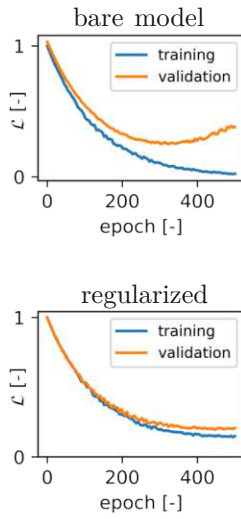


Fig. 4.6: Typical learning curves of unregularized and a regularized network.

Dropout [155] is an equally powerful regularization technique based on the idea of model combination. It aims to create a network (total number of nodes n) that is somewhat similar to an average of a vast collection of 2^n different “slimmed down” networks. Slim networks are spawned from the underlying architecture by temporarily ignoring a randomly chosen subset of all nodes within the network (see Fig. 4.7). A hyperparameter p controls the probability with which to keep a node. These slim virtual networks all share the same weights and biases (total number of parameters is not increased by dropout) and only differ in their connectivity. We can also view this as training 2^n slim networks where each individual network is updated very seldomly. Procuring a real average of all this models at prediction time quickly gets out of reach. We can however use the full network so long as its weights are multiplied by p to ensure that the expected output of a node at training time matches the actual output at test time to create an approximate average of 2^n different networks. This idea of diversifying the realizations of a network structure aims to make the output features of each individual node more useful and avoids training far too complex co-adaptations into the model (several nodes relying heavily on few others) which are less likely to correctly apply to novel data (i.e. less overfitting). Empirical evidence suggests that this a very successful method to reduce generalization errors. This improvement comes at the cost of another hyper parameter p and slower convergence with respect to the number of epochs.

Data augmentation Another approach to help with generalization is to artificially enlarge the available training set S_t by explicitly generating several altered data points. This often goes hand in hand with ensuring the model complies with desired invariances of the underlying data. A prime example comes up in pattern recognition (e.g. detecting cats in pictures should work regardless of their position and orientation within a given picture) where augmentations can involve mirroring, rescaling or rotation [156]. While having the model learn these invariances by applying symmetry operations to the training data it might be preferable to pre-process the data and extract invariant features and use those for training a model [157–159].

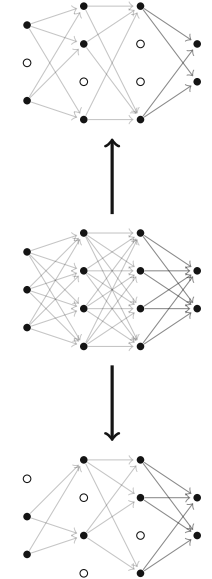


Fig. 4.7: Schematic explanation of slimming networks by randomly dropping nodes.

4.1.3 Convolutional neural networks

It is fairly straightforward to imagine that there is a vast freedom in the architecture of neural networks [160]. Besides to number and size of layers one can also change the connectedness of individual nodes. This can involve connections skipping some layers altogether (residual networks [161]), closed loop structures with internal memory (recurrent networks [162] and *long short-term memory* networks [163]) and various forms of more sparsely connected networks (convolutional networks [164–166], CNN), the latter of which we will briefly discuss here.

CNNs adhere to two main principles for connecting nodes in adjacent layers: *locality* (i.e structure conserving) and *shared weights* (i.e. translational invariance). Layers in convolutional networks can be thought of as 2D arrays where locality implies that a neuron in layer $l + 1$ is linked to only a “local” subset of the neurons in layer l . This connectedness is achieved by a so called *kernel* or *filter* which is typically a small 2D array that stores weights.

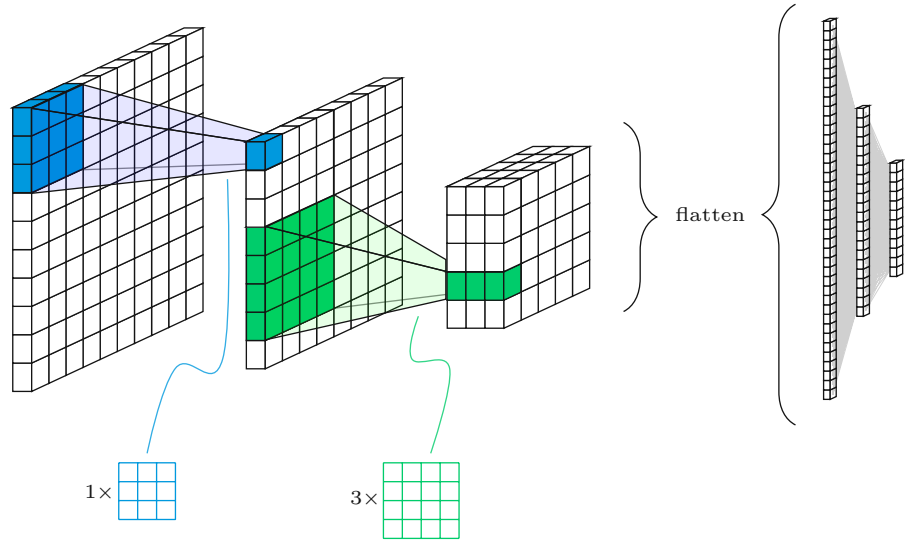


Fig. 4.8: Diagrammatic structure of a convolutional network with two convolutional layers (shape and number of filter kernels indicated for each layer) connected to fully-connected layers on the output side.

layer type & size	# of parameters
dense 128 ² \downarrow 64 ²	67,108,864
conv. (3 × 3) 16 × 128 ² \downarrow 64 × 64 ²	9,280

Tab. 4.2: Comparison of the number of trainable parameters necessary for connecting two layers of a neural network of type dense or convolutional.

That same filter is then used to compute the activations for all neurons in layer $l + 1$ (shared weights) by traversing it across the previous layer with a given stride length (see Fig. 4.8). A convolutional layer typically consists of several *channels* that hold different representations of the data and are often referred to as *feature maps* (often depicted as a third dimension to the 2D arrays). The desired number of channels in layer l determines the depth of the filter/kernel and we will employ separate kernels for each channel in layer $l + 1$:

$$a_{c,p}^{(l)} = \theta \left(\sum_{c'} \sum_{j \in U(p)} w_{c,c',p}^{(l)} a_{c',p'}^{(l-1)} + b_c^{(l)} \right) \quad \text{with } l \in [1, L] \quad (4.10)$$

where $p = (\text{row}, \text{column})(p')$ are 2D index vectors and $c(c')$ runs over all channels in layer $l(l + 1)$ respectively. $U(p)$ constitutes a local environment depending on the kernel size. In short the action of a convolutional layer is element-wise multiplication with the kernel followed by subsequent summation.

A convolutional layer is thus best suited to process data with underlying spacial correlations (e.g. object detection in images). CNNs therefore extract local attributes that are gradually processed into higher-order feature maps as the information propagates through layers that decrease in height and width but grow in depth (# of channels). This compression in the first two dimensions occurs naturally due to the convolution with kernel sizes greater than one but can be customized by appropriate use of *padding* [167] and/or *pooling* [168]. Zero padding can avoid premature information loss at the border nodes in shallow layers (i.e. it keeps the height and/or width constant during convolution) caused by the natural decrease in layer size:

$$h^{(l+1)} = \frac{h^{(l)} - k_y^{(l)}}{s^{(l)}} + 1 \quad (4.11)$$

where h represents the height of the respective layer, $k_y^{(l)}$ ist the height of the Kernel matrix and $s^{(l)}$ the stride. Pooling on the other hand is used to actively reduce the dimensionality of the feature maps by extracting pertinent details at the expense of discarding irrelevant information. This downsampling procedure which increases the feasible depth of convolutional layers by economizing on parameters while acting as a countermeasure to overfitting [168] can be implemented in different variations (see Fig. 4.9).

In some sense convolutional layers enable a form of automated preprocessing of the data. They act as trainable feature extractors with a comparatively managable number of parameters due to locality and shared weights (see Table 4.2). This automatically preprocessed information is then typically fed into few fully-connected feed-forward layers that transform the data into the desired output (i.e. classification or regression).

4.2 Gaussian Process Regression

Gaussian processes (GPs) are stochastic models that represent a collection of random variables with the probability distribution of any finite subset of which being a multivariate Gaussian [169]. They follow an inherently different regression paradigm than most other machine learning algorithms: If one wishes to find a scalar valued function with vector valued inputs $f: \mathbb{R}^n \rightarrow \mathbb{R}$ that is most *consistent* with training data, the most common approach is to restrict the available function space to some class of appropriate functions, the *best* of which is thereafter chosen by tuning parameters that when varied essentially span the elected sub space of functions. This *parametric* approach inelegantly depends on the users ability to correctly choose a suitable class of functions that is capable of adequately modeling the underlying patterns within the data. GPs however employ a more abstract but vastly powerful strategy of establishing Bayesian prior probabilities over function space that can be used to extract a seemingly parameter-free *likeliest* function via inference.

I will try to introduce GPs in a way short enough for the methods section of this thesis yet descriptive enough to easily follow its vainly application for defect parametrization later on. I advise the avid reader to study the definitive book on GPs [169], the original publication [170] or alternatively harness some of the concise yet vividly picturesque introductory web articles [171, 172] available.

4.2.1 Multivariate Gaussian

The normalized probability density of a univariate (1D) Gaussian distribution (or normal distribution, see Fig. 4.10) for a random variable $x \in \mathbb{R}$ is given by:

$$p(x; \mu, \sigma) = \frac{1}{\sqrt{2\pi\sigma^2}} e^{-\frac{(x-\mu)^2}{2\sigma^2}} \quad (4.12)$$

original feature map			
9	2	8	6
5	0	9	4
0	4	0	0
7	9	3	5

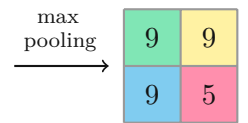


Fig. 4.9: Exemplary depiction of different pooling prescriptions.

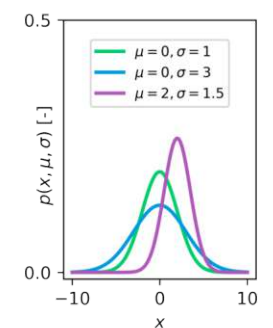


Fig. 4.10: One dimensional Gaussian with exemplary means and variances.

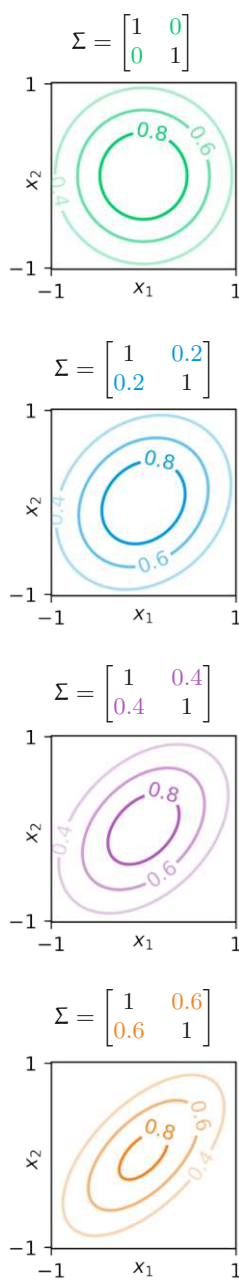


Fig. 4.11: Contour plots of two dimensional Gaussian distributions labeled with percentiles. Subplots correspond to different Covariance matrices.

with mean $\mu \in \mathbb{R}$ and variance $\sigma^2 \in \mathbb{R}_0^+$.

Its generalization to a d dimensional vector of random variables $\mathbf{x} = (x_1, x_2, \dots, x_d)^T \in \mathbb{R}^d$, where every linear combination $\mathbf{a} \cdot \mathbf{x}$ (with arbitrary but constant vector $(a_1, a_2, \dots, a_d)^T \in \mathbb{R}^d$) is normally distributed results in the *joint normal distribution* or *multivariate Gaussian*:

$$p(\mathbf{x}; \mu, \Sigma) = \frac{1}{(2\pi)^{d/2} |\Sigma|^{1/2}} e^{-\frac{1}{2} (\mathbf{x}-\mu)^T \Sigma^{-1} (\mathbf{x}-\mu)} \quad (4.13)$$

where the argument of the exponential is still a quadratic form which now involves a mean vector $\mu = (\mu_1, \mu_2, \dots, \mu_d)^T \in \mathbb{R}^d$ and the symmetric positive definite *covariance* matrix $\Sigma \in \mathbb{R}^d \times \mathbb{R}^d$ which holds the covariance $\text{Cov}(x_i, x_j)$ of all possible pairs of random variables in \mathbf{x} :

$$\text{Cov}(x_i, x_j) = \langle x_i x_j \rangle - \langle x_i \rangle \langle x_j \rangle \quad (4.14)$$

The covariance matrix thus expresses the individual variances of the random variables on its diagonal while the off-diagonal elements describe how correlated two components of \mathbf{x} are (see Fig. 4.11).

Given such a d dimensional distribution one can repeatedly sample random vectors $\{\mathbf{x}\}_s \forall s \in [1, n_{\text{samples}}]$ and plot their components in a scatter plot (see Fig. 4.12) for different correlation strengths in the covariance matrix (off diagonal elements of Σ). If the components are entirely uncorrelated (i.e. $\Sigma_{ij} = 0 \forall i \neq j$) then any sample vector will be a collection of independent values that form a seemingly random and incoherent pattern (green markers in Fig. 4.12a). However, increasing correlation will lead to smoother patterns due to the proclivity of neighbouring elements to take somewhat similar values (purple markers in Fig. 4.12a) or almost identical values for very strong (and long ranged) correlation (i.e. all components are very likely to assume the same random value, orange markers in Fig. 4.12a). While individual samples of the same distribution will obviously differ, samples originating from multivariate Gaussians with different covariances will when viewed as a collection differ in their smoothness. Since both means $\mu = 0$ and diagonal parts of Σ remain unchanged for these different distributions the ensemble average over many samples will always give zero for all components of \mathbf{x} with equal variance (see Fig. 4.12b).

marginalization extract partial information by integrating the original distribution $p(\mathbf{x}_a, \mathbf{x}_b)$ along dimensions of no interest:

$$p(\mathbf{x}_a) = \int_{\mathbf{x}_b} p(\mathbf{x}_a, \mathbf{x}_b) d\mathbf{x}_b \quad (4.15)$$

conditioning determine the probability distribution of a subset of variables while fixing the remaining ones to some value (i.e. formulate a condition for them). This is typically done via Bayesian inference (Bayes rule):

$$p(\mathbf{x}_a | \mathbf{x}_b = \mathbf{y}) = \frac{p(\mathbf{x}_a, \mathbf{x}_b)}{p(\mathbf{x}_b)} \quad (4.16)$$

If the original and marginalized distributions are all Gaussians the conditional distribution is also guaranteed to be Gaussian with adapted mean vector $\tilde{\mu}$ and covariance matrix $\tilde{\Sigma}$:

$$\mu = (\mu_a, \mu_b)^T \rightarrow \tilde{\mu} = \mu_a + \gamma_{ab} \gamma_{bb}^{-1} (\mathbf{y} - \mu_b) \quad (4.17)$$

$$\Sigma = \begin{bmatrix} \gamma_{aa} & \gamma_{ab} \\ \gamma_{ab}^T & \gamma_{bb} \end{bmatrix} \rightarrow \tilde{\Sigma} = \gamma_{aa} - \gamma_{ab} \gamma_{bb}^{-1} \gamma_{ab}^T \quad (4.18)$$

In the context of this d-dimensional distribution we can exploit a convenient property of multivariate Gaussians: They are closed under both *conditioning* and *marginalization*. This algebraic property of the resulting distribution after either fixing a coordinate or tracing over it is again a Gaussian allows one to make use of analytical expressions for both processes. If we again examine samples from the 40-dimensional Gaussian used in Fig. 4.12 but this time condition components x_0, x_{12}, x_{27} and x_{38} to fixed values we will necessarily draw samples that are guaranteed to “pass through” these points but retain some randomness in the other components.

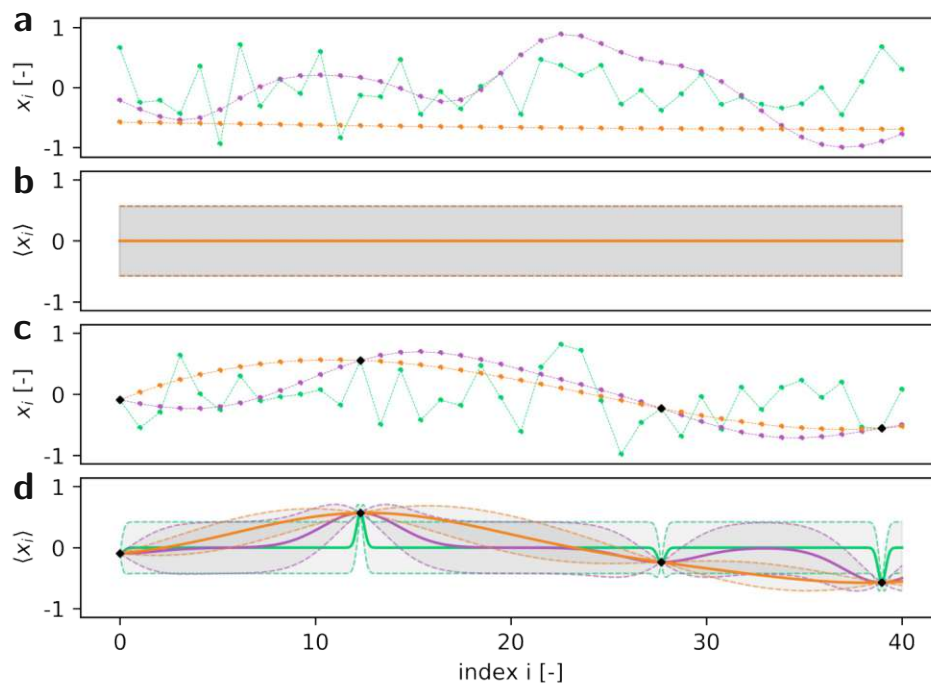


Fig. 4.12: Colors correspond to different degrees of correlation in the covariance matrix similar to Fig. 4.11. **a** Three random vectors \mathbf{x} sampled from a 40 dimensional Gaussian. **b** Interpolated mean and 1σ intervals (light grey area between dashed lines). **c** Three random vectors \mathbf{x} sampled from a 40 dimensional Gaussian conditioned to four training data points (marked as black diamonds). **d** Interpolated mean and 1σ intervals for the conditioned Gaussian.

From here it is quite straightforward to imagine a kind of ensemble average over various such samples to give a most probable, average function that approximates the underlying data pattern. Since all the distributions are Gaussians we can calculate the corresponding mean vector $\tilde{\mu}$ analytically (Eq. (4.17)) without the need for evaluating sample averages. Moreover we can also calculate the conditioned variances and use them as a measure of uncertainty for our regression fit (i.e. which coordinates of our random vector are least determinate and therefore benefit most from acquiring additional training data points). This process gives us both an optimal non-parametric candidate function for the gathered data (see solid lines in Fig. 4.12d) as well as an (potentially even more valuable) error bar (see hued regions bounded by dashed lines in Fig. 4.12d). Such an error estimate is especially important for fitting problems for which every data point to be acquired is computationally expensive (i.e. the objective function $f(x)$ is difficult to evaluate) and thus one wishes to avoid unnecessary sampling (especially so in high dimensional input domains). In these cases the error estimation allows for efficient global optimization via *Bayesian optimization* schemes.

4.2.2 Gaussian Process

A *Gaussian process* (GP) is a stochastic process [173] and can be viewed as an infinite-dimensional generalization of the Gaussian probability distribution and therefore acts as a distribution over functions (i.e. continuous domains). We therefore replace the mean vector μ by a *mean function* $m(x)$, define the covariance matrix Σ by a *covariance- or kernel function* $k(x, x')$ and denote our random variable (function value) $f(x)$ as:

$$f(x) \sim \mathcal{GP}(m(x), k(x, x')) \quad (4.19)$$

The crux of this concept comes with realizing that so long as we only ever query the function at a finite number of points the closedness of Gaussians under marginalization implies that this result has to be identical to taking infinitely many points into account (i.e. examining a larger set does not change the distribution over the smaller set). This property is often referred to as *marginalization property* or *consistency* and necessitates that all possible finite queries of the GP are consistent with one another (this is also at the heart of what makes GPs computationally tractable).

Assume we have n_t training input/output pairs $(x_t, y_t)_i \forall i \in [1, n_t]$ and n_p inputs x_p at which we aim to predict. With this we can imagine a joint training/prediction prior as a GP with zero mean:

$$\mathcal{GP}(\mathbf{0}, \Sigma_{t+p}) \quad \text{and} \quad \Sigma_{t+p} = \begin{bmatrix} \Sigma_t & \Sigma_{tp} \\ \Sigma_{pt} & \Sigma_p \end{bmatrix} \quad (4.20)$$

We predict by conditioning on the observed training outputs y_t which will again yield a GP with a predictive mean and variance function:

$$m(x) = \Sigma_{xt} \Sigma_t^{-1} y_t \quad (4.21)$$

$$K(x, x') = \Sigma_t - \Sigma_{xt} \Sigma_t^{-1} \Sigma_{tx} \quad (4.22)$$

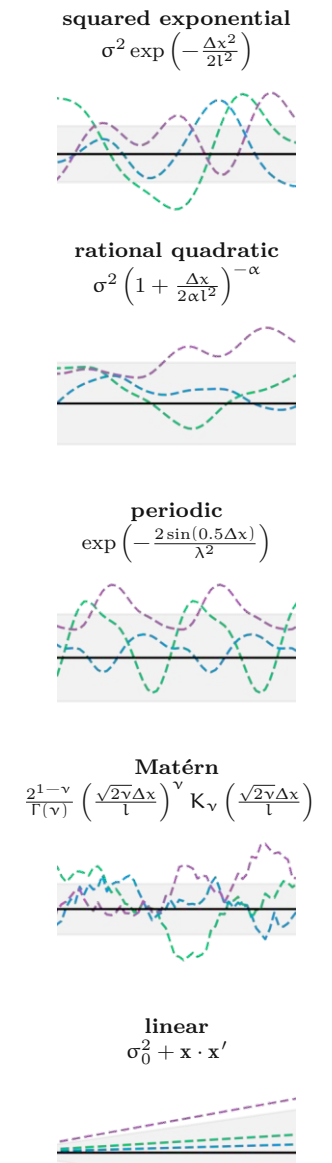
with $x(x') \in \{x_p\}_{1 \leq i \leq n_p}$. While this is in principle a fully correlated prediction (i.e. it provides predictive correlations between any pair of prediction outputs) it is often sufficient to use the marginal variances (the diagonal part of Σ_t , $x = x'$) to gauge the uncertainty of a prediction. While the matrix inversion in the predictive mean $m(x)$ Eq. (4.21) costs $\mathcal{O}(n_t^3)$ we can precompute $\Sigma_t^{-1} y_t$ and only calculate the weighted sum of these basis functions for a prediction at x in $\mathcal{O}(n_t)$, as long as the training set remains unchanged. If we also want a confidence estimate preparatory work does not help anymore. Eqs. (4.21) and (4.22) are typically implemented via Cholesky decomposition [174]. We can typically initialize our GP with a zero mean function but have to be more thoughtful about the covariance matrix which is typically created from a kernel function $k(x, x')$. These kernel functions are also used in other ML algorithms (e.g. support vector machines [175]) and are conceptually speaking some form of similarity measure in some abstract, higher dimensional feature space [176, 177].

kernel functions denoted $k(x, y) : \mathbb{R}^n \times \mathbb{R}^n \rightarrow \mathbb{R}$ correspond to computing a dot product of some feature vectors $\chi(x) : \mathbb{R}^n \rightarrow \mathbb{R}^m$ without explicit knowledge about this potentially higher-dimensional feature space. A generic example kernel function:

$$k(x, y) := (1 + x \cdot y)^2 \quad (4.23)$$

$$= 1 + x_1^2 y_1^2 + x_2^2 y_2^2 + 2x_1 y_1 + x_2 y_2 + 2x_1 x_2 y_1 y_2 \quad (4.24)$$

would thus correspond to calculating a dot product of the two vectors $(1, x_1^2, x_2^2, \sqrt{2}x_1, \sqrt{2}x_2, \sqrt{2}x_1 x_2)$ and $(1, y_1^2, y_2^2, \sqrt{2}y_1, \sqrt{2}y_2, \sqrt{2}y_1 y_2)$ in a 6 dimensional feature space. In the same sense we can interpret a kernel of the form $k(x, y) = \exp(-\|x - y\|^2)$ acting as an inner product in an infinite dimensional feature space when viewed as a Taylor expansion.



Tab. 4.3: Common kernels/covariance functions (if stationary: $k(x, x') = k(\Delta x)$) with representative functions sampled from the prior distribution (zero mean and variance indicated in black and grey respectively).

The choice of kernel function determines the properties (e.g. smoothness) of the underlying sample functions and thus calls for a careful selection depending one the particular process we try to model. There is a variety of common kernel functions (see Table 4.3) that can be broadly divided into *non-stationary* and *stationary* kernels with the latter remaining invariant under translations (they only have relative coordinates as arguments). A detailed introduction to kernel choice is given in [178]. The flexibility of choosing a kernel does not stop at the common kernels found in Table 4.3. We can also combine several kernels into a new one (that we believe — given some domain knowledge — better reflects the underlying patterns) by either adding or multiplying them (see [170, 172] for details).

All these kernel functions will naturally introduce some hyper parameters θ to the GP (e.g. length scale l , amplitude σ , scale mixture parameter α , ...). Another upside of the full probabilistic nature of GPs is that they come with an automatic selection process for these parameters that does not involve any form of cross validation. While analytically calculating a Bayesian posterior $p(\theta|y_t)$ might work in some cases the generally more robust approach is to minimize the negative log marginal likelihood cost function with respect to θ :

$$\log(p(y|\theta)) = -\frac{1}{2}y_t^T \Sigma_t^{-1} y_t - \frac{1}{2} \log |\Sigma_t| - \frac{n_t}{2} \log(2\pi), \quad (4.25)$$

where the first term measures how well the model fits the training data points y_t , the second penalizes model complexity (Occam's razor) and the last accounts for normalization. We thus aim to maximize the probability of the monitored data given our model. Despite the non-convexity of this minimization problem standard conjugate gradient descent methods in combination with randomly initiated restarts typically avoid local minima reasonably well. Involved gradients are readily computable with the numerical bottleneck of the entire optimization again being the matrix inversion of Σ . The number of hyper parameters in standard kernel functions is typically well manageable and overfitting is usually not an issue. In problems with multidimensional inputs $x \in \mathbb{R}^d$ some of the hyper parameters (e.g. length scale l) may be split up into individual parameters for each dimension $l_i \forall i \in [1, d]$. Optimizing them individually can to some extent include automatic *feature selection* or *relevance detection* [179] with the downside of quickly growing the number of hyper parameters.

Part II

Application

Chapter 5

Manipulating Quantum dots through lattice defects

“Science is what we understand well enough to explain to a computer; art is everything else.”

Donald E. Knuth

This chapter summarizes my first project during my PhD [180] and represents a natural extension to calculations started during my master thesis. We model the influence of lattice defects on the level structure of graphene quantum dots (GQDs). We study both the adiabatic level spacing “landscape” — orbital splitting and valley splitting — as well as transition dynamics between GQD-states. The system is modeled using a tight-binding approach with onsite- and hopping parameters in the vicinity of the defect region extracted from density functional theory via Wannier orbitals while time propagation is done using Magnus operators. Different defect types, such as double vacancy, Stone-Wales, flower and Si substitution are considered. We predict tunable valley splittings of the order of 2–20 meV. The level structure can thus be tailored at will by engineering appropriate defect geometries.

Unique electronic properties and long spin coherence times make graphene [23, 181, 182] a promising host material for quantum dots which might one day replace GaAs as the state-of-the-art material for both spintronic [183–186] and valleytronic applications [15, 187, 188]. Unfortunately, patterning graphene to form quantum dots yields devices dominated by edge effects [189, 190]. The gapless spectrum of graphene makes electrostatic confinement challenging. Recent developments towards so called edge-free quantum dots in single-layer graphene by a combination of electric and magnetic fields [14, 191–196] pave the way for graphene quantum dots (GQDs) with a level spectrum free of edge effects. GQDs are appealing host materials for spin-qubits [184, 186]. These are unfeasible without controlled breaking of the valley degree of freedom of graphene. The hexagonal symmetry of the honeycomb lattice results in two inequivalent electronic states in graphene, so-called valleys, which we label with “+” and “−”. Quantum states in pristine graphene carry this valley index $\tau = \pm$ as an additional quantum number. Imagining a setup of two singly occupied graphene quantum dots that are controllably coupled by an exchange interaction would (together with single spin rotations) present all the ingredients required for general quantum computation gates.

However, the additional valley quantum number allows for both electrons to occupy the same dot even in a tripllett spin state and thus heavily suppresses a necessary singlet-triplet splitting $J \neq 0$. Apriori this cannot be remedied in single layer graphene given the intrinsic valley degeneracy. In this project we simulate the spectrum of electrostatically defined GQDs in the presence of lattice defects. In particular, we focus on the controlled breaking of the valley symmetry by defects close to the GQD. Tremendous improvement in the synthesis of graphene nanostructures [64, 65] has enabled very clean samples with high mobility and low defect density. Instead of many randomly distributed defects hampering device performance, one can envision exploiting specific lattice defects in graphene which actively tune the level spectrum of edgeless GQDs in their close vicinity. The possibility to purposefully create a certain defect density via high-energy particle beam bombardment [66, 197, 198] in graphene may ultimately develop towards systematically placing certain defects in a controlled manner.

5.1 Smoothly confined quantum dots in graphene

Inducing smooth electrostatic confinement in single layer graphene involves combining an out-of-plane magnetic field (to ensure Landau quantization) with an electric field. The Landau level energies $E_L^{(n)}$ for pristine graphene in a perpendicular magnetic field B are given by [23]

$$E_L^{(n)} = v_F \cdot \text{sgn}(n) \sqrt{\frac{2\hbar e}{c} |B| |n|} \quad \text{with} \quad n \in \mathbb{Z}, \quad (5.1)$$

with Fermi velocity v_F . The energy gaps between Landau levels ($\Delta E_0 = E_L^{(1)} - E_L^{(0)} \approx 80\text{meV}$ for $B = 7\text{T}$) allow electrostatic confinement given a suitable electrostatic potential. This potential can be induced by a scanning tunneling microscopy (STM) tip hovering over the graphene flake [14, 191] (see Fig. 5.1).

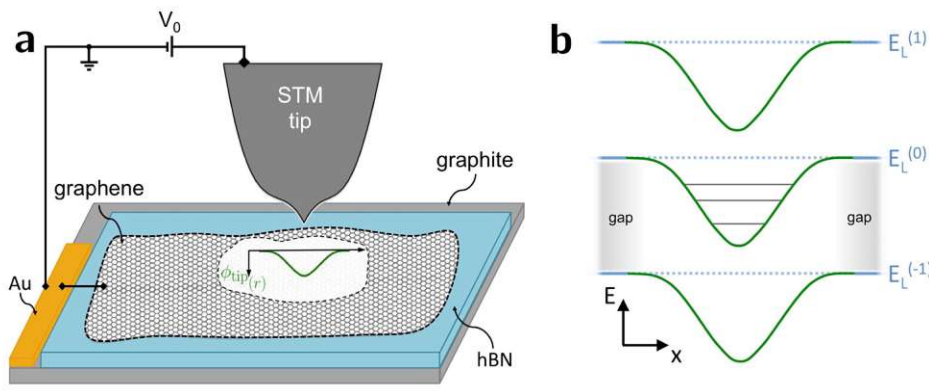


Fig. 5.1: **a** Schematic setup of STM tip and graphene flake on an hBN substrate. **b** Achieving confinement within the first Landau gap

We assume that substrate effects are small compared to the tip-induced confinement, as readily achieved using an unaligned atomically flat substrate such as hexagonal boron nitride (hBN). The STM tip locally shifts the

energy relative to the Landau levels. The resulting smooth confinement avoids any physical edges and hosts four-fold near-degenerate spin-valley quadruplets [14]. The energy spacing between the quadruplets is determined by the electrostatic environment created by the STM tip. In practice [14], one finds values of the order of 10 meV, about one order of magnitude smaller than ΔE_0 . The homogeneous magnetic field used for inducing Landau quantization leads to a small spin splitting on the order of 800 μ eV (at $B = 7$ T) between the two spin doublets of the quadruplet. The GQDs defined by a mobile STM tip can easily be moved with respect to the graphene lattice, as opposed to GQDs created by patterning of the lattice. Creating the GQD with an STM tip also provides an elegant way to measure the energies of individual quantum dot states via charging events [14]. Since the spectrum of the quantum dot reacts sensitively to the local electronic environment it can be used as a sensitive probe of the local electronic structure [191]. Exchanging the STM tip for an array of electric gates could also provide motion on relevant time scales for dynamic switching between dot states.

This project includes: I) our approach for accurately modeling quantum dot states in the presence of defects, II) calculations on the effect of several lattice defects (double vacancy, Si substitution and flower defect) on the quantum dot states, with a particular focus on valley symmetry breaking induced by these defects. We identify several avoided crossings within the valley subspace, suggesting that the valley splitting changes sign when the dot passes through the defect. III) We finally show how such crossings can be exploited to dynamically obtain a desired state by transitioning the crossing (in real space) either adiabatically or diabatically (i.e. at different traversal velocities).

5.2 Model

We model a finite-sized, rectangular graphene flake with an area of approximately 120×100 nm² using a tight-binding Hamiltonian

$$\hat{H}(E) = \sum_i s_i \hat{c}_i^\dagger \hat{c}_i + \sum_{\langle i,j \rangle} t_{ij} \hat{c}_i^\dagger \hat{c}_j + \Sigma(E) \quad (5.2)$$

with $\hat{c}_i^\dagger (\hat{c}_i)$ representing the creation (annihilation) operators of a quasiparticle at site i with position r_i , s_i the onsite (diagonal) matrix elements and t_{ij} the hopping amplitudes between sites i and j . The sum over j runs over the nearest-neighbour sites included: we use up to 10th nearest-neighbour hopping with values taken from density functional theory by Wannierization [112]. An energy-dependent self-energy [199, 200] $\Sigma(E)$ implements open boundary conditions on all four sides (see Fig. 5.2a). This avoids edge effects and also filters out delocalized states [189]. We do not include physical spin. A perpendicular, homogeneous magnetic field (7 T) enters the hopping matrix elements t_{ij} via a Peierls's phase. For now, we neglect the influence of the hBN substrate, except for its effect on the electrostatic environment. We will explicitly consider the influence of (substrate-induced) disorder below.

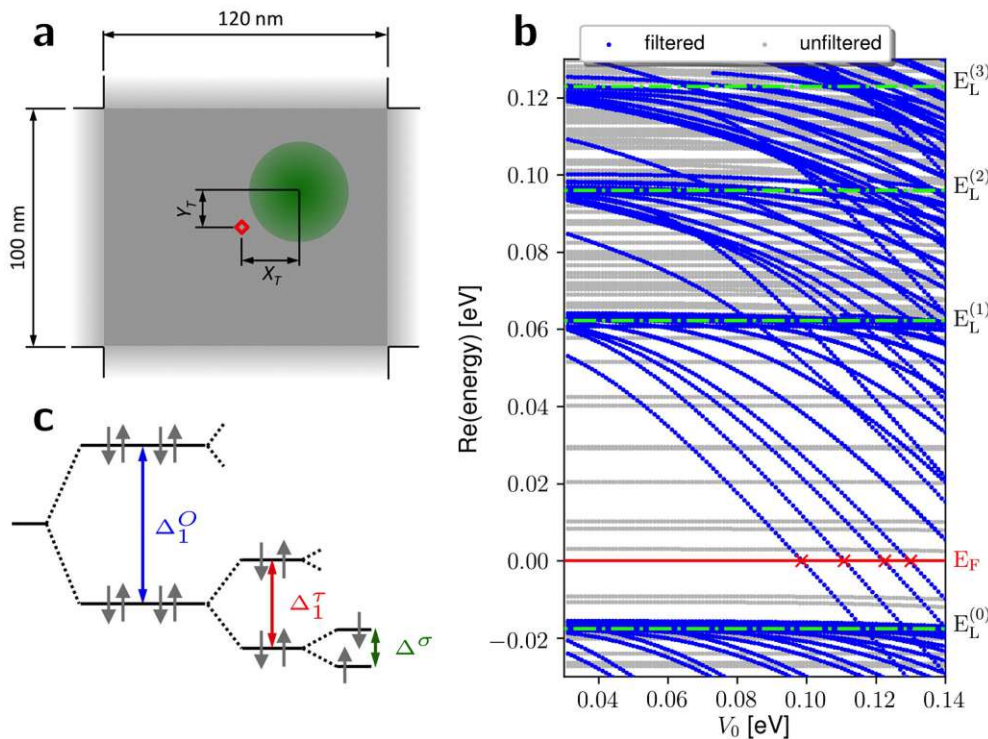


Fig. 5.2: **a** Schematic depiction of the model graphene-flake with red marker indicating the embedding position for defects (flake center) and the green circle representing the GQD (possibly shifted relative to the defect by $\mathbf{R}_T = (X_T, Y_T)$). **b** sequence of eigenenergies (real part) around the Dirac point for different values of tip voltage (and thus “depth” of the GQD potential) filtered for localized (low imaginary parts $\Gamma_{i,\tau}$, blue dots) and delocalized states (high imaginary parts $\Gamma_{i,\tau}$, grey dots). Landau level energies (horizontal dot-dashed green lines) as well as the Fermi level for defining occupied GQD states are indicated (red line). **c** Energy level diagram for the lowest two orbitals of a GQD with orbital splitting Δ_1^O , valley splitting Δ_1^T and spin splitting Δ^σ indicated.

To model the electrostatic environment due to an STM tip at a voltage V_0 , we numerically solve a classical Poisson equation [14] with the following parameters: $r_{\text{tip}} = 120 \text{ nm}$, $\epsilon_{\text{hBN}} = 4$, $\epsilon_{\text{gr}} = 2.5$ and a thickness of the hBN substrate $d_{\text{hBN}} \approx 30 \text{ nm}$. Following [201] we fit an analytic function to arrive at a rotationally symmetric potential

$$\phi_{\text{tip}}(\mathbf{r}) = \begin{cases} -V_0 \cdot \cos^5\left(\frac{\pi}{2\alpha}|\mathbf{r}|\right), & |\mathbf{r}| < \alpha \\ 0, & |\mathbf{r}| \geq \alpha \end{cases} \quad (5.3)$$

with

$$\alpha = 2309|V_0| \sqrt{1 + \sqrt{\frac{0.4}{0.005 + |V_0|}}}. \quad (5.4)$$

which can be easily implemented into our tight binding calculations (see supplemental information of [14] for details regarding the tip potential calculation). At typical tip voltages we obtain a potential well of approximately 20 nm in diameter.

We then solve the eigenproblem

$$\left[\hat{H}(E_F) + \sum_l \phi_{tip}(\mathbf{r}_l - \mathbf{R}_T) \hat{c}_l^\dagger \hat{c}_l \right] |\Psi_j^\tau\rangle = \varepsilon_{j,\tau} |\Psi_j^\tau\rangle \quad (5.5)$$

for eigenvalues within an energy range of interest via Krylov methods [202], where j counts the orbital energy levels and $\tau = +, -$ refers to the valley index of graphene. Here, E_F is the Fermi level of the surrounding graphene, which is tuned into the bulk Landau gap to optimize confinement. We model level spacings obtained in experiment, where one scans the tip potential and detects charging events whenever a GQD level is occupied [14]. We can solve Eq. (5.5) for a given V_0 to determine eigenenergies $\varepsilon_{j,\tau}(V_0)$ (Fig. 5.2b). Since the self-energy contained within the Hamiltonian breaks time-reversal symmetry (it includes only outgoing lead modes, not incoming ones), (Eq. (5.5)) yields complex eigenvalues $\varepsilon_{j,\tau} = \epsilon_{j,\tau} - i\Gamma_{j,\tau}$. The imaginary part $\Gamma_{j,\tau}$ describes the coupling to the environment — we can thus easily distinguish between states localized within the GQD (blue lines in Fig. 5.2b) and delocalized Bloch states (gray lines in Fig. 5.2b, $\Gamma < 190\mu\text{eV}$ gives a reasonable threshold). We extract the values of V_0 at which eigenvalues corresponding to localized states cross the Fermi level E_F [red crosses in Fig. 5.2b]. Recalculating for different displacements $\mathbf{R}_T = (X_T, Y_T)$ of the tip potential allows us to map out a “level spacing landscape”,

$$V_0^{j,\tau}(\mathbf{R}_T, E_F) : \quad \varepsilon_{j,\tau}(\mathbf{R}_T; V_0^{j,\tau}) = E_F. \quad (5.6)$$

We simplify the eigenvalue problem Eq. (5.5) by evaluating the now energy-dependent Hamiltonian (due to the energy-dependent selfenergy for the open boundaries) at E_F instead of $\varepsilon_{j,\tau}$ to avoid solving an otherwise quite cumbersome non-linear eigenvalue problem. This approximation becomes exact in the limit $\varepsilon_{j,\tau} \rightarrow E_F$, which is exactly the eigenenergy of each dot-state solution in Eq. (5.6) (red crosses in Fig. 5.2b). For a pristine graphene lattice, level (j, τ) crosses the Fermi level at constant tip potential ($V_0(\mathbf{R}_T) = V_0^{j,\tau} \pm 1\mu\text{eV}$) independent of tip displacement. We conclude that there are no sizeable finite-size or edge effects due to the boundary of our simulation cell.

Analytical solutions for free Dirac fermions in a magnetic field are the valley pairs[23]:

$$|\Psi_j^+\rangle = \begin{pmatrix} |\Phi_{|j|-1}\rangle \\ |\Phi_{|j|}\rangle \end{pmatrix}, \quad |\Psi_j^-\rangle = \begin{pmatrix} |\Phi_{|j|}\rangle \\ |\Phi_{|j|-1}\rangle \end{pmatrix}, \quad (5.7)$$

where the $|\Phi_j\rangle$ are eigenstates of a harmonic oscillator that can be expressed in Hermite polynomials. The orbital index j differs by one on the two sublattice components and when $j \equiv 0$, the other component “ $|j| - 1$ ” vanishes.

In the case of an additional confinement potential which (approximately) conserves valley symmetry, the structure of the solution for the two valleys suggested by Eq. (5.7) remains intact,

$$|\Psi_j^+\rangle = \begin{pmatrix} |\varphi_a\rangle \\ |\varphi_b\rangle \end{pmatrix}, \quad |\Psi_j^-\rangle = \begin{pmatrix} |\varphi_b\rangle \\ |\varphi_a\rangle \end{pmatrix}, \quad (5.8)$$

with the $\varphi_{a,b}$ now determined numerically by the exact shape of the confinement potential. The radially symmetric tip potential in Eq. (5.5) suggests a description via radial ($n_r \in \mathbb{N}_0$) and angular ($m \in \mathbb{Z}$) quantum numbers for the modified GQD states.

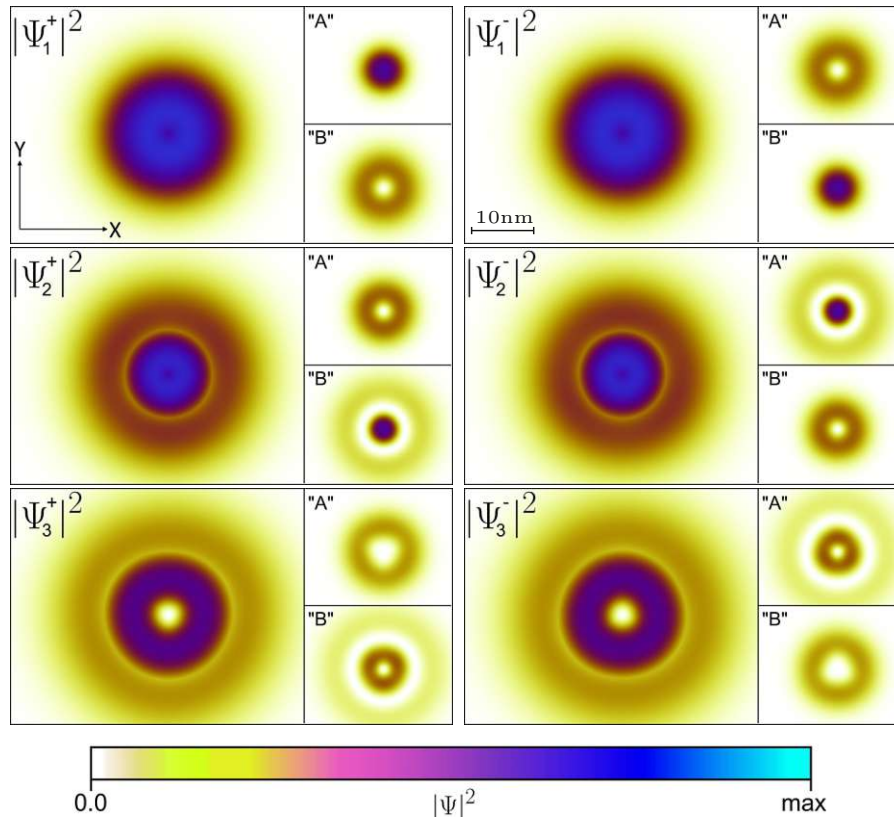


Fig. 5.3: Probability density of the first six (one valley pair per row) GQD eigenstates as well as their sublattice projected density (A/B insets) for the pristine system.

A possible adiabatic mapping from LL index N to allowed combinations of n_r and m can be formulated [203, 204]. The simulated eigenstates (Fig. 5.3), indeed, resemble the structure suggested by the analytical solution in (Eq. (5.7)) perfectly. We obtain doubly valley degenerate GQD states ($\Delta^\tau \approx 0$ meV), separated by orbital splittings $\Delta^O \approx 20$ meV. Additionally considering physical spin would yield a spin splitting $\Delta^\sigma = 800$ μ eV at 7 T. Clean numerical separation of the degenerate valley pairs can only be achieved via a small mass term ($V_{AB} = (+1, -1)$ meV) with opposite sign on the two sublattices. In subsequent calculations that include lattice defects we use these states as reference valley-states. We project the dot

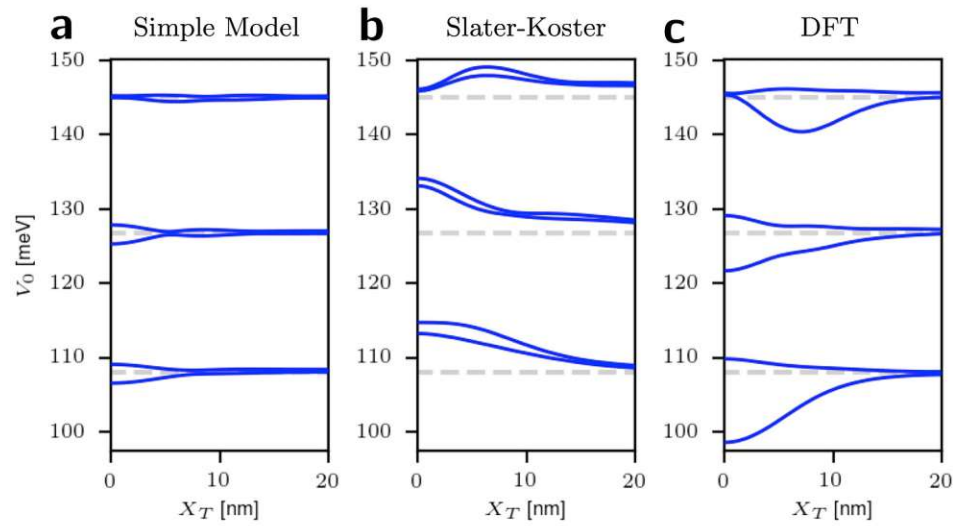


Fig. 5.4: Level spacing landscape for different embedding methods of the double vacancy defect for GQD displacement in x-direction.

wavefunctions on the corresponding $\langle \Psi_i^+ |$ as a measure for the residual valley polarization

$$P_\tau = |\langle \Psi_i^+ | \Psi_i^\tau \rangle|^2, \quad (5.9)$$

where $|\Psi\rangle$ represents a GQD state in the presence of a defect while $|\psi\rangle$ is the corresponding state of the pristine system with the same displacement of the tip.

How do lattice defects modify the level spectrum of the GQD? We include defects at the center of our flake by suitably tuning the onsite and hopping elements in Eq. (5.2). Then, we study the change of the level spectrum, (Eq. (5.5)), as a function of quantum dot displacement \mathbf{R}_T (see Fig. 5.2a).

Since the quantum dot eigenstates sensitively probe the local electronic environment, care must be taken to correctly model the various defects. We consider, in order of increasing accuracy and numerical cost, different approaches for the simple case of a lattice double vacancy:

- (a) The poor man's description of a vacancy simply removes the corresponding orbitals entirely, while everything else remains unchanged.

More elaborate approaches are based on some level of density functional theory (DFT). We use the VASP software package for DFT calculations [205–208] and refer to our earlier work for technical details [209].

- (b) Based solely on the relaxed defect geometry obtained from DFT (or, potentially, from a molecular dynamics simulation or STEM / STM measurements), one can parametrize the defect based on a simple Slater-Koster model [210, 211].

Finally, one can extract tight-binding parameters directly from the DFT result, without the need for empirical models. We use Wannier90 [212–214] and project only on the carbon p_z orbitals, since those dominate the electronic structure around the Fermi energy:

- (c) We extract the parametrization of the entire defect from a 6×6 DFT supercell calculation.

In the full defect calculation (c) the tight-binding parameters obtained by Wannier90 reproduce the DFT band structures of the fully relaxed defect geometry, with a maximal deviation of 4 meV in an energy range around the Dirac point (± 1.25 eV). While numerically quite costly, this approach should be the most accurate one, and can be used to benchmark the two more approximative methods. Unfortunately, both (a),(b) heavily underestimate the induced valley splittings compared to the fully wannierized embedding (see Fig. 5.4). Since the qualitative agreement of method (b) (Slater-Koster, Fig. 5.4b) also seems lacking, we conclude that using such a general parametrization is not accurate enough for the present problem (agreeing results for other defects not shown). In contrast, the very simple method (a), inherently only usable for vacancies, provides an — admittedly rough — qualitative estimate of induced valley splittings.

The asymmetry of the induced valley splitting (relative to the gray lines in Fig. 5.4 representing the pristine system) at displacement $X_T = 0$ is only seen when using a full DFT supercell calculation. The resulting level spectrum landscape of a defect would therefore appear to be an intricate function of all hopping terms. None of the low level methods provide a reasonable alternative to a full Wannierization of the defect super cell (method (c)). We therefore employ method (c) in all subsequent calculations.

5.3 Tuneable Valley Splittings

We henceforth investigate the influence of various defects, such as double vacancy, a silicon substitution and a flower defect on the potential landscape $V_0^{i,\tau}(\mathbf{R}_T)$. These defects induce a sizeable valley splitting Δ^τ as well as a series of avoided crossings in the valley subspace. Our findings prove robust even in the presence of moderate, long-range correlated disorder (representing influence of the hBN substrate), as outlined below. These findings suggest that a suitable arrangement of defects on the lattice can be used to engineer a desired series of avoided crossings. A graphene flake with correctly placed defects could thus serve as a scaffold for quantum-mechanical few-level systems with tailored interactions.

Double Vacancy A double vacancy strongly perturbs the valley symmetry of a GQD (see Fig. 5.5) resulting in a sizeable, asymmetric valley splitting of the lowest orbital ($\Delta_1^\tau \approx 13$ meV) when the tip is located at the defect, $\mathbf{R}_T = (0, 0)$. This splitting decreases for the second orbital to about 8meV and vanishes completely for the third orbital due to the decreasing probability density of the wavefunctions at the GQD center (see Fig. 5.3). At $\mathbf{R}_T = (0, 0)$ the valley pairs split into an energetically favourable, localized state, and a delocalized state at an energy similar to the pristine system. In a double vacancy, with the sublattice corresponding to the “upper” missing atom labelled as “A”, the wavefunction in the upper semicircle predominantly localizes on the “B” sublattice, and vice-versa for the lower hemisphere

(see Fig. 5.6). The energy of the state is thus lowered by avoiding the inter-sublattice hopping to the missing atom.

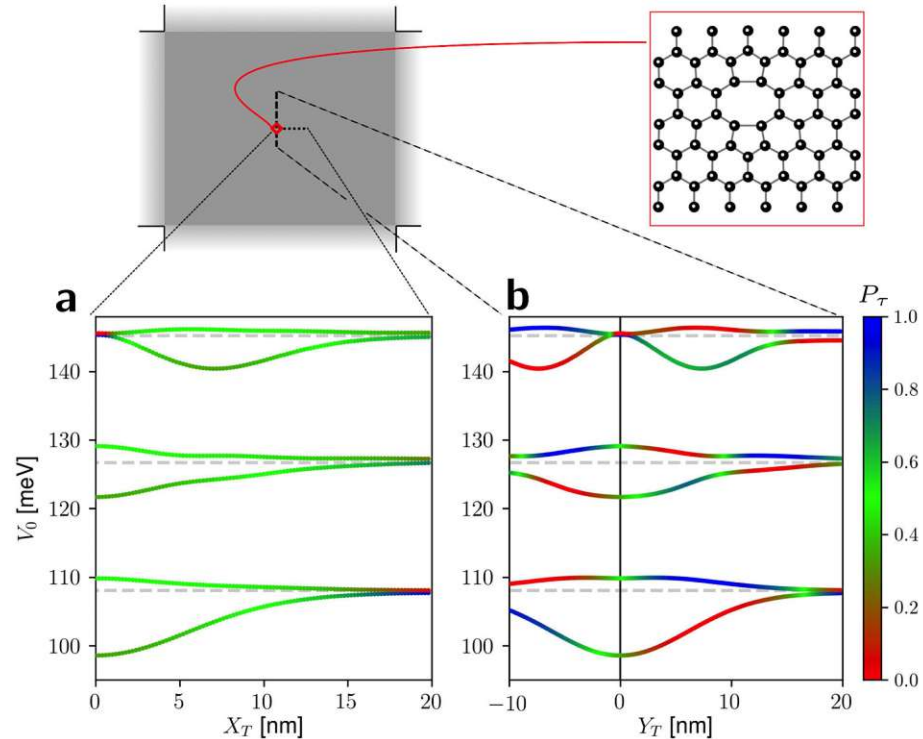


Fig. 5.5: Displacement dependent level spectrum for the lowest GQD states (first three valley pairs) in the presence of a double vacancy defect at the indicated position (red marker in flake schematic) for GQD displacement in **a** x-direction and **b** y-direction. The color scale represents the squared overlap between defect and pristine wavefunctions P_τ as defined in Eq. (5.9).

The dependence of the induced valley splitting Δ_i^τ on the distance to the defect correlates with the radial density distribution of the corresponding pristine wavefunctions $|\Psi_i^\tau\rangle$: We plot P_τ (see Eq. (5.9)) as colorscale in the level-spacing landscapes. States with $P_\tau = 0$ (red) or 1 (blue) have perfect overlap with the pristine valley solutions of Eq. (5.8), whereas $P_\tau = 0.5$ (green) indicates a balanced superposition within the pristine valley basis (“valley mixing”). The splitting Δ^τ and valley mixing gradually decrease and are lost when there is no more density at the defect site. The lowest — and thus narrowest — orbitals regain the characteristic structure of Eq. (5.8) at a distance of about 20 nm (see red/blue color scaling associated with $P_\tau = 0, 1$ in Fig. 5.5). While the magnitude of the induced valley splitting Δ^τ is independent of the direction of displacement of the GQD, the respective states differ substantially (compare Fig. 5.5a,b). For displacements perpendicular to the axis through the two removed carbon atoms of the double vacancy (x-direction in our coordinate system) we find no well-defined valley polarization P_τ , (Eq. (5.9), green lines in Fig. 5.5a) indicating a maximal mixing of the valley states as soon as the defect is within the typical radius of the respective GQD orbital. At very small

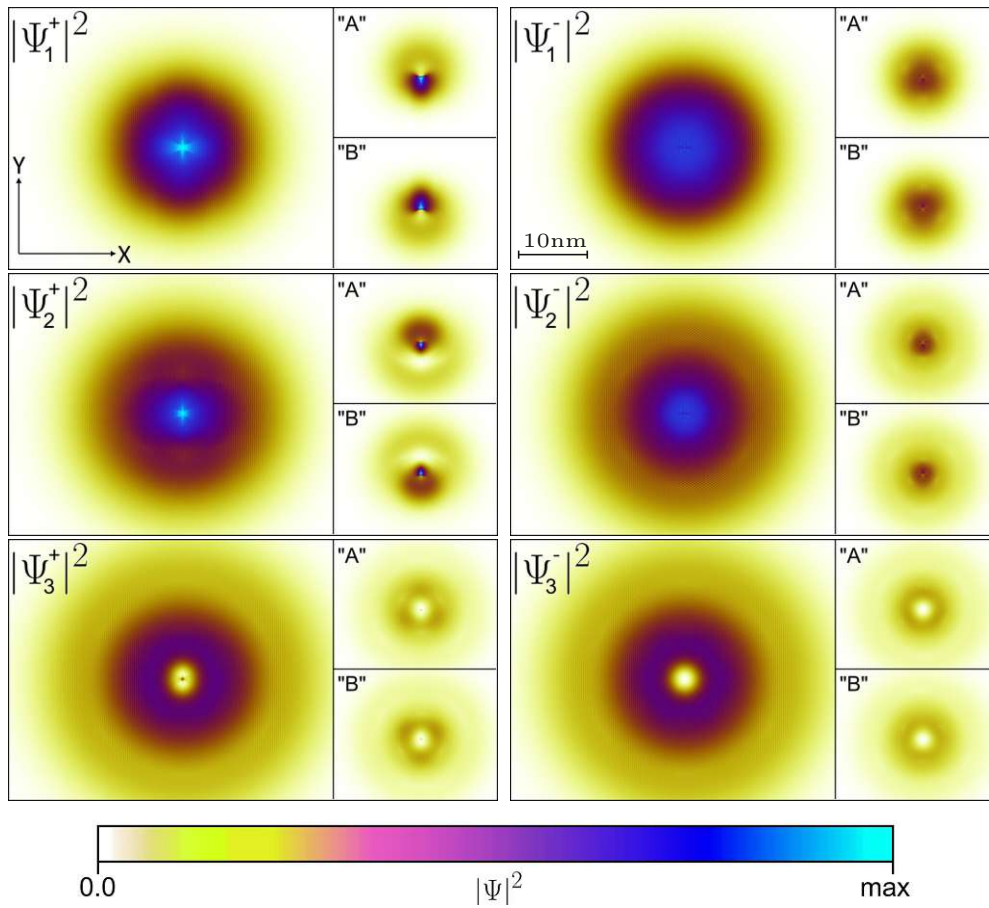


Fig. 5.6: Probability density in the presence of a double vacancy for $\mathbf{R}_T = (0, 0)$. The panels show the first six (one valley pair per row) GQD eigenstates as well as their sublattice projected density (A/B insets)

distances ($X_T < 5$ nm) this mixing is no longer restricted to a specific valley subspace as $P_+ + P_-$ no longer add up to one. Displacing the GQD parallel to the double vacancy (y -direction) reveals a fundamentally different evolution of P_τ including several avoided crossings connected by regions where $P_\tau \approx 0$ or 1 (Fig. 5.5b). Displacing the tip in y direction induces an asymmetry with respect to the vacant atom positions, which leads to a sequence of avoided crossings as the maxima of probability density pass over the defect position. This asymmetry is also reflected in the sublattice projected densities (top left of Fig. 5.6) and gives an intuitive understanding of the valley inversion that occurs when the tip is displaced in $\pm y$ direction.

Flower Defect The flower defect, a 30° rotation of a region containing seven carbon rings [215, 216] (see inset in Fig. 5.7a), induces valley splittings of similar magnitude as the double vacancy at $\mathbf{R}_T = (0, 0)$ (Fig. 5.7a). However, the splitting opens in a very symmetric way, $\epsilon_\pm^{\text{flower}} \approx \epsilon_0 \pm \Delta^\tau / 2$ (gray dashed lines in Fig. 5.7a), while the strong localization at the double vacancy site induces an asymmetric valley splitting, $\epsilon_+^{\text{vacancy}} \approx \epsilon_0$ and $\epsilon_-^{\text{vacancy}} \approx \epsilon_0 - \Delta^\tau$. Despite being a pure relocation defect with comparatively large extent, the level spectrum seems to approach the pristine limit much

sooner when increasing the GQD-defect distance. Moving the GQD in x-direction produces an almost identical response of the levels as in (Fig. 5.7a), confirming the well preserved rotational symmetry of the flower defect.

Silicon Substitution The level spectrum with a silicon substitution defect [217] shows far smaller valley splittings (2meV for the lowest orbital). Its comparatively weak perturbation to the valley symmetry is also reflected by values of P_τ close to 0 and 1 (red/blue color scale) with very narrow avoided crossings. The lowest orbital shows no valley inversion at all (Fig. 5.7b).

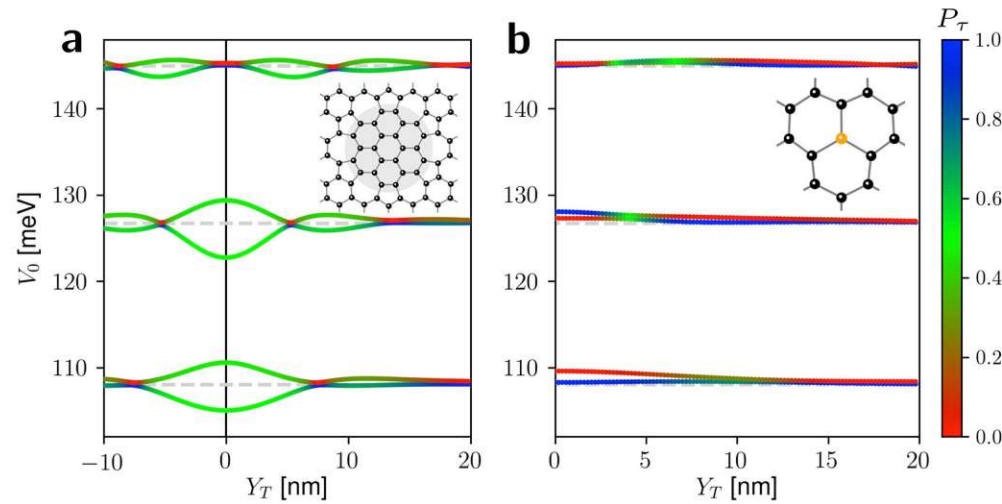


Fig. 5.7: GQD energies as function of quantum dot position $\mathbf{R}_T = (X_T, Y_T)$ relative to **a** a flower defect and **b** a Si substitution defect for GQD displacement in y-direction.

Magnetic field The magnetic field is what enables smooth confinement in the first place by creating the confinement gap due to Landau quantization. We want to emphasize that increasing (decreasing) the magnitude of the magnetic field to first order only resizes this confinement gap and thus merely globally shifts the level spectrum landscape to higher (lower) values of V_0 . Investigating the system at different field strengths (not shown) reveals that valley splittings Δ_i^τ are not significantly sensitive to the magnetic field strength.

Disorder Some additional disorder (e.g. due to substrate interaction) will undoubtedly be present in the experiment. We create a correlated disorder potential $V_D(\mathbf{r})$ with various correlation lengths l_{corr} and amplitudes $V_D^0 = \sqrt{\langle V_D^2 \rangle}$, and $\langle V_D \rangle = 0$, by convolution of uncorrelated disorder with a Gaussian kernel. This should adequately represent the typical potential landscape of graphene on a non-aligned hBN substrate even in the presence of possible defects/impurities in the hBN.

Very large l_{corr} of the order of the GQD size ($\text{FWHM} \approx 20\text{nm}$) merely result in global shifts to all GQD levels with almost no changes to the level splittings. In contrast, the influence of short-ranged disorder is a priori not clear. However, since our system is deep in the Landau regime, another

important length scale is given by the magnetic length ($l_B \propto 1/\sqrt{B}$), which in our case ($|B| \approx 7\text{T}$) evaluates to about 9.4 nm. The system thus averages over disorder on length scales below this limit, and since $\langle V_D \rangle = 0$ the level spectrum landscape recovers the unperturbed shape.

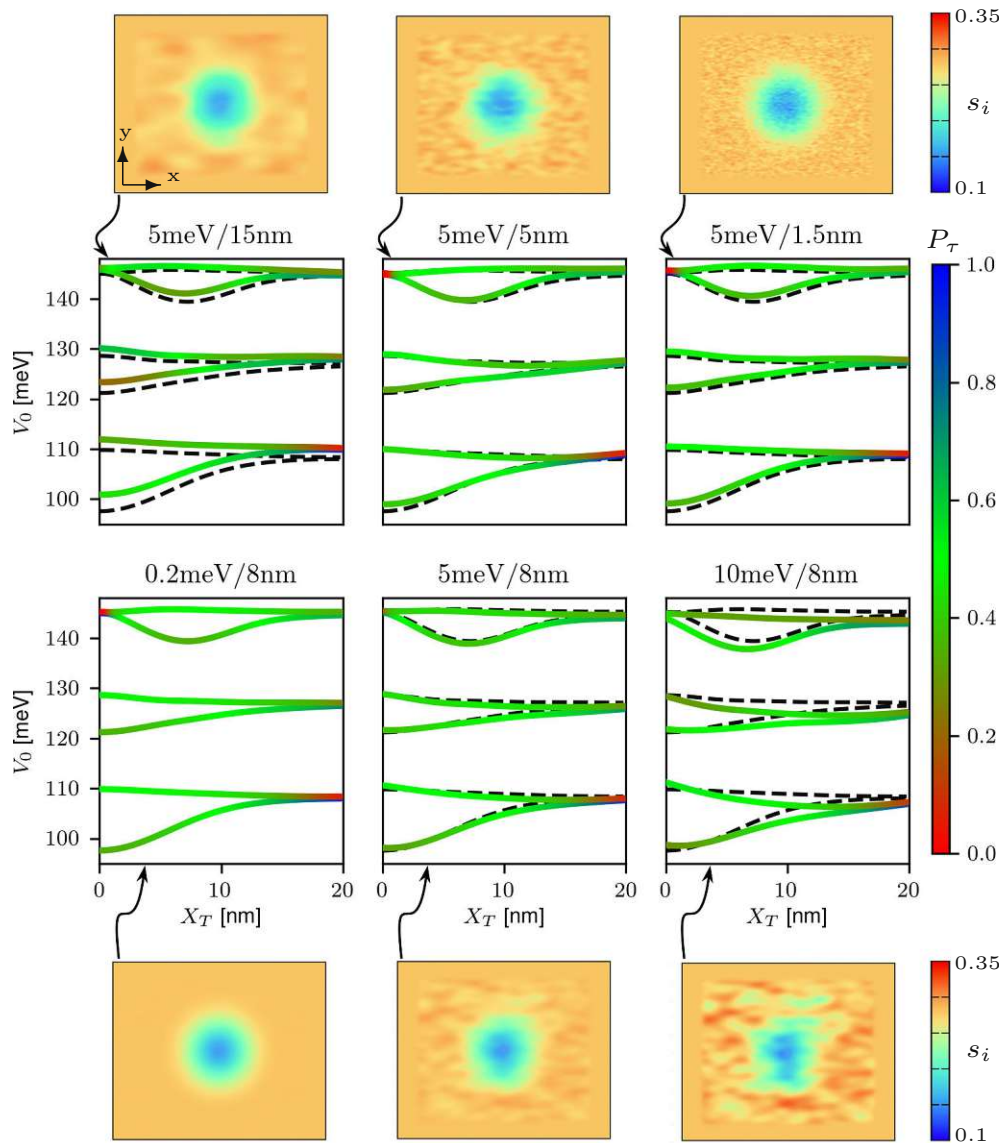


Fig. 5.8: Level spectrum landscapes for the double vacancy defect (with GQD displacement in x-direction) in the presence of correlated disorder (dashed black lines correspond to vanishing disorder). The subplots are labelled with values for both $\sqrt{\langle V_D^2 \rangle}$ and l_{corr} . Each subplot is additionally referenced by a sketch of the total onsite potential s_i [eV] throughout the graphene flake ($120 \times 100\text{nm}^2$) to put the included disorder into perspective.

We consider valley projections for the double vacancy (Fig. 5.8) as in (Fig. 5.6), but with additional disorder. Both the induced valley splitting as well as the wavefunction character P_τ are robust for various amplitudes and characteristic length scales of the disorder. Typical disorder up to a strength of 10 meV with correlation lengths between 1.5nm and 15nm only slightly distorts the level spectrum landscape, and most importantly, has no effect on the magnitude of the level splitting. The two main changes of the wavefunction due to disorder are: (i) some density is induced at the vacancy site ($|\Psi_i^\tau|^2(r=0) \neq 0$) for all orbitals, which leads to valley mixing, and (ii) regions of low values of P_τ for large V_D (green colorscale in Fig. 5.8) appear because the valley doublet in the pristine basis becomes poorly suited to accurately represent the distorted wave functions.

5.4 Transition Dynamics

In the static system, lattice defects can induce sizeable valley splittings Δ^τ of an order comparable to the orbital splitting Δ^O . We now investigate the dynamics of moving the GQD with respect to the defect on time scales relevant for the electronic dynamics. We find that dynamically traversing the GQD in the vicinity of such defects provides an elegant approach to drive transition between GQD states. An experimental realization will require much shorter time scales than those accessible via moving an STM tip. While dynamically generating a moving potential-well via electronic gates seems plausible, fabricating an array of gates on the nm scale (as is required for this task) remains a challenging aspect with current resolution limits of electron beam lithography [218].

To elucidate the dynamics near an avoided crossing between two valley states, we consider a toy Hamiltonian of the form

$$H(t) = \frac{1}{2} \begin{bmatrix} \alpha t & \Delta \\ \Delta & -\alpha t \end{bmatrix}, \quad (5.10)$$

describing the general structure of an avoided crossing: for the diabatic Hamiltonian with conserved symmetry (i.e., $\Delta = 0$), the two eigenenergies become degenerate at $t = 0$. For broken symmetry (i.e., finite Δ), degenerate perturbation theory yields an avoided crossing with an energy spacing of Δ . Landau-Zener theory [219, 220] provides a straightforward analytical approach to estimate the diabatic transition probabilities for propagating an initially valley-pure eigenstate past the avoided crossing:

$$\rightarrow P_{\text{diabatic}}^{(\text{LZ})} \propto \exp\left(-\frac{\pi\Delta^2}{2\alpha}\right) \quad (5.11)$$

The movement of the GQD is parametrized by the time t , and thus $\alpha = v_T \cdot |\nabla_r(\varepsilon_{i,-} - \varepsilon_{i,+})|$, where $v_T = \partial_t \mathbf{R}_T$ is the traversal velocity of the GQD. The second term represents the slope of the spectral landscape of a valley doublet in real space. Close to an avoided crossing we consider one valley doublet as an effective two level system ($\Delta^\tau \ll \Delta^O$) such as the one modeled by the toy Hamiltonian of (Eq. (5.10)). Different traversal

velocities v_T allow for either adiabatic (low speeds) or diabatic (high speeds) propagation of an initial eigenstate. To simulate the dynamics, we use state-of-the-art time propagation via Magnus operators with adaptive time steps based on computable upper error bounds for the Krylov approximation [221] and error estimates of the Magnus integrator [222]:

$$|\Psi(t_B)\rangle = \hat{U}(t_B, t_A) |\Psi_2^+\rangle \quad (5.12)$$

We propagate an initial state $|\Psi_2^+\rangle$ at $(X_T, Y_T) = (0, 5.6)$ nm, indicated by the black dot and arrow in (Fig. 5.9b), from “A” to “B” (see Fig. 5.9a). The crossing has to be approached by an instantaneous GQD eigenstate in level “1” with a well defined velocity v_T . We therefore have to smoothly accelerate from a static eigenstate, which restricts the selection of possible crossings. We choose a rather wide (i.e. large Δ in Eq. (5.10)) avoided crossing (between third and fourth GQD level of the double vacancy in y -direction, see Fig. 5.9b). An even wider avoided crossing would require a larger traversal velocity to achieve diabatic switching (Eq. (5.11)), reaching values that cannot be sufficiently smoothly accelerated to, because the neighbouring avoided crossings would be in too close proximity. Narrower (i.e. small value for Δ in Eq. (5.10)) avoided crossings (e.g. see the avoided crossings generated by the flower defect in Fig. 5.7a) would result in much too long traversal times (this time for the adiabatic result) beyond our computational time limits. In experiment much larger time scales would be accessible, and thus narrower avoided crossings should be considered.

As we propagate our initial wave function from “A” to “B” (Fig. 5.9) we project $|\Psi(t)\rangle$ onto the third ($|\Psi_2^+\rangle$) and fourth ($|\Psi_2^-\rangle$) orbitals of the static calculations of the otherwise identical system. The projection $Q_\tau(t)$ on the valley $\tau = \pm$ at displacement $X_T(t)$ is given by

$$Q_+(t) = |\langle \Psi_2^+ | \Psi(t) \rangle|^2, \quad Q_-(t) = |\langle \Psi_2^- | \Psi(t) \rangle|^2, \quad (5.13)$$

and shown in (Fig. 5.9c). Note that we project onto the static defect state at the same GQD position, not the pristine state.

Performing these calculations for a range of different traversal velocities v_T reveals the expected diabatic switching for faster traversal. We calculate the “final” projection values of $|\langle \Psi_2^- | \Psi(t) \rangle|^2$ after the avoided crossing has been traversed (blue crosses in Fig. 5.9c) as a function of the corresponding velocity (Fig. 5.9d). We find surprisingly good agreement with the simple two-level Landau-Zener formalism. The distorted nature of the underlying avoided crossing impedes a precise evaluation of the parameters $|\nabla_r(\epsilon_{i,-} - \epsilon_{i,+})|$ and Δ used in the Landau-Zener formula. Due to the exponential sensitivity of the transition curve on these parameters, a fit to our numerical data for the transition probability in Fig. 5.9d is much more accurate than estimating these parameters directly from the shape of the avoided crossing in Fig. 5.9b.

We thus determine $|\nabla_r(\epsilon_{i,-} - \epsilon_{i,+})| = 163 \mu\text{eV/nm}$ and $\Delta = 1.9 \text{ meV}$ from a fit to the data points in Fig. 5.9d, and find these values entirely consistent with the shape of the avoided crossing of the level spacing landscape. Quantitatively predicting the required transition speed from the shape of the avoided crossings might therefore prove difficult. Nevertheless, the

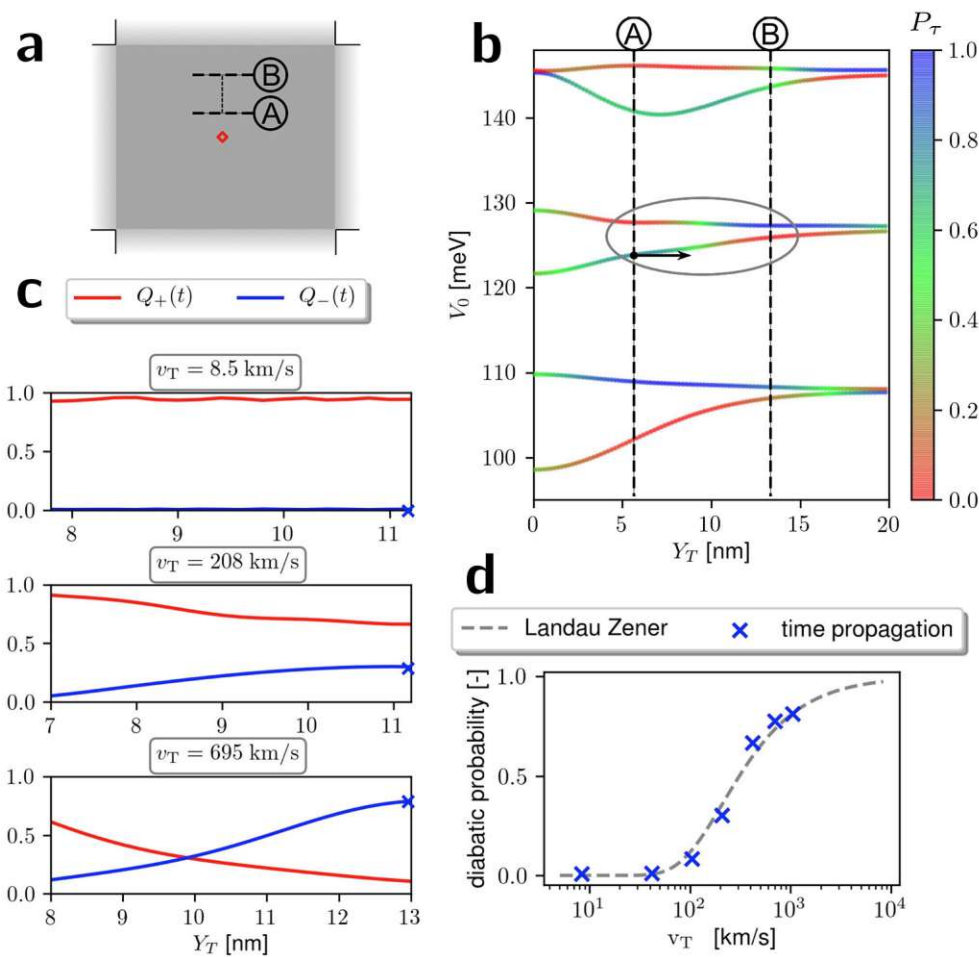


Fig. 5.9: **a** Schematic overview of the graphene flake with initial and final y-coordinate of the GQD center indicated by lines labelled "A" and "B". **b** Level spectrum landscape of the double vacancy defect with the avoided crossing between levels 3 and 4 centered between lines "A" and "B" which correspond to the ones in a). **c** Squared projections (as labelled) of the propagated state as a function of y-coordinate. **d** Final values of the projections in c) superposed onto the analytical function for the diabatic transition probability.

qualitative dependence of the diabatic transition probability on the traversal speed still offers an elegant way to enact controlled transitions between GQD levels, a necessary first step for possible applications in emerging quantum technologies.

5.5 Conclusion

We have modeled the response of the level spectrum of smoothly confined graphene quantum dots to lattice defects in tight-binding calculations. By embedding a local defect parametrization, obtained from Wannier-projection of DFT super cell calculations, into an extended pristine lattice (also parametrized from DFT) we present an elegant way of manipulating the level spectrum of edge-free GQDs by making use of some common imperfections of graphene lattice structures. We identify several avoided crossings within the valley doublets for the different quantum dot states. Conversely, measuring the evolution of the quantum dot eigenenergies with dot position would provide a sensitive probe for the electronic structure of the defect. Transition dynamics in these GQD-defect systems are well described by Landau-Zener theory.

Employing the defects for dynamic control of electronic states within the GQD, demonstrated as theoretically possible, will be challenging in experimental setups. Scanning tunneling microscopy tips are not designed to be moved rapidly and one would instead need to spatially and temporally control the GQD via an array of electronic gates. We feel that the feasibility of such an array of gates depends on the resolution limits of current electron beam lithography [218]. While creating an array of several gates on a scale of 10 - 15 nm (as is the traversal distance for the presented crossing) with a resolution of at best 1 - 3 nm seems challenging at the moment (but not entirely out of reach in the near future) we also stress that there is some “customizability” for the shape of an avoided crossing when allowing for more complex systems that involve more than a single isolated point defect (i.e. two close-by defects can be of different type and have varying orientation or distance in relation to the GQD).

The predicted defect-induced valley splittings Δ^τ on the order of up to 12 meV should be experimentally accessible and warrant further research.

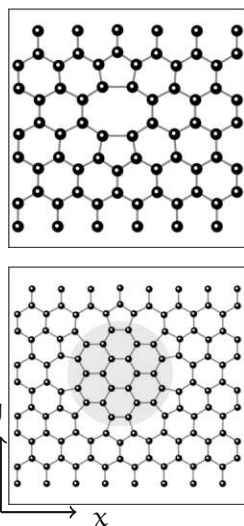


Fig. 6.1: Lattice geometry of double vacancy (top) and flower defect (bottom) in single layer graphene.

Chapter 6

Defect parametrization via Machine Learning

“If you torture the data long enough, it will confess.”

R. Coase

In this section we present an automated ML workflow to generate accurate tight-binding parametrizations for defects. We achieve ab-initio density functional theory accuracy for a wide range of material properties using only band energies and defect geometry as inputs. We test several machine learning methods that map the atomic and electronic structure of a defect onto a sparse tight binding parameterization. Since Multi-layer perceptrons (i.e. shallow feed-forward neural networks) perform best we adopt them for final benchmarks that carefully assess the accuracy of our parametrizations in terms of bandstructure reconstruction, local density of states, electronic transport and level spacing simulations for two common defects in single layer graphene (SLG). The developed approach is general and can be applied to a wide range of other materials, enabling accurate large-scale simulations of material properties in the presence of different defects.

6.1 Ab-initio modeling of defect super cells

Calculating the electronic structure and transport properties of nano devices containing millions of atoms requires suitable techniques to tackle the different length scales involved. On the atomic scale, accurate but expensive DFT methods provide precise parameters for large-scale tight-binding approaches that operate on the entire nanodevice. Such a multi-scale approach has been well established for pristine materials. The description of defects proves inherently more challenging, with only a few established approaches that differ substantially in accuracy and effort (see Chapter 5). An accurate description of how these defects modify the electronic structure of a system is thus key for exploring potential applications of novel materials.

In recent years, machine learning (ML) has facilitated new research lines in materials science and chemistry [223–234]. This project aims for an ML based scheme that achieves Wannier TB accuracy with much simpler inputs (i.e. only band structure and geometry information). Ultimately we do not want to merely generate a parametrization for a defect but embed it into a large scale system and perform subsequent calculations to

study multi-scale effects in realistic systems. The efficiency of applying TB parametrizations typically scales with the sparseness of the TB Hamiltonian (typically a banded matrix with the only non-zero coupling elements close to the main diagonal [235]). Therefore we want to be able to tune the sparseness of our machine-learned TB parameters at will to obtain a desired balance of accuracy and efficiency. To remain accurate despite fewer tuning parameters implied by improved sparsity, we will adjust the parametrization to specific energy regions of interest (i.e. close to the Fermi edge). This proof-of-concept aims to strike a balance between the laborious but excellent Wannier parametrizations and customary but limited empirical models such as Slater-Koster (SK) [236–238]. In addition to providing such a middle ground, our model achieves predefined sparseness with only minor (quantitative) shortcomings in a comprehensive set of benchmarks. We aim to develop an easy-to-use framework that can efficiently produce TB parametrizations of any given defect in a material. In this section we will generate machine-learned TB models for two common defects in single layer graphene (double vacancy and flower defect, see Fig. 6.1).

6.2 Tight binding model

Tight-binding methods (TB) are well established for modelling electronic and transport properties of large scale systems. A suitable parametrization for a given system can be generated with different aspirations of accuracy: Starting point can be either a set of symmetry-adapted empirical parameters (e.g. Slater-Koster) or a more accurate ab-initio-based description typically obtained by projecting extended Bloch states on a truncated set of suitably chosen localized basis functions (Wannierization [124, 239–241]). In contrast to pristine materials the description of defects is an inherently more intricate problem as the necessary super-cell size increases while its symmetry is diminished. This customary increase in system size entails challenges for the selection of relevant bands in the much more densely populated Brillouin zone and necessitates profound experience for the choice of basis functions to accurately represent the ab-initio calculation within a TB model. While the usability of a Slater-Koster approach is hardly affected by the change in system size its validity suffers due to its inability to describe the qualitative changes to the electronic configuration of complicated defects.

Without loss of generality we will focus on 2D systems. Such systems with n_o orbitals can then be described by a TB Hamiltonian of the generic form:

$$\mathcal{H} = \sum_i^{n_o} s_i \hat{c}_i^\dagger \hat{c}_i + \sum_{\langle i,j \rangle} \gamma_{ij} \hat{c}_i^\dagger \hat{c}_j. \quad (6.1)$$

Here $\hat{c}_i^\dagger (\hat{c}_i)$ are the creation (annihilation) operators of a quasiparticle at site i with position r_i , $s_i = \langle i | \mathcal{H} | i \rangle$ the onsite (diagonal) matrix elements and $\gamma_{ij} = \langle i | \mathcal{H} | j \rangle$ the hopping amplitudes between sites i and j . For single layer graphene we will only take into account a single p_z orbital per carbon site. In more complicated materials (i.e. several orbitals per lattice site) indices i, j may subsume atomic and orbital information. For sufficiently localized

orbitals, the magnitude of γ_{ij} quickly decays for increasing interatomic distances $|\mathbf{r}_i - \mathbf{r}_j|$. Omitting such elements below a certain threshold (e.g. 1meV) can make \mathcal{H} sparse.

Given a converged DFT Hamiltonian in a basis of Bloch functions, optimal values for s_i , γ_{ij} can be directly calculated using maximally localized Wannier functions [212–214, 242] (see Section 3.5). In practice, however, exactly evaluating the s_i, γ_{ij} proves not optimal: after tedious iteration to find suitable Wannier functions, the final degree of localization — i.e., the distance beyond which overlaps between orbitals are small enough to be neglected — may be several unit cells [112]. To obtain a more sparse description, one can directly fit a small set of TB parameters s_i, γ_{ij} to reproduce the DFT BS in an energy region of interest. The second sum in Eq. (6.1) then only runs over the n -th nearest-neighbour (NN) sites [Fig. 3.1], where $|\mathbf{r}_i - \mathbf{r}_j| < r_{NN}$ with a cutoff radius r_{NN} controlling the sparseness.

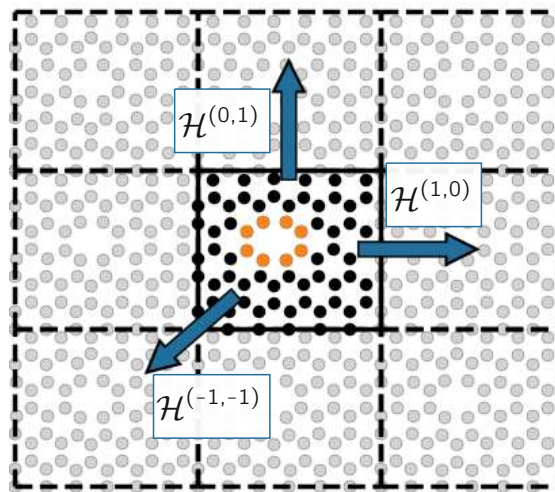


Fig. 6.2: Interaction of a defect supercell with its periodic images (defect region highlighted in orange). The center cell itself is described by $\mathcal{H}^{(0,0)}$, the interactions to its neighboring cells by $\mathcal{H}^{(\lambda_x, \lambda_y)}$ — for large super cells such as this only the nearest-neighbor interactions between cells, i.e., $\lambda_x, \lambda_y \in \{-1, 0, 1\}$ are non-zero.

Plane wave based DFT calculations describe periodic systems and we account for the Bloch phase of the periodic wave function by adding corresponding phase factors in the periodic images of the Hamiltonian. The periodic Hamiltonian matrices $\mathcal{H}^{(\lambda_x, \lambda_y)}$ determine the interaction of sites in the original cell $(0, 0)$ with sites in the periodic image of the cell (λ_x, λ_y) translated along a linear combination of lattice vectors $\{\lambda_x \cdot \mathbf{R}_x, \lambda_y \cdot \mathbf{R}_y\}$. The full Hamiltonian in \mathbf{k} -space thus reads:

$$\mathcal{H}(\mathbf{k}) = \sum_{\lambda_x, \lambda_y} e^{i\mathbf{k} \cdot (\lambda_x \mathbf{R}_x + \lambda_y \mathbf{R}_y)} \mathcal{H}^{(\lambda_x, \lambda_y)} \quad (6.2)$$

Note that the set of s_i, γ_{ij} entirely determines the matrix elements of $\mathcal{H}^{(\lambda_x, \lambda_y)}$ while the grouping into periodic cells just accounts for the periodicity of the lattice. A system of interest is thus fully described by a set of lattice vectors and parameters s_i, γ_{ij} yielding the Hamiltonian matrices

$\{\mathcal{H}^{(\lambda_x, \lambda_y)}\}$. The indices $\lambda_x, \lambda_y \in [-m, m]$ with $m \in \mathbb{N}_0$ determine the range of non-zero interactions between periodically shifted unit cells. In practice, we truncate at $|m| = 1$ given the large defect super cells in this thesis (see Fig. 6.2).

Given the large super cells of defect systems we have to consider a reduction of the number of free parameters for the TB Hamiltonian. For much smaller pristine systems a (more manageable) TB Hamiltonian has recently been directly parameterized with a ML approach [243]. In our case, if we were to only enforce hermiticity, our TB Hamiltionian of Eq. (6.2) would feature $\frac{n_o(n_o+1)}{2} + 4n_o^2$ independent parameters s_i, γ_{ij} , which quickly gets out of hand. Considering a medium-sized defect supercell with 70 orbitals this would require approximately 25000 independent parameters. We can however employ the residual symmetries of a defect structure to further reduce the number of parameters our ML model needs to optimize. To obtain a robust framework, we aim for a simple mapping between the hopping matrix elements γ_{ij} and local geometry information. Finding such

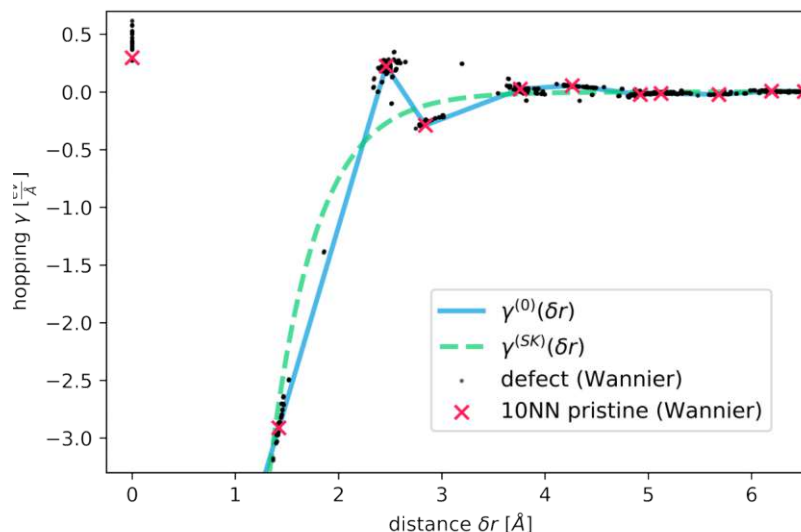


Fig. 6.3: Distance-hopping map for all entries of a Wannier parametrization for the double vacancy defect in SLG (black dots) with both a Slater-Koster based initialization (taken from [210]) $\gamma^{(SK)}(\delta r)$ (dashed green line) as well as another initialization $\gamma^{(0)}(\delta r)$ defined as spline interpolation between the 10th-NN distance-hopping values of a bulk singler layer graphene cell (red crosses). The hoppings at distance zero represent the onsite energies s_i .

a simple mapping seems daunting as coordination numbers of atoms around the defect site will in general differ substantially from those in the bulk. A general mapping therefore seems to require detailed information about the local chemical environment. We avoid additional, complex geometrical parameters by exploiting that for the pristine bulk lattice, there are only a few distances (the nearest-neighbour spacings, red crosses in Fig. 6.3) while a relaxed defect geometry features many different distances. We generate the γ_{ij} purely as a mapping of distance $\gamma_{ij} = \gamma(|\mathbf{r}_i - \mathbf{r}_j|)$ to obtain an efficient and compact representation of the final TB Hamiltonian. A sufficiently fine, discontinuous mapping between atomic distance and

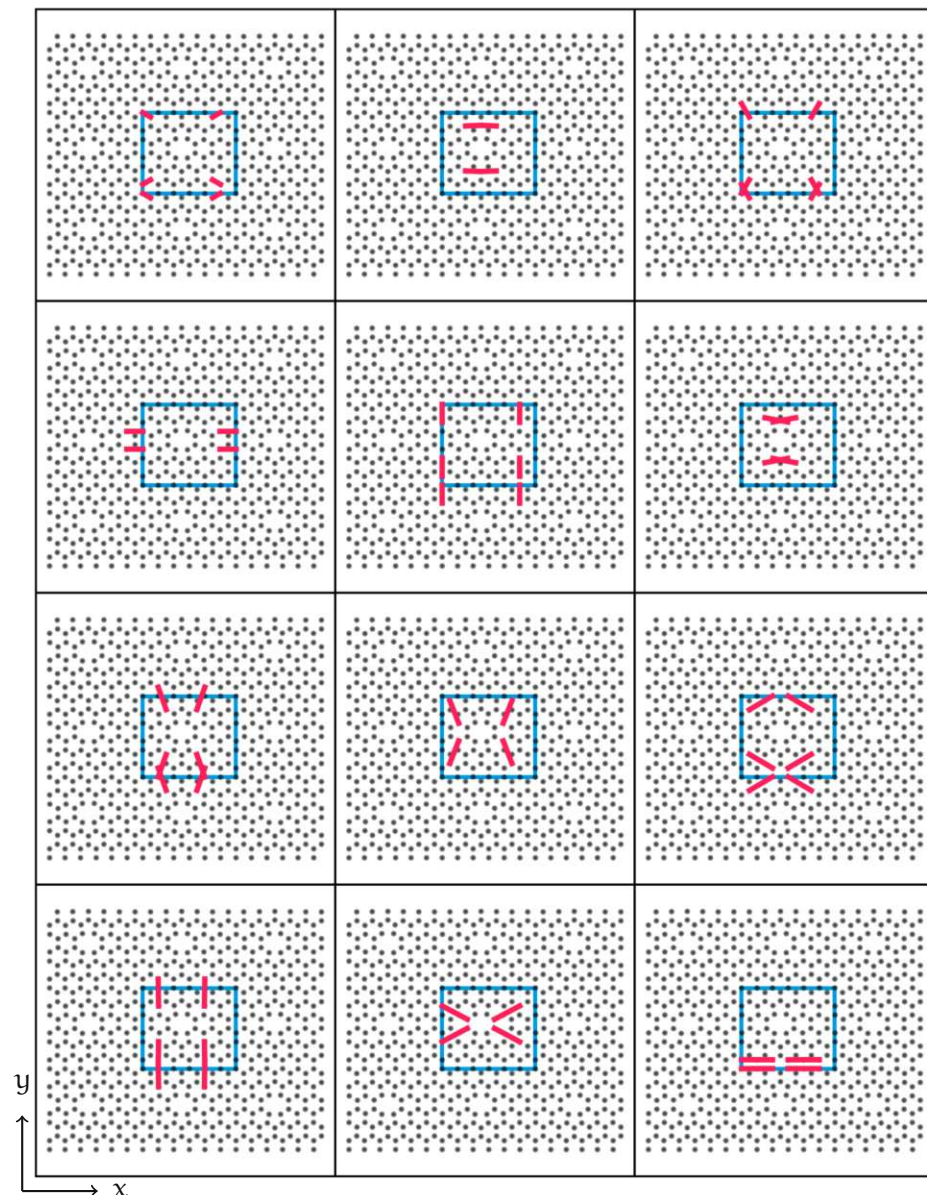


Fig. 6.4: Non complete selection of representative distance classes with the symmetry related interactions highlighted in red (defect super cell indicated in blue).

hopping parameters essentially implies assigning an individual hopping parameter to each unique distance — except for degeneracies implied by symmetries, which should, indeed, have the same hopping interaction. A parametrization on distance alone thus yields a hermitian Hamiltonian correctly accounting for symmetries by construction. We can also simply choose a cutoff length r_{NN} above which no orbitals share a finite hopping value, to obtain a more sparse description. We discretize the interval $[0, r_{NN}]$ into n_c equidistant bins l with $l \in [1, n_c]$ using

$$\gamma_{ij} = \gamma(|\mathbf{r}_i - \mathbf{r}_j|) = \gamma_l, \quad l = \text{ceil} \frac{|\mathbf{r}_i - \mathbf{r}_j|}{\Delta r}, \quad (6.3)$$

with $\Delta r = r_{NN}/n_c$ the discretization step, and $\text{ceil}(x)$ the ceiling function picking the smallest integer l with $l \geq x$.

We append a minimal set of onsite terms $\{s_i\}$ (accounting for symmetries) to the set of hopping values $\{\gamma_l\}$ with $l \in [1, n_c]$ to obtain a full TB parameterization, denoted for brevity as $\{\gamma_l\}$. We can then establish a bijective mapping from this list of interactions to full Hamiltonian matrices and vice versa. r_{NN} provides a tunable parameter for the desired sparseness of our TB model (up to how distant a neighbouring orbital interacts with another one).

The number of bins n_c controls the coarseness of the discretization and can be adapted depending on the distribution of inter-orbital distances in a given structure. As long as the discretization Δr is fine enough, we only establish a convenient way of simultaneously addressing all symmetry-related interactions. For the two SLG defects we choose as benchmark systems, we decrease Δr until the number of different γ_l no longer increases (i.e. each value γ_l only addresses the hopping terms connected by symmetry, $\Delta r \approx 10^{-4}\text{\AA}$). At first glance, this prescription for grouping and setting the relevant interaction elements in a TB Hamiltonian seems quite similar to distant-dependent Slater-Koster parametrizations [210, 211, 244] (e.g. dashed green line in Fig. 6.3). However, the discrete distance-hopping map only decouples symmetries and hermiticity from the parameter search and introduces little to no unnecessary simplification. We do not need to consider the local geometric configuration (screening) of interacting orbital pairs as long as the discretization is fine enough to distinguish all different hoppings not related by symmetry. Indeed, we do not aim for a smooth mapping $\gamma(r_{ij})$, but rather for a distinct hopping parameter for all “different” couplings. Consequently, two neighbouring values γ_l and γ_{l+1} can in principle take entirely different values. From TB parameters $\{\gamma_l\}$ one can easily calculate a TB BS by diagonalizing the \mathbf{k} -space Hamiltonian of Eq. (6.2) to obtain band energies $\epsilon_{b,k}^{\text{TB}}$ and eigenfunctions $|\psi_{b,k}\rangle$ via the eigenvalue problem:

$$\mathcal{H}(\mathbf{k}) |\psi_{b,k}\rangle = \epsilon_{b,k} |\psi_{b,k}\rangle \quad (6.4)$$

The full set of TB parameters thus straightforwardly yields a BS with minimal numerical cost, ($\{\gamma_l\} \rightarrow \mathcal{H} \rightarrow \epsilon_{b,k}^{\text{TB}}[\gamma_l]$).

6.3 Inverse band structure problem

Obtaining a BS from Eq. (6.2) and Eq. (6.4) for a given Hamiltonian $\mathcal{H}^{(\lambda_x, \lambda_y)}$ is straightforward. However, to find the optimal Hamiltonian that best reproduces a given DFT BS $\{\epsilon_{b,k}^{\text{DFT}}\}$ we need to solve the inverse problem ($\{\epsilon_{b,k}\} \rightarrow \mathcal{H}$, Fig. 6.5). There is no straightforward (or unique) solution to this problem as highlighted by the plethora of TB parametrizations for any given material. Since $\{\epsilon_{b,k}^{\text{TB}}\}$ can be quickly evaluated, generating pairs of (arbitrary) sets $\{\gamma_l, s_i\}$ and the resulting BS $\{\epsilon_{b,k}^{\text{TB}}\}$ on the TB level is easy. We can then use ML algorithms to identify the set of TB parameters which produces a TB BS in closest agreement with DFT.

To select a ML algorithm suitable for the inverse problem, we need to quantitatively compare different approaches. We will grade several ML

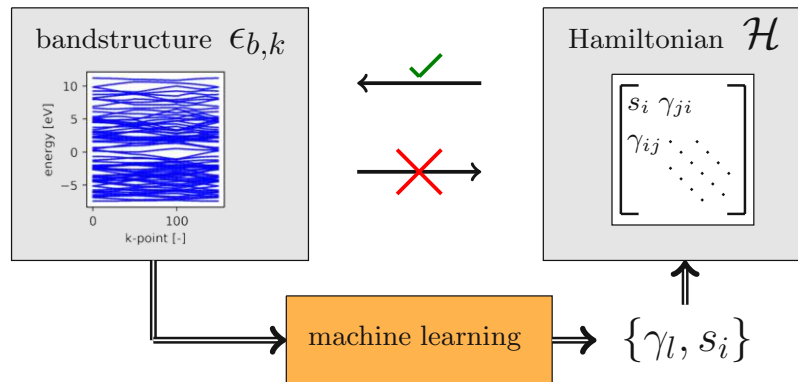


Fig. 6.5: Schematic of the inverse BS problem: for a given Hamiltonian, calculating a BS is trivial. By contrast, there is no constructive algorithm to obtain a Hamiltonian from a BS. Using ML, we aim to find such an inverse mapping from BS data (scalar energy values $\epsilon_{b,k}$ for each band b and k-point k) to a minimal list of TB parameters $\{\gamma_l, s_i\}$ (for each distance and onsite class l) which describes a full TB Hamiltonian \mathcal{H} .

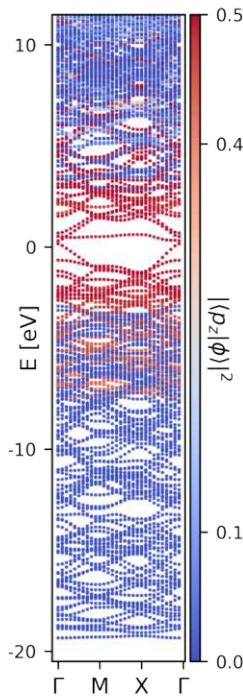


Fig. 6.6: DFT band structure for the double vacancy defect. Color map represents the projection of the corresponding Bloch states onto atomic p_z orbitals.

approaches both in terms of computational efficiency (how quickly do we arrive at an answer) as well as quality. Since the TB parameters themselves are not physical observables, we resort to derived quantities such as the BS. To obtain a quantitative criterion for the quality of a parametrization we evaluate the difference of the final converged result to the DFT BS $\{\epsilon_{b,k}^{\text{DFT}}\}$,

$$\delta_\epsilon[\{\epsilon_{b,k}\}] = \sum_j^{n_k} \sum_b^{n_b} \left(\epsilon_{b,k_j} - \epsilon_{b,k_j}^{\text{DFT}} \right)^2. \quad (6.5)$$

Starting from a plane-wave based density functional theory (DFT) code (VASP) we wish to only parametrize the p_z orbitals in single layer graphene (since only these contribute to electronic properties in the relevant energy ranges). We therefore extract bands featuring a finite overlap $|\langle p_z | \phi \rangle|^2$ with a generic p_z orbital from the DFT band structure (BS) above a certain threshold ($|\langle p_z | \phi \rangle|^2 = 0.25$ works well in our case). Unfortunately this procedure fails at very high energies where the band character for a vast number of overlapping virtual bands becomes challenging to determine on the DFT level (Fig. 6.6). After having determined a final set of parameters, we will further assess their quality by also considering the local density of states (LDOS), transport properties as well GQD states with defects. We do this a posteriori because these calculations are numerically too demanding to use during training. Despite this lack of high-energy bands ($\epsilon > 5$ eV), we will see that our model still achieves ab-initio accuracy.

6.4 Algorithm comparison

In this section we introduce and compare several state-of-the-art ML algorithms applied to the inverse band structure problem. To tackle such a high-dimensional, non-uniquely solvable inversion problem, we test variations of gradient-less descent (GLD) [245, 246], both multilayer perceptron (MLP) and convolutional neural network (CNN) as well as Bayesian optimiza-

tion via Gaussian process regression (GPR) [170] as possible optimization methods.

We include the conceptually most simple gradient-less descent and Slater Koster (SK) as a reference method to assess the benefit of more intricate approaches. All our ML methods produce reasonable parameter sets as exemplified by the small errors (δ_ϵ) in Tab. 6.1. Comparing also the time required to obtain a parametrization, we observe considerable differences between the approaches and therefore selected only the MLP for our final benchmarks. Below we briefly introduce each approach and discuss its pros and cons.

All the methods introduced require an initial guess for the compressed TB parameter list introduced in Eq. (6.3) (and thereby an initial full Hamiltonian). Depending on the quality of this initial guess the convergence rate of the following algorithms will change and some parameters have to be adjusted. We determine an initial distance-hopping map $\gamma^{(0)}(\delta r)$ based on the TB parameters of the pristine material, to obtain an initial TB Hamiltonian $H_{\text{TB}}^{(0)}$. We assume some reasonable parametrization of the pristine material exists - it is far simpler to extract a 10th-NN TB description for the bulk material than it is for a defect structure. For materials where even the bulk cell proves challenging to “wannierize” one could resort to empirical or recent machine-learning approaches [243] for the initial parameter set. We initialize $\gamma^{(0)}(\delta r)$ as a linear interpolation between the ten distance-hopping pairs extracted for the bulk material (see blue line and red markers in Fig. 6.3). We have validated this spline initialization for several defects in graphene and found that already such a (physically unmotivated) prescription for a TB parametrization outperforms a common Slater-Koster parametrization of graphene (see Table 6.1 and dashed green line in Fig. 6.3). However, both of these initialization choices (spline from pristine system, Slater Koster) allow for a cutoff radius r_{NN} to tune sparseness.

method	δ_ϵ [-]	time [hh:mm]
Wannier	1.23	$N_{\text{trial}} \times 00:50^{01}$
MLP	3.09	02:20
CNN	3.48	60:00
GLD	3.73	01:30
GPR	6.2	>24:00
Slater Koster	54.72	-
Spline ⁰²	13.92	-

Tab. 6.1: Comparison of both performance [in terms of BS error δ_ϵ , see Eq. (6.5)] and time efficiency of several ML approaches to the inverse BS problem of the double vacancy in SLG. While the underlying data sets are not necessarily equal for the different optimization algorithms we still find this to be a legitimate comparison.

6.4.1 Gradient-less descent

GLD is a zeroth-order, model-free optimization technique [245, 246] that does not rely on an underlying gradient estimate (such an estimate can get expensive to come by in high dimensional spaces). It solves the inverse problem by repeated application of the forward problem. Since we cannot expect the desired optimal parametrization to be unique we implement this with both exploration and exploitation in mind.

$$\gamma_j \rightarrow \gamma_j(1 + \eta_{\text{rel}} f_1) + \eta_{\text{abs}} f_2 \quad (6.6)$$

Starting from an initial parameter list $\gamma^{(0)}(\delta r)$ we add noise according to Eq. (6.6). We then calculate the corresponding band structure and the approximation error (\mathcal{L}_ϵ) to the desired band structure and keep track of

⁰¹While wannier90 is impressively efficient for a single run, it will typically require of the order of $N_{\text{trial}} \approx 20$ trial runs to identify correct parameters and achieve convergence in our experience.

⁰²introduced in Section 6.4 and Fig. 6.3.

the best one. We continue to alternately add noise ($\eta_{\text{rel}}^{(i)}, \eta_{\text{abs}}^{(i)}$) to either the initial parameter set or ($\eta_{\text{rel}}^{(b)}, \eta_{\text{abs}}^{(b)}$) to the currently best parameter set and thereby explore parameter space without the need to evaluate gradients. The noise amplitudes can also be adapted as the algorithm progresses so as to not overshoot a possible optimum (see Fig. 6.7). While this algorithm manages to consistently minimize the band structure approximation error we find that it cannot match the performance of the MLP model (Section 6.4.3) generated from an equal number of samples. Despite reasonable δ_e (Table 6.1), the extracted parametrizations seem to perform less convincing for derived quantities. We attribute this to the fact that this algorithm can only really optimize all the TB parameters individually and does not build a model than learns about their correlation.

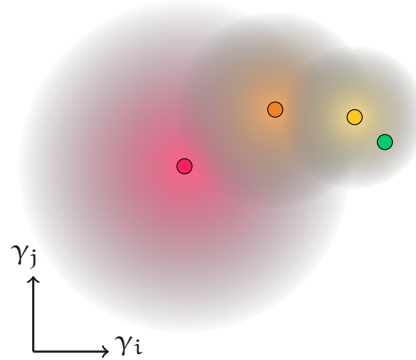


Fig. 6.7: 2D schematic of the high dimensional search via the GLD algorithm. Initial parameter set (red dot) and its vicinity (red-grey circle) followed by successively improved (orange, yellow) parameter sets with their respective n-balls

6.4.2 Bayesian optimization

We implement an active learning algorithm utilizing Bayesian inference via Gaussian Processes (GP's). Our algorithm trains a Gaussian process that maps input TB parameters $\{\gamma_1\}$ to the BS mismatch δ_e . An acquisition function (introduced in the next paragraph) tailored to minimize δ_e then decides whether a new $(\{\gamma_1\}, \{\epsilon_{b,k}^{\text{TB}}\})$ -pair is added to the data set. Such an active learning strategy results in compact datasets. Similarly to our GLD approach we explore our parameter space via random noise added to an initial parameter set $\gamma^{(0)}(\delta r)$. Having gathered several thousand initial exploration points we then fit a Gaussian process with the TB parameters as inputs and the corresponding band structure approximation error (\mathcal{L}_e) as output.

At the beginning we generate 3000 samples to manage an initial “coarse” fit of the Gaussian Process which works best when employing a radial basis function (RBF) kernel. Henceforth a newly generated parameter list (adding noise to the initial list according to Eq. (6.6)) is used to query the GP about an estimate of BS error \mathcal{L}_e (as well as its uncertainty about that prediction).

These results are then used as arguments for an acquisition function (see Fig. 6.8) of the following form:

$$A(\mathcal{L}_\epsilon, \sigma_\epsilon) = 0.95 \left(1 - \tanh(\kappa * \frac{\sqrt{\mathcal{L}_\epsilon}}{\sigma_\epsilon}) \right) + 0.05 \quad (6.7)$$

Where κ is chosen such that the acceptance rate of the 3000 initial samples would have been roughly 0.75. The acquisition function takes values between 0.05 and 1 for any given input and represents the acceptance probability for a proposed parameter set for which the Gaussian process predicts BS error \mathcal{L}_ϵ with uncertainty σ_ϵ . This acceptance probability of at least 0.05

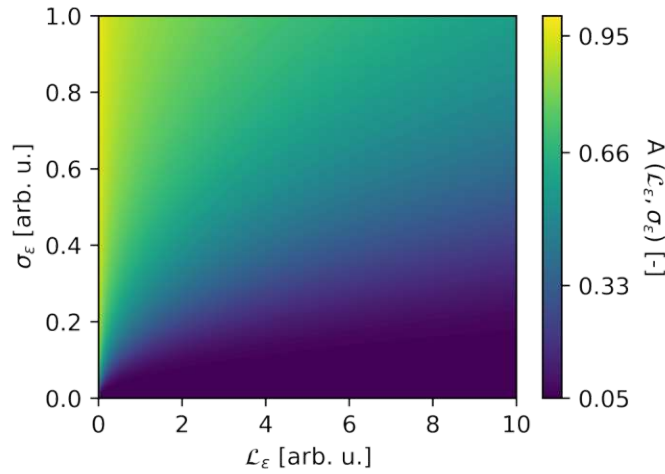


Fig. 6.8: Contour plot of the probability to add a sample to the training data (i.e. acquisition function $A(\mathcal{L}_\epsilon, \sigma_\epsilon)$) depending on both GP predicted BS error as well as GP uncertainty.

increases for very good candidates (low BS error \mathcal{L}_ϵ) and for candidates where the GP is not very confident of its prediction in line with our efforts to balance exploration and exploitation. Accepting a parameter list means we calculate its real BS error and add this sample pair to our training data set. Once a predefined batch size of accepted data points is reached we refit the GP and thus consecutively improve its inference power. An on-average decreasing uncertainty for any given prediction means that the algorithm will become more and more selective over time (see Fig. 6.9). A rejected parameter list will not have its real BS error calculated and the loop continues with another proposed parameter list.

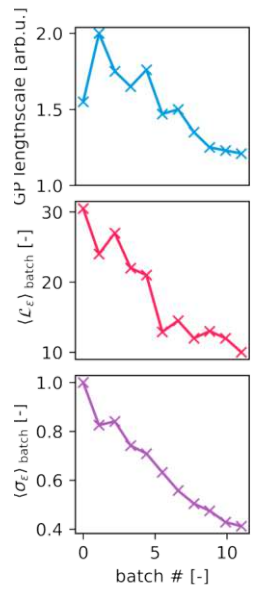


Fig. 6.9: Convergence of (top) length scale l of the RBF kernel in the GP, (center) batch-averaged band structure approximation error and (bottom) batch-averaged uncertainty of the GP queries.

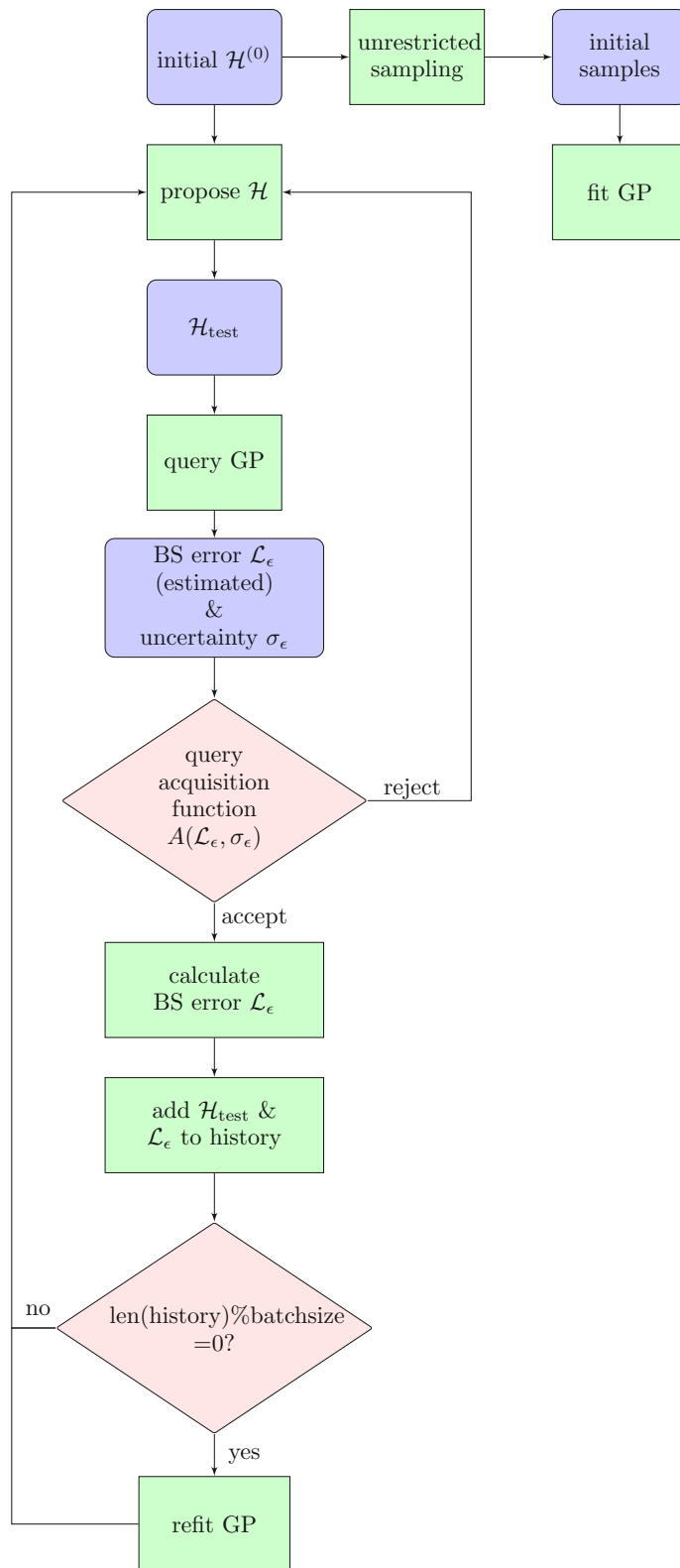


Fig. 6.10: Schematic flow chart of the active learning approach via Gaussian Process and an acquisition function. The right branch represents preliminary sampling that allows for an initial fit of the GP. The left branch describes the main algorithm that then employs and successively improves the GP.

Our implementation of active learning thus manages to omit calculating many band structures and their approximation errors by first invoking an incredibly efficient GP query and acquisition decision. We spent a fair amount of time to optimize this approach but (given the much worse results than the other methods) ultimately acknowledged that it is not the right method for this particular optimization problem. We find that all the time saved by only calculating the BS for “promising” candidates is subsequently lost in the refitting of the GP which scales unfavourably with the number of training points (discussed in Section 4.2.2). We ascribe this to the fact that Gaussian processes are not particularly suited to high-dimensional (lots of training points necessary to approximate the loss surface) optimization problems where sample points are not very costly to generate (such as TB band structure calculations).

6.4.3 Neural network models

In this section we describe the workflow of the network based algorithms (multi-layer perceptrons and CNNs) of which we ultimately choose the multi-layer perceptron for the final benchmarks of our machine learned TB parametrizations.

Convolutional neural networks

CNNs are reasonably deep, sparsely connected neural networks that are designed for automatic feature extraction from the input band structure. They excell at exploiting correlations in their input data (e.g. the continuous lines forming a BS). We aim to train a network that directly maps a given band structure $\{\epsilon_{b,k}^{\text{TB}}\}$ onto a list of TB parameters $\{\gamma_l\}$. Apart from the structure of the involved neural network the workflow is identical to the MLP algorithm (see Section 6.4.3 for details). Naturally we will provide our input BS as a 2D matrix with the entries holding energy values, where each row represents a single band and each column a \mathbf{k} -point (see Fig. 6.11). Despite a reduction of trainable parameters compared to MLPs, the convolutional setups we benchmarked resulted in significantly longer training times but slightly worse BS losses (Table 6.1). The best performing CNN in our testing consists of three sparsely connected blocks (five convolutional layers of increasing depth followed by a max pooling layer) and ends in two fully connected layers (see Table 6.2).

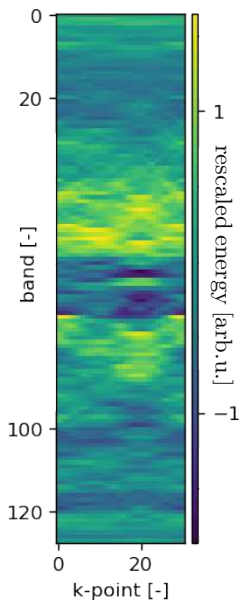


Fig. 6.11: Visualization of the input form of the band structure data into the CNN.

Multi-layer perceptron models

Multi-layer perceptrons (MLPs) are shallow feed-forward neural networks. Here we demonstrate that MLPs can also solve the inverse problem directly by mapping band structures onto TB parameters. We add regularization via dropout layers and train them on $(\{\epsilon_{b,k}^{\text{TB}}\}, \{\gamma_l\})$ -pairs. We then make a final TB parameter prediction for $\{\epsilon_{b,k}^{\text{DFT}}\}$. In our investigations, MLPs outperform all alternative approaches in accuracy at approximately equal or even lower computational cost (Table 6.1). We attribute this to the strong interdependence between the different TB parameters: an almost identical band structure can be described by several different parameter sets, while

layer type	output shape	# of parameters
conv2d	(30,55,4)	40
conv2d	(30,55,4)	40
conv2d	(30,55,8)	40
conv2d	(30,55,8)	40
conv2d	(30,55,16)	40
pooling_2d	(15,28,16)	0
conv2d	(15,28,4)	2320
conv2d	(15,28,4)	2320
conv2d	(15,28,8)	2320
conv2d	(15,28,8)	2320
conv2d	(15,28,16)	2320
pooling_2d	(15,14,16)	0
conv2d	(14,13,16)	1040
conv2d	(13,12,16)	1040
conv2d	(12,11,32)	2080
conv2d	(11,10,48)	6192
conv2d	(10,9,32)	6176
pooling_2d	(5,5,32)	0
flatten	800	0
dense	500	400,500
dense	475	237,975

Tab. 6.2: Convolutional neural network setup used in Table 6.1 containing 668 839 trainable parameters for the double vacancy defect. The CNNs we considered are made up of feature selection blocks (convolutional layers + pooling) followed by a shallow dense network.

changing only a single parameter (with the others fixed) will substantially change it. Such a system is better represented by the fully connected network as opposed to model-free optimization schemes optimizing the different parameters individually. The MLP model is the one that we will explore and benchmark more closely in the remaining sections of this chapter.

6.5 Machine learning workflow

6.5.1 Data set generation

Before we can query our MLP to predict hopping parameters for the DFT BS of a defect system we need to procure appropriate training data in the form of BSs and their corresponding parameter lists. We do so entirely on the TB level, i.e. without requiring any DFT input, by randomly sampling the vicinity of a reasonable initial guess in TB parameter space.

Having obtained a starting guess for $H_{\text{TB}}^{(0)}$ (see discussion in the third paragraph of Section 6.4) we calculate the training dataset by solving the forward problem ($\mathcal{H} \rightarrow \epsilon_{b,k}$) many times with random fluctuations

added to $H_{\text{TB}}^{(0)}$. We sample approximately 150,000 training band structure-Hamiltonian pairs per defect. We generate samples until further increase of the dataset size no longer reduces the BS error (see Fig. 6.12). Starting from the initial parameter list $\{\gamma_j\}$ (generated either via bulk wannierization or some Slater-Koster model) we I) randomly choose a subset of these parameters, II) add relative and absolute noise to all chosen parameters individually:

$$\gamma_j \rightarrow \gamma_j(1 + \eta_{\text{rel}} f_1) + \eta_{\text{abs}} f_2 \quad (6.8)$$

with amplitudes η_{abs} , η_{rel} and random variables f_1 , f_2 , III) unfold the parameter list into a full TB Hamiltonian and calculate the corresponding band structure. We find that this procedure is robust as long as the amplitudes η of the added noise (η_{rel} and η_{abs}) are large enough to explore sensible value ranges of any given TB parameter (i.e. the neural networks can “interpolate” rather than “extrapolate” unknown hopping values). These noise amplitudes thus depend on the quality of the initial parameter list $\{\gamma_j\}$. In practice it seems generally advisable to slightly overestimate rather than underestimate them. We choose $\eta_{\text{rel}} = 0.25$ and $\eta_{\text{abs}} = 0.05$ for both defects under consideration. A suitable choice of these amplitudes should be feasible for any given material. We also experiment with sampling the random variables f_1 and f_2 from different distributions (uniform, Gaussian, Laplace) and find that while differences are marginal, sampling from a uniform distribution $f \in [-1, +1]$ yields the best results.

Finally we then train the MLP to correlate changes in the shape of bands to corresponding modifications of values for specific TB parameters.

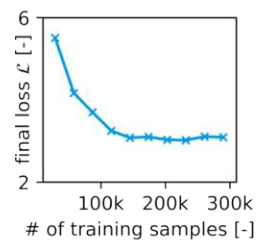


Fig. 6.12: Convergence study for the network performance (i.e. the quality of its produced band structure) depending on the size of the training set.

6.5.2 Training

As alluded to in Section 6.4, we adopt a multilayer perceptron to map BSs to TB parameters. The MLP takes all BS data $\{\epsilon_{b,k}\}$ as 1D vector $(\epsilon_{k_0}, \dots, \epsilon_{k_n})$ and outputs TB parameters as another 1D vector $\{\gamma_l\}$ holding the different hopping values for every distance as well as the minimal set of onsite energies necessary for building the entire TB Hamiltonian. We find optimal performance using three hidden network layers and choose their sizes via linear interpolation of the sizes for input- and output layer.

The range of BS inputs and TB parameter outputs covers several orders of magnitude. This wide spread necessitates Gaussian scaling of both inputs and outputs across all samples. Drop-out regularization (20% at the input layer) effectively avoids overfitting. By applying the distance-hopping map procedure to TB Hamiltonians of the two defect structures, we obtain a number of output parameters that strongly varies with the desired sparseness of the model (see Table 6.4). The sampling density of our BS in k space determines the number of input neurons in our network. We find sampling the Brillouin zone path with 30 points (i.e. $30 \times n_o$ input values for the network) to be a sufficient compromise between resolving BS features while keeping the input layer size manageable.

We emphasize that we aim to train a single-use network that is specifically tailored to one specific defect in a given material, as opposed to training a general MLP for predicting parameters for different defects. Such an

layer type	# of neurons	# of parameters
dense	1,650	2,724,150
dropout	1,650	0
dense	1,259	2,078,609
dense	868	1,093,680
dense	475	412,775

Tab. 6.3: Structure of the multilayer perceptron architecture used for the double vacancy defect.

approach would fail to capture the peculiarities and details of the individual defects. Our training approach is very robust and straightforward, enabling a much faster workflow than manually converging a well-behaved Wannier parametrization. Indeed, for large systems converging a Wannier parametrization can even prove quite elusive, while our MLP based approach should still work. Fig. 6.13 provides a complete (but hopefully assessable) view of the entire ML process.

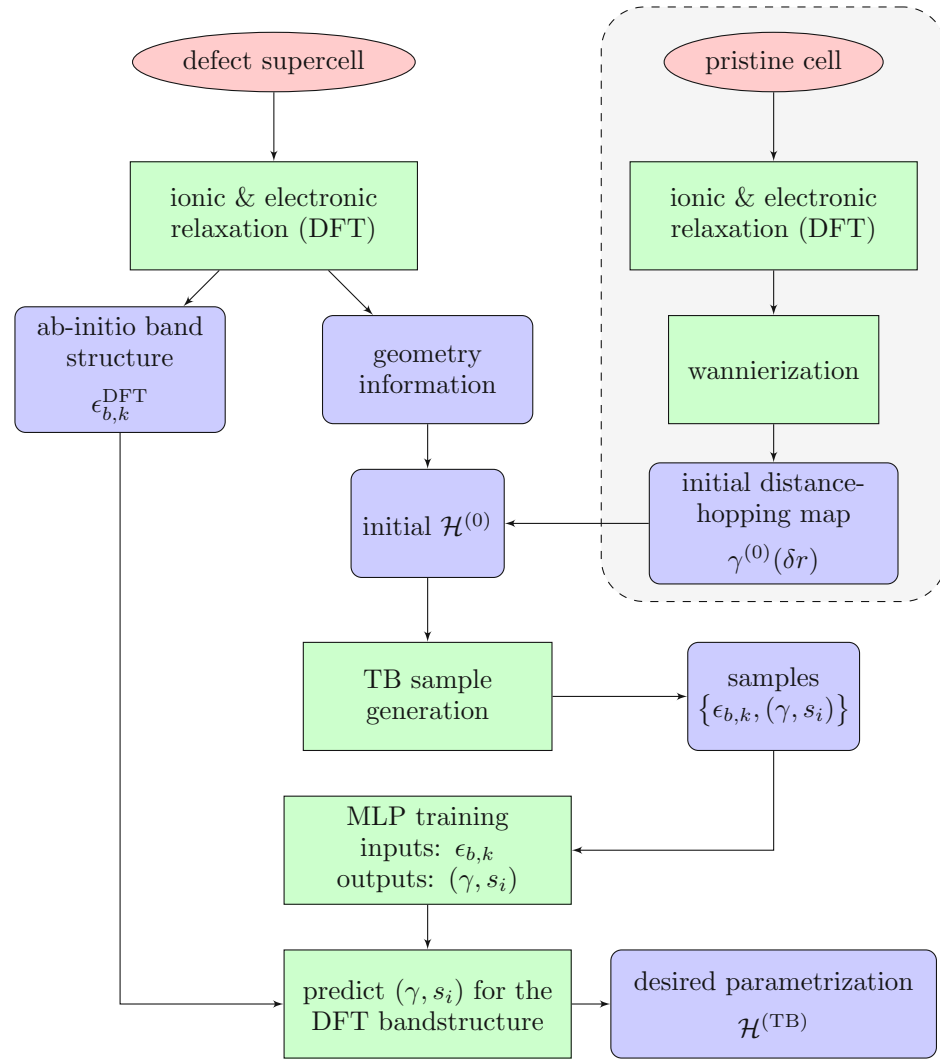


Fig. 6.13: Schematic flow chart of the steps to produce a machine learned TB parametrization of a defect system. The hued section on the right can be replaced with an initial $\gamma^{(SK)}$ from Slater-Koster theory for materials with challenging bulk cells. Cornered green nodes represent calculation processes and rounded blue nodes represent data.

We train the MLP on $N_s = 150,000$ data points, since performance converges and does not improve further by providing more samples (see

Fig. 6.12). We employ a custom loss function that accounts for both parameter loss and BS mismatch of the predictions:

$$\mathcal{L} = \mathcal{L}_\gamma + a_\epsilon \mathcal{L}_\epsilon \quad (6.9)$$

$$\mathcal{L}_\epsilon = \sum_{b=1}^{n_b} \sum_{j=1}^{n_k} \left(\epsilon_{b,k_j}^{(p)} - \epsilon_{b,k_j}^{(t)} \right)^2 \quad (6.10)$$

$$\mathcal{L}_\gamma = \sum_l^{n_p} (\gamma_l^{(p)} - \gamma_l^{(t)})^2 \quad (6.11)$$

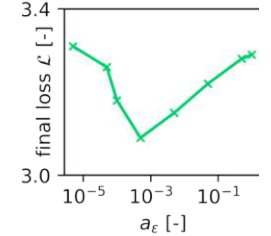


Fig. 6.14: Convergence study for the network performance (i.e. the quality of its produced band structure) depending on a_ϵ .

With a_ϵ as a weighting factor, $\epsilon_b^{(t)}(k_j)$ ($\epsilon_b^{(p)}(k_j)$) the true (predicted) value of band b at k-point j and $\gamma_l^{(t)}$, ($\gamma_l^{(p)}$) the true (predicted) value for the hopping (or s_i) of distance l , which we know for each pair of random Hamiltonian and associated BS in the training set. While an exact solution of the inverse band structure problem implies zero parameter loss, $\mathcal{L}_\gamma = 0$, we find that adding a physical observable, i.e., the actual BS mismatch \mathcal{L}_ϵ to the loss function improves convergence. We achieve optimal performance for $a_\epsilon \approx 5 \times 10^{-4}$ (see Fig. 6.14).

6.5.3 Models for sparse parametrizations

The numerical effort in using a given TB parametrization strongly depends on the sparsity of the TB Hamiltonian, i.e., the number of non-zero hopping elements γ_{ij} . To improve performance, one can introduce a smaller cutoff length r_{NN} requiring that all interactions beyond the NN-th nearest neighbour are set to zero. We denote this as x_{NN} for the models generated in this work. Generating sparser TB models barely requires changes to our ML workflow yet enables vast performance gains for subsequent application of the TB models (Eq. (6.14)). The initial parameters $\gamma^{(0)}(\delta r)$ can again be taken from the spline interpolated bulk parameters (but cut off at r_{NN}).

We will end up with fewer individual parameters (see Table 6.4) in a sparser TB description, generally allowing for a less accurate fit. However, in many applications the interesting physics is confined to a specific energy region, most commonly around the Fermi edge. Depending on the desired sparseness it proved beneficial to introduce additional weighting $w(\bar{\epsilon}_b^{(t)})$ into the BS loss function:

structure	n_o	sparseness (# of neighbours)	n_p (# of parameters)
double vacancy	70	10NN	475
		5NN	168
		3NN	120
flower defect	128	10NN	842
		5NN	344
		3NN	173

Tab. 6.4: Number of independent TB parameters for a given sparseness in both defect structures under consideration.

$$\mathcal{L}_\epsilon = \sum_{b=1}^{n_b} \sum_{j=1}^{n_k} \left(\epsilon_{b,k_j}^{(p)} - \epsilon_{b,k_j}^{(t)} \right)^2 w(\bar{\epsilon}_b^{(t)}) \quad (6.12)$$

$$\bar{\epsilon}_b^{(t)} = \frac{1}{n_k} \sum_{j=1}^{n_k} \epsilon_{b,k_j}^{(t)} \quad (6.13)$$

Restricting long-range interactions increasingly compromises the accurate reconstruction of the entire band structure. We achieved best results by focusing on the energy bands close to the charge neutrality point ($E=0$) by reducing the number of input bands for the MLP (i.e. this mimics a step function for $w(\bar{\epsilon}_b^{(t)})$) all together and thus reduce both network size and computational cost for training. Employing a zero-centered Gaussian distribution with appropriate width for $w(\bar{\epsilon}_b^{(t)})$ achieves similar results at higher computational costs.

6.6 Benchmarks

Our machine learned TB parameters cannot be directly verified as they are no physical observables. Their exact values are not necessarily unique so long as they are capable of accurately reproducing derived quantities. We thus test the quality and validity of our extracted parametrizations with respect to BS, local density of states (LDOS), quantum transport and GQD-spectra which we found to be highly sensitive to the local electronic configuration of defects (see Chapter 5).

6.6.1 Band structure / LDOS

For each defect, we calculate the LDOS on both the TB and DFT level thus enabling direct comparison to DFT results (as compared to the additional benchmarks discussed below in which the Wannier TB parametrization is the only reference). LDOS and BS are shown for the double vacancy and flower defect in Fig. 6.15 and Fig. 6.16, respectively.

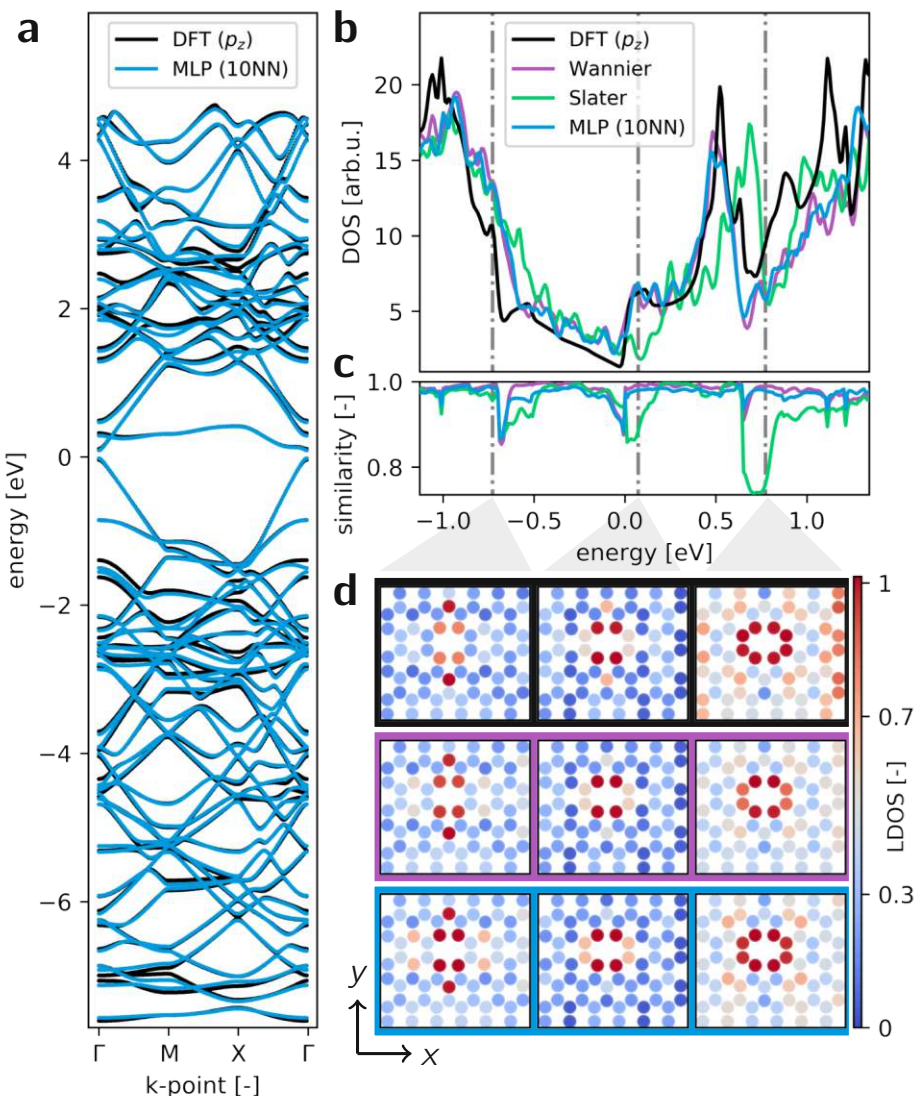


Fig. 6.15: **a** BS of the SLG double vacancy supercell along Γ MX Γ of both DFT calculation and MLP TB-model. **b** p_z -projected density of states of the supercell. **c** Cosine similarity of the local density of states between different TB models and the DFT result. **d** LDOS at the three energies (left to right) indicated by vertical dash-dotted grey lines in b,c) for DFT, Wannier, MLP respectively (top to bottom, colored boxes match line colors in b,c).

Our 10th-NN ML TB model displays excellent agreement with the DFT BS (Fig. 6.15a) over a large energy window. While exact symmetries are captured via the distance-hopping map, noticeable disagreement regarding the exact width of some avoided crossings prove as the most challenging

aspects for the MLP. In terms of the total density of states (DOS) the 10th-NN ML-TB-model is on par with the Wannier-TB-model. While neither can capture all the features of the ab-initio DOS both reproduce it much better than general Slater-Koster models (see Fig. 6.15b and Fig. 6.16b). Since the deviations to the DFT DOS are present for both the machine learned and the Wannier parametrization we ascribe them to approximations of the TB formalism rather than a deficiency of our MLP algorithm.

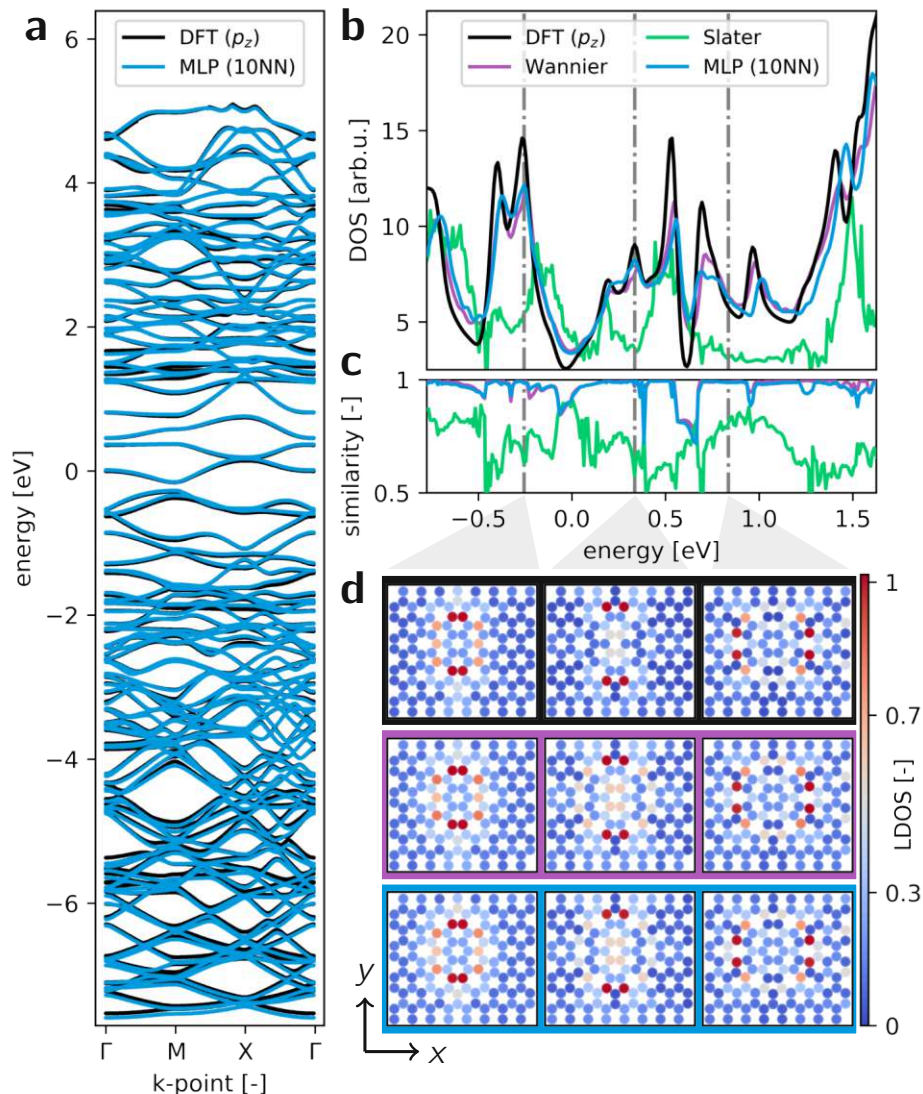


Fig. 6.16: **a** BS of the SLG flower defect supercell along Γ -M-X- Γ of both DFT calculation and MLP TB-model. **b** p_z -projected density of states of the supercell. **c** Cosine similarity of the local density of states between different TB models and the DFT result. **d** LDOS at the three energies (left to right) indicated by vertical dash-dotted grey lines in b,c) for DFT, Wannier, MLP respectively (top to bottom).

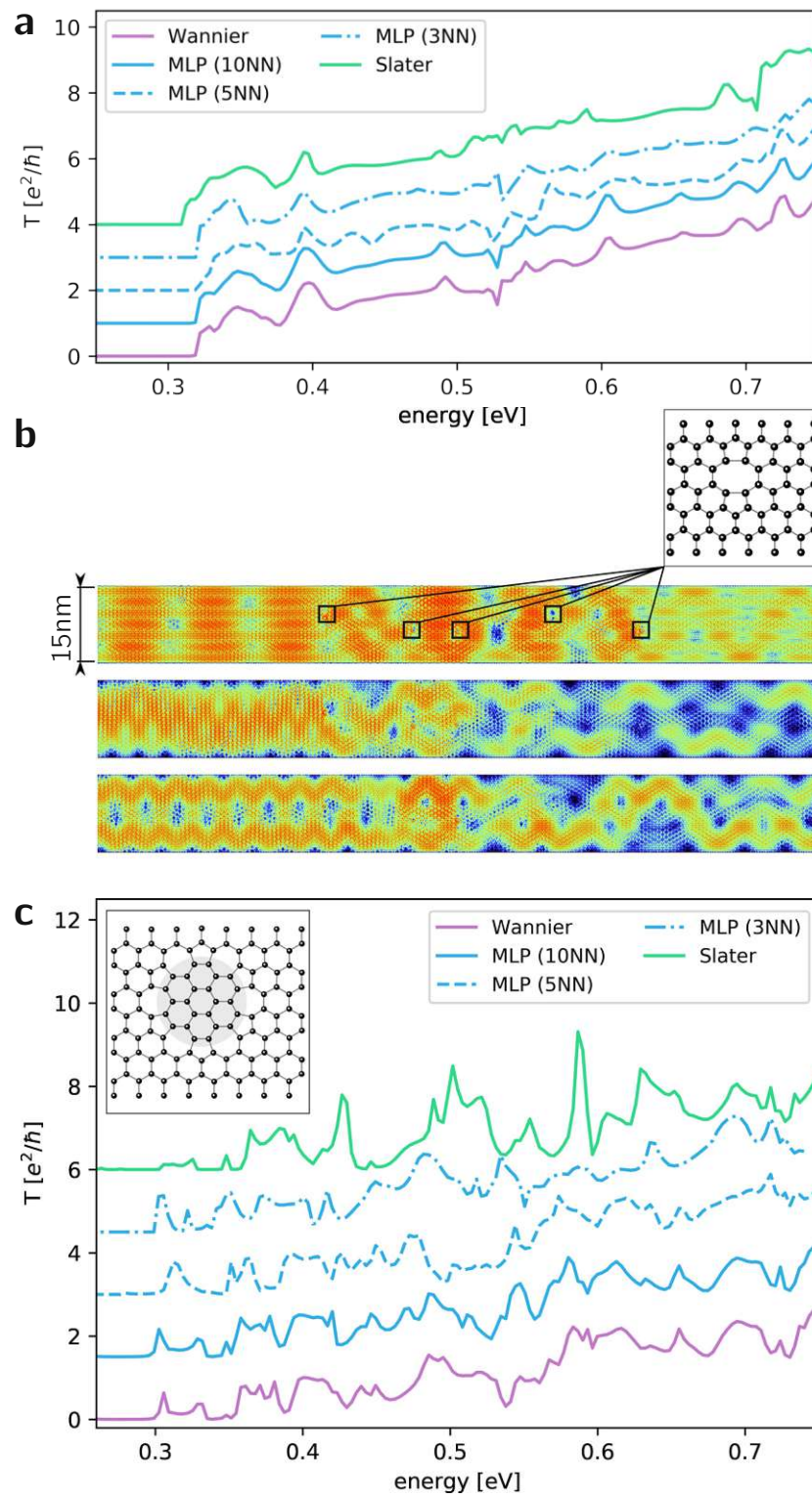


Fig. 6.17: Energy dependent transmission $T(E)$ for different TB parametrizations of the **a** double vacancy and **c** flower defect in SLG (vertically offset for clarity). **b** Scattering density plots for the three lowest modes at $E = 0.7\text{ eV}$ in the double vacancy setup with ribbon-width and embedded defect positions indicated.

The spatial information of the LDOS provides an even more detailed comparison, which we analyze both visually (Fig. 6.15d-f and Fig. 6.16d-f) at relevant energies (indicated as dash-dotted vertical grey lines in (Fig. 6.15b,c and Fig. 6.16b,c) and numerically via the cosine-similarity of individually normalized LDOS distributions with respect to the DFT results over the entire energy range (Fig. 6.15c and Fig. 6.16c). The results show that the MLP parametrizations not only capture the total DOS very well but also its spatial distribution (on par with Wannier) over a wide energy range.

6.6.2 Electronic Transport

State-of-the-art modular recursive Green's function methods (MRGM) (see Section 3.4 or [116, 247] for a more thorough introduction) profit immensely from sparse Hamiltonian matrices. Applying our sparse ML-TB-parametrizations to electronic transport calculations is therefore especially interesting. We study the different TB-parametrizations by embedding the defect supercells at five random but reproducible positions within a 15nm wide zig-zag SLG ribbon of length $\approx 130\text{nm}$ (Fig. 6.17b). Employing our MGRM code we obtain the energy-dependent transmission $T(E)$ which uniquely portrays the multiple scattering events occurring in systems with several defects and compare $T(E)$ for the different parametrizations.

The 10th-NN ML-TB parametrizations accurately reproduce the transmission signature $T(E)$ for both defects (Fig. 6.17a,c). Our results also highlight the limited transferability [248] of Slater-Koster parametrizations to different defect geometries: While the SK-TB-parameters for the double vacancy (Fig. 6.17a) produce a somewhat useful transmission curve its performance degrades drastically when applied to the flower defect (Fig. 6.17c).

Our sparser ML-TB parametrizations with interactions only up to the 3rd- or 5th-nearest neighbour still outperform the SK-parametrization. The loss in accuracy when enforcing very sparse Hamiltonians (3rd-NN) is a priori hard to quantify. While the TB description of the double vacancy seems more robust with respect to restraining long-range interaction than that of the flower vacancy (compare Fig. 6.17a and Fig. 6.17c) the 5th-nearest neighbour parametrization seems to strike an appropriate balance between computational performance gain:

$$\begin{aligned} t_{\text{Transport}}^{\text{10NN}} &: 10\text{m}42\text{s} \\ t_{\text{Transport}}^{\text{5NN}} &: 1\text{m}26\text{s} \\ t_{\text{Transport}}^{\text{3NN}} &: 0\text{m}49\text{s} \end{aligned} \quad (6.14)$$

and accuracy.

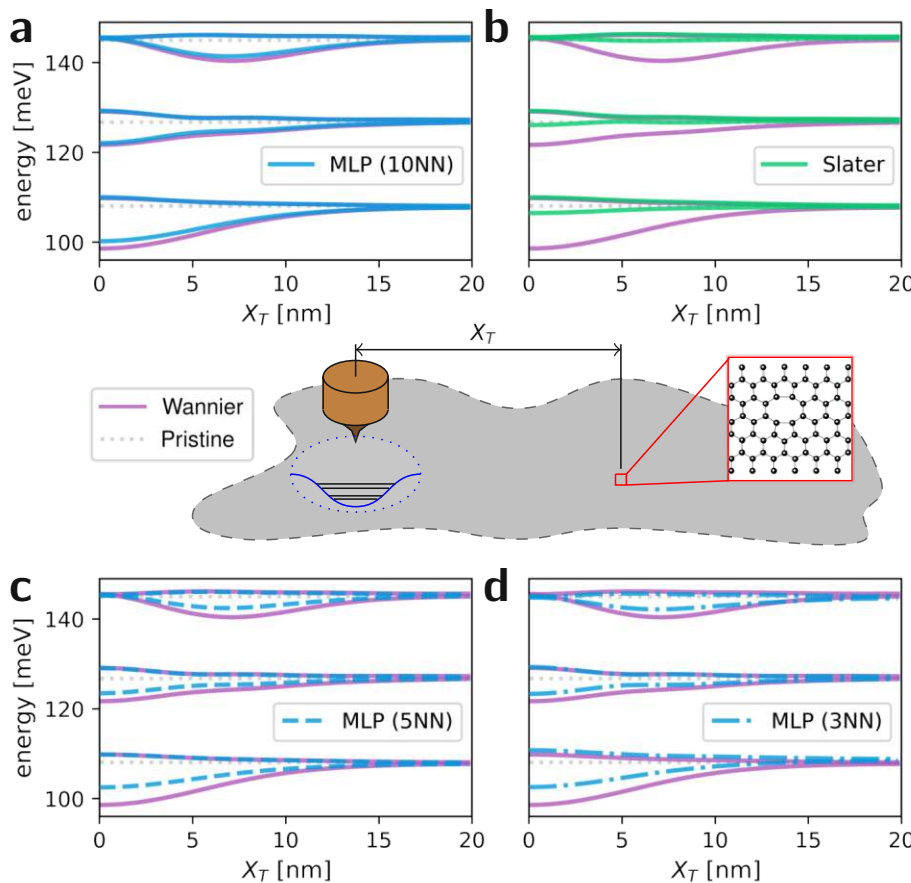


Fig. 6.18: Level spectrum landscapes calculated with different TB parametrizations of the double vacancy in SLG compared against the Wannier parametrization [**a** MLP(10NN), **b** Slater-Koster, **c** MLP(5NN), **d** MLP(3NN)]. Inset shows schematic sketch of the underlying system: We calculate the level spectrum (orbital and valley quantum number, spin is omitted) as a function of the position of an STM-tip (brown) induced (smoothly confined) GQD relative to an embedded defect in a large graphene flake (grey rectangle). Dotted grey lines represent the level structure of a pristine GQD with doubly degenerate orbitals.

6.6.3 GQD spectra

Another highly sensitive probe of our parametrizations comes in the form of smoothly-confined SLG quantum dots [192, 196]. We consider the influence of nearby lattice defects on the level spectrum of GQD's [180] as a benchmark for how well different TB-parametrizations model the local electronic configuration. Smoothly confining electrons in SLG retains the valley degeneracy which, omitting spin, yields doubly degenerate states. In the vicinity of a lattice defect this degeneracy is lifted as a function of defect-GQD distance [180] (see Fig. 6.18). The resulting level spectra as a function of GQD displacement X_T work as a unique fingerprint of the electronic structure of a defect.

We again find excellent agreement between the Wannier and the 10th-NN ML-TB parametrization. Conventional approaches such as Slater-Koster heavily underestimate the induced valley splittings Δ^τ and fail to capture

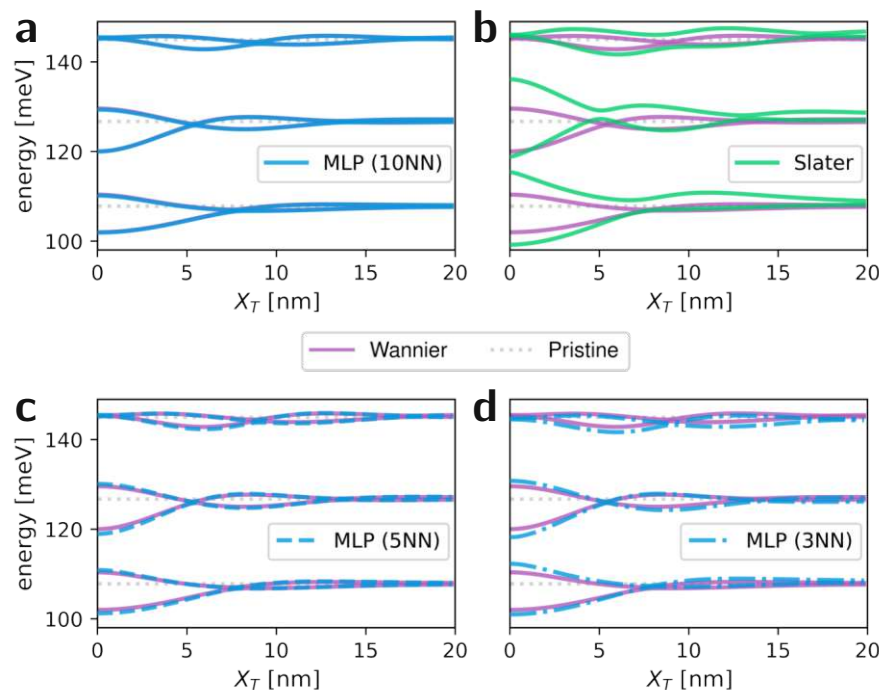


Fig. 6.19: Level spectrum landscapes calculated with different TB parametrizations of the flower defect in SLG compared against the Wannier parametrization [**a** MLP(10NN), **b** Slater-Koster, **c** MLP(5NN), **d** MLP(3NN)].

the characteristic asymmetry of the lowest splitting for the double vacancy (Fig. 6.18c,d). The sparse ML parametrizations (3^{rd} -NN or 5^{th} -NN) still work quite well. Both slightly underestimate the induced splittings but manage to reproduce some of the asymmetry of the splittings for the double vacancy. The sparse ML-TB descriptions work especially well for the flower defect in this benchmark: qualitative agreement remains excellent and the quantitative changes to the induced valley splittings with increasing sparseness remain minor. The Slater Koster model highly overestimates splittings and fails to reproduce several of the sharp avoided crossings.

A shortcoming of this initial algorithm that learns purely distance based interaction mappings is its inapplicability to materials that involve more complex orbital structure (e.g. TMDs, crumpled graphene, ...). Since this introduces additional directional dependency to the learnable hopping parameters we will try to generalize our approach in the next section. Incorporating the basic idea of Slater-Koster and assigning spherical harmonics to the angular part of the involved orbitals allows us to then learn several distance depending maps that originate from the typical convention of Slater-Koster parameters.

6.7 Machine learning discrete Slater-Koster maps for a selenium di-vacancy in WSe₂

Here we show an elegant generalization of our machine learned distance-hopping map formalism to systems with a much richer orbital basis such as transition metal dichalcogenides (TMDs). Our exemplary system of choice is a selenium divacancy in WSe₂ (see Fig. 6.20).

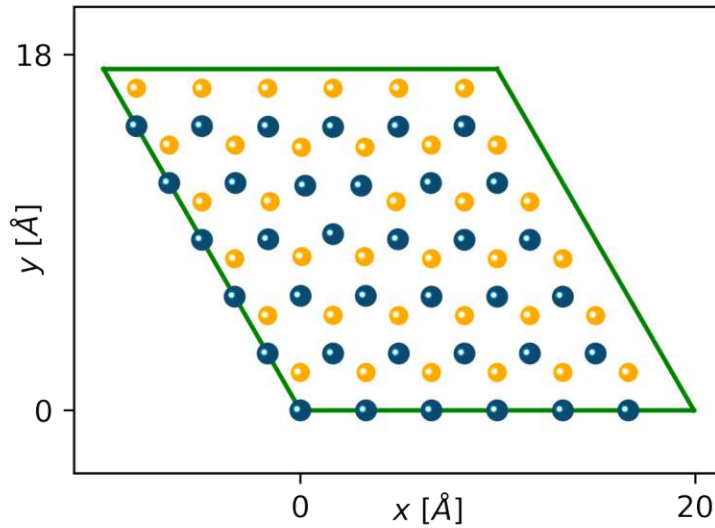


Fig. 6.20: Relaxed 6 × 6 super cell of a selenium divacancy in WSe₂.

The relevant energy bands in WSe₂ are built from the p_x, p_y, p_z orbitals of selenium and the d-orbitals of tungsten (d_{z²}, d_{xz}, d_{yz}, d_{xy}, d_{x²-y²}). Since the involved orbitals are no longer spherical in the x – y plane and the finite thickness of a single WSe₂ layer also introduces hoppings in z direction an assignment of interaction values based solely on inter-orbital distance is not sufficient. We therefore adapt our distance-hopping map formalism to distance dependent Slater-Koster (SK) parameters [211].

For this particular system we promote the SK parameters V_{pp-σ}, V_{pp-π}, V_{p_d-σ}, V_{p_d-π}, V_{d_d-σ}, V_{d_d-π}, V_{d_d-δ} to discretized, distance dependent maps which are then treated formally identical to the simple γ distance-hopping maps from before, e.g.:

$$V_{pp-\pi} \rightarrow V_{pp-\pi}(|\mathbf{r}_i - \mathbf{r}_j|) = V_{pp-\pi}^{(l)}$$

with $l = \text{ceil} \frac{|\mathbf{r}_i - \mathbf{r}_j|}{\Delta r}$ (6.15)

The only difference being that these distance maps do not directly give Hamiltonian entries but parameters that once decorated with direction cosines (i.e. plugged into the well known SK formulas) yield Hamiltonian entries. We stress that this proliferation of SK parameters does not necessarily lead to long range interaction with remote neighbours but results in several different nearest neighbour parameters (a relaxed defect cell features a multitude of nearest neighbour distances) that are utilized only for setting interactions between symmetry related orbital partners. A cut-off radius r_{NN} for the longest distance up to which finite interactions may occur can also be readily implemented.

As starting point for generating a parametrization for the divacancy system we choose an established SK parametrization [211]. For the sake of convenience but without loss of generality we omit the spin degree of freedom which is typically incorporated by a split-off spin-orbit term. We produce a DFT band structure for the pristine system and optimize the SK parameters via gradient descent (for the pristine cell there are only 12 parameters in total, see Fig. 6.21a) such that the highest valence and lowest conduction bands are best reproduced (Fig. 6.21b).

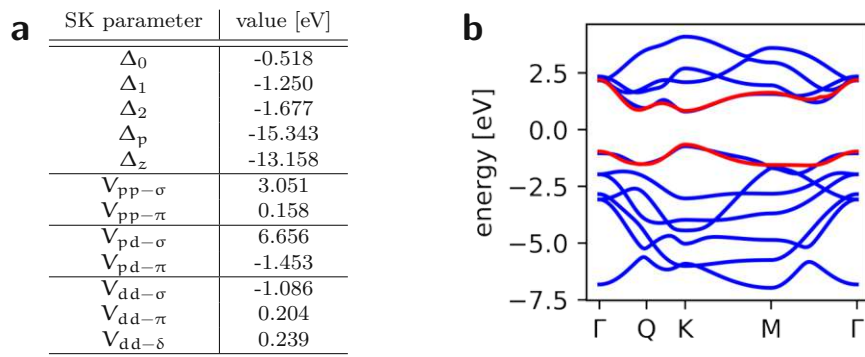


Fig. 6.21: **a** Table for the SK parameters for the pristine system optimized for the system without spin degree of freedom (starting from [249]). **b** Corresponding band structure of the pristine system (DFT in blue, SK for the lowest conduction and highest valence band in red).

The only input our ML approach with discrete Slater Koster maps (learned by an MLP) requires is a relaxed supercell geometry and a target band structure both of which we acquire in DFT calculations. We focus on both valence and conduction band edges as well as the 3 mid-gap defect states (D1, D2, D3) the upper two of which are doubly degenerate. Given the complexity of TMDs, providing a valid description within this energy range suffices to model photo-luminescence emissions, exciton dynamics and electronic transport.

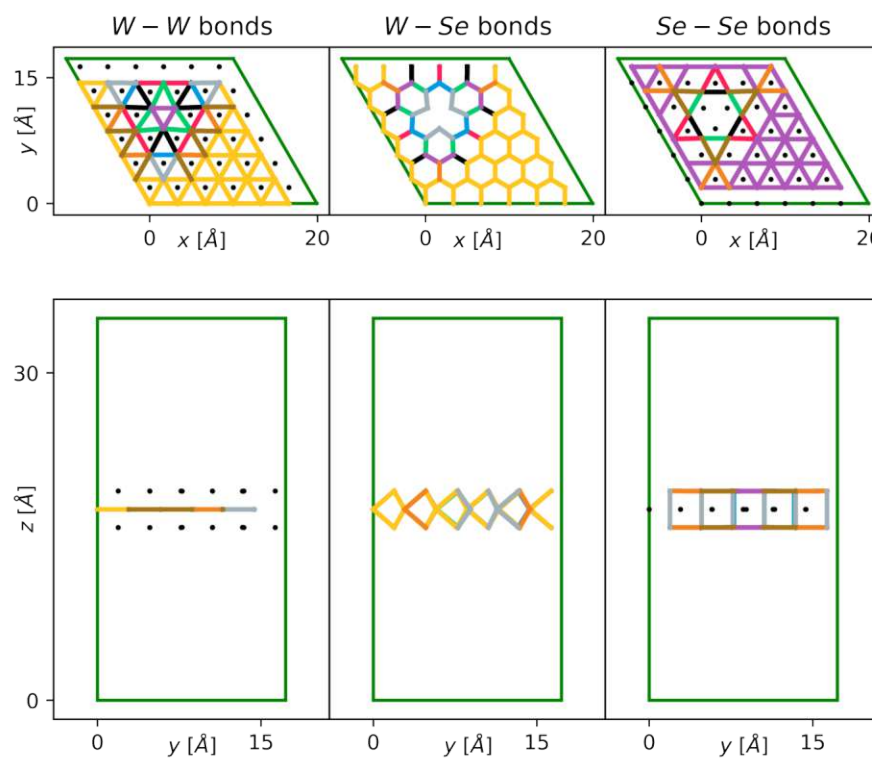


Fig. 6.22: Grouping of hoppings into 2NN (in this context first neighbour of a W atom being a Se and the second neighbour being another W irrespective of distance class) SK distance maps (line colors correspond to different distance classes l , see Eq. (6.15)) for (left) tungsten-tungsten bonds, (center) tungsten-selenium bonds, (right) selenium-selenium bonds. Periodic unit cell borders are drawn in dark green.

Starting point for the sample generation are discrete SK maps filled with pristine SK parameters (see Fig. 6.21). We adapt the onsite energies of the vacancy-adjacent W atoms to shift the flat defect bands fully into the energy gap and allow the network to set the onsite parameters of these three sites individually to account for potential bond reconstruction.

We then generate 200,000 band structure - SK map sample pairs via random noise added to the parameters γ (see Eq. (6.6)), where γ now refers to the concatenated discretized SK maps (e.g. $V_{pp-\sigma}^{(1)}$) as well as a minimal set (with respect to symmetry) of onsite parameters ($\Delta_0, \Delta_1, \Delta_2, \Delta_p, \Delta_z$ per atom). We train a shallow MLP and predict these in total 261 parameters of our combined SK maps (plus onsite) for the DFT band structure.

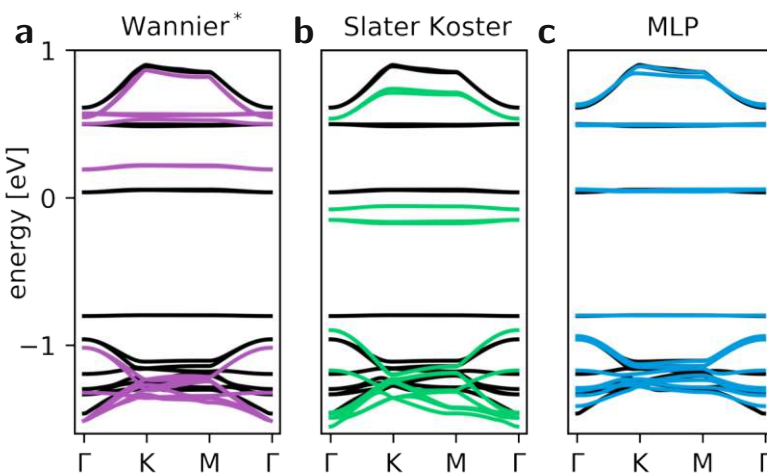


Fig. 6.23: Relevant bands around E_F for the 6×6 Se divacancy super cell of WSe_2 for **a** a *poorman's Wannier description (i.e. vacancy with pristine wannier parametrization), **b** Slater Koster parametrization (from the pristine system), **c** machine-learned parametrization based on discrete Slater Koster maps with r_{NN} cutoff that allows for up to 3NN interactions between kindred atoms (i.e. $\text{W} - \text{W}$ or $\text{Se} - \text{Se}$).

The band structure of our defect cell parametrized by this MLP prediction agrees very well with the original DFT band structure (see Fig. 6.23c). The energy and degeneracy of defect states D1, D2, D3 is reproduced remarkably well. We find an inadvertent small splitting of the conduction band maxima for our sparse description. However, since the much more important minima of the conduction bands are reproduced accurately we feel that this model should allow for accurate TB simulations (e.g. PL spectra). The quality of our ML based TB parametrization is further highlighted when we compare to the often utilized, alternative models of poor-man's vacancies (see Fig. 6.23a,b). In these models a pristine parametrization (either based on maximally localized Wannier functions or standard Slater Koster parameters) is applied to the defect cell and the vacant atoms are then simply removed without affecting the adjacent interaction values. These models not only severely misjudge the energies of the flat defect bands (or do not even give the correct number of mid-gap states) but also deliver a sub par description for the valence and conduction band edges.

Analyzing the orbital composition of the defect states by calculating the l, m -resolved density of states (DOS) reveals astounding agreement of orbital character for the flat defect bands as well as band edges (see Fig. 6.24). While the overall height of the defect related DOS peaks (D1, D2, D3) agree quite well the DFT calculation underestimates the relative intensity of the band edges. We ascribe this to the fact that the optimal choice of Wigner-Seitz radii when determining DOS for multi-elemental systems is not unambiguous and affects localized (defect) and delocalized (Bloch bands) differently. Since the agreement of band edges is already well assessed on the band structure level (see Fig. 6.23c) we omit further DOS calculations and view Fig. 6.23c predominantly as a composition analysis of the defect peaks.

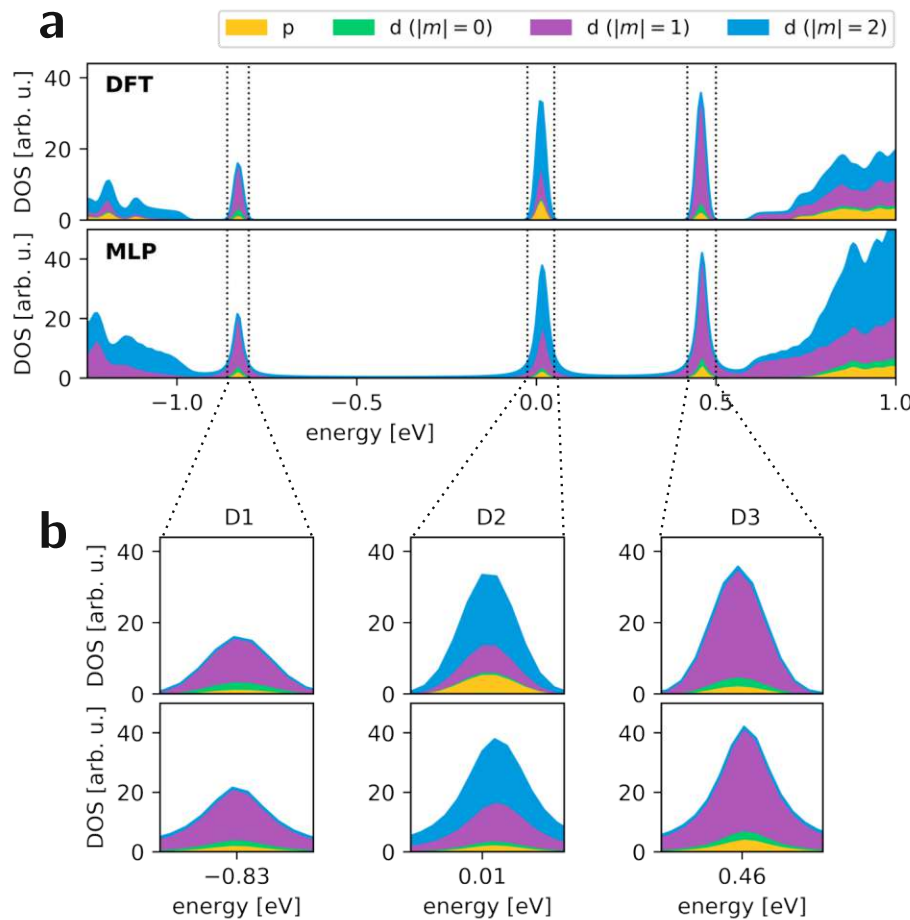


Fig. 6.24: DOS (including analysis of orbital contributions, see color scheme) near E_F for the 6×6 Se divacancy super cell of WSe₂. **a** DFT result vs. tight-binding DOS for the MLP Slater Koster map parametrization of Fig. 6.23c. **b** Zoom-ins of the midgap defect states D1, D2, D3.

Summarising, we have shown that the concept of machine learned, discrete distance hopping maps can be generalized to materials with arbitrarily complicated orbital structure by promoting Slater Koster parameters to distance dependent maps. The finite thickness of WSe₂ also showcases the applicability to systems beyond 2D (i.e. any 3D crystal with defects).

6.8 Conclusion

We have successfully implemented a ML algorithm to derive a tight-binding Hamiltonian that accurately reproduces the band structure details for general defect supercell structures in graphene. This model requires a target BS and geometry information as inputs and allows for optimization towards a predefined sparseness of the desired TB description. The comparatively poor performance (see Table 6.1) of effective Slater-Koster methods strongly highlights the need for more accurate defect descriptions tailored to the corresponding electronic structure, which simply cannot be captured without additional DFT calculations. The ML TB parametrizations yield accuracy on

par with a full Wannier description, yet at substantially reduced cost. Given the considerably less complex input (energy values and atomic positions) than required by state-of-the-art iterative projection based methods (full DFT solution including Bloch states) our method should prove better suited for high-throughput material analysis. The algorithm allows for optimization towards target sparseness and thus greatly reduces computational demands in subsequent applications of the TB descriptions. This sparse description of a defect system can be understood as a constrained optimization problem where ML offers elegant ways to find the sparse description with an optimal balance between accuracy and efficiency.

Our comprehensive benchmarks (LDOS, transport, quantum states directly influenced by the defects) clearly outline the prowess of ML in obtaining DFT-quality results of defects in devices without substantial additional cost beyond the initial DFT calculation of the defect. The remaining minor discrepancies in the highly sensitive GQD benchmark underline how the long-range interactions dictated by the underlying physics ultimately determine the accuracy of effective short-range descriptions: since we cut off long-range hoppings in the TB Hamiltonian, the sparse parametrization underestimates the range of the change in electronic structure induced by the defect. As a consequence, energy splittings between the two valley states are underestimated for small point defects like a vacancy (Fig. 6.18): only a tiny fraction of the quantum dot wavefunction (those few orbitals close to the defect) can actually contribute to the defect-induced energy shift. By contrast, an extended defect like the flower (Fig. 6.19) is much better described. However, we generally found both qualitative and quantitative agreement of Wannier-TB-parameters (reference system) and the ML TB parameters of our MLP based approach.

We have also started to generalize our approach to more complex 2D material classes. For materials with a richer orbital structure (e.g. TMDs with five d-orbitals on the metal site and six p orbitals on the chalcogen sites) one may adopt a mixture of Slater-Koster and discrete-distance-hopping-map approach by following the usual scheme for the angle dependent assignment of interactions (i.e. direction cosines for the spherical harmonic nature of the respective orbitals) but promoting the typical Slater-Koster parameters ($V_{pp-\sigma}$, $V_{pp-\pi}$, $V_{pd-\sigma}$, $V_{pd-\pi}$, $V_{dd-\sigma}$, $V_{dd-\pi}$, $V_{dd-\delta}$, ...) to discretized distance dependent maps (in principle identical to γ in the graphene part of this work).

We have provided a proof-of-principle for an — admittedly somewhat academic (spin-less) — selenium di-vacancy in WSe₂. The adapted algorithm based on Slater-Koster maps was able to accurately parametrize this defect in a way that also manages to accurately capture the underlying orbital character of both conduction and valence bands close to the Fermi energy (an obvious prerequisite for employing such a parametrization in studies of optical material properties). Our approach can be generalized to systems with relevant spin texture by either introducing additional Slater-Koster maps for different spin channels ($\gamma_{\uparrow\uparrow}$, $\gamma_{\uparrow\downarrow}$, $\gamma_{\downarrow\downarrow}$) or employing a split-off spin-orbit coupling term.

All the promising prospects aside there is still lots of room for conceptual advancements: Employing a band-structure based loss function for the

parametrization of the WSe₂ di-vacancy required initial manual tweaking of onsite elements to match the number of mid-gap states. This need for vague comparability of the interesting part of the band structure certainly presents one obstacle to novel defect studies. To this extent we have begun collaboration with Henry Fried from the group of Ludger Wirtz at the Universite du Luxembourg to explore options of Green's function (a quantity that can also be extracted from DFT calculations) based loss functions. The underlying idea would be that this energy dependent function would prove more robust than the topological intricacies of directly comparing two band structures. Another aspect that warrants investigation is that our revised algorithm requires a Slater-Koster description for the bulk material. Since these parametrizations may also be non-orthogonal tight-binding descriptions one would also have to think about including the overlap matrix (apart from the Hamiltonian) into the optimization strategy.

In summary, modern machine learning algorithms have found their way into many aspects of physics and chemistry. Their potential applications reach from tight-binding [250] all the way to strongly correlated electrons [251]. The tough challenge of conceptualizing a meaningful and beneficial application where they can support or even replace long proven methods seems very exciting and warrants further research.

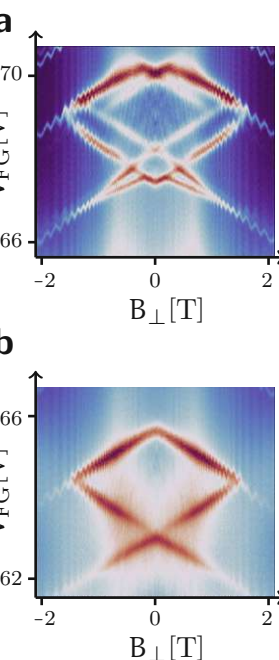


Fig. 7.1: Absolute value of the differential conductance $|dI/dV_{fg}|$ as a function of both V_{fg} and B_\perp measured across the **a** $N = 2$ coulomb peak and **b** $N = 1$ coulomb peak. See Fig. 7.2 for a sketch of the experimental setup. (These impressive measurements were performed by S. Möller et. al. in the group of C. Stampfer at the RWTH Aachen.)

Chapter 7

Two particle spectra of bilayer graphene quantum dots

“Creative minds are uneven, and the best of fabrics have their dull spots.”

H.P. Lovecraft

This project stems from a discussion with the group of C. Stampfer at the RWTH Aachen regarding their finite bias spectroscopy measurements of the two-electron spectra in a bilayer graphene (BLG) quantum dot in a perpendicular magnetic field. At the time they presented us with differential conductance maps as a function of gate voltage and magnetic field. While the single particle ($N = 1$) measurements seemed plausible the results for the transition between $N = 1$ and $N = 2$ occupancy of the quantum dot displayed a rich and somewhat puzzling structure (see Fig. 7.1 or [9] for the final results and explanation). Naturally both Thomas Fabian (a friend, colleague and more senior PhD student of Florian at the time) and I set out to try and explain the underlying two particle spectrum. Therefore the contents of this chapter are to be understood as a joint effort of the two of us.

7.1 Introduction

Graphene presents itself as a promising candidate for hosting spin Q-bits⁰¹ (low spin-orbit coupling [252], spin and valley degrees of freedom, tunable g-factors [253]). Bilayer graphene, as repeatedly demonstrated [254, 255], allows for gate-defined quantum dots (without the need for a Landau gap in contrast to SLG) with controllable occupancy. With the future implementation of singlet-triplet Q-bits [256] in mind it is especially interesting to understand two particle states within these systems.

⁰¹Notation following David Mermin in his lecture notes [257] on quantum computation: “Unfortunately the preposterous spelling “qubit” currently holds sway for the quantum system. Although qubit honors the English rule that *q* should be followed by *u*, it ignores the equally powerful requirement that *qu* should be followed by a vowel. My guess is that “qubit” has gained acceptance because it visually resembles an ancient English unit of distance, the homonymic cubit. To see its ungainliness with fresh eyes, it suffices to imagine that Dirac had written *qunumber* instead of *q-number*, or that one erased transparencies and cleaned ones ears with *Qutips*.“

7.2 Model and numerical trickery

We choose to model a spherical quantum dot on the level of a $\mathbf{k} \cdot \mathbf{p}$ Hamiltonian in a BLG system. We therefore transform the momentum operators ($\mathbf{p}_i = -i\partial_i$) of Eq. (2.3) into cylindrical coordinates,

$$\partial_x = \cos(\phi)\partial_r - 1/r \sin(\phi)\partial_\phi \quad (7.1)$$

$$\partial_y = \sin(\phi)\partial_r + 1/r \cos(\phi)\partial_\phi \quad (7.2)$$

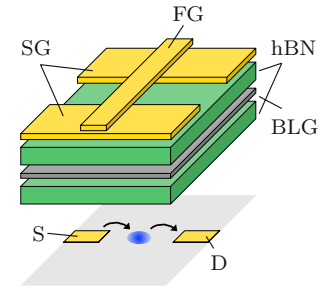


Fig. 7.2: Sketch of the experimental system (as imagined by a theorist) used for the measurements (see Fig. 7.1) in the group of C. Stampfer. FG...finger gate, SG...side gates, S...source, D...drain.

and arrive at

$$H_\tau = \hbar v_f \begin{bmatrix} 0 & e^{i\tau\phi}(i\tau\partial_r - \frac{1}{r}\partial_\phi) \\ e^{-i\tau\phi}(i\tau\partial_r + \frac{1}{r}\partial_\phi) & 0 \end{bmatrix} \quad (7.3)$$

for the single layer and

$$H_\tau = \begin{bmatrix} m_A & \hbar v_f e^{i\tau\phi} \alpha_\tau^- & 0 & 0 \\ \hbar v_f e^{-i\tau\phi} \alpha_\tau^+ & m_B & \gamma_1 & 0 \\ 0 & \gamma_1 & m_{A'} & \hbar v_f e^{i\tau\phi} \alpha_\tau^- \\ 0 & 0 & \hbar v_f e^{-i\tau\phi} \alpha_\tau^+ & m_{B'} \end{bmatrix} \quad (7.4)$$

where $\alpha_\tau^\pm = (i\tau\partial_r \pm 1/r\partial_\phi)$, for the Bernal stacked bilayer system. An ansatz of the form,

$$\Psi_{\tau,m}(r, \phi) = \left(e^{i(m+\tau)\phi} a^{m+\tau}(r), e^{im\phi} b^m(r), e^{im\phi} A^m(r), e^{i(m-\tau)\phi} B^{m-\tau}(r) \right)^T \quad (7.5)$$

then separates radial ($a(r), b(r), A(r), B(r)$) and angular components of the wavefunction. Following [258] we include a magnetic field via minimal coupling in symmetric gauge:

$$\alpha_\tau^\pm = (i\tau\partial_r \pm \frac{1}{r}\partial_\phi) \rightarrow (i\tau\partial_r \pm \frac{1}{r}\partial_\phi \mp i\frac{eBr}{2}) \quad (7.6)$$

We attempt a numerical solution of this system on a real space radial lattice to incorporate a smooth Fermi-like confinement potential:

$$m_A = m_B = -m_{A'} = -m_{B'} = \frac{\Delta V}{2} + \frac{V_{\text{inf}}}{e^{\frac{r_0-r}{\gamma}} + 1} \quad (7.7)$$

where r_0 controls the extension, $\gamma = 10\text{nm}$ defines a characteristic length scale, ΔV opens a band gap and V_{inf} acts as the infinite radius boundary condition of the confinement potential. Unfortunately, straightforward discretization yields unphysical solutions. This phenomenon is known as *fermion doubling* (additional solutions appear due to the *Nielsen-Ninomiya* theorem [259, 260] from lattice gauge theory, this issue seems to be known yet little communicated in the graphene community [261–263]). Out of several options to avoid this (*Wilson fermions* [264] — adding a second order derivative as a mass term to break chiral symmetry, *Kogut-Susskind fermions* [265, 266] — employing a staggered lattice to break translational invariance) we adopt the latter and formulate our equations on slightly shifted lattices for

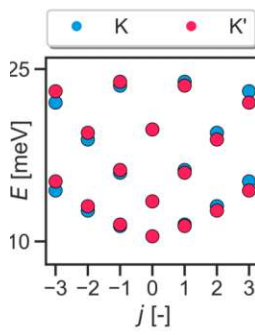


Fig. 7.3: Single particle spectrum in a BLG quantum dot ($r \approx 50\text{nm}$) as a function of total angular momentum $j = m + \tau$ at $B = 0$.

four sublattice components (i.e. in single layer terminology $\Psi_{\tau,m}^{(A)}$ resides on radii $\{j \cdot \delta r \mid j \in [1, N_r]\}$ and $\Psi_{\tau,m}^{(B)}$ dwells on radii $\{(j+1/2) \cdot \delta r \mid j \in [1, N_r]\}$). This entails slightly custom formulations for the numerical derivatives [267] but, once coded, requires no further attention.

The single particle spectrum of such a BLG quantum dot for $B = 0$ can be categorized by a total angular momentum $j = m + \tau$ with the solutions remaining invariant under the combined symmetry operations (see Fig. 7.3):

$$j \rightarrow -j \quad (7.8)$$

$$\tau \rightarrow -\tau \quad (7.9)$$

$$B \rightarrow -B \quad (7.10)$$

Unfortunately the staggering introduces “edge” states which are very localized at $r = 0$ and break valley symmetry since one of the staggered sub lattices lives closer to the center. We filter these unphysical solutions and carefully restore the original symmetry by averaging two solutions [i.e. $(\Psi(m, \tau, B) + \Psi^*(-m, -\tau, -B))/2$]. Finally we generate interpolating functions for the now correctly determined single particle wavefunctions. The evolution of energy levels with non zero magnetic field approaches the Landau level energies in an infinitely large BLG system (yellow curves in Fig. 7.4).

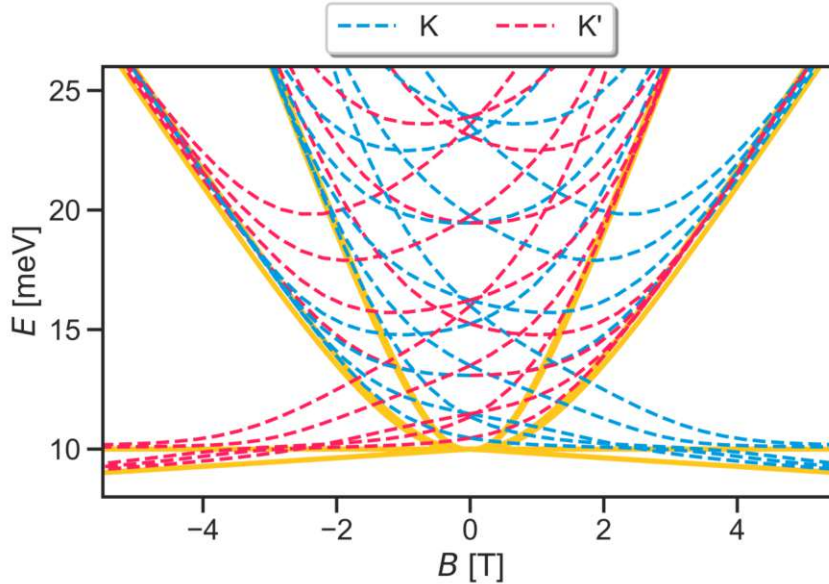


Fig. 7.4: Evolution of single particle energy levels in a BLG quantum dot with perpendicular magnetic field B . Valleys K and K' are colored blue and red respectively. Yellow curves show analytic solutions (following [268]) of Landau levels in an infinite BLG system.

Equipped with reasonable single particle states in a BLG quantum dot we next choose a two-particle basis in which we calculate and then re-diagonalize the Coulomb operator $\hat{C} = 1/2 \sum_{i \neq j} 1/\|\mathbf{r}_i - \mathbf{r}_j\|$. Since the Coulomb interaction is diagonal in spin space we select spin singlet ($S = 0$)

$$|\sigma^{-x}\rangle = \frac{1}{2} (|\uparrow\downarrow\rangle - |\downarrow\uparrow\rangle) \quad (7.11)$$

and tripllett states ($S = 1$)

$$|\sigma^{-z}\rangle = |\uparrow\uparrow\rangle \quad (7.12)$$

$$|\sigma^{+x}\rangle = \frac{1}{2} (|\uparrow\downarrow\rangle + |\downarrow\uparrow\rangle) \quad (7.13)$$

$$|\sigma^{+z}\rangle = |\downarrow\downarrow\rangle \quad (7.14)$$

where $S = s_1 + s_2$. Since none of these mix during the re-diagonalization we effectively treat these blocks separately. We omit an identical classification for the valley quantum number (i.e. $|\tau^{-x}\rangle, |\tau^{-z}\rangle, |\tau^{+x}\rangle, |\tau^{+z}\rangle$) since to us it was a priori unclear whether valley was still a good quantum number. That usually depends on the characteristic length scales of the involved potentials. While our confinement potential is certainly smooth enough we remain unsure how to estimate the effects of steep parts in the $1/r$ potential. The allowed spin singlet states are thus of the form:

$$\Psi_{\tau_1, m_1, \tau_2, m_2}^S(\mathbf{r}_1, \mathbf{r}_2) = \sigma^{-x} \cdot \begin{cases} \Psi_{\tau_1, m_1}(\mathbf{r}_1) \Psi_{\tau_2, m_2}(\mathbf{r}_2) & \text{for } (\tau_1, m_1) = (\tau_2, m_2) \\ \frac{1}{\sqrt{2}} (\Psi_{\tau_1, m_1}(\mathbf{r}_1) \Psi_{\tau_2, m_2}(\mathbf{r}_2) + \Psi_{\tau_2, m_2}(\mathbf{r}_2) \Psi_{\tau_1, m_1}(\mathbf{r}_2)) & \text{for } (\tau_1, m_1) \neq (\tau_2, m_2) \end{cases} \quad (7.15)$$

and necessarily feature a symmetric orbital and valley character while the spin triplets further separate into blocks with $m_s = -1, 0, 1$ that consists of states:

$$\Psi_{\tau_1, m_1, \tau_2, m_2}^T(\mathbf{r}_1, \mathbf{r}_2) = \frac{\Psi_{\tau_1, m_1}(\mathbf{r}_1) \Psi_{\tau_2, m_2}(\mathbf{r}_2) + \Psi_{\tau_2, m_2}(\mathbf{r}_2) \Psi_{\tau_1, m_1}(\mathbf{r}_2)}{\sqrt{2}} \cdot \begin{cases} \sigma^{-z} \\ \sigma^{+x} \\ \sigma^{+z} \end{cases} \quad (7.16)$$

Calculating the respective Coulomb matrix elements,

$$\langle \Psi_{1,2}^S | \hat{C} | \Psi_{3,4}^S \rangle = \begin{cases} \langle \Psi_1(\mathbf{r}_1) \Psi_2(\mathbf{r}_2) | \frac{q^2}{4\pi\epsilon\epsilon_0 \|\mathbf{r}_1\|^2} | \Psi_3(\mathbf{r}_1) \Psi_4(\mathbf{r}_2) \rangle & , \Psi_1 = \Psi_2 \wedge \Psi_3 = \Psi_4 \\ \langle \Psi_1(\mathbf{r}_1) \Psi_2(\mathbf{r}_2) | \frac{q^2}{4\pi\epsilon\epsilon_0 \|\mathbf{r}_1\|^2} | \Psi_3(\mathbf{r}_1) \Psi_4(\mathbf{r}_2) \rangle \cdot \sqrt{2} & , \Psi_1 = \Psi_2 \vee \Psi_3 = \Psi_4 \\ \frac{q^2}{4\pi\epsilon\epsilon_0} (\langle \Psi_1(\mathbf{r}_1) \Psi_2(\mathbf{r}_2) | \frac{1}{\|\mathbf{r}_1\|^2} | \Psi_3(\mathbf{r}_1) \Psi_4(\mathbf{r}_2) \rangle + \langle \Psi_1(\mathbf{r}_1) \Psi_2(\mathbf{r}_2) | \frac{1}{\|\mathbf{r}_1\|^2} | \Psi_4(\mathbf{r}_1) \Psi_3(\mathbf{r}_2) \rangle) & , \Psi_1 \neq \Psi_2 \wedge \Psi_3 \neq \Psi_4 \end{cases} \quad (7.17)$$

$$\langle \Psi_{1,2}^T | \hat{C} | \Psi_{3,4}^T \rangle = \frac{q^2}{4\pi\epsilon\epsilon_0} (\langle \Psi_1(\mathbf{r}_1) \Psi_2(\mathbf{r}_2) | \frac{1}{\|\mathbf{r}_1\|^2} | \Psi_3(\mathbf{r}_1) \Psi_4(\mathbf{r}_2) \rangle - \langle \Psi_1(\mathbf{r}_1) \Psi_2(\mathbf{r}_2) | \frac{1}{\|\mathbf{r}_1\|^2} | \Psi_4(\mathbf{r}_1) \Psi_3(\mathbf{r}_2) \rangle) \quad (7.18)$$

brings its own challenges.

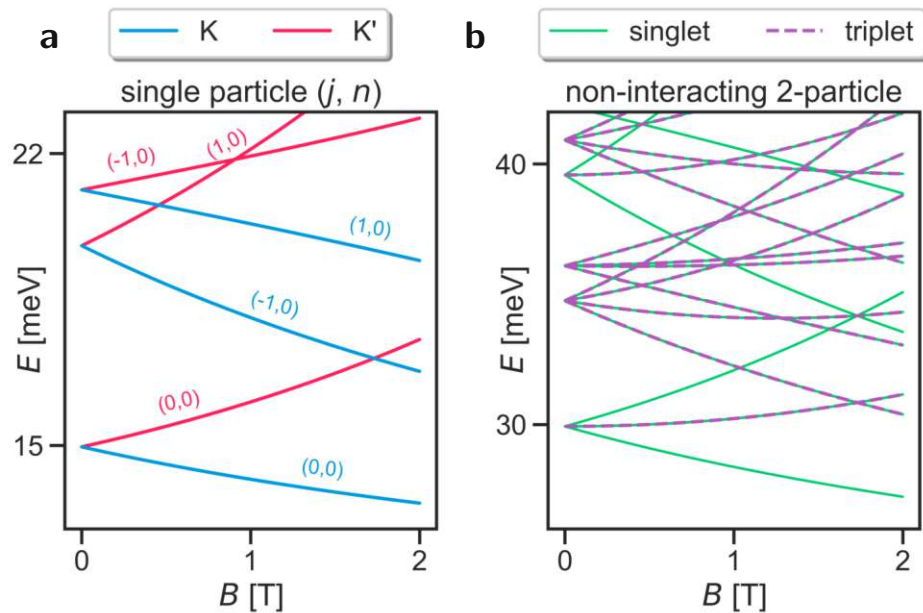


Fig. 7.5: **a** Single particle energies for states of the lowest radial quantum number n . **b** Energy $E_1 + E_2$ for the non-interacting singlet and triplet states introduced in Eqs. (7.15) and (7.16).

We employ Mathematica [269] to calculate the four-center integrals of Eqs. (7.16) and (7.17) with our interpolated single particle wave functions. Achieving convergence is possible by following [270] and adopting an ingenious expansion⁰¹ of $1/r$ in polar coordinates [271] using Legendre functions $Q_{m-1/2}$ of the second kind of half-integer degree:

$$\frac{1}{|\mathbf{r}_1 - \mathbf{r}_2|} = \frac{1}{\sqrt{r_1 r_2} \pi} \sum_{m=-\infty}^{\infty} \Re \left[Q_{m-1/2} \left(\frac{r_1^2 + r_2^2 + (z_1 - z_2)^2}{2r_1 r_2} \right) \right] e^{im(\phi_1 - \phi_2)} \quad (7.19)$$

where $\mathbf{r} = (r, \phi, z)$ and $\Re[\cdot]$ is the real part. This powerful relation renders all the angular parts of the integrals in the Coulomb matrix elements analytically tractable as the exponential contributions of the inverse distance $\frac{1}{|\mathbf{r}_1 - \mathbf{r}_2|}$ need to exactly cancel the exponents of the participating wavefunctions to give a non-zero matrix element (i.e. the angular parts of the wavefunctions pick out a single term of the infinite sum in Eq. (7.19)). Applying this to

⁰¹ There exists an even more general form of Eq. (7.19) known as “Heine identity” [272].

one of the menacingly looking integrals for a Hartree term of specific spinor components:

$$\langle 1, 3 | \frac{1}{r_{12}} | 2, 4 \rangle = \int_0^{2\pi} d\phi_1 d\phi_2 \int_{0^+}^\infty r_1 r_2 dr_1 dr_2 \cdot e^{-i(m_1 + \tau_1)\phi_1} a_1^*(r_1) e^{i(m_2 + \tau_2)\phi_1} a_2(r_1) \cdot e^{-i(m_3 + \tau_3)\phi_2} a_3^*(r_2) e^{i(m_4 + \tau_4)\phi_2} a_4(r_2) \cdot \frac{1}{\sqrt{r_1 r_2} \pi} \sum_{M=-\infty}^{\infty} \Re \left[Q_{M-1/2} \left(\frac{r_1^2 + r_2^2 + (\Delta z)^2}{2r_1 r_2} \right) \right] e^{iM(\phi_1 - \phi_2)} e^{-i\mathbf{K}_{\tau_1} \cdot \mathbf{r}_1} e^{i\mathbf{K}_{\tau_2} \cdot \mathbf{r}_2} e^{-i\mathbf{K}_{\tau_3} \cdot \mathbf{r}_3} e^{i\mathbf{K}_{\tau_4} \cdot \mathbf{r}_4} \quad (7.20)$$

we only need to numerically evaluate the two radial integrals

$$4\pi^2 \int_{0^+}^\infty \frac{\sqrt{r_1 r_2}}{\pi} dr_1 dr_2 a_1^*(r_1) a_2(r_1) a_3^*(r_2) a_4(r_2) \cdot \Re \left[Q_{M-1/2} \left(\frac{r_1^2 + r_2^2 + (\Delta z)^2}{2r_1 r_2} \right) \right] e^{-i\mathbf{K}_{\tau_1} \cdot \mathbf{r}_1} e^{i\mathbf{K}_{\tau_2} \cdot \mathbf{r}_1} e^{-i\mathbf{K}_{\tau_3} \cdot \mathbf{r}_2} e^{i\mathbf{K}_{\tau_4} \cdot \mathbf{r}_2} \quad (7.21)$$

where Δz is the layer separation of BLG, if and only if M in Eq. (7.21) fulfills $M = m_1 + \tau_1 - m_2 - \tau_2 = m_3 + \tau_3 - m_4 - \tau_4$. Lastly we remain unable to accurately converge this integral if different valleys occur (i.e. this introduces increasingly oscillatory terms of the form $e^{i\Delta\mathbf{K} \cdot \mathbf{r}}$) and therefore can only assume them to vanish. This also involuntarily “solves” our lack of clarity regarding valley mixing discussed in the singlet triplet basis introduction.

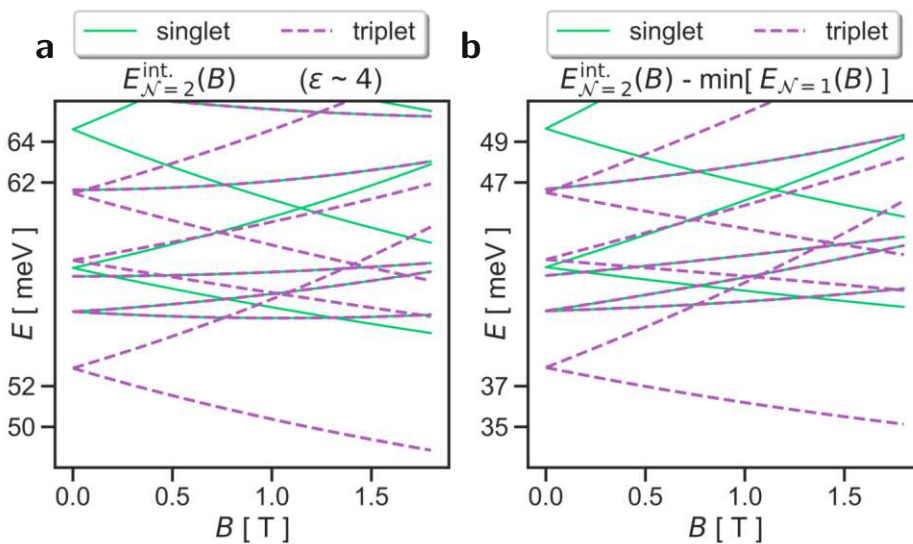


Fig. 7.6: **a** Interacting two-particle spectrum for an effective dot radius of about 30nm using $\epsilon_{hBN} = 3.6$ to account for screening. **b** same as **a** but now with the lowest single particle energy subtracted (as a function of magnetic field, see Fig. 7.5).

We account for screening of the hBN sandwich structure by an effective $\epsilon \approx 3.6$ and calculate the interacting two particle spectrum for several dot sizes. Results show that the Coulomb interaction introduces significant

reordering of the spectrum. For small magnetic fields the ground state has triplet character due to favorable exchange interaction (see Fig. 7.6a). For larger magnetic fields (not shown) the magnetic field evolution of the single particle states dominates and the ground state may again have singlet character. While our results seem physical and agree quite well with previous works [270] we do not seem to compare well with the experimental data from the Stampfer group. Fig. 7.6b subtracts the lowest (and therefore occupied) single particle energy for every magnetic field and should at least to some extent already resemble the differential conductance measurements (see Fig. 7.1). One of our first suspicions (possibly quite oblate dots in the experimental setup) is tough to investigate since the assumption of sphericity enters fairly early into our model. We nevertheless started thinking about a more general model that utilizes a full tight-binding Hamiltonian and thus arbitrarily shaped TB wavefunctions.

Shortly thereafter A. Knothe et.al from the Fal'ko group seemed to have solved the puzzle [9, 273] by introducing symmetry breaking short-range interaction terms

$$H_{SR} = \frac{1}{2} \int \sum_{(i,j)} g_{ij} \left[\Psi^\dagger(\mathbf{r}) \xi_i^{AB} \xi_j^{\tau} \Psi(\mathbf{r}) \right]^2 d\mathbf{r} \quad (7.22)$$

where $\xi_i^{AB} (\xi_j^{\tau})$ are Pauli matrices in sublattice (valley) space and $(i, j) \in [(x, x), (x, y), (y, x), (y, y), (z, z), (z, 0), (0, z)]$. The coupling constants g_{ij} introduce various forms of symmetry breaking (intervalley scattering, current-current interactions) and are to my understanding mainly used as fit parameters.

7.3 Conclusion

We model the interacting two-particle spectrum of BLG quantum dots by rediagonalizing a bare Coulomb kernel. After jumping over many numerical hurdles we end up with reasonable results that agree with previously established works. However, our model apparently lacks some necessary symmetry breaking and thus falls short of explaining the experimental data from Aachen. I nevertheless choose to include this chapter into my thesis since we (Thomas and I) have spent significant time on it and it is my understanding that negative results (while less encouraging) should also be communicated. In terms of prospects I expect that the rapid improvement of bilayer graphene based, electrostatically confined quantum dots will also be interesting in the context of magic-angle tBLG. The efforts of several groups to confine electrons in a quantum dot that is surrounded by superconducting bulk is both puzzling and impressive at the same time. Theoretical support for such an achievement would obviously require calculation methods beyond the single-particle picture.

Chapter 8

Photoluminescence in strained WSe₂

“If you want to have good ideas,
you must have many ideas.”

Linus Pauling

Mechanical strain is a very powerful tuning knob for the optical and electronic properties of layered two-dimensional materials. While the strain response of bright free excitons is broadly understood, the behavior of dark free excitons (long-lived excitations that generally do not couple to light due to spin and momentum conservation) or localized excitons related to defects remains mostly unexplored. Here, we study the strain behavior of these fragile many-body states on suspended WSe₂ kept at cryogenic temperatures. We find that under the application of strain, dark and localized excitons in monolayer WSe₂ — a prototypical 2D semiconductor — are brought into energetic resonance, forming a new hybrid state that inherits the properties of the constituent species. The hybridized exciton reported here may play a critical role in the operation of single quantum emitters based on WSe₂. This project is a collaboration with the group of S. Heeg at the Humboldt Universität zu Berlin [274]. Pablo Hernández López (Berlin) and Kirill Bolotin (Berlin) implemented an electrostatic based straining technique capable of straining suspended WSe₂ at cryogenic temperatures and performed measurements of photoluminescence spectra that display intriguing resonance properties. Based on work of my doctoral predecessor Lukas Linhart (TU Wien) I have built a strain dependent TB approach to study the hybridization of conduction band states with localized defect levels. Despite a fairly simple theoretical study of single-particle dipole matrix elements we find surprisingly good agreement with experimental data.

8.1 Introduction

Excitons (Coulomb-bound electron-hole complexes) are responsible for the strong absorption of light in 2D transition metal dichalcogenides [275–277]. These many-body states control valley properties in these materials [278, 279], and can condense into various correlated quantum states at low temperatures [280, 281]. Previous studies focused mostly on “bright” free excitons characterized by their large oscillator strength and intense optical activity. In TMD systems such as WSe₂ or WS₂ spin selection rules prohibit the radiative recombination of the ground state excitons composed of electron

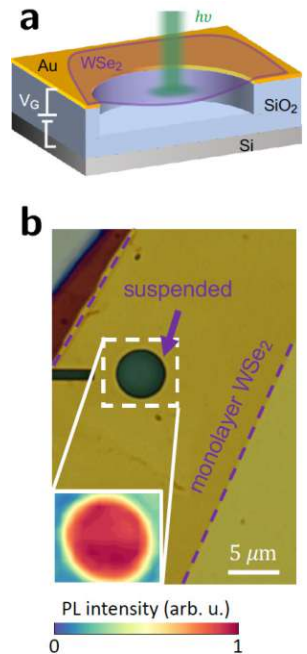


Fig. 8.1: **a** Schematic of the device and measurement scheme. Applying a voltage V_G between a suspended WSe₂ monolayer suspended and the back-gate introduces strain. We record PL spectra at the center of the suspended WSe₂ where the strain is spatially homogeneous and biaxial in nature. **b** Microscope image of a typical device. Inset: Room temperature PL map of the neutral exciton at 1.66eV in the unstrained ($V_G = 0V$) membrane.

and hole wavefunctions in the same valley [282]. Other energetically close excitons composed of a hole wavefunction localized in the K valley and an electron in the Q or K' valleys (or vice versa) are dark due to the required momentum transfer. While these “dark” excitons [283–285] usually only interact weakly with light due to several selection rules (spin and momentum conservation, see Section 2.2 for the electronic structure of pristine WSe₂) the understanding of these (and other) excitonic species could be crucial for understanding and exploiting TMDs in future applications. In all cases, dark excitons feature greatly increased charge lifetime, spin lifetime, and diffusion length compared to their bright counterparts [286–288]. These properties (desirable for future spintronic applications) created research interest targeted towards storing and transporting quantum and classical information [289, 290]. In the presence of lattice defects the existence of spatially localized, mid-gap defect states allow excitonic species that are delocalized in reciprocal space [291] and optically active. In addition, defect-related states function as broadly tunable quantum emitters, one of the fundamental building blocks of quantum information technologies allowing the generation of entangled photons [292–297]

Mechanical strain modifies the energies and the hierarchy of these excitonic species. The strain induced energy shift of energy bands [298, 299] varies across different bands and k-space regions. Excitonic species built from these bands inherit the corresponding energy shifts. The conduction/valence band gap at the K/K' valleys decreases at ~100 meV/% for uniform biaxial strain [300]. Naturally all excitonic species associated with these valleys (dark/bright neutral excitons, dark/bright trions, bi-excitons, and their phonon replicas) redshift at about the same rate.

In contrast, excitons residing in the Q valleys of WSe₂ display much weaker strain dependence [301, 302], while localized excitons associated with defects are essentially unaffected by strain [298, 299, 303]. Thus one could employ the strain response signature to identify excitonic species. For some strain values energy alignment between band minima at K and K' with the localized defect states can occur and cause them to hybridize [287, 304, 305]. Therefore mechanical strain engineering can be used to identify, generate, and tune novel hybridized excitonic states in TMDs and poses interesting questions: (I) What are the properties of the hybridized states? One can expect them to inherit the traits of the involved excitons before hybridization⁰¹. This is especially noteworthy should bright, defect-related, localized excitons hybridize with free dark K/K' excitons as they feature high oscillator strength and long diffusion length, respectively [287, 304, 305]. (II) Are there possible applications for the hybridized states? As strain is required for the operation of TMD-based quantum emitters, we believe that the hybridized states may be critical for the operation of these emitters. In a wider scope the ability to manipulate the emission from long-lived dark states may prove important for various excitonic transport

⁰¹ When we speak of the hybridization of excitons (i.e. many body states) we refer to a picture of hybridization of the underlying single particle states. Excitons that initially consist of different single particle states (e.g. conduction band minima at K vs. localized defect level) also “hybridize” when their mutually different single particle states intermix.

devices [289]. (III) How do we realize strain-induced hybridization experimentally? Observing well-separated excitonic peaks via optical spectroscopy requires clean, controllably strained devices operating at cryogenic temperatures. In contrast, most existing strain-engineering techniques either function only at room temperature [306–309] or do not allow in-situ control of the strain level [310–314]. This project addresses these questions via an electrostatic-based straining approach capable of straining a suspended WSe₂ monolayer at very low temperatures. In addition to the well-known free bright excitons we identify two types of excitonic species: (I) the free dark excitons localized at K/K' valleys and (II) a pair of bright localized excitons related to shallow defect states. These two types are distinguishable by their strain dependencies and can be brought into energetic resonance at $\sim 1\%$ and $\sim 2.5\%$ strain (dependent on temperature). At resonance, we observe signatures of the formation of the new hybridized state, including strongly increased photoluminescence of dark excitons and signatures of avoided crossing behaviour between dark and defect related excitonic species. Strikingly, some signatures of energetic resonance survive up to room temperature allowing us to observe pure defect emission.

8.2 Experimental Photoluminescence of strained WSe₂

We strain to monolayer WSe₂ by applying a gate voltage V_G between a monolayer WSe₂ membrane suspended on top of a circular hole etched into an Au/SiO₂/Si substrate and an electrode below (see Fig. 8.1). This approach combines several key advantages: (I) electrostatic straining functions at cryogenic temperatures, unlike other straining approaches that only work near room temperature (e.g. bending elastic substrates or pressurizing a 2D membrane with gas, [307–309]). (II) We can create large strain values of up to a few percent (higher than the limits of other techniques [306, 313]). (III) Suspended 2D materials are not affected by substrate-related scattering and therefore feature high optical quality necessary to resolve closely-spaced excitonic states [315–317, 319]. Unfortunately using electrostatic forces for straining means that the carrier density inside the device changes together with the mechanical strain. Therefore, a careful analysis disentangling the effects of doping and strain is required (see Fig. 8.5).

The device (see Appendix Chapter B for fabrication details) is loaded into an optical cryostat and measured via photoluminescence (PL) spectroscopy. We establish the quality of our device by identifying excitonic species and start by exploring the low gate voltage regime $|V_G| < 80$ V, where changes in the carrier density dominate the optical response of WSe₂ (Fig. 8.2). Measuring at a temperature of 100K (where only the most intense excitons are visible) we observe narrow PL peaks corresponding to neutral exciton (X^0) and charged triions (X^+ , X_T^- , X_S^-) at energies close to reported values [315–318]. The X^0 peak width of 7.5meV is close to the 4 – 6 meV reported at $T < 5$ K for high-quality WSe₂ encapsulated in hBN samples [315, 320].

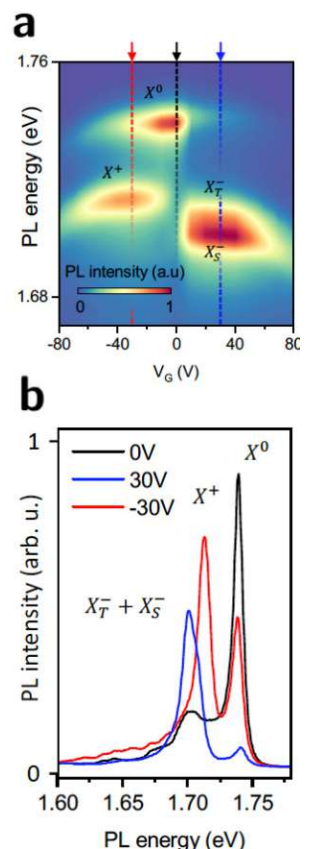


Fig. 8.2: **a** PL spectra as a function of V_G at $T = 100\text{K}$. **b** Cuts of (a) for fixed V_G . Neutral exciton (X^0 , 1.738eV), positively charged trion (X^+ , 1.713eV), negatively charged intervalley trion (X_T^- , 1.708eV), and negatively charged intravalley trion (X_S^- , 1.701eV) appear at the energies close to what is reported in literature for high-quality hBN encapsulated devices [315–318]. The near-zero charge neutrality point and the disappearance of the X^0 peak outside of the $-50\text{V} < V_g < +10\text{V}$ region confirm the good optical quality of our samples.

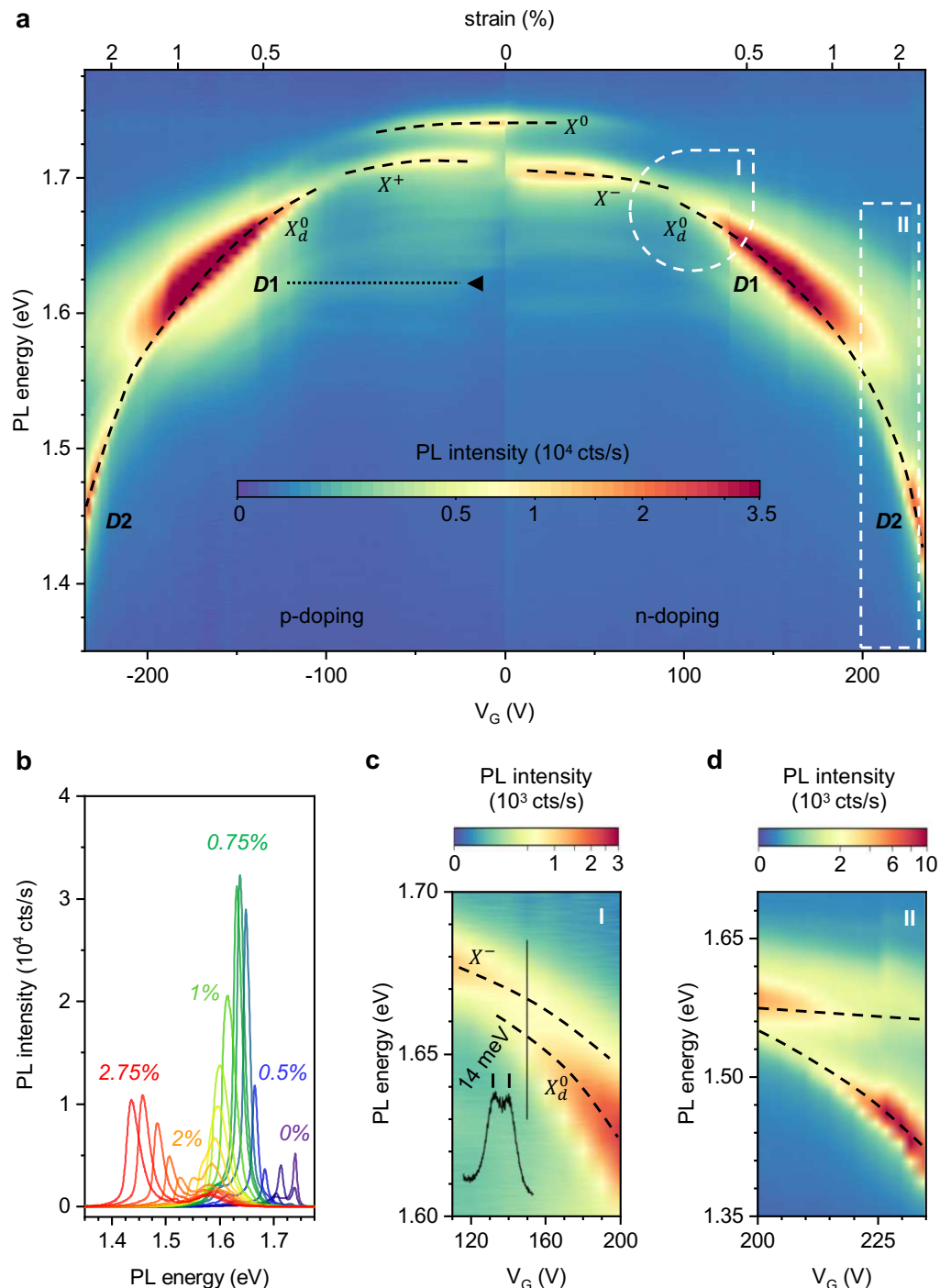


Fig. 8.3: **a** PL map (device 1) at $T = 100\text{K}$ with individual spectra shown in **b**. Free excitonic states X^0 , $X^{+/-}$, X_d^0 red-shift with increasing strain (black, dashed lines as a guide to the eye). The state X_d^0 develops strong intensity maxima at energies 1.63eV (D1) and 1.45eV (D2). The strain-independent states close to the position of D1 associate with defects are marked with a dotted line. See Fig. B.2a in Appendix chapter Chapter B for an offset plot of the PL spectra. **c** High-resolution map of the region I (device 2). The state X^- disappears with increasing strain while the state X_d^0 arises ~ 14 meV below it. **d** Detailed map of the region II (marked with white dashed lines in (a)) from device 1.

8.2.1 Decoupling doping- and strain-induced effects

Examining the behaviour of the system in the high voltage regime $|V_G| > 80$ V (where strain effects become dominant) we observe a redshift in the energetic position of the excitons X^0 , X^- , X^+ with increasing gate voltage (Fig. 8.3). The redshift is equal for both polarities of V_G . This behaviour is a well-characterized effect of mechanical strain [308, 319, 321]. In general, uniform biaxial strain in WSe₂ results in a downshift of all excitonic peaks at a constant rate of 100 meV/% [322]. We use this rate to fit the observed peak shifts to voltage dependent strain values Eq. (8.2) and extract an effective 2D Young's modulus of 100 N/m, close to previously reported values [319] (see Fig. B.4 in Appendix Chapter B). With this we can relate a given V_G to both the carrier density n and strain level ϵ induced in our device:

$$n = C_G V_G + n_0 \quad (8.1)$$

$$\epsilon \approx \begin{cases} \alpha V_G^4 + \epsilon_0 & \text{for } \alpha V_G^4 \ll \epsilon_0 \\ \beta V_G^{4/3} & \text{for } \alpha V_G^4 \gg \epsilon_0 \end{cases} \quad (8.2)$$

Here C_G is the gate capacitance of the device, α , β represent constants dependent on device geometry, ϵ_0 and n_0 are intrinsic strain and charge doping, respectively. Eq. (8.1) and Eq. (8.2) indicate that when the gate voltage is low (i.e. $|V_G| < (\epsilon_0/\alpha)^{1/4} \sim 100$ V in a typical device) it mostly controls the carrier density without efficiently introducing strain. At large $|V_G|$, mechanical strain starts to change rapidly, while being symmetric with respect to the sign of V_G . Experimentally we disentangle the effects of doping and strain in our gated devices by comparing two PL intensity maps vs. V_G measured on the same device with different intrinsic doping levels (Fig. 8.5).

We reach strain values of almost 3% in our suspended WSe₂ devices [299] and have verified the voltage-strain conversion via optical interferometry (see Fig. B.3 in Appendix Chapter B). The induced strain profile across the suspended region is displays sharp gradients along the border and little variation in its center (Fig. 8.4).

We also observe trends that are not expected from a simple model based on Eq. (8.2) that only considers spectral redshift due to strain and gating-related redistribution of the oscillator strength between trions and neutral excitons. Our first and most striking finding is the highly non-monotonic evolution of the PL intensity with increasing strain (see Fig. 8.3a). After an initial intensity drop the PL intensity increases towards a maximum (labelled D1) at $V_G = \pm 160$ V ($\sim 0.7\%$ strain) and 1.63 eV. The integrated PL intensity reaches a factor 6 higher than the combined intensities of neutral excitons and trion for $V_G = 0$ V. PL intensity then drops and peaks again with another maximum (labelled D2) at $V_G = \pm 230$ V ($\epsilon \sim 2.5\%$) at a PL energy of 1.45 eV. We see that the state associated with this enhanced PL intensity emerges 14 meV below the trion state. The trion gradually disappears (Fig. 8.3c) and dominates the PL when it approaches the energies

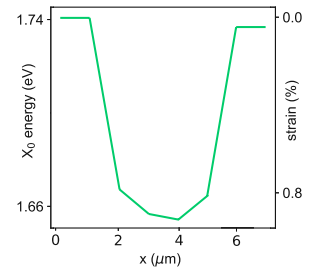


Fig. 8.4: Neutral exciton PL energy of a suspended WSe₂ monolayer (device 2) at $T = 77$ K and $V_G = -200$ V measured across a line scan through the center of the membrane. The redshift of the neutral exciton energy with respect to its unstrained value is converted to strain (right axis). We observe sharp steps of nearly 1% strain around the borders of the membrane (5 μm diameter) and small strain gradients ($< 0.07\%/\mu\text{m}$) around its center, confirming that the strain is spatially homogeneous within the area probed by the laser spot (800 nm radius).

of D1 and D2. From its energy position, we identify⁰¹ the state as a dark exciton, X_d^0 [323].

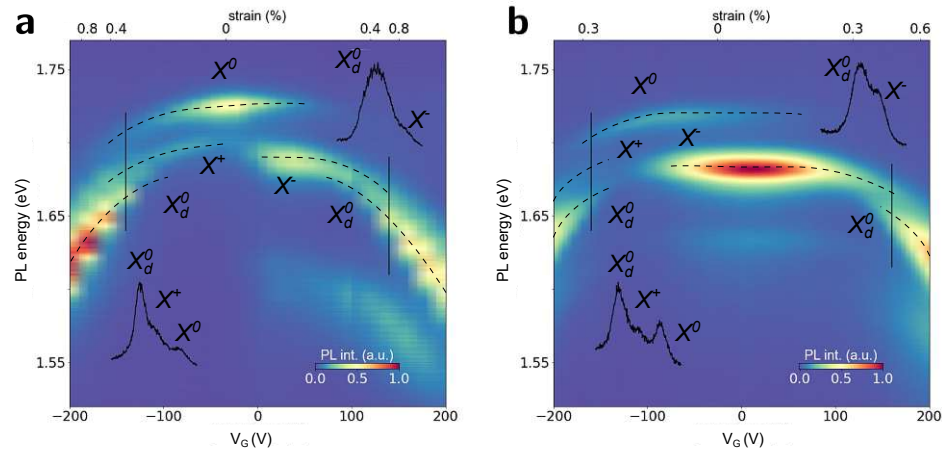


Fig. 8.5: **a** and **b** show PL vs. V_G on device 2 at 77 K (excitation 532nm, 10 μW) from two measurements performed three months apart. Degradation of monolayer WSe₂ over time due to chemical instability varies the defect and initial charge carrier concentrations of the samples. Excitonic species are marked with dashed lines and labeled. Individual spectra extracted from the black solid lines are shown in insets nearby. The PL spectrum at $V_G=0$ is dominated in **a** by neutral excitons and in **b** by negative trions. We therefore conclude that the sample is close to charge neutrality in **a** and initially electron doped in **b**. The main doping-related effect, the redistribution of oscillator strength between neutral exciton and trions, happens symmetrically for negative and positive voltages around the charge neutrality point, $V_G=0$ in (a) and $V_G \approx -100\text{V}$ in **b**. The brightening of the dark neutral exciton (X_d^0), however, happens at roughly the same energy for the two V_G polarities in both **a** and **b** because it is caused by the strain-driven hybridization of X_d^0 with a defect state when their energetically approach. We thus decouple strain and doping effects based on the fact that doping-induced changes in the PL depend on the polarity of V_G whereas strain-induced changes are symmetrical with respect to the sign of V_G .

We also observe faint lines around 1.6 eV for $|V_G| < 100\text{V}$ (see black triangle in Fig. 8.3a). Their PL energy is largely strain-independent. Furthermore, these features exhibit saturating power dependence that clearly distinguishes them from the near-linear dependence for neutral excitons and trions (see Fig. B.1 in Appendix Chapter B). Saturating power behaviour is characteristic of defect-related states [291, 324, 325] while strain-independence suggests that the underlying state has vanishing contributions from conduction band Bloch states.

8.3 Modeling hybridization on the single particle level

Given the diameter ($\approx 5\mu\text{m}$) and expected curvature of the suspended monolayer in relation to the irradiation spot size of the laser ($\approx 1\mu\text{m}$) we assume a homogeneous biaxial strain at the optically active monolayer region (see Fig. 8.4). In order to study strain dependent photoluminescence of a WSe₂ monolayer we generate TB models based on MLWF [120, 124, 125,

⁰¹The energetic proximity between dark exciton and trion requires high resolution measurements to resolve the two peaks.

239–241] from several uniformly strained DFT calculations of the pristine system (see Section 2.2.1 for a concise introduction to pristine WSe₂). We therefore perform fully spin-polarized, structural and electronic optimization of a pristine WSe₂ unitcell with the DFT software package VASP [205–208] and find an energetically favorable lattice constant of 3.322 Å. We ultimately aim to interpolate between Wannier descriptions of a few differently strained WSe₂ calculations. In order to achieve this we produce strain sampling calculations at strains $\epsilon \in [-1\%, 0\%, +1\%, +2\%, +3\%]$.

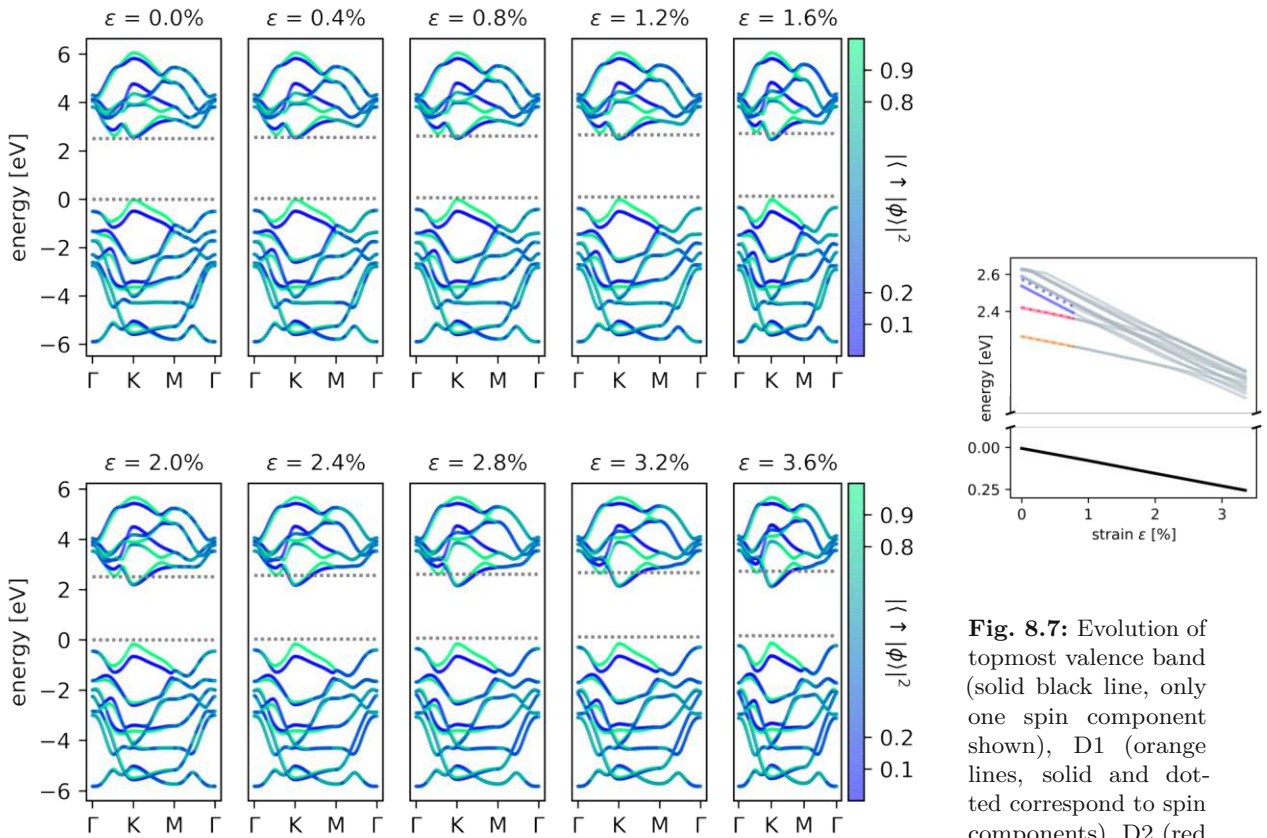


Fig. 8.6: Band structure of pristine WSe₂ calculated from Hamiltonians interpolated according to Eq. (8.3). Color indicates spin-up (\uparrow) projection of the underlying Bloch states ϕ . Band gaps for all strains are corrected by about 1.2 eV via scissor operators.

Our calculations encompass 35 Å vacuum in z direction and use a $25 \times 25 \times 1$ Monkhorst-Pack \mathbf{k} -space grid. Our exchange-correlation functional of choice is Perdew-Burke-Ernzerhof (PBE) in a generalized gradient approximation. Relative positions of the selenium atoms are fully relaxed (using a conjugate gradient algorithm) to residual forces less than 10^{-2} eV/Å for each strain value. Stretching the system also induces lateral contraction with the layer thickness (i.e. the distance between the two selenium atoms along the z direction) shrinking by about 1.4% at +2% in-plane strain. Plane wave energy cutoff is set to 500 eV and the systems are electronically converged to $\delta E \approx 10^{-9}$ eV.

We then produce TB descriptions based on maximally localized Wannier functions (involving (with spin) six p-orbitals on each chalcogen site and ten

Fig. 8.7: Evolution of topmost valence band (solid black line, only one spin component shown), D1 (orange lines, solid and dotted correspond to spin components), D2 (red lines) and bottom of the spin split conduction band (blue lines). Coloring valid for strains up to 0.8%. For higher strains the bands start to continuously intersect and are colored grey. potential clashes with the zz edge of the graphene flake in an unintended and non-physical manner.

d-orbitals on the metal site, see Section 3.5) for these systems. The disentanglement converges after roughly 500 iterations with window parameters (outer: [-12.0eV, 6eV], inner: [-12.0eV, 0.5eV]) to final spreads between 49 and 46 Å² depending on the involved strain. We thus obtain both the periodic Hamiltonian as well as the position operator in Wannier basis for subsequent calculations of dipole matrix elements. In order to accurately investigate at intermediate strain values we linearly interpolate the matrix entries of both the periodic Hamiltonian and periodic position operator between two sampling points ϵ_a, ϵ_b (i.e. $\epsilon_a, \epsilon_b \in [-1\%, 0\%, +1\%, +2\%, +3\%]$):

$$\hat{H}^{\lambda_x, \lambda_y}(\epsilon) = \hat{H}^{\lambda_x, \lambda_y}(\lfloor \epsilon \rfloor) + (\epsilon - \lfloor \epsilon \rfloor) \left(\hat{H}^{\lambda_x, \lambda_y}(\lceil \epsilon \rceil) - \hat{H}^{\lambda_x, \lambda_y}(\lfloor \epsilon \rfloor) \right)$$

$$\hat{r}^{\lambda_x, \lambda_y}(\epsilon) = \hat{r}^{\lambda_x, \lambda_y}(\lfloor \epsilon \rfloor) + (\epsilon - \lfloor \epsilon \rfloor) \left(\hat{r}^{\lambda_x, \lambda_y}(\lceil \epsilon \rceil) - \hat{r}^{\lambda_x, \lambda_y}(\lfloor \epsilon \rfloor) \right) \quad (8.3)$$

Here λ_x, λ_y runs over all relevant periodic real space cells that have non vanishing coupling elements⁰¹. We have taken care to ensure that the Wannier bases of the different DFT sampling points are converged to consistent solutions that allow for meaningful interpolation. This interpolation enables us to efficiently calculate the band structure of pristine WSe₂ for arbitrary strains (up to about 3%, see Fig. 8.6). Semi-local DFT severely underestimates the resulting single particle band gaps [43]. We correct this in TB via a scissor operator [52] that results in a band gap of 2.5 eV which agrees with both experimental and many-body GW calculations [44, 301, 302].

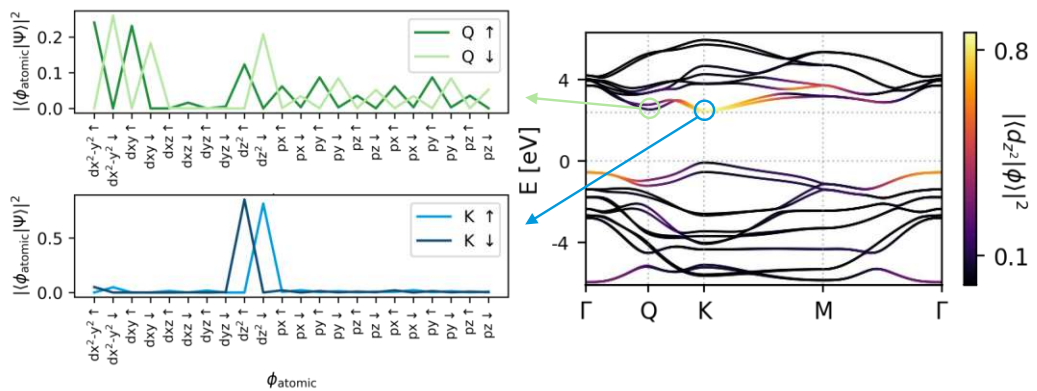


Fig. 8.8: Composition of the wavefunction at the K- and Q-valley minima of the conduction band as calculated by our Wannier model. Unlike the strongly strain-dependent K-valley band minimum, composed of only dz² orbitals, the band minimum at Q features many different orbitals whose strain dependencies could be thought to cancel each other out, explaining the weak strain dependence of the Q-valley.

The influence of strain is different for conduction and valence band and also \mathbf{k} -dependent. Tensile strain predominantly causes the conduction band minima at K/K' to shift downwards in energy. The strongly spin-split valence band also migrates to lower energies around K/K' but does so at a much lower rate. The competing minimum of the conduction band

⁰¹ Given the small unit cell these are quite a lot. (i.e. $\lambda_x \in [-16, 16]$ and $\lambda_y \in [-9, 9]$)

at Q (indirect band gap) seems mostly unaffected by strain and becomes increasingly energetically separated from the K/K' minimum at larger tensile strains. This observation is consistent with literature and also holds for expensive GW+BSE [301] and even scGW calculations [302]. An insight of our Wannier model is the stark difference in composition for the conduction band at the respective minima at Q and K (see Fig. 8.8).

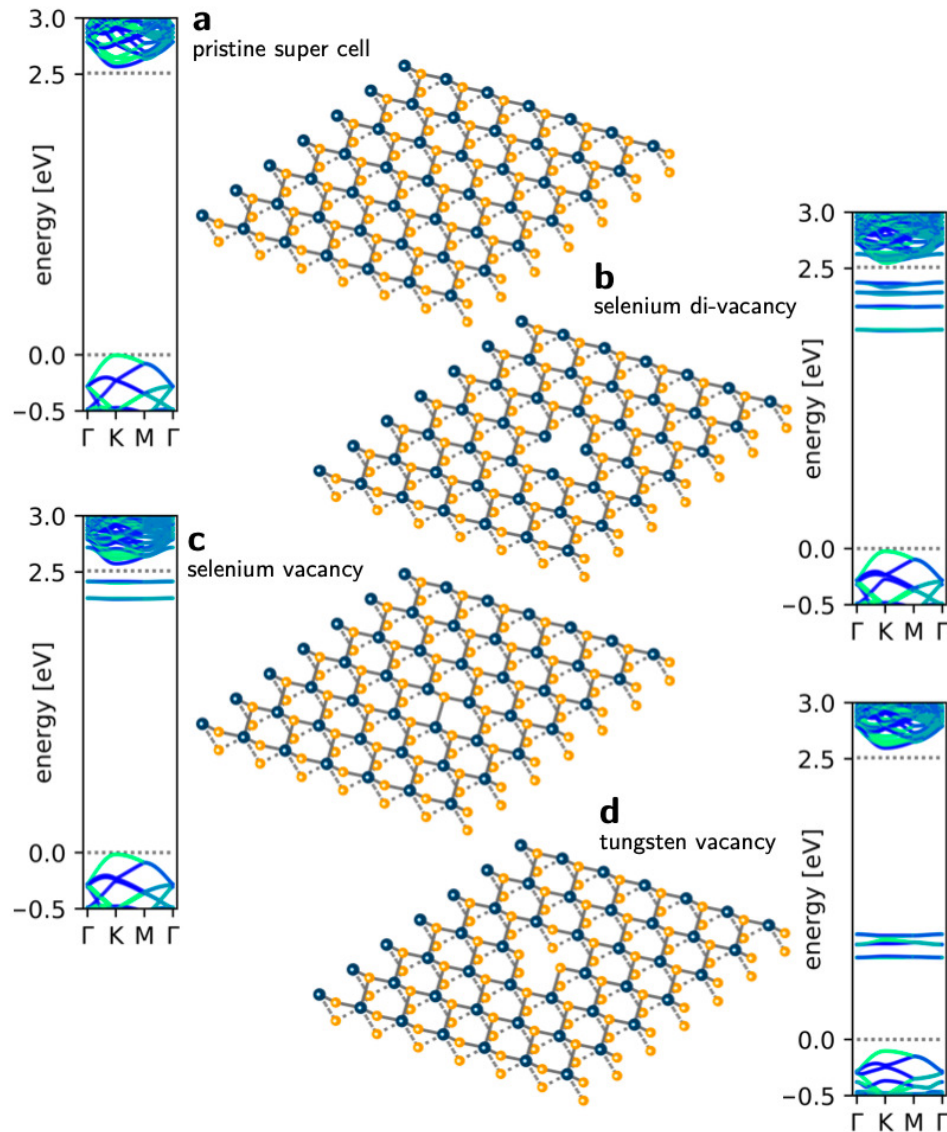


Fig. 8.9: Tight binding band structure along Γ -K-M- Γ and lattice plots for 7×7 super cells of tungsten diselenide for **a** pristine reference, **b** selenium di-vacancy defect, **c** selenium mono-vacancy defect, **d** tungsten vacancy. Horizontal dotted lines serve as guide to the eye for the pristine band gap with scissor correction applied.

While the conduction band minima at K (which shifts more strongly with strain) is predominantly composed of dz^2 like orbitals, the Q minimum features a mixture of states with various orbital characters. The strain dependence of these states could to some extent “cancel out”.

8.4 Transition matrix elements of defect supercells

We model the intensity variations of the PL peaks with increasing strain discussed in Section 8.2 as single particle effects: Strain causes the bulk conduction bands to shift energetically downwards through localized defect levels which leads to hybridization and a strong increase in oscillator strength. We omit more accurate but far more elaborate GW calculations [326–328] that would be required for quantitative corroboration since the proposed mechanism should already be well captured in the single particle picture and allow for qualitative analysis. In order to probe this hypothesis we study optical transitions between the relevant bands in a poor man’s 17×17 defect super cell⁰¹.

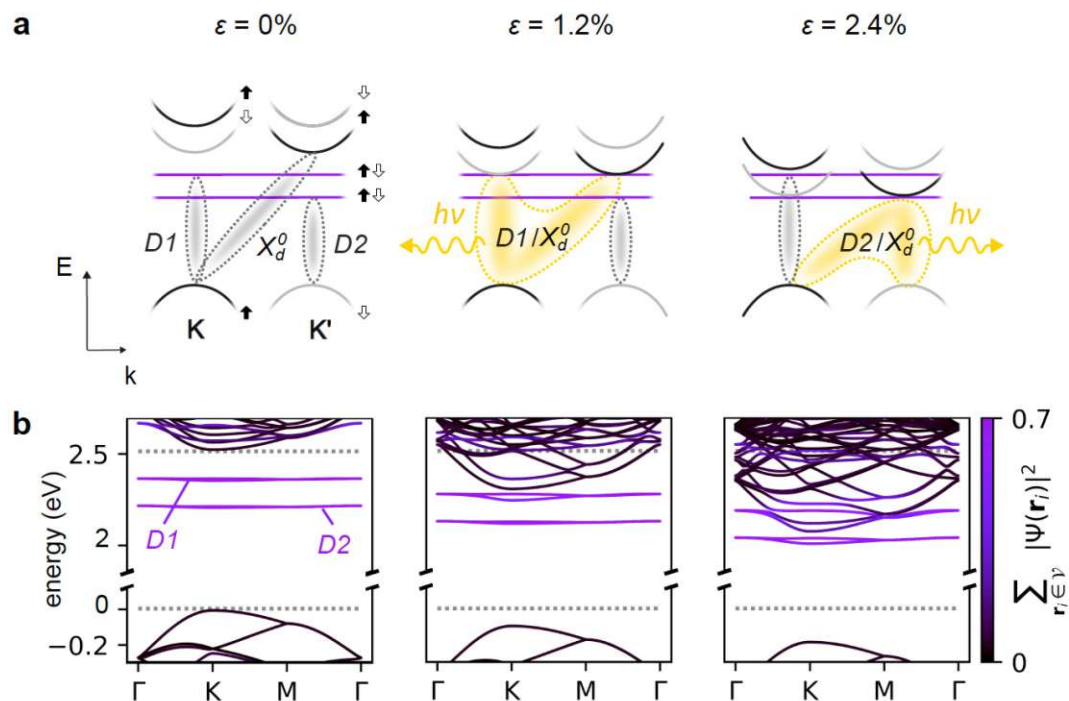


Fig. 8.10: **a** Schematic illustration of the K and K' valley bandstructure of WSe₂ at several different strain levels. Filled and empty arrows denote spin. **b** Corresponding bandstructure calculated via maximally localized Wannier functions. The color scale of the bands denotes their degree of localization in the immediate vicinity \mathcal{V} of the defect site. Dark excitonic states X_d^0 associated with the K point becomes resonant with excitons related to defect-related mid-gap states D1 and D2 at 1.2% and 2.4% strain. The resonance between X_d^0 and D1/D2 is determined by the total strain. Since intrinsic strain is temperature-dependent due to the thermal extension of involved materials as well as other effects [329], strain values at which the hybridization occurs also depend on temperature, as discussed in detail in Section 8.7.

A comparison between different defect candidates (Se-vacancy, Se-divacancy, W-vacancy) strongly favours the simple Se-vacancy due to both number and energy of midgap defect levels (see Fig. 8.9). The selenium mono vacancy features two defect levels (four with spin) with shallow donor character. Conduction, defect and valence bands all shift downwards in energy under tensile strain but do so at different rates (cb: $-74 \text{ meV}/\%$, D1: $-71 \text{ meV}/\%$, D2: $-73 \text{ meV}/\%$, vb: $-182 \text{ meV}/\%$)⁰². The spin split conduction bands then undergo a sequence of avoided crossings with the two defect levels D1 and D2. We expect optical transitions to be the dominant decay channel for the excitons in our system (cryostat temperatures) and thus calculate dipole matrix elements

$$|\mathbf{J} \cdot \langle \Psi^v | \hat{\mathbf{r}} | \Psi^c \rangle|^2 \quad (8.4)$$

with topmost valence wavefunction $|\Psi^v\rangle$ and conduction wave function $|\Psi^c\rangle$ (this nomenclature counts defect levels as conduction bands) and polarization vector \mathbf{J} . We extract the position operator from Wannier90 [120, 124, 125, 239–241]:

$$\langle \mathbf{R}, \mathbf{n} | \hat{\mathbf{r}} | \mathbf{0}, \mathbf{m} \rangle = i \frac{V}{(2\pi)^3} \int e^{i\mathbf{k} \cdot \mathbf{r}} \langle \mathbf{n}, \mathbf{k} | \nabla_{\mathbf{k}} | \mathbf{m}, \mathbf{k} \rangle d\mathbf{k} \quad (8.5)$$

Due to the starkly different strain dependence of competing conduction band minima at K and Q (see Fig. 8.6) we limit the transition to the direct bandgap at the K point but also consider the possibility of momentum relaxation at the lattice defect (non radiative transition from K to K') followed by radiative decay into the valence band which features opposite spin polarization in the other valley. This is incorporated by an overlap integral of almost degenerate (to within $\pm 2.5 \text{ meV}$) states at the two valleys.

$$|\mathbf{J} \cdot \langle \Psi_K^v | \hat{\mathbf{r}}(\mathbf{K}) | \Psi_K^c \rangle|^2 \times (1 + |\langle \Psi_K^{c_n} | \Psi_{K'}^{c_n} \rangle|^2) \quad (8.6)$$

In order to compare with experimental data we calculate PL intensity (oscillator strength, see Eq. (8.4)) as a function of PL energy $\Delta E_{c \rightarrow v}$ and strain ϵ . We shift our PL energy axis by an exciton binding energy of 0.8 eV for all conduction-valence band transitions [54] which is naturally missing from our single particle analysis.

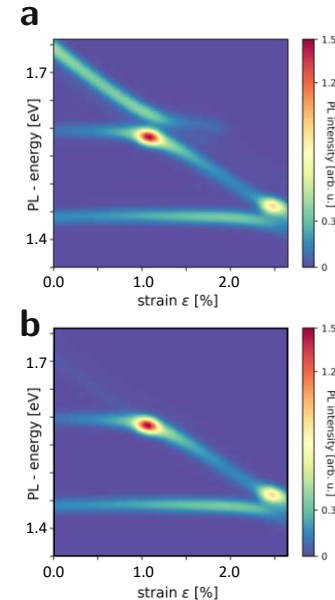


Fig. 8.11: Modeled PL intensity for a 17×17 Se single vacancy super cell in WSe_2 (i.e. the expression of transition matrix elements in Eq. (8.6) evaluated at K and K') plotted as a function of strain ϵ and PL energy. **a** no relative weighting of bright and dark feature, **b** bright feature suppressed by a factor of $e^{-(36 \text{ meV}/8.6 \text{ meV})} \approx 1/66$ (to account for thermal population differences). We include a Gaussian smearing of width 10 meV for all energies.

⁰¹ Both the successful implementation of my machine learning based defect parametrization algorithm (Chapter 6) as well as its extension to TMDs (Section 6.7) had not yet been achieved at the start of this project. I meanwhile also have a Wannier description of a fully relaxed 6×6 defect super cell. Embedding this into a larger pristine supercell (for meaningful defect concentrations) and redoing the calculation presents the prospect of studying polarization retention in future projects as such questions require exact knowledge of which symmetries the relaxed defect breaks.

⁰² Note that the rate of relative redshift between valence band and conduction band agrees well with the value assumed (100 meV/%, [322]) for transforming gate voltage to effective strain in Section 8.2 for the experimental data.

8.5 Comparison to experimental data

The experimentally observed strong increase in photoluminescence occurs when a strain-related modification of the energy spectrum brings the dark exciton X_d^0 into an energetic resonance with defect-related states D1,D2.

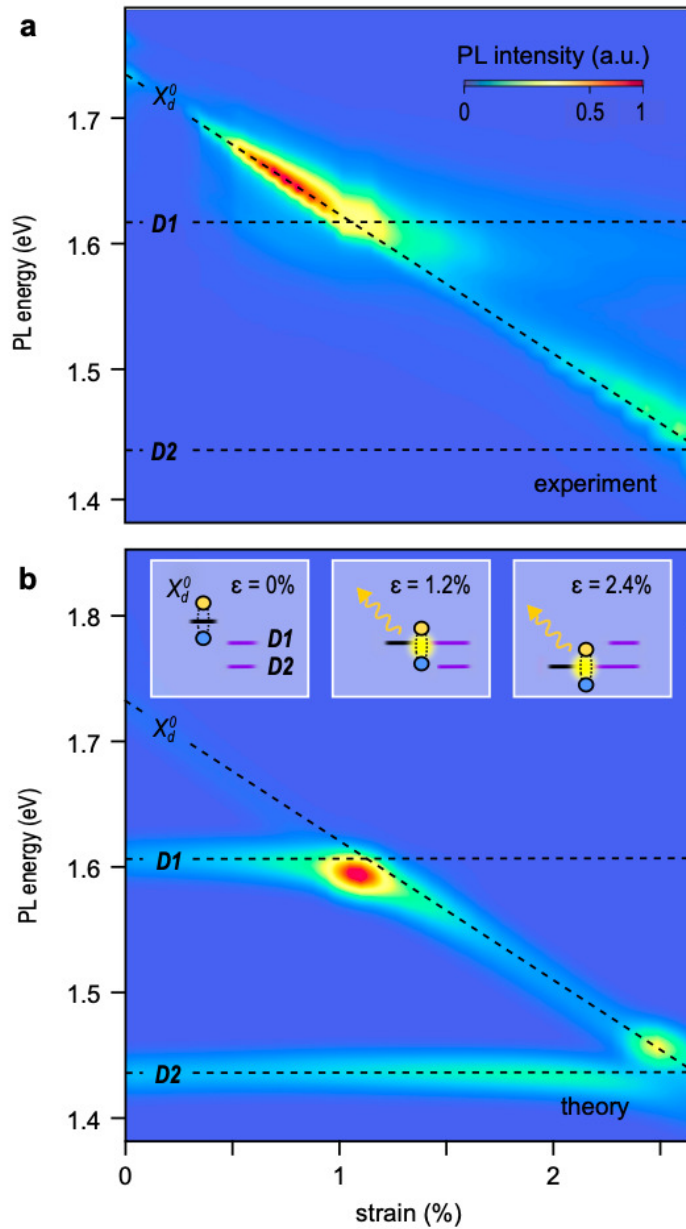


Fig. 8.12: Experimental (**a**) and modelled (**b**) PL spectra map of WSe₂ vs. strain. Different shift rates vs. strain for the defect-related states D1,D2 and a dark excitonic state X_d^0 are evident. When X_d^0 is energetically resonant with either D1 (around $\varepsilon \sim 1.2\%$) or D2 (around $\varepsilon \sim 2.4\%$) a strong increase in oscillator strength and avoided-crossing type behaviour occur. Insets show on- and off- resonant alignment between dark- and defect-related excitons.

This is especially striking since D1 and D2 are virtually invisible in unstrained devices. We explain these changes in intensity via strain-related

hybridization between the dark exciton X_d⁰ and defect-related states D1 and D2, as predicted by our tight-binding model (Fig. 8.10). Direct comparison of the experimental PL data, now plotted as a function of strain (Fig. 8.12a) to the theoretical evaluation of dipole matrix elements (Eq. (8.6), Fig. 8.12b) reveals solid agreement.

The fully spin resolved TB model can clearly capture the relative intensity of the bright and dark excitonic features (see Fig. 8.11). Since our model only calculates oscillator strength and does not in fact model the occupation of the corresponding energy bands we suppress the bright exciton by a factor of $e^{-(36\text{meV}/8.6\text{meV})} \approx 1/66$ (to account for thermal population differences). All of the features of the experiment are evident in our simulation, including the linear shift of X_d⁰ with strain, near strain-independence of D1/D2 and an order of magnitude increase in PL intensity when X_d⁰ into resonance with D1 or D2. At the strain values where the dark conduction band produces avoided crossings with the defect levels, hybridization occurs and the PL intensity forms peaks since momentum and spin selection rules no longer fully extinguish the PL signal.

It is also worth discussing several differences between experiments and theory. The shape of the region of increased PL in the experimental measurements is much more elongated than in the simulation data. Whether this is due to a potential mixture of differently contributing defect types in the real system might be up for discussion (see closely spaced midgap states of e.g. the double Se vacancy defect in Fig. 8.9). The experimental D1 maxima also features a subtle horizontal “tail” of PL intensity that is absent in Fig. 8.12 due to the artificial occupation suppression of the bright band and all other above (i.e. the large number of virtual bands crossing D1 Fig. 8.7 can — if not suppressed — also form a ridge like structure that at least visually however seems more “connected” to the bright exciton feature). Since our model only calculates oscillator strength and does not in fact model the filling of the defect energy bands we see quite pronounced horizontal intensity features at the defect energies. These should however only become effectively populated (and thus visible) once the conduction bands approach their energy due to strain. To confirm our interpretation, we have considered other phenomena that may contribute to non-monotonic variation of PL intensity in the next section.

8.6 Other possible contributions to PL intensity of the suspended WSe₂ system

Several phenomena can contribute to gate-dependent changes in PL intensity and potentially produce signatures similar to the ones ascribed to hybridization between bright and localized excitons. Here, we discuss such artefacts and show that none of them can explain our observations:

- **Fermi level changes** Changes of the gate voltage V_G produce changes in the Fermi level of our device in addition to the changes in strain. In principle, changes in the Fermi level affect photoluminescence spectra. However, the gradual increase in E_F only produces a Stokes shift in

the energetic positions of trion vs. neutral excitons and a gradual decrease in the intensity of all excitonic peaks due to phase-space filling effects and screening [320]. In contrast, our experimental data exhibits sharp peaks and avoided crossing signatures at specific strain values.

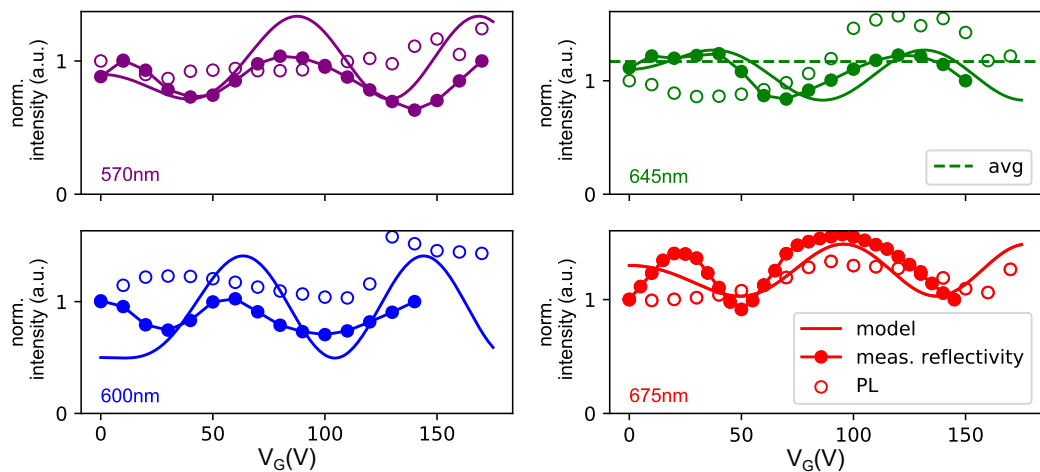


Fig. 8.13: One artefact that can produce non-monotonous changes in the PL intensity vs. V_G — and hence appear similar to the signatures observed — arises due to optical interference. We expect the total PL intensity — by which we mean the integrated intensity of all PL peaks peaks in a spectrum — to vary proportional to the membrane displacement. Here, we quantify the possible contribution of this effect. We examine the integrated PL intensity vs. V_G (empty symbols) for different excitation wavelengths (570, 600, 645, 675 nm) on device 5 at room temperature. Room temperature PL intensity in this range of V_G is roughly constant with most changes likely arising from interference effects. Indeed, we see that for all excitations, the variation in the signal remains small, but its phase shifts, as expected for interference. Furthermore, the signal matches the calculated laser intensity at the position of the device vs. V_G for same wavelengths using a simple model based on transfer matrices that captures interference effects (solid lines). In addition, we also plot the normalized reflectivity vs. V_G (curves are upshifted for clarity). As expected, this data is similar to the PL intensity data as the reflectivity maxima coincide with the maxima in absorption. We therefore ascribe the modulations seen in the figure to interference effects. Note that the maximum modulation due to interference is found for 645 nm (green empty symbols) and it is smaller than a 30 % of the average intensity. This allows us to set 30 % as an upper boundary for the effect of interference in the experimental data.

- **Interference effects** The space between the WSe₂ membrane and a reflective Si backgate forms an optical cavity where the excitation laser beam interferes with itself. This interference results in a spatial modulation in the laser intensity inside the cavity. When the membrane actuated by V_G deflects, its center moves with respect to the interference pattern leading to changes in absorption. Changes in absorption, in turn, affect PL emission, so the overall PL intensity ultimately reflects the spatial modulation of the laser intensity. To carefully analyze the contribution of this effect we carried out optical interferometry and photoluminescence excitation measurements described in Fig. 8.13. These measurements indicate that the contribution of the interference to V_G -dependent changes in PL intensity

is small (< 30 % of the overall PL signal at zero strain) and does not significantly affect our observations (the change of the overall PL signal intensity we attribute to hybridization is about a factor of six compared to PL at zero strain).

- **Changes in absorption** As strain is applied to the WSe₂ monolayer, its optical absorption spectrum gradually shifts with respect to the excitation laser kept at $\lambda = 532\text{nm}$. Changes in absorption, in turn, affect the overall brightness of photoluminescence. For the absorption spectrum of monolayer WSe₂, however, our excitation energy of 2.33 eV lies well above the two main excitonic resonances A and B [330]. Using available data, we estimate that at 100 K absorption should increase 30% from its unstrained value between 0 and 1.5% strain. It then decreases slowly as the strain is increased above > 1.5 %. In contrast, our experimentally observed PL intensities do not reflect these changes in absorption. The PL intensity increases 6 times at 0.75% compared to the unstrained value, decreases and then increases again 2 times at 2.4%. The difference between the PL emission behaviour with strain and the expected changes in absorption for the same strain values allow us to dismiss absorption as the main cause of the observed experimental features.
- **Strain-dependent scattering between K- and Q-valleys** Strain-dependent scattering between K- and Q-valleys of WSe₂ has been previously invoked to explain strain-dependent changes of the PL intensity [299, 319]. It was argued that the strain increases the energy separation between the K- and Q-valleys thereby suppressing K-Q intervalley scattering. This, in turn, reduces the linewidth of the bright neutral exciton [299]. We do observe a corresponding reduction of the bright neutral exciton linewidth at room temperature with increasing strain up until 0.75 %. However, for strain > 0.75 % the observed linewidth of the emission increases as PL splits in two bands. Continuous distancing of the K- and Q- valleys can explain neither the two PL resonances arising at different strain values nor the splitting of the PL emission in two bands. We therefore conclude that strain-induced changes in the relative energies of the K- and Q-valleys cannot account for the observation of hybridized peaks and other features seen in the experiments.

To summarize, none of the phenomena discussed above can meaningfully contribute to the non-monotonic changes in PL spectra seen in experiment.

8.7 Temperature dependent data

Having understood the strain induced hybridization of dark free and bright defect-related excitons, we can now discuss the temperature dependent nature of the states undergoing hybridization. For this, we turn to more complex data at temperatures between 10 K and 300 K (Fig. 8.14) and observe several trends:

(I) The strain tunability of the excitonic states decreases at low temperatures (e.g. $V_G = 200$ V generates 2.2% strain at 300 K and only 0.9% at 10 K). This difference is readily explained by the temperature-dependence of both intrinsic strain and the mechanical constants (e.g. Young's modulus) of WSe₂ [331, 332].

(II) Despite a strong temperature-dependent blueshift in the unstrained X^0 and $X^{+/-}$ excitonic peaks with decreasing T the strong enhancement in the PL intensity occurs at roughly constant energy for T = 10, 100, 300 K (dashed lines in Fig. 8.14). This is consistent with strain-independent defect-related excitons D1 and D2.

(III) At T ≥ 100 K the state hybridizing with D1/D2 — and thus dominating the photoluminescence — matches the energy of X_d^0 . At T = 10 K we observe more complex behaviour (Fig. 8.14a, see Appendix Chapter B for individual spectra). A state that lies ~ 80 meV (~ 87 meV) below X^0 for p- (n-) doping dominates the spectrum. This state is faint at zero strain, redshifts with strain at the same rate as other excitonic states, and its intensity reaches a maximum when it is brought into resonance with the defect-related state D1. The energy of that state is within a cluster of states related to dark trions X_d^+ , X_d^- and their phonon replicas [315, 333]. This suggests that at low temperatures the strain-driven hybridization between dark trions X_d^+ , X_d^- and the defect state D1 dominates the emission. At low temperature is likely the increased population of dark trions [334] that fuels this shift in relative intensities.

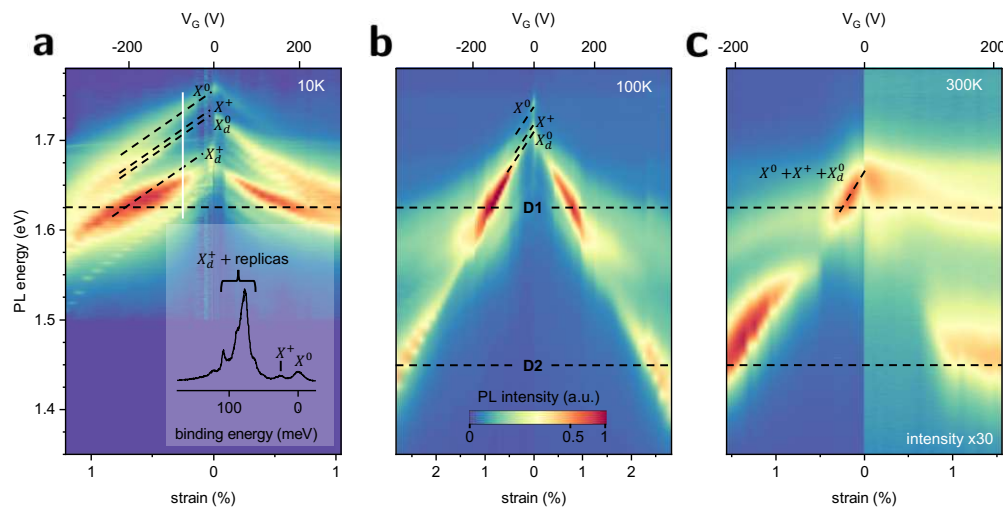


Fig. 8.14: PL spectra vs. strain maps acquired at **a** T=10 K, **b** 100 K, **c** 300 K. An individual spectrum at 10K measured under 0.25% strain (-140 V) and marked with a white, solid line is shown in the inset of (a). While the energy of the unstrained, free excitonic states (X^0 , X^+ , X_d^0 , the corresponding spectral lines are marked with dashed lines) blueshifts with lowering temperature, the features D1 and D2 associated with the corresponding defects stay roughly energy-independent. Due to the temperature-related changes in mechanical constants, only the D1 state is resolved at 10 K within our accessible V_G range. In contrast, we resolve the hybridization with both states D1 and D2 at 100 K and 300 K. As opposed to the T=10 K data in (a) that is symmetric with respect to p- and n- doping, the intensity of the n-branch at 300 K in (c) is roughly 30 times lower than that for the p-branch. Note that the voltage scales in (a-c) are not linear.

(IV) In contrast to lower T we see a pronounced asymmetry between positive and negative voltages in both intensity and structure of the PL spectrum at 300 K (Fig. 8.14c). Since our setup induces strain independent of the sign of V_G , this asymmetry must arise from changes in the carrier density. At n-doping (i.e. $V_G > 0$) the PL intensity is 30 times lower than on the p-side (i.e. $V_G < 0$). Furthermore we do not see any features associated with free excitons or linear strain dependence at n-doping and only observe weakly dispersing features at the energies of states D1/D2 that do not seem to undergo hybridization. We speculate that this behaviour may be related to the small oscillator strength of free excitons seen at room temperature for substrate-supported WSe₂ samples for n-doping [335–337]. This suggests that the features seen on the n-side are the intrinsic contributions from localized defect states D1/D2 that are in this regime not masked by other much stronger excitons.

8.8 Conclusion

We have shown that mechanical strain can bring dark- and localized defect-states into resonance and form a new hybridized state with large oscillator strength. That state dominates light/matter interactions in WSe₂. The outlined phenomenon can in principle occur between any pair of excitonic states that have different strain dependencies as long as they are not protected by some remaining symmetry (i.e. in our case the defect both introduces localized states and allows for avoided crossings with conduction bands). Point defects other than the Se vacancies discussed here can also be involved, as long as they feature localized defect states sufficiently close to the conduction band edge (i.e. within range of strain induced redshift). The hybridized state we observe is likely key for the operation of single quantum emitters in WSe₂. These devices generate highly non-uniform strain in WSe₂ by deposition onto e.g. a bed of pillars. At the point of maximal strain (e.g. the pillars' top) the hybridization conditions are fulfilled and dark excitons effectively release their energy as photons while the strain gradient “funnels” all excitonic species (including dark) towards this point of highest strain. Since the lifetime of dark excitons is much longer than that of their bright cousins, our work shows that the area from which this funneling process “collects” the energy is much larger than what was thought previously. Similar processes may happen in other TMD materials, especially in WS₂, where the ground state is also dark [338]. Our results also suggest the use of mechanical strain to fingerprint excitonic complexes in TMDs (e.g. free and defect-related excitons respond to strain very differently allowing their unambiguous identification).

Recent experimental PL measurements of WSe₂ single photon emitters employing atomic force microscopy to carefully introduce nano-indents near lattice defects [339] might be the final confirmation of the strain-induced spectral shift/hybridization mechanism. Our current modeling of the PL map based entirely on single-particle quantities and the continuing research interest from experimental groups calls for a follow-up investigation

of these systems via more refined techniques such as re-diagonalizing a *Bethe-Salpteter Kernel* or following the *GW* approximation.

Furthermore, I have meanwhile managed to produce a Wannier parametrization of a complete 6×6 Se single vacancy defect super cell. Since this model also includes lattice relaxation we can now study polarization retention of the strained defect system. Abhijeet Kumar from the group of Kirill Bolotin has recently reached out to us with interesting experimental data that suggests that the defect hybridized exciton appears to break the expected symmetry between σ_- and σ_+ excitation. Since the retention of chirality certainly depends on the remaining symmetries of the defect the fully relaxed defect geometry is a necessary building block for future studies. A theory to describe the new valley-polarization measurements (via Kerr microscopy) will also have to model the excitation to some extent. Since the new data from the Universität zu Berlin is time-resolved, this would also provide an exciting opportunity to study the dynamic aspect of this polarization flip.

Chapter 9

Grain boundaries as valley filters

“Equipped with five senses, man explores the universe and calls the adventure science.”

Edwin Hubble

This chapter reports on a joint project with my project student Siyar Duman (an excellent project- and later on master student in our group). The idea for the project came from the motivation to possibly extend the controlled symmetry breaking discussed in Chapter 5 from point defects to one-dimensional line defects or grain boundaries and quickly grew into a brainstorming about other interesting physics of these systems. One successful “wannierization” and literature search on these defects later I stumbled across a relatively short paper with an even more succinct title [15]. The authors employ a fiendishly simple 1NN TB model of the 5-8-5 line defect in graphene to corroborate a very elegant series of symmetry arguments that state that any line defect that is mirror-symmetric along its main axis results in valley filtering, the efficiency of which depends on the angle of incidence of the scattered electron.

The main motivation for this project is thus to figure out whether this angle dependent valley filtering holds for a 10NN TB description of symmetric grain boundaries generated from fully relaxed DFT calculations. To this extent we generate Wannier parametrizations for two symmetric grain boundaries, embed them into a scattering geometry that allows for variation of the angle of incidence (via a Berry-Mondragon-like guiding potential [39, 340]) in electronic transport simulations and analyze the valley character of both transmitted and reflected amplitudes. Carefully disentangling effects from the trajectory-controlling potential we find that valley polarization only occurs at narrow energy windows near bound defect states. Angle dependence of transmitted polarization (while qualitatively similar) is generally not well approximated by a simple sine function (as predicted in [15]). I conceived the project, generated the Wannier descriptions and came up with the scattering geometry. Siyar implemented the angle variation potential, executed the transport calculations and evaluated all results.

9.1 TB models for symmetric line defects

We perform DFT structural and electronic optimization with the VASP software package [205–208] for two types of line defects that are mirror-symmetric with respect to their longitudinal direction. The first being the exact same line defect for which the valley filtering properties have been proposed in [15] (henceforth referred to as 5-8-5 line defect, see Fig. 9.1a). It is essentially the reconstruction of two graphene flakes telescoped into each other along the armchair (AC) direction. The calculations encompass $3 \times 9 \times 1$ k-points with a plane wave cutoff of 600eV. Ionic positions are converged to forces less than 10^{-2} eVÅ $^{-1}$. The relaxed unit cell size in y-direction is found to be 4.9219Å with the PBE functional [107] and 25Å of vacuum added in z-direction. After the final electronic relaxation to $\delta E \approx 10^{-9}$ eV we employ Wannier90 [212–214] to generate 185 Wannier functions (initially starting from atom-centered p_z and bond-centered s orbitals) disentangling (outer window [−28.5eV, 8.4eV], frozen window [−28.5eV, −0.12eV]) physical from vacuum states converges after 1036 iterations. Successive minimization of the spread functional results in a total spread of 146.87Å 2 after 199230 iterations.

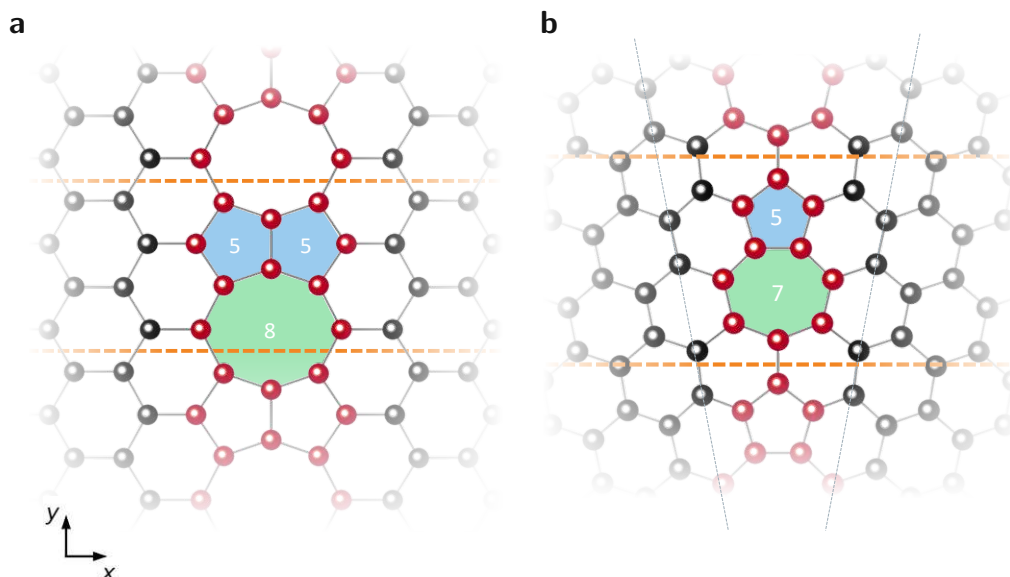


Fig. 9.1: **a** Relaxed pentagon/octagon (indicated in blue and green respectively) geometry of a 5-8-5 line defect resulting from two graphene flakes shoved into each other along the arm chair direction. Grain boundary adjacent atoms are colored red. Dashed orange lines indicate periodicity in y direction. **b** Relaxed pentagon/heptagon (indicated in blue and green respectively) geometry of a tilt line defect (classified via grain boundary indices $m = 1, n = 2$ according to [341]) resulting from two graphene flakes rotated by $\theta = 21.8^\circ$ (arm chair orientation of both sides indicated by dotted grey lines). Grain boundary adjacent atoms are colored red. Dashed orange lines indicate periodicity in y direction.

The second line defect under consideration is a so called tilt grain boundary (see Fig. 9.1b). These kind of periodic grain boundaries arise from a finite misorientation angle between two graphene flakes and are described with

coincidence site lattice (CSL) theory. Such grain boundaries are uniquely classified via two indices (m, n) that build the generating vector out of the pristine lattice vectors [341],

$$\mathbf{B}_1 = m\mathbf{a}_1 + n\mathbf{a}_2 \quad (9.1)$$

similar to the description of moiré patterns. The periodicity d and misorientation angle θ of these grain boundaries follow from commensurability conditions [342]

$$d_{m,n} = \|\mathbf{B}_1\| = a\sqrt{m^2 + mn + n^2} \quad (9.2)$$

$$\theta_{m,n} = 2\arcsin\left(\frac{|n - m|}{2\sqrt{m^2 + mn + n^2}}\right) \quad (9.3)$$

We choose a line defect with $m = 1$ and $n = 2$ that results in reasonable y periodicity of $d = 6.5112\text{\AA}$. In order to also achieve periodicity in x direction the DFT supercell for this defect involves two grain boundaries rotated 180° to one another. We use a Monkhorst grid $(3 \times 5 \times 1)$ with a plane wave cutoff of 350eV . After the final electronic relaxation to $\delta E \approx 10^{-8}\text{eV}$ we again employ Wannier90 [212–214] to generate 340 Wannier functions with otherwise identical parameters to the 5-8-5 line defect.

9.2 Valley filtering via symmetry

The valley filtering properties proposed in [15] follow from simple symmetry arguments for low energy (\mathbf{k} remains restricted to the vicinity of K/K' valleys) quasiparticle waves with well defined angle of incidence to the line defect α . The full system is described via a Hamiltonian of the form

$$\hat{H} = \hat{H}_0 + \hat{H}_D + \hat{V} \quad (9.4)$$

the three terms of which account for pristine graphene, line defect and their interaction respectively. In the limit of vanishing wave vectors the reflection operator $\hat{\Pi}$ commutes with the translation operators both along and perpendicular to the line defect axis (i.e. $\hat{T}_{||}$ and \hat{T}_{\perp}). This allows us to write solutions in terms of eigenstates of the reflection operator $\hat{\Pi}$ ($|+\rangle, |-\rangle$) with \mathbf{k} dependent, unimodular, complex coefficients a_+, a_- ,

$$|\Psi_{\mathbf{k}}\rangle = a_+|+\rangle + a_-|-\rangle. \quad (9.5)$$

Assuming a 1NN TB model we can now argue that since $|-\rangle$ has a node along the mirror axis, it can not contribute to transport across the line defect. This results in transmission and transmitted valley polarization of the form:

$$T_{\tau} = |\langle +|\Psi_{\tau}\rangle|^2 = \frac{1 + \sin(\tau\alpha)}{2} \quad (9.6)$$

$$P_T = T_K - T_{K'} = \sin(\alpha) \quad (9.7)$$

where $\tau = \pm 1$ describes the valleys K/K'. While this deduction involves several approximations (no transversal confinement, 1NN TB, low energy limit) we may at least expect some degree of valley polarization for reasonably high angles of incidence even in our more realistic simulations.

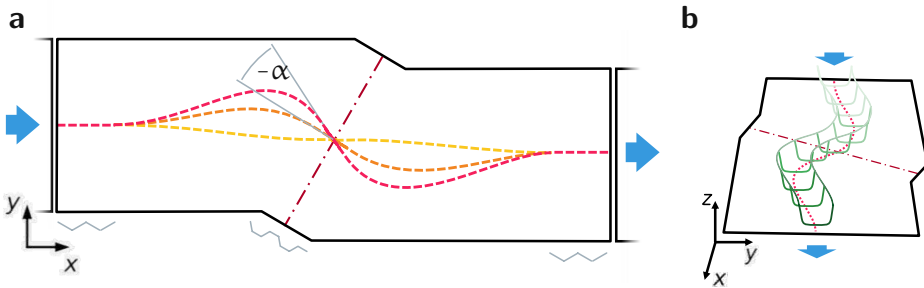
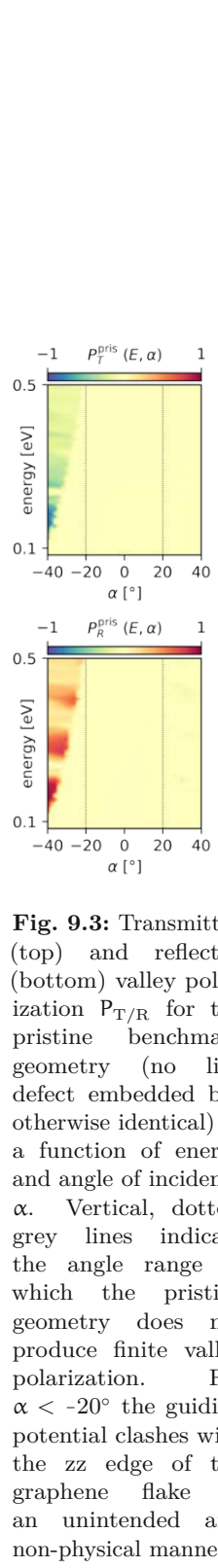


Fig. 9.2: **a** Top view schematic of the zig-ac-zig geometry employed for transport calculations through the 5-8-5 line defect (see Fig. 9.1a). The line defect is oriented along the brown, dot-dashed line. The half-infinite zig-zag edged leads are attached at the left and right ends. Dashed lines (red, orange, yellow) represent the center of the guiding potential used for manipulating the angle of incidence α . **b** Perspective view of the same geometry as in **a** with a schematic cross section of the guiding potential Eq. (9.9)

9.3 Transport geometry

In order to study the valley polarization effects of the line defects in terms of Landauer Büttiker [343] transport with our modular recursive Green's function code [116, 344] we need to identify the valley character of the incoming and outgoing lead modes. In this formalism the first desired information is the surface Green's function of the semi-infinite leads [115] attached to the scattering geometry (which encompasses the defect)

$$\mathcal{G}_{L/R} \hat{H}_{L/R} = \sum_{L/R} |L/R\rangle \underbrace{e^{ik\Delta x}}_{\beta} \langle L/R| \quad (9.8)$$

where $|L/R\rangle$ refers to left- or right-moving states respectively and $\beta := e^{ik\Delta x}$ are the eigenvalues of the lead eigenproblem.

While there has been much ingenuity implemented by my predecessors (Thomas Fabian [114], Lukas Linhart [83]) for efficiently solving for the lead modes (involving a Jacobi-Davidson eigensolver as well as a mode sorting algorithm that involves singular value decomposition for highly degenerate unit cells [345]) it turns out that identifying the valley character of a lead mode is best done via the sign of the imaginary part of the eigenvalue β . In “normal” systems where the band minimum is at Γ open modes would be located around $(1, 0)$ in the complex β plane. For graphene we expand around K/K' (i.e. $\pm(2\pi)/(3a)$) which makes the sign of the imaginary part of β a unique valley descriptor for 1D transport calculations. However this procedure comes with several prerequisites:

- 1) by definition it only works for low energy solutions (i.e. the close vicinity of K/K').

- 2) the lead needs to feature zig-zag (ZZ) boundaries to avoid K and K' being projected onto each other along the imaginary β axis.
- 3) The term Δx in β can (for artificially degenerate unit cells) also make the extraction of valley information impossible (exponentiating of signs or in other words over-rotation on the complex unit circle).

Our transport geometry of choice (Fig. 9.2) meets these conditions by connecting the 5-8-5 line defect region via two trapezoidal shaped regions to half-infinite zz leads. Furthermore we also employ a guiding potential of the form

$$V_{CS}(d_{\perp})\sigma_z = \left(e^{-\gamma(d_{\perp} + \frac{W}{2})} + e^{\gamma(d_{\perp} - \frac{W}{2})} \right) \sigma_z \quad (9.9)$$

that is used to both change the effective angle of incidence $\alpha \in [-40^\circ, 40^\circ]$ and gets rid of any influence of zig-zag or armchair edges. $V_{CS}(d_{\perp})$ is a double exponential tub potential that defines the cross section of the guiding channel along $y_{CS}(x)$ (e.g. yellow, orange or red dashed curves in Fig. 9.2a). This center line is defined via cubic splines connecting straight regions at lead source and drain as well as a straight region close to the crossing with the defect line. d_{\perp} represents the orthogonal distance to this center line $y_{CS}(x)$. σ_z is a Pauli matrix in sublattice space which can only be applied where the sublattice assignment of lattice sites is meaningful (i.e. we replace σ_z with a unity matrix in sublattice space for the sites that make up the defect). In order to unequivocally determine the source of any valley polarization effects we build an essentially identical copy of this scattering geometry without embedding the line defect to allow for blank tests of the intricate guiding potential setup (see Fig. 9.3). Transport calculations of this benchmark system for varying angles reveal the limitations of our guiding potential setup. While transmission through the geometry is close to unity for all angles $\alpha \in [-40^\circ, 40^\circ]$ (not shown) we find finite valley polarization for extreme angles below -20° (see Fig. 9.3). Inspection of the corresponding scattering densities (Fig. 9.4) reveals that the guiding potential (high curvatures for large angles) collides with the zz edges of our graphene flake for these angles. Since this effect also occurs at smaller angles for increasing energy we restrict the following analysis to the “trustworthy” angle regime of $\alpha \in [-20^\circ, 20^\circ]$ (vertical dotted grey lines in Fig. 9.3) where we have certainty that any valley polarization encountered in the defect geometry is caused only by the presence of the defect.

Since such a benchmarking system is not viable for the rotated line defect (one cannot connect two rotated graphene sheets without the grain boundary) we only present results for the 5-8-5 line defect. A similar analysis for the tilt grain boundary in Fig. 9.1b is an ongoing project.

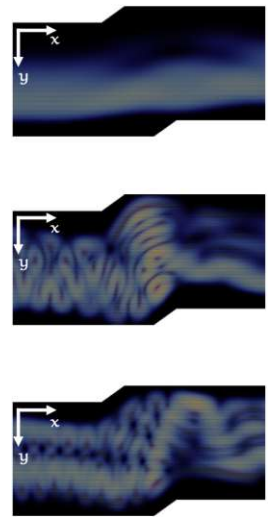


Fig. 9.4: Exemplary scattering densities in the pristine reference geometry at $E = 0.5\text{eV}$ (color scale from black to red) for (top) zero node mode, $\alpha = 30^\circ$, (center) zero node mode, $\alpha = -15^\circ$, (bottom) single node mode, $\alpha = -4^\circ$.

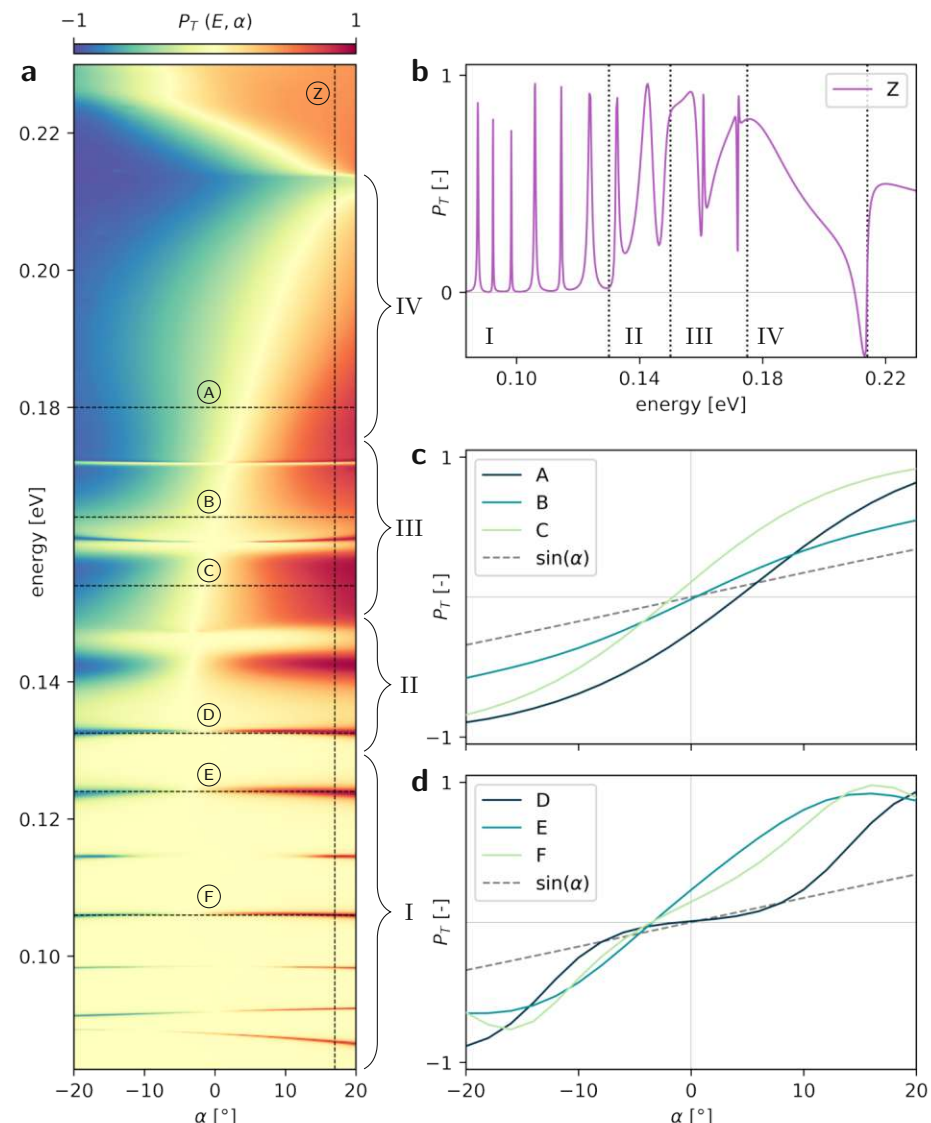


Fig. 9.5: **a** Transmitted valley polarization $P_T(E, \alpha)$ Eq. (9.11) for the 5-8-5 linedefect geometry presented in Fig. 9.2. Curly brackets indicate energy regions I-IV referred to in the discussion. Dashed lines indicate coordinates of cuts presented in panels b-d. **b** Constant angle cut of panel a ($\alpha = 17^\circ$). Dotted, vertical lines separate qualitatively different behaviour (I ... isolated peaks, II ... emerging background, III ... pronounced background with sharp "Fano-like" resonances, IV ... monotonic decline before mode opening). **c** Constant energy cuts of panel a (A ... 0.18eV, B ... 0.163eV, C ... 0.154eV). Grey, dashed line plots $\sin \alpha$ for visual comparison. **d** Constant energy cuts of panel a (D ... 0.18eV, E ... 0.163eV, F ... 0.154eV). Grey, dashed line plots $\sin \alpha$ for visual comparison.

9.4 Valley polarization and bound defect states

The main properties of interest — valley polarization of transmitted and reflected wave — can be readily defined via the valley channel resolved total transmission and reflection:

$$P_R(\alpha, E) := \frac{R_{KK} + R_{KK'} - R_{K'K} - R_{K'K'}}{R_{\text{tot}}} \quad (9.10)$$

$$P_T(\alpha, E) := \frac{T_{KK} + T_{KK'} - T_{K'K} - T_{K'K'}}{T_{\text{tot}}} \quad (9.11)$$

with $R_{K'K}$ ($T_{K'K}$) the reflection (transmission) coefficient of an incoming K wave scattered into a K' state and R_{tot} (T_{tot}) the total reflection (transmission).

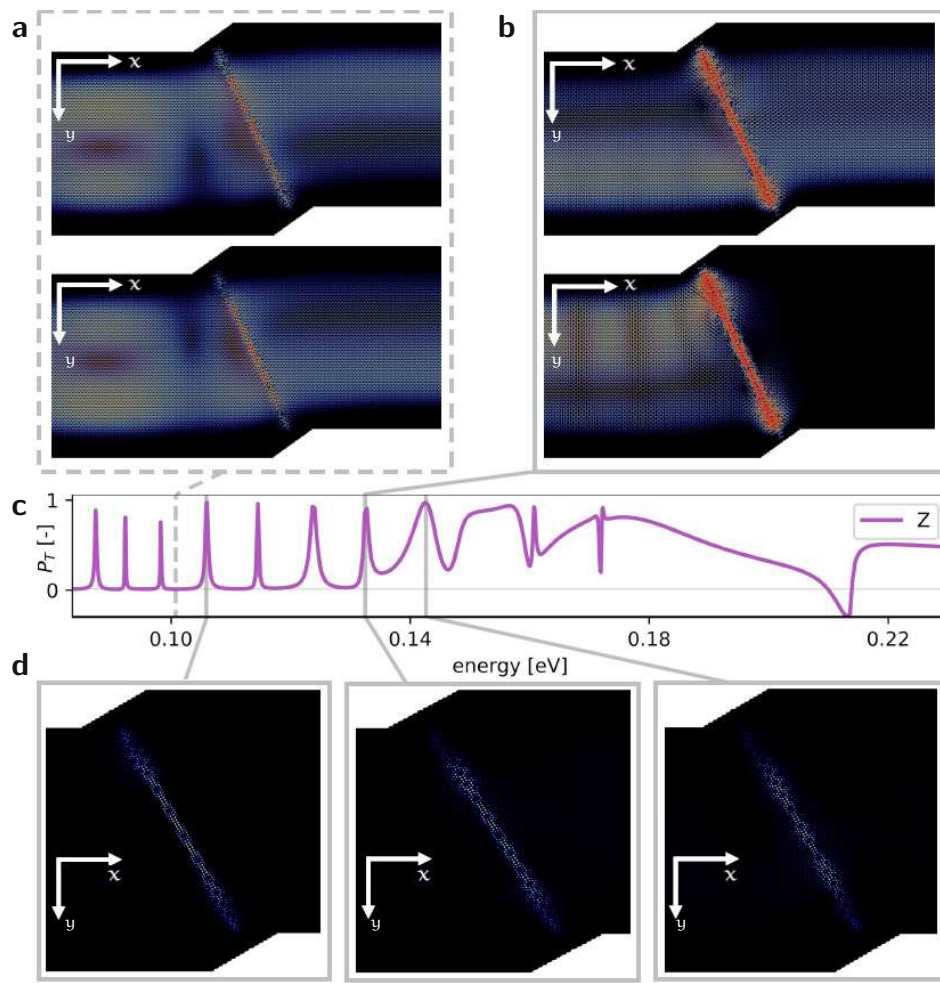


Fig. 9.6: Scattering density at **a** a generic energy with no significant valley polarization P_T and **b** at a polarization resonance. (see respective energies in panel c). **c** P_T for the 5-8-5 defect geometry (see also panel b in Fig. 9.5). **d** Probability density for bound states at the energies indicated in panel c. Resonances in transmitted valley polarization correspond to the existence of bound defect states.

We calculate valley polarization for both the transmitted and reflected currents for energies $E \in [0.08\text{eV}, 0.23\text{eV}]$ for the 5-8-5 line defect geometry. In this energy regime our lead supports two open modes which are degenerate and correspond to the valleys K/K' respectively. Our calculations reveal a surprisingly rich transmitted polarization landscape $P_T(E, \alpha)$ (see Fig. 9.5a) that features several sharp polarization maxima along the energy axis (see Fig. 9.5b) and smooth but in general nonlinear angle dependence (see Fig. 9.5c,d). We can identify four energy regimes with qualitatively different behavior for P_T : (I) $E \in [0.08\text{eV}, 0.13\text{eV}]$ with separate sharp ($\text{FWHM} \approx 0.8\text{meV}$), (II) $E \in [0.13\text{eV}, 0.151\text{eV}]$ broader peaks with increasing background, (III) $E \in [0.151\text{eV}, 0.175\text{eV}]$ pronounced background superposed by very narrow, asymmetric resonances, (IV) $E \in [0.175\text{eV}, 0.214\text{eV}]$ slowly decreasing background without peaks and sign reversal before new mode opening at 0.214eV. Focusing only on angle dependence for a moment we can compare constant energy cuts (see Fig. 9.5c,d) with the simple sine expression of [15]. While $P_T(\alpha, E = \text{const.})$ is monotonically increasing in regions (III) and (IV) (cuts through the extended background, see Fig. 9.5c) our calculations yield consistently larger polarization than that of Eq. (9.7). We note varying slopes and shifts in the position of the zero-crossing for different energies. Cuts through the sharper maxima (Fig. 9.5d) in regions (I) and (II) show non-monotonicity with $P_T(\alpha, E = \text{const.})$ featuring two inflection points in $\alpha \in [-20^\circ, 20^\circ]$.

A similar analysis for $P_T(\alpha, E = \text{const.})$ (see Fig. 9.7) reveals in general inverse valley polarization. Interestingly enough the line defect appears to introduce net scattering between valleys as the total valley polarization of incoming ($P_{\text{in}} = 0$) and outgoing waves $P_{\text{out}} := P_T + P_R \neq 0$ differ. Whether this unexpected loss of valley symmetry is caused by the line defect itself or only in combination with guiding potential remains elusive in our analysis. While one may expect the reflected wave to interact more intensely with the grain boundary (i.e. reflection requires a larger change in momentum) the reflected wave features lower valley polarization than the transmitted counterpart.

Both $P_T(\alpha = \text{const.}, E)$ and $P_R(\alpha = \text{const.}, E)$ (Fig. 9.5b and Fig. 9.7b) display pronounced peaks for some energies. The scattering densities for the two incoming modes (K/K') at these energies reveal strong resonance at the defect site with starkly different mode resolved transmission (i.e. K simply passes the boundary while K' appears almost entirely reflected, see Fig. 9.6a,b). We conjecture resonances with bound defect states as the origin of the energetically narrow but strong valley polarization (in both transmission and reflection). To this extent we have also calculated eigenstates of the transmission geometry by replacing the half-infinite leads with hard walls. We indeed find that the peaks in valley polarization can be identified with localized eigenstates of the grain boundary (see Fig. 9.6c,d). This is furthermore supported by the angle independence of the resonance features (see Fig. 9.5a). We explain the tilt of the two lowest resonance lines in region (I) with the lower defect states primarily probing the bottom of the guiding potential (also present for the eigenstate analysis) and thus experience a slight energy shift depending on α . Without demand for completeness we point out that width, shape and intensity of the eigenstate

resonances depend on their particular single particle spacing, real space localization and symmetry properties.

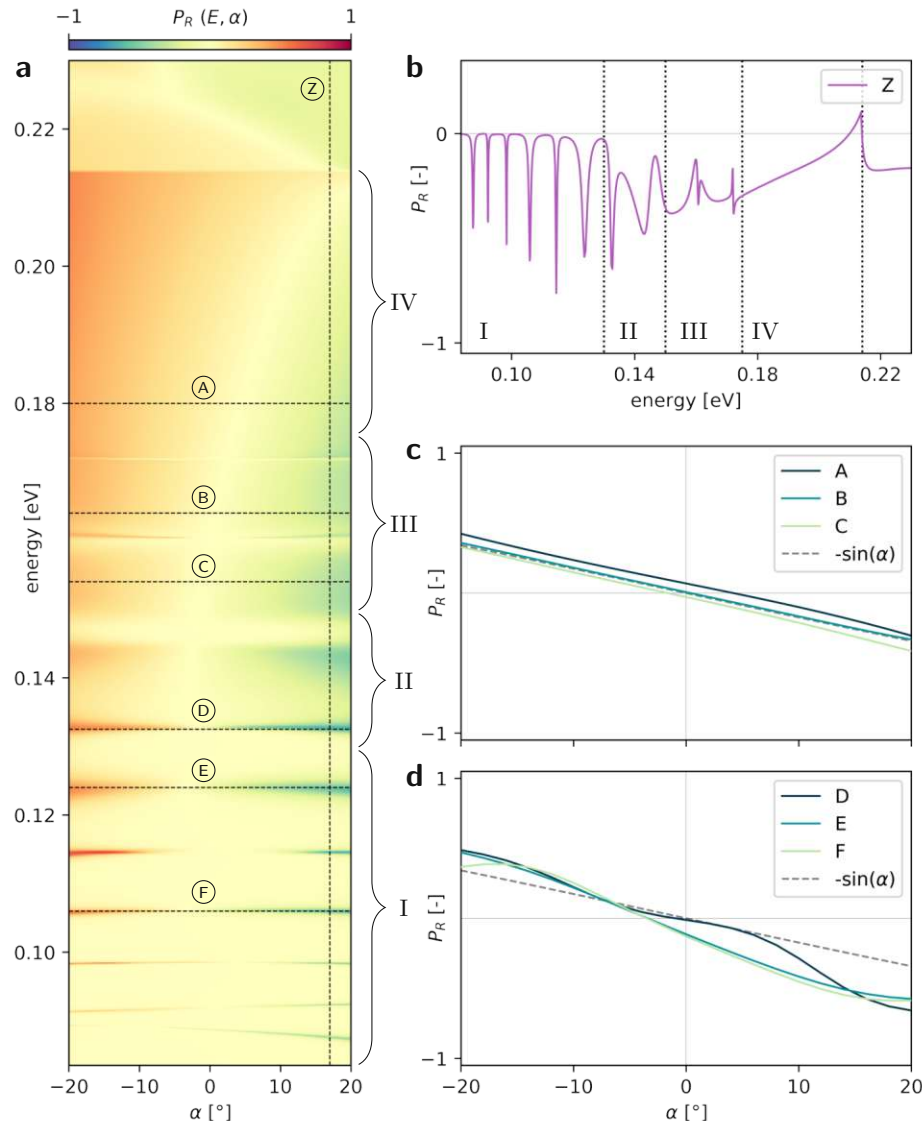


Fig. 9.7: **a** Reflected valley polarization $P_R(E, \alpha)$ Eq. (9.10) for the 5-8-5 linedefect geometry presented in Fig. 9.2. Curly brackets indicate energy regions I-IV referred to in the discussion. Dashed lines indicate coordinates of cuts presented in panels **b-d**. **b** Constant angle cut of panel **a** ($\alpha = 17^\circ$). Dotted, vertical lines separate qualitatively different behaviour (I ... isolated peaks, II ... emerging background, III ... pronounced background with sharp “Fano-like” resonances, IV ... monotonic decline before mode opening). **c** Constant energy cuts of panel **a** (A...0.18eV, B...0.163eV, C...0.154eV). Grey, dashed line plots $\sin \alpha$ for visual comparison. **d** Constant energy cuts of panel **a** (D...0.18eV, E...0.163eV, F...0.154eV). Grey, dashed line plots $\sin \alpha$ for visual comparison.

9.5 Conclusion

We have extended the simple symmetry analysis of [15] to realistic transport calculations with an ab-initio derived 10NN TB parametrization for the 5-8-5 line defect. While we could not validate the simple angle dependence of Eq. (9.7) our calculations yield a much richer valley polarization landscape with sophisticated energy dependence. Nevertheless the valley filtering properties of this grain boundary survive the extension from 1NN TB to TB models accounting for long range interactions and seem to rely on resonances with bound defect levels.

In a next step we will try to produce a similar analysis of the second (rotated) grain boundary (see Fig. 9.1) to verify if the observed behavior is reproducible. The relative rotation of the two leads makes disentanglement of effects due to the curving geometry from boundary induced polarization tricky. We will then also focus on the resonant behaviour of the valley filtering aspect since some of the resonance peaks appear to differ in character. It might also be worthwhile to study a non mirror-symmetric line defect since this symmetry is the underlying argument of [15].

Chapter 10

Mapping quantum Hall edge states in graphene

“Man prefers to believe what he prefers to be true.”

Francis Bacon

This chapter reports on a collaboration with the group of M. Morgenstern at the RWTH Aachen and focuses on the experimental measurements and Poisson calculations done by Tjorven Johnson (RWTH) as well as large scale TB calculations on my part. In this joint project we study quantum Hall edge states in single layer graphene. Experimentally created with a partially covering back gate they are the paradigmatic example of the bulk-boundary correspondence. These states are typically prone to elaborate reconstructions and thus call for detailed investigation via scanning tunneling microscopy (STM). We probe a gated p-n interface in graphene at magnetic fields up to 7T. The Landau levels bend across the interface, exhibit plateaus at the Fermi level, feature multiple charging lines as fingerprints of the tip-induced quantum dot (QDOT) and show a branching of higher Landau levels close to the interface. By comparison with tight-binding calculations, we disentangle the contributions of the edge states and the quantum dot. The comparison reveals, that, depending on gate voltage, the branching can either be caused by the orbital structure of the edge states or by the development of confined states in the quantum dot across the junction. This marks a vital step for understanding intrinsic edge state properties with the unprecedented spatial resolution of scanning tunneling microscopy.

10.1 Introduction

In the classification of topological insulators the so called *bulk-boundary correspondence* principle relates the bulk related Chern number of a material to Hall-current-carrying edge states [346–348]. Investigations into the spacial structuring of these edge modes into compressible/incompressible strips [349, 350] due to Coulomb interactions as well as more complicated reconstructions (e.g. *neutral upstream modes* at filling factor $\nu = 1$, [351–353]) has advanced their understanding in recent years even into the fractional quantum Hall regime [354–357]. Despite impressive predictions and indirect experimental evidence for some of them (e.g. neutral upstream modes via shot noise measurements [358, 359]) detailed experimental, spacial analysis of the internal structure of quantum Hall (QH) edge states has remained elusive.

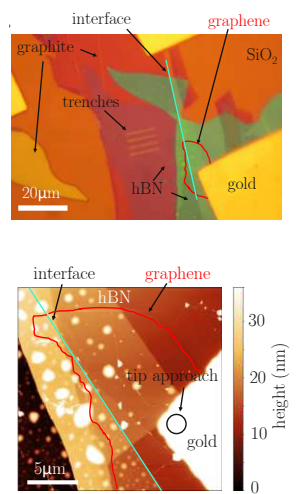


Fig. 10.1: (top) Optical image of the finalized sample with different areas marked. The graphene area is encircled (red line) as determined by atomic force microscopy (AFM). The graphene has been ruptured during the transfer, such that the trenches within the graphite are not used. The studied lateral interface is marked (blue line) separating the graphite gate area on the left and an area without graphite gate on the right. (bottom) AFM image acquired in tapping mode at ambient conditions, Si-cantilever, $f_{\text{res}} = 325$ kHz. The rim of the contacted graphene flake is marked by a red line. The circle indicates the intended landing position of the STM tip.

To the best of our knowledge, all previous studies employing single electron transistors [360], electrostatic force microscopy [361–363], scanning gate microscopy [364–366], scanning capacitance microscopy [367], microwave impedance microscopy [368] and scanning superconducting quantum interference device (SQUID) microscopy [369] could not resolve internal edge state structures due to being limited to spacial resolutions well above the magnetic length. Unfortunately previous STM measurements also could not resolve edge states at graphene boundaries due to a heavily screening graphite substrate [370]. During the final preparation of this project, we became aware of measurements attempting to probe quantum Hall edge states at the physical edge of graphene on hBN/SiO₂/Si. They did not find signatures of edge states, likely due to a too strong edge potential [371].

Our work applies scanning tunneling microscopy to an interface between different filling factors in single layer graphene at perpendicular magnetic fields of 7 T [372]. The key challenge in such a setup is the formation of a quantum dot underneath the tip tip-induced quantum dot (TIQD) [14, 191, 373] which can locally disturb the edge state structure and thus obscure the measurements. We infer size and depth of this TIQD from charging lines in the experimental data and model their dependence on gate voltage and tip position via Poisson simulations. We then quantitatively account for these effects in large-scale tight binding (TB) calculations that allow for comparison of the local density of states (below the tip) with experimental maps of dI/dV_{sample} as a function of V_{gate} , x_{sample} and V_{sample} . This analysis reveals parameter regimes in which the perturbation of the edge states (due to the TIQD) is negligible thus allowing cartography of edge states with much improved spacial resolution.

10.2 Experimental Observations

The graphene sample is prepared via dry stacking (3 nm graphite, 23 nm hBN, exfoliated monolayer graphene, Si/SiO₂, see Fig. 10.2c). We create a tunable potential step by only partially covering the graphite back gate (see Fig. 10.1). Both graphite and graphene are contacted via gold electrodes (shadow mask evaporation). We apply an additional voltage V_{sample} (against ground) to the graphene in order to record the tunneling current I (Fig. 10.2c). Our main observable is dI/dV_{sample} (proportional to the LDOS at $E - E_F = eV_{\text{sample}}$). Additional derivation with respect to V_{gate} , i.e. $d^2I/(dV_{\text{sample}}dV_{\text{gate}})$, can improve visibility for some features.

Setting the STM tip above the graphite back gate (far from the interface) the $dI/dV_{\text{sample}}(V_{\text{gate}}, V_{\text{sample}})$ shows the Landau levels LL n ($n \in \mathbb{Z}$) as bright, stepped LDOS lines (due to pinning to E_F , [374–376]), see Fig. 10.2. Appropriate LL indices n can be ascertained by the sequence of energy spacings. At negative V_{gate} (hole doping) pinning plateaus remain close to E_F while LL0 and positive LL features appear pinned at slightly positive V_{sample} . We can therefore assume that the measured features do not correspond to intrinsic LLs but are in fact perturbed by the TIQD [373]. The localized states within a quantum dot in a magnetic field can broadly be classified

via radial n_r and angular quantum numbers m (we will discuss this in more detail in Section 10.4).

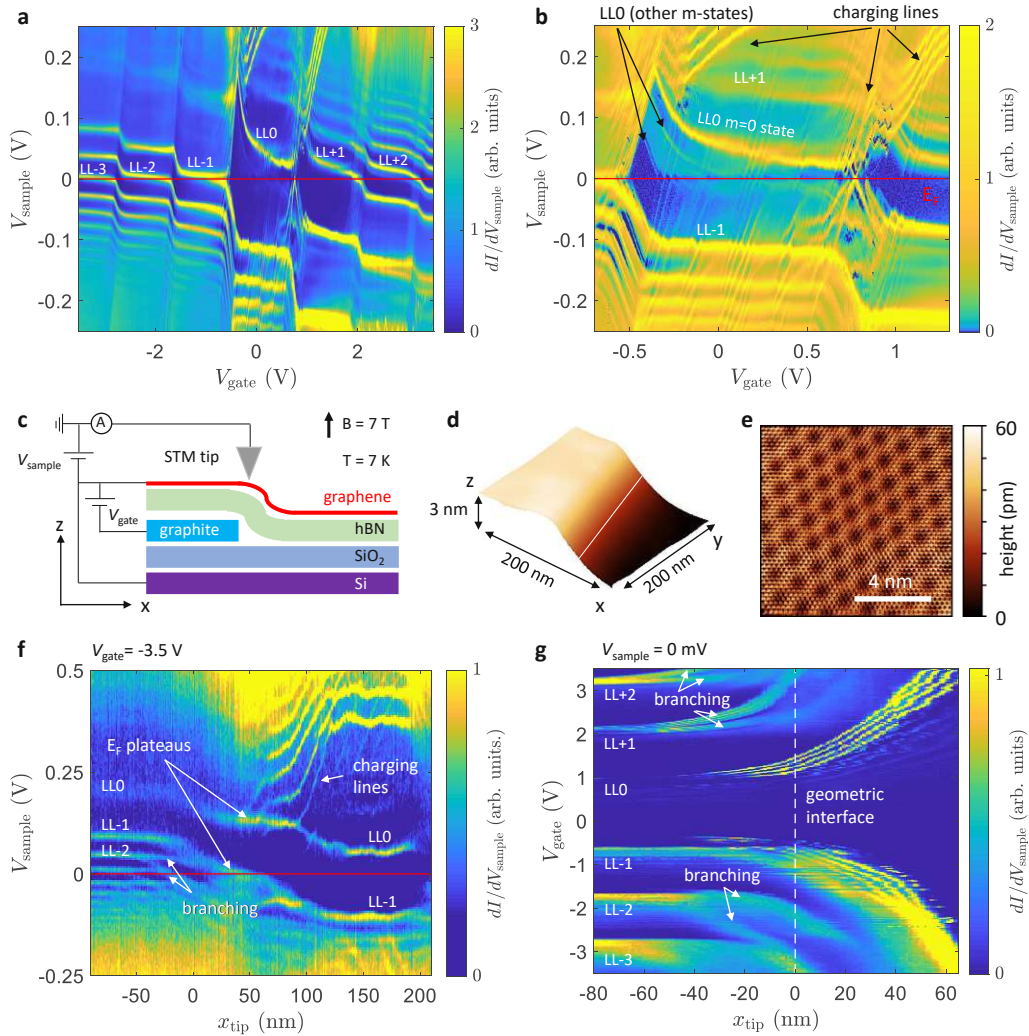


Fig. 10.2: **a** $dI/dV_{\text{sample}}(V_{\text{gate}}, V_{\text{sample}})$ on a graphene area far away from the lateral interface. Landau level features $\text{LL}n$ are marked. The tip-sample distance is stabilized at current $I_{\text{stab}} = 1$ nA and voltage $V_{\text{stab}} = -250$ mV. **b** Zoom into the area where the LL₀ lines cross E_F ($V_{\text{sample}} = 0$ V). The marked bright line above E_F corresponds to the ($m = 0$)-orbital of LL₀ confined in the TIQD. The replica of this line at lower V_{sample} are other confined m -states of LL₀. Charging lines run from the lower left to the upper right. The ones that cross an m -state at E_F are caused by the charging of exactly this m -state. Quadruplets of charging lines showcase the spin and valley degeneracy of graphene. **c** Sample layout with circuitry, graphite thickness: 3 nm, hBN: 23 nm, SiO₂: 300 nm. The graphite is used to partially gate the graphene. **d** STM topography of graphene with a step marking the onset of the underlying graphite defined as $x_{\text{tip}} = 0$ nm (white line), $I = 200$ pA, $V_{\text{sample}} = -500$ mV. **e** STM topography of graphene with atomic resolution and moiré lattice due to a mutual rotation of the graphene and the underlying hBN by 11.1° , $I = 1$ nA, $V_{\text{sample}} = -250$ mV, $V_{\text{gate}} = 3.5$ V. **f** $dI/dV_{\text{sample}}(x_{\text{tip}}, V_{\text{sample}})$ across the lateral interface, $I_{\text{stab}} = 200$ pA, $V_{\text{stab}} = -500$ mV, $V_{\text{gate}} = 3.5$ V. **g** $dI/dV_{\text{sample}}(x_{\text{tip}}, V_{\text{gate}})$ across the lateral interface, $I_{\text{stab}} = 1$ nA, $V_{\text{stab}} = -250$ mV, $V_{\text{sample}} = 0$ V.

The brightest lines in Fig. 10.2b thus correspond to ($m = 0$)-states (due to their antinode in the center of the TIQD) and parallel, fainter dI/dV_{sample} lines correspond to ($|m| > 0$)-states with larger confinement energy [203]. Since the ($|m| > 0$)-states appear at lower V_{sample} relative to the ($m = 0$)-states our TIQD has hole character. The displacement of the pinning plateaus relative to E_F indicates the depth of the TIQD for varying V_{gate} (i.e. the dot is very shallow at negative V_{gate}).

Additional lines with opposite incline (due to V_{gate} and V_{sample} compensating) in Fig. 10.2a,b are charging lines [377] caused by abrupt changes in current due to the Coulomb repulsion of each additional electron added to the TIQD [191]. Charging lines can cause kinks in the plateaus of LL0 and LL-1 (see Fig. E.1 in Chapter E). The charging lines located at the right end of plateaus at E_F appear strongest (see Fig. E.2 in Appendix Chapter E) thus again corroborating the hole-like character of the TIQD (($m = 0$)-states are filled first and have the highest impact due to their central antinode). Increasingly negative V_{gate} removes more electrons (i.e. charges holes into the TIQD). The increased lateral distance of these states relative to the tip center induce less change in the LDOS beneath the tip and thus appear as fainter features.

The sample geometry (see Fig. 10.2c) with its partially covering graphite back gate creates a lateral interface of different filling factors the position of which can be readily determined by height measurements via STM (see Fig. 10.2d). We do not study moiré physics as graphene and hBN are strongly rotated in our sample ($\approx 11.1^\circ$, see Fig. 10.2e, [191]).

We can inspect the evolution of LL energies by traversing the STM across the interface (changing x_{tip}) while also varying V_{sample} (Fig. 10.2f) or V_{gate} (Fig. 10.2g). At e.g. $V_{\text{gate}} = -3.5\text{V}$ the difference in filling left (E_F between LL-3 and LL-4) and right (E_F between LL0 and LL-1) of the interface (henceforth located at $x_{\text{tip}} = 0$) is readily visible in Fig. 10.2f. While occupied states (LL-1 close to $x_{\text{tip}} = 0$) display plateaus pinning close to E_F the unoccupied LL0 state appears pinned slightly shifted, indicating the influence of the TIQD on the position of the compressible stripes [349]. The flatness of the potential around the interface (compressible stripes) being surrounded by steeper sections (incompressible stripes) is also reflected in the evolution of charging lines with x_{tip} (labeled “charging lines” in Fig. 10.2f). Most strikingly we find an unexpected “branching” of LL-2 and LL-1 at $x_{\text{tip}} \in [-50, 0] \text{ nm}$ which we analyze in more detail below.

Considering the evolution of dI/dV_{sample} at E_F (i.e. $V_{\text{sample}} = 0$) across the interface for different heights of the potential step (i.e. varying V_{gate} (Fig. 10.2g)) we observe — as expected — strong influence on the left side ($x_{\text{tip}} < 0$) with many LLs shifting across E_F . However the back gate continues to influence LL n features up to $x_{\text{tip}} \approx 60\text{nm}$ with weakening extent. We again observe quadruplets of charging lines indicating the presence of a TIQD. Interestingly we again find prominent branching of the LL n states as they cross the interface. We will explain this branching with TB simulations including a realistic potential deduced from Poisson simulations in the following sections.

10.3 Rescaled TB model

We simulate a rectangular single layer graphene flake in terms of a 3rd nearest-neighbour TB model:

$$\mathcal{H} = \sum_i s_i \hat{c}_i^\dagger \hat{c}_i + \sum_{\langle i,j \rangle} \gamma_{ij} e^{2\pi i \Phi_{ij}} \hat{c}_i^\dagger \hat{c}_j. \quad (10.1)$$

where s_i is the on-site energy, γ_{ij} are hopping parameters and the magnetic field $\mathbf{B} = (0, 0, B_z)^T$ is included via a Peierls phase:

$$\Phi_{ij} = \frac{1}{\Phi_0} \int_{r_i}^{r_j} \mathbf{A} \cdot d\mathbf{r} \quad (10.2)$$

with magnetic flux quantum $\Phi_0 = h/e$ and vector potential in Landau gauge $\mathbf{A} = Bx\hat{y}$.

In order to make experimental sizes computationally accessible we employ a rescaled graphene Hamiltonian. Inversely scaling interatomic distances (increasing them by a factor 10) and Hamiltonian coupling elements (reducing them by a factor 10) allows us to study realistically sized quantum dots and quantum hall edge states without qualitatively altering their energy spectra [378]. This approach holds since we do not expect the physical lattice scale of graphene to be a necessary ingredient for the measured phenomena. Our model system thus consists of a rectangular graphene sheet 400nm × 220nm in size.

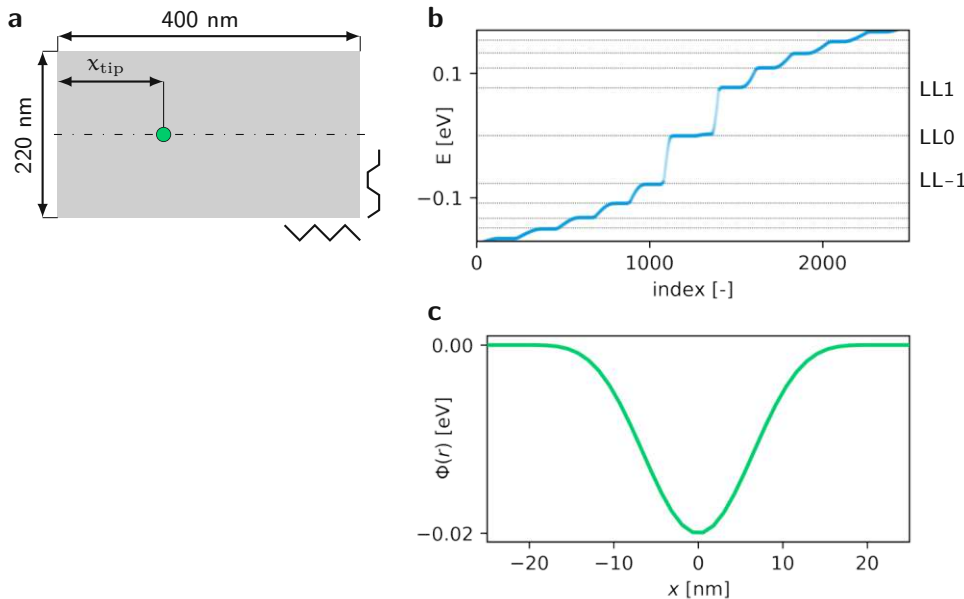


Fig. 10.3: **a** Top view of the simulated graphene sheet (scaled by a factor 10) with edge types and center position of the QDQT potential indicated. **b** Eigen-energies of the finite graphene sheet in **a** at a magnetic field of 7T. Horizontal grey lines indicate analytical Landau level energies (Eq. (5.1)). **c** Electrostatic potential imprinted on the graphene sheet by a hovering STM tip (resulting from a fit in [14, 180] and taken unaltered for shallow potentials).

10.4 Quantum dot states in single layer graphene (revisited)

Before we turn to the interplay of tip induced QDOT and quantum Hall edge stages we study localized QDOT states of this system in isolation. This initial analysis is somewhat similar to previous works [14, 180, 379] and somewhat extends the investigation in Chapter 5. At this stage we do not consider screening effects that would result in “wedding cake” like potential shapes [380] accompanied by regions of compressible and incompressible electron liquids [381]. These alterations will be introduced to the combined potential landscape of QDOT and back gate induced PN potential step as these potentials vary enough to pierce several Landau levels in energy.

To this extent we calculate roughly 2000 eigenstates in the graphene flake described in the paragraph above (see Fig. 10.3a) for a magnetic field of 7T with a tip induced potential identical to that in Chapter 5:

$$\Phi_{\text{tip}}^{(0)}(\mathbf{r}) = \begin{cases} -V_0 \cdot \cos\left(\frac{\pi}{2\alpha}|\mathbf{r}|\right)^5 & , |\mathbf{r}| < \alpha \\ 0 & , |\mathbf{r}| \geq \alpha \end{cases} \quad (10.3)$$

with α defined in Eq. (5.4) for a depth of $V_0 = 20\text{meV}$.

The resulting spectrum (see Fig. 10.3b) shows pronounced Landau quantization as well as a small number of geometry dependent eigenstates due to finite system size. We can also clearly identify localized quantum dot states which are energetically shifted by the tip potential. Inspecting some of these states closer (see Fig. 10.6) reveals their typical sub lattice structure Eq. (5.7) [23]. The orbital index j differs by one on the two sublattice components and when $j \equiv 0$, the other component “ $|j| - 1$ ” vanishes. In an attempt to extract radial ($n_r \in \mathbb{N}_0$) and angular quantum numbers ($m \in \mathbb{Z}$) we perform the following analysis: The number of radial nodes is easily determined visually by inspecting the radial density distributions plotted in Fig. 10.6. The angular quantum number is somewhat trickier to determine. We first have to account for the Bloch phase $e^{i\mathbf{k}\cdot\mathbf{r}}$ that the wave functions pick up depending on which valley ($\mathbf{K} = (4\pi/(3a), 0)$, $\mathbf{K}' = -\mathbf{K}$) they dwell in (since our confinement potential is smooth valley is still a good quantum number, see Appendix Chapter C). We can then select a slim annular region close to the radial maximum of each state, renormalize within this area and calculate overlap integrals $|\langle m' | \phi \rangle|^2$ with test functions of the form $\langle \mathbf{r} | m' \rangle = e^{im'\phi(\mathbf{r})}$ where ϕ is the azimuthal angle of an orbital site calculated with respect to the center of the QDOT potential and $m' \in [-10, 10]$. This overlap should become large only if the angular quantum number of the QDOT state m is equal to m' and thus effectively allows to determine m (see Fig. 10.6).

We find that possible adiabatic mappings between LL index N and the radial and angular quantum numbers (Eqs. (10.4) and (10.5), as formulated in [203] for spherical infinite mass boundary conditions and zig-zag boundary conditions of the continuum Dirac-Weyl Hamiltonian respectively) are not entirely applicable. There are some exceptions that fulfill neither of the two proposed mappings:

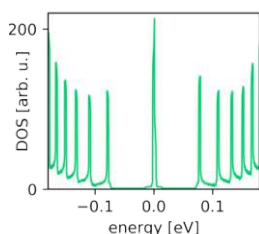


Fig. 10.4: Total density of states of the graphene flake pictured in Fig. 10.3 at $B = 7\text{T}$ for relevant energies.

$$N = n_r + \frac{m + |m|}{2} \quad (10.4)$$

$$N = n_r + \frac{m + |m|}{2} - \Theta(m) \quad (10.5)$$

It may appear that unambiguously determining the angular quantum number of a state only works for the lowest QDOT orbitals of each Landau levels but it is in fact the rescaling of our graphene system that is at fault for e.g. Fig. 10.6b due to amplifying the effects of trigonal warping and therefore undermining m as a good quantum number.

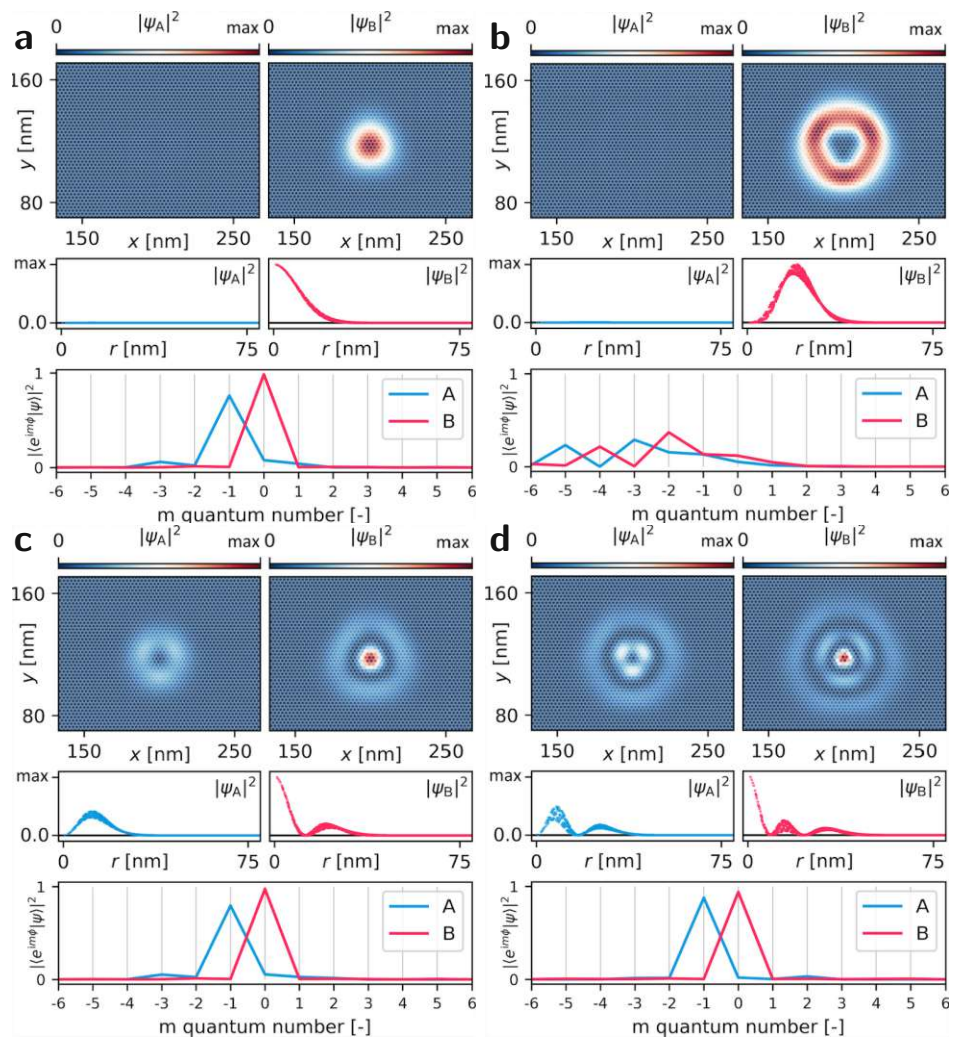


Fig. 10.6: In depth analysis of four QDOT states (**a** LL0 #0, **b** LL0 #4, **c** LL1 #2, **d** LL2 #4) including 2D color plots of sub lattice densities $|\psi_{A/B}|^2$, radial density distribution and overlap (within an annulus close to the density maximum) with azimuthal test functions of the form $|e^{im\phi}\rangle$ (top, center and bottom subplots for each panel **a**, **b**, **c**, **d**).

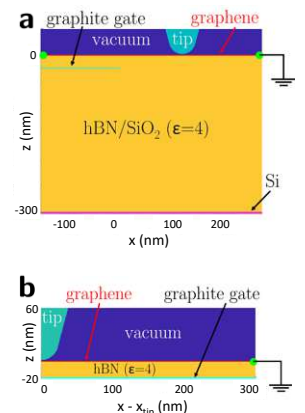


Fig. 10.5: **a** 2D Cartesian geometry as used for the Poisson simulations including the lateral interface. The potentials Φ_{tip} and Φ_{gate} are applied to the tip and the graphite gate, respectively. **b** Cylindrical geometry as used for simulations of the TIQD without lateral interface (i.e. the graphite gate covers the entire area).

10.5 Poisson calculations for the potential of TIQD and PN junction

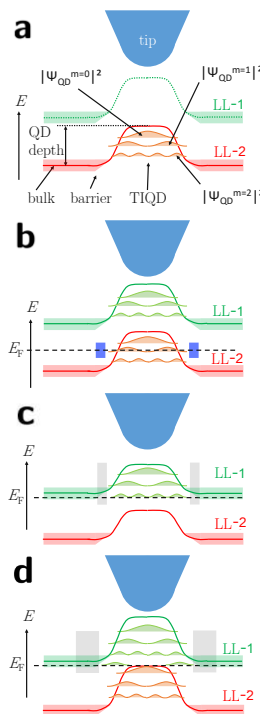


Fig. 10.7: **a** Band bending of two adjacent LL_n due to the TIQD potential. The probability density of the confined states of LL_2 are added at their confinement energy and labeled with its azimuthal quantum number m . **b** Same as (a) with added E_F line. The blue shaded areas mark the onset of the insulating surrounding. **c** E_F at the charging position of the last state from LL_1 . Tunnel barrier indicated in grey. **d** Sketch with two states at E_F enabling simultaneous charging of both LL.

In order to perform meaningful TB calculations for comparison with scanning tunneling spectroscopy (STS), we need the 2D potential profile on the graphene in the vicinity of the interface which consists of the potential step induced by the graphite gate and the TIQD. The exact shape of these potentials depends on both to the applied voltages V_{gate} between graphite gate and graphene as well as V_{sample} between the tip and graphene (Fig. 10.2c), their corresponding work function mismatches as well as the geometry of the two metallic electrodes and STM tip (see Fig. 10.5). Furthermore screening effects within graphene gapped density of states (DOS) in the magnetic field cause the potential steps to exhibit plateaus at potential values that correspond to LL energies (effective screening caused by high DOS).

We employ a “home-made” Poisson solver of the Morgenstern group at the RWTH Aachen to generate our potential landscape. This implementation is limited to 2D coordinate systems (we can only extract 1D line cuts of the resulting potential which we will reconcile later on when transferring the potential to the TB system) and disregards confinement effects and requires the DOS of graphene at 7 T (peaks at LL_n energies given by Eq. (10.6), [23]) as a fixed input parameter and accounts for finite temperature via Fermi-Dirac smearing.

$$E_{LLn} = v_F \cdot \text{sgn}(n) \sqrt{2\hbar e |B| |n|}, \quad n \in \mathbb{Z}, \quad (10.6)$$

The thickness of the hBN ($d_{\text{hBN}} = 23.5$ nm) is deduced from atomic force microscopy (AFM) images. Both, hBN and SiO_2 exhibit a dielectric constant $\epsilon = 4$. We choose a reasonable value $d_{\text{tip}} = 0.6$ nm for the distance between graphene and the tip apex since it barely influences the results [14, 191, 382]. The tip is assumed to be metallic with a shape consisting of a half sphere with radius r_{tip} located at the lower end of a cone with opening angle 30° .

In the Poisson simulations, the sample is grounded and the tip is set to a variable potential Φ_{tip} . The potential of the tip reads $\Phi_{\text{tip}} = e \cdot (-V_{\text{sample}} + \Delta V_{\text{sample}})$ with applied graphene voltage V_{sample} and ΔV_{sample} being the voltage required to achieve flat band conditions below the tip for $\Phi_{\text{gate}} = 0$ eV. We employ Gaussian broadened (FWHM of 7 meV) DOS of LL in graphene at a perpendicular magnetic field of 7 T.

Furthermore we will determine the other crucial input parameters of the Poisson simulation, ΔV_{sample} , ΔV_{gate} and r_{tip} , from experimental data by employing the observed charging lines. The tip radius r_{tip} correlates with the lateral size of the TIQD, i.e. with the distance of charging lines, whereas ΔV_{sample} and ΔV_{gate} affect the potential depth of the TIQD, i.e. the onset of charging lines for each LL_n . We employ a crossing of charging lines originating from different LL_n at negative V_{gate} (see Fig. 10.9a). The assignment of a charging line to a specific LL_n relies on its intersection with a LL_n LDOS feature at E_F ($V_{\text{sample}} = 0$ V). Therefore the charging lines on the left of Fig. 10.9a originate from LL_2 . They represent the first few holes of LL_2 that are added to the TIQD. Close to the crossing of this charging line with E_F , LL_2 of the surrounding graphene must be

completely occupied with electrons (Fig. 10.7b), since the filling factor of the surrounding graphene must always be larger than the filling factor of a hole-type TIQD. Either, E_F of the surrounding graphene is in the gap between LL-2 and LL-1 or it is at states of the rim of LL-2 that are known to be localized [383, 384]. Both situations provide an insulating barrier for the confined charge carriers in the TIQD, such that screening of the added charge is strongly suppressed. Thus a strong change of the DOS by charging the TIQD results in a bright charging line. The charging lines appearing on the right of Fig. 10.9a belong to the last holes from LL-1 that are charged into the TIQD. They exhibit a steeper slope since these states are, on average, located further away from the capacitive center of the tip. In the surrounding bulk, E_F must be located within LL-1, again since the filling factor of the bulk must be larger than the local filling factor of a hole-type TIQD (Fig. 10.7c). The crossing point of two charging lines from LL-3 and LL-2 implies that QD states from both LLs are at E_F simultaneously. This is naturally realized by a ring like charge distribution with occupied hole states including the first state from LL-3 in a central disk and occupied hole states only from LL-2 in an annulus around the disk (Fig. 10.7d).

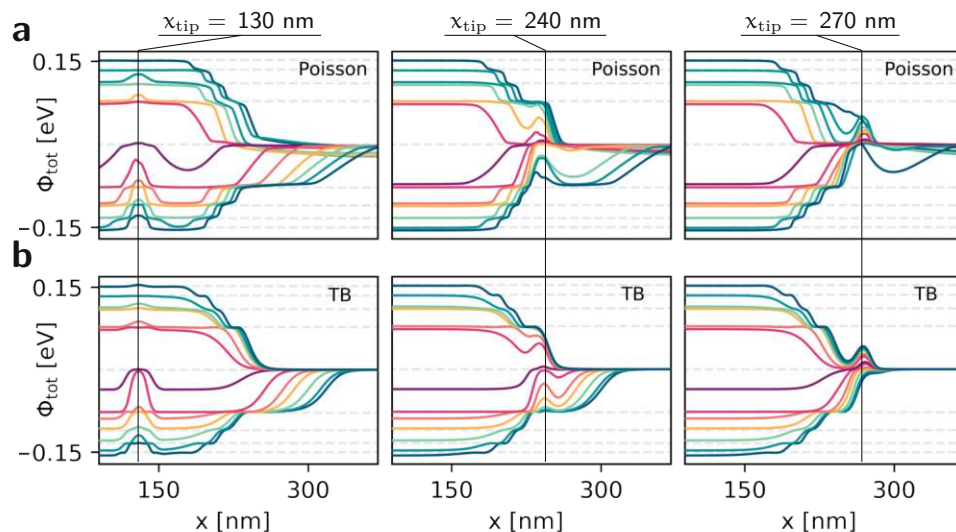


Fig. 10.8: **a** Potential calculated with a Poisson solver along a 1D trajectory (evaluated for varying x at fixed z_{graphene}) perpendicular to the PN junction for different values of V_{gate} (from -3V to $+3.5\text{V}$ in 0.5V increments). **b** 2D analytical potential (i.e. true function of x and y) given in Eq. (10.7) used for the TB system sketched in Fig. 10.3a evaluated along the center line in zig-zag direction for different values of η with fixed λ . Columns in both subplots correspond to different tip positions (as indicated by vertical black lines).

Such a configuration is not uncommon for quantum dots in B field and sometimes called a “wedding cake” [380]. At such a crossing point the QD depth approximately equals the known energy gap between LL-1 and LL-2 of 38.9 meV (Eq. (10.6)). Here, we ignore the finite energetic width of the bulk Landau levels since not being a dominant error. Furthermore we also observe a crossing of charging lines associated with LL-2 and LL-3 (see Fig. E.3 in Appendix Chapter E) resulting in an implied TIQD depth of 30.5 meV at this voltage configuration. These depths come from the Poisson simulations at varying Φ_{tip} and Φ_{gate} (see Fig. E.4a in Appendix Chapter E).

Subsequently, we find pairs of $(\Phi_{\text{gate}}, \Phi_{\text{tip}})$ that feature the two TIQD depths at the two crossing points (38.9 meV, 30.5 meV) and, at the same time, the energetic distances in Φ_{gate} and Φ_{tip} that are identical to the voltage distances between the two crossing points ($\delta V_{\text{gate}} = 0.95$ V, $\delta V_{\text{sample}} = 0.15$ V) (see Fig. E.4b in Appendix Chapter E). This analysis leaves us with two possible combinations for ΔV_{sample} and ΔV_{gate} out of which we choose the configuration that features better agreement between measured and calculated LDOS maps from the Poisson simulation (see Fig. E.5 in Appendix Chapter E) resulting in $\Delta V_{\text{gate}} = -200 \pm 50$ mV and $\Delta V_{\text{sample}} = -180 \pm 50$ mV. We deduce the remaining fit parameter r_{tip} from the distance of charging lines in the experiment: In the Poisson simulations, we determine the additional charge within the TIQD, ΔQ_{QD} , that is caused by a potential change $\Delta \Phi_{\text{tip}}$ in Φ_{tip} direction or $\Delta \Phi_{\text{gate}}$ in Φ_{gate} direction. Note that $e \Delta Q_{\text{QD}} / \Delta \Phi_{\text{gate}}$ is directly the capacitance of the TIQD with respect to the gate as often used for analyzing quantum dots in transport experiments [385]. The total charge Q_{QD} within the TIQD is calculated by spatially integrating the confined charge carrier density up to the edge of the TIQD. We compare $\Delta Q_{\text{QD}} / \Delta \Phi_{\text{gate}}$ and $\Delta Q_{\text{QD}} / \Delta \Phi_{\text{tip}}$ for various r_{tip} with the experimental number of charging lines per voltage. For this purpose, we select groups of charging lines with regular voltage distances implying only minor contributions from orbital energy, i.e., from the confinement energy neglected in the Poisson simulations. We determine their average distance and use the average of all such groups for $V_{\text{gate}} < 0$ V and $V_{\text{sample}} > 0$ V. Preselection of groups of regular charging lines deals with the fact that some of the charging lines might not be visible due to imperfect confinement at E_F or strong screening from the surrounding graphene. In a first step we estimate r_{tip} by adapting the ratio of $(\Delta Q_{\text{QD}} / \Delta \Phi_{\text{gate}}) / (\Delta Q_{\text{QD}} / \Delta \Phi_{\text{tip}})$ to the corresponding ratio observed in the experiment (slope of the charging lines) and then refine via the agreement of absolute values of $\Delta Q_{\text{QD}} / \Delta \Phi_{\text{gate}}$ and $\Delta Q_{\text{QD}} / \Delta \Phi_{\text{tip}}$ with the experimental ones. The parameter r_{tip} is varied until the absolute values fit favorably resulting in $r_{\text{tip}} = 25$ nm (see Fig. E.6 in Appendix Chapter E). We check for consistency by repeating the determination of ΔV_{sample} and ΔV_{gate} with the new value for r_{tip} but find that these two values barely depend on r_{tip} . We finally calculate the full potential profile across the PN interface for multiple configurations of tip position x_{tip} , V_{gate} and V_{sample} (see Fig. 10.8a).

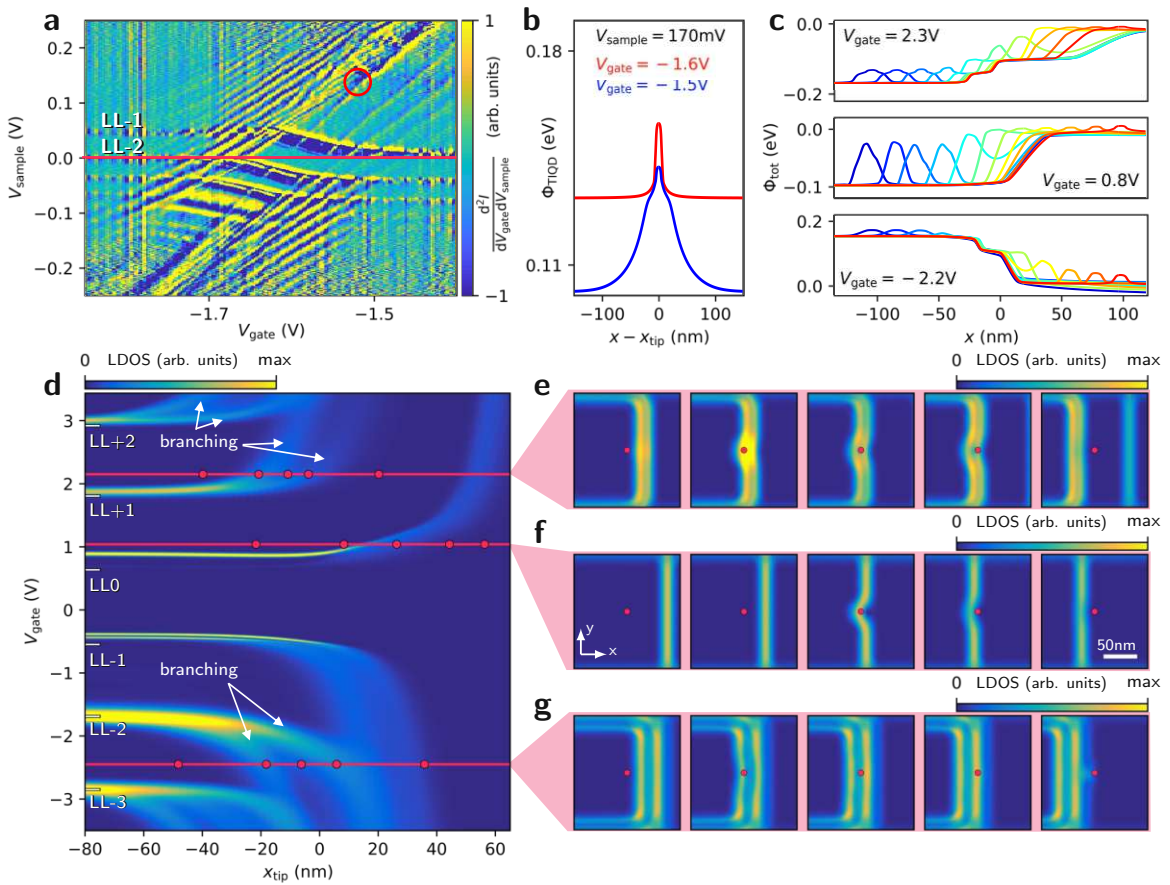


Fig. 10.9: **a** $d^2I/dV_{\text{sample}}dV_{\text{gate}}(V_{\text{gate}}, V_{\text{sample}})$ at the transition from LL-2 to LL-1 being located at E_F (red line), $I_{\text{stab}} = 1 \text{ nA}$, $V_{\text{stab}} = -250 \text{ mV}$. The crossing point of the first ($m = 0$)-charging line of LL-2 with the last charging line belonging to LL-1 is marked (red circle). Such crossings for various adjacent LL n are used to determine ΔV_{sample} and ΔV_{gate} as input parameters for the Poisson calculations. **b** Potential of the TIQD without lateral interface for the marked V_{sample} , V_{gate} as resulting from the Poisson simulations. **c** Profile line through the potential of superposed TIQD and lateral interface, $V_{\text{sample}} = 0 \text{ V}$, $x_{\text{tip}} \in [-130, +100] \text{ nm}$ with increments of 20 nm (blue to red), V_{gate} as marked. The potentials are used as input for the TB simulations. **d** LDOS($x_{\text{tip}}, V_{\text{gate}}$) at $V_{\text{sample}} = 0 \text{ V}$ as resulting from the TB simulations. The LDOS is averaged over a circular region (radius $\approx 1.5 \text{ nm}$) around the vector x_{tip} describing the position of the tip center. White horizontal lines on the left mark the bulk LL n . The marked branching of various LL n states around $x_{\text{tip}} = 0 \text{ nm}$ qualitatively matches the experimental ones (Fig. 10.2g). Red lines with red dots mark V_{gate} and x_{tip} , respectively, as used in e–g. **e** LDOS as a function of real space coordinates x, y , $V_{\text{gate}} = 2.15 \text{ V}$. The columns are for different x_{tip} marked by red dots (also in d). **f** Same as e, $V_{\text{gate}} = 1.05 \text{ V}$. **g** Same as e, $V_{\text{gate}} = -2.45 \text{ V}$.

10.6 From 1D Poisson to 2D Tight binding

Having converged the resulting potential landscape of both subsystems (TIQD Φ_{tip} and backgate induced PN junction Φ_{PN}) as well as their combination Φ_{tot} , we now need to transform this 1D potential data to be able to apply this on a 2D TB lattice. To this extent we parametrize the total potential,

$$\Phi_{\text{tot}}(\mathbf{r})^{(\text{TB})} = q \left(\lambda(\eta, x_{\text{tip}}) \Phi_{\text{tip}}^{(\text{TB})}(\mathbf{r}) + \eta \Phi_{\text{PN}}^{(\text{TB})}(\mathbf{r}) \right) \quad (10.7)$$

as a superposition of a spherical cosine well (similar to $\Phi_{\text{tip}}^{(0)}$ in Eq. (10.3)) and what is in essence a composition of Fermi functions \mathcal{F}^{01} that models the PN step. λ and η are physically immaterial parameters that control the magnitude of both potential components. $\mathbf{r} = (x, y)^T$ denotes the position vector within the graphene plane.

We also incorporate the flattened regions of the calculated potential surface, that arise from pronounced screening at energies close to Landau levels via a “quenching function”,

$$q(f) = f \left(1 - \sum_i a_i g(f, b_i, c_i) \right) \quad (10.8)$$

a_i [10^{-2}]	b_i [eV]	c_i [meV]
1.6	-0.43	17
1.8	-0.39	25
0.6	-0.34	52
1.2	-0.21	82
1.1	0	50
1.2	0.21	82
0.6	0.34	52
1.8	0.39	25
1.6	0.43	17

Tab. 10.1: Fit parameters used for the quenching function $q(f)$ defined in Eq. (10.8).

that locally modifies the potential values by subtracting Gaussians from the unperturbed weight factor of one. The $g(f, b_i, c_i)$ are Gaussians⁰² centered at b_i with standard deviation c_i evaluated at f weighted with prefactors a_i . f represents the unquenched potential function in units of eV. The a_i , b_i , c_i with $i \in [LL-4, \dots, LL+4]$ are fit parameters determining the slope and extent of the flat potential areas (compressible regions) for each LLn. To compare with the experimental data we account for ΔV_{sample} and ΔV_{gate} by adequate energy shifts. Unfortunately, in order to account for all the intricacies of the Poisson potential a combination of manually customizing shapes and least square fit routines results in somewhat convoluted⁰³ expressions for the 2D TB potential. The TIQD part that is fed into the quench function (in Eq. (10.7)) reads:

$$\Phi_{\text{tip}}^{(\text{TB})}(\mathbf{r}, \mathbf{R}_{\text{tip}}; \eta) = \begin{cases} \cos^5 \left(\frac{\pi}{2} \frac{|\mathbf{r} - \mathbf{R}_{\text{tip}}|}{31.95} \right), & |\mathbf{r} - \mathbf{R}_{\text{tip}}| < 31.95 \\ 0, & |\mathbf{r} - \mathbf{R}_{\text{tip}}| \geq 31.95 \end{cases} \quad (10.9)$$

⁰¹ $\mathcal{F}(x, \mu, \sigma) = \frac{1}{e^{(x-\mu)/\sigma} + 1}$

⁰² $g(x, \mu, \sigma) = \frac{1}{\sqrt{2\pi\sigma^2}} e^{-\frac{(x-\mu)^2}{2\sigma^2}}$

⁰³ I apologize in advance if at some point anyone has to try and comprehend all the following expressions in full detail.

weighted with prefactor

$$\lambda(\eta, x_{\text{tip}}) = -0.06 - \frac{0.0005 \mathcal{F}(x_{\text{tip}}, 2200, 30)}{(\eta + 0.19)^2 + 0.005} + \left(0.06 - 0.08(\eta + 0.42)\right) \times \\ \left(1 - \mathcal{F}(x_{\text{tip}}, 2700, 20)\right) \mathcal{F}\left(\eta, 0.2 + \left(\frac{x_{\text{tip}} - 1300}{180}\right)^8, 0.01\right) \quad (10.10)$$

For the PN step we end up with a potential expression of the form:

$$\Phi_{\text{PN}}^{(\text{TB})}(x) = \mathcal{F}(x, 2216, 14) + \Theta(-\eta) \max(-0.13, \eta) \times \\ \mathcal{F}\left(x, 2216 - 2300\eta \mathcal{F}(x_{\text{tip}}, 2700, 20), 14\right) \mathcal{F}(-x, -2216, 14) \quad (10.11)$$

These expressions demand length and position parameters in units of Å. The resulting potential manages to account for all of the relevant features generated by the Poisson solution. Variations in TIQD depth and effective radius with respect to the height of the PN step (generated by the interplay of tip and back gate voltage) are well accounted for in the fitted potential surface. Flattening of the potential near Landau level energies also resembles the Poisson calculation to a high degree and results in staircase-like PN transition and wedding-cake shaped TIQD potentials. The pronounced shift of the lowest of the PN steps for negative η (positive V_{gate}) from $x = 220\text{nm}$ towards larger x -coordinates is also incorporated. Traversing the STM tip coordinates in this system effectively transitions between a circular TIQD well (with varying shape depending on V_{gate}) left of the PN junction, an elongated and somewhat skewed intermediate TIQD on top of the PN transition to an again circular TIQD on the right of the interface with a depth and shape that is almost independent of V_{gate} (see Fig. 10.10). A quantitative comparison of Poisson and TB potentials for three example configurations in Fig. D.19 in Appendix Chapter D reveals deviations in the few meV regime that we regard as irrelevant considering the uncertainties of the Poisson simulations such as the negligence of confinement effects and the assumption of a circular symmetric STM tip.

10.7 Understanding STM measurements via LDOS maps

We aim to understand the dI/dV_{sample} measurements in terms of LDOS calculations built from single particle states. We thus calculate roughly 250 eigenstates around E_F for varying configurations of V_{gate} and x_{tip} and then build up a local density of states with spectral width of about 3meV to capture temperature broadening of the experiment (measurements are done at 6K, [382]). This LDOS which parametrically depends on both the height

and form of the potential step induced by the partially covering back gate (both controlled via η in TB calculations) as well as the position of the tip induced quantum well, is then summed over a circular region ($r \approx 1.5\text{nm}$) around the tip position \mathbf{R}_{tip} .

The resulting parametric LDOS map displays features very similar to the experimental data (see Fig. 10.11a). A regularly spaced pattern of horizontal lines that can be assigned to individual LLs (any irregularities in spacing are due to varying TIQD depth with respect to V_{gate}) seemingly starts bending and splitting when the STM tip reaches the slope of the PN junction. Crucially, the branching features of the various LL_n states are correctly reproduced while $\text{LL}0$ does not exhibit any branching. The bending is obviously just a consequence of the effective decoupling of STM tip and back gate (i.e. the tip moves into the region of graphene that is no longer covered by the back gate). In other words, the Landau level gap 0/-1 (encountered at $V_{\text{gate}} = 0$ in the left half of Fig. 10.11a) is effectively stretched to fill the entire vertical range at the right end of Fig. 10.11a. The favourable agreement calls for a detailed study of the complete $\text{LDOS}(x, y)$ map at various x_{tip} as is easily accessible via the TB calculations.

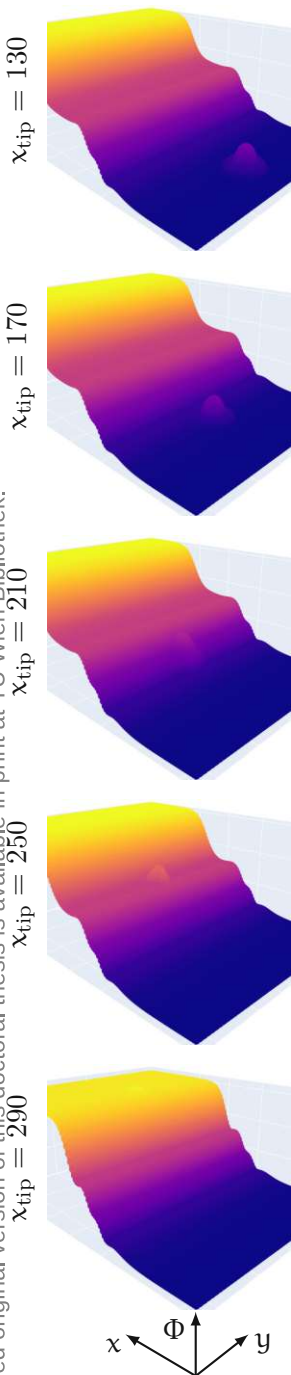


Fig. 10.10: Array of 3D surface plots of Φ_{tot} for varying x_{tip} (indicated in nm) and fixed $\eta = -0.4$.

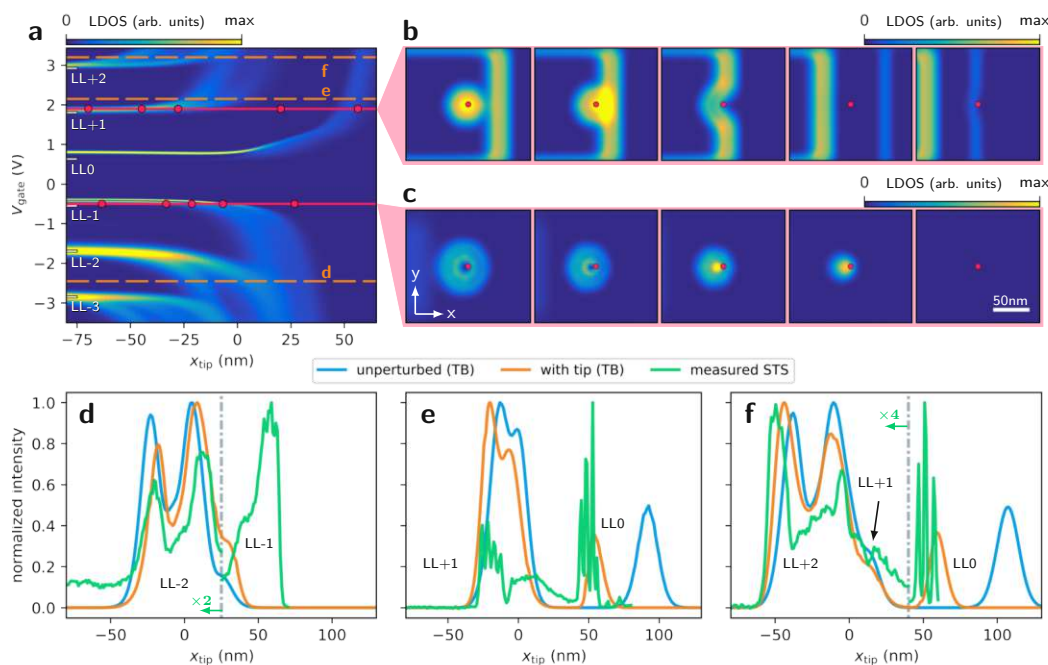


Fig. 10.11: **a** Same data set as in Fig. 10.9d with different red lines and dots according to b–c and additional dashed orange lines indicating V_{gate} of the line profiles in d–f. **b, c** LDOS(x, y) as marked in a and x_{tip} marked by the red dot in each panel as well as in a. **d–f** Profile lines along the dashed lines in a (orange), across the calculated LDOS at the same V_{gate} , but without the TIQD (blue) and across the experimental data of Fig. 10.2 at the same V_{gate} (green). The experimental profiles have been horizontally shifted by +5 nm (d), +20 nm (e), +10 nm (f) to ease the comparison. Additional intensity adjustments as marked are used to compensate for the strong charging lines that are not included in the simulation. The peak fine structure is a fingerprint of the charging lines (compare Fig. 10.2g).

The calculations reveal that the branching⁰⁴ is a consequence of the internal structure of the edge state wave functions at the interface (see Fig. 10.9e-g). The STM tip strides across quantum hall edge states and encounters a sequence of density dips and peaks. The number of these branching lines depends on the momentary filling set by V_{gate} . For example, the edge state belonging to LL-2 (Fig. 10.9g) exhibits two antinodes that result in two arms of a branching LL-2 state (Fig. 10.9d). By contrast, the edge state of LL0 with a single antinode (Fig. 10.9f) does not show branching in the probed LDOS (Fig. 10.9d).

The precise shape of the bending branches in Fig. 10.9d is characteristic for the size and depth of the TIQD at the respective tip and back gate voltages. However, a local displacement of the edge state by the TIQD (apparent in Fig. 10.9e-g) only shifts the lateral position of the edge state center with minor influence on its internal structure (i.e. a pronounced quantum well will noticeably deform the otherwise straight edge states and encounter the density maxima at smaller x_{tip} coordinates). Fig. 10.11b-c confirms that the intense horizontal LDOS lines observed to the far left of the lateral interface (Fig. 10.11a) are caused by states of the TIQD. These states are shifted in energy across the interface and, hence, can disappear from the probed energy window. Thus, only the weaker LDOS features across the interface contain the desired edge state information.

To elucidate the remaining influence of the TIQD, we also compare the calculated cross-section of the LDOS related to the edge states (blue lines in Fig. 10.11d-f) to the measured $dI/dV_{\text{sample}}(x_{\text{tip}})$ (green lines in Fig. 10.11d-f) and to the simulated $dI/dV_{\text{sample}}(x_{\text{tip}})$ including the TIQD (orange lines in Fig. 10.11d-f). Favorably, the twofold antinodal structure of LL-2 (Fig. 10.11d) and LL+2 (Fig. 10.11f) appears very similarly in all three curves (i.e. peak distances and relative intensities are alike). This good agreement for LL-2 can be traced back to the fact that the TIQD is absent at the interface region (Fig. 10.9c, lower frame, $-20 \text{ nm} < x_{\text{tip}} < 20 \text{ nm}$). Analyzing the distance of antinodes Δx in more detail (see Fig. 10.13) reveals $\Delta x = 31 \pm 1 \text{ nm}$ in the experiment largely independent of V_{gate} . In the TB calculations with TIQD, we find $\Delta x = 23 \pm 2 \text{ nm}$ slightly decreasing with increasing V_{gate} . Generally the experimental distance of antinodes is larger by $\sim 25\%$. Slightly larger distances in the experiment are also observed for LL+1 (Fig. 10.11e), with values largely independent from V_{gate} in experiment ($\Delta x = 25 \pm 2 \text{ nm}$) and simulations ($\Delta x = 15 \pm 1 \text{ nm}$) (Fig. 10.13a,b), and for LL+2 (Fig. 10.11f). A straightforward explanation would be that this increase in distance is caused by electron-electron repulsion that causes mixing with higher LLs.

⁰⁴ In the TB calculations we also see another form of splitting (albeit a smaller one) for some Landau levels (e.g. LL-1) at the far left of the transition region (see Fig. D.10 in Appendix Chapter D). This occurs whenever a pronounced quantum well enables resolving individual QDOT levels. As the QDOT then tilts as it traverses the PN junction the sensing STM tip then passes through radial maxima of the QDOT states before the loss of spherical symmetry and decrease in QDOT depth results in a mixing and finally fading of the feature in $(V_{\text{gate}}, x_{\text{sample}})$ space. Unfortunately both the absence of charging energies in the TB formalism as well as the resolution of the experimental data does not allow for meaningful comparison of this theoretical observation.

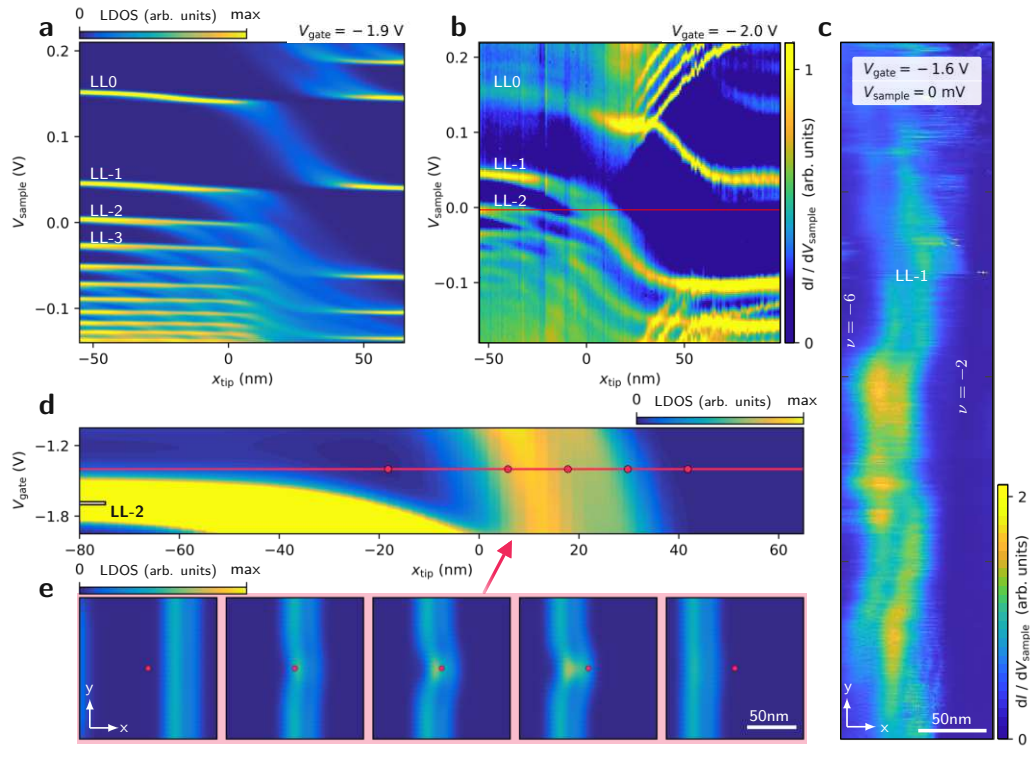


Fig. 10.12: **a** Simulated LDOS(x_{tip} , V_{sample}) across the lateral interface, while including the TIQD, $V_{\text{gate}} = -1.9$ V. **b** Measured $dI/dV_{\text{sample}}(x_{\text{tip}}, V_{\text{sample}})$, $V_{\text{gate}} = -2.0$ V, $I_{\text{stab}} = 200$ pA, $V_{\text{stab}} = -250$ mV. **c** $dI/dV_{\text{sample}}(x_{\text{tip}})$ along the lateral interface (y direction) featuring the LL-1 edge state at E_F , $V_{\text{gate}} = -1.6$ V, $V_{\text{sample}} = 0$ V, $I_{\text{stab}} = 1$ nA, $V_{\text{stab}} = -250$ mV. Filling factors ν are marked on both sides of the interface. **d** Zoom into Fig. 10.11a (simulated LDOS, $V_{\text{sample}} = 0$ V) at larger contrast to visualize the internal structure of the LL-1 edge state. **e** Simulated LDOS(x, y) across the interface for various x_{tip} marked by red dots (also in d), $V_{\text{gate}} = -1.4$ V (red line in d).

Tab. 10.2: Average Δx values from experimental data (STM) and TB simulations (LDOS) of selected edge states. See Fig. 10.13 for individual data points.

We also verify our results in an effective 1D system of unscaled graphene and calculate Landau level wave functions of an 80 nm long graphene slice in the presence of a magnetic field, a constant potential gradient (i.e. a linear potential in y -direction) as well as periodic boundary conditions in x -direction. This model finds $\Delta x = 25$ nm. The slope of the potential (0.8 meV/nm) is chosen in between the slopes observed on the plateaus at the interface within the Poisson simulations (0.1 – 0.2 meV/nm) and the average slope found across the lateral interface (1.5 – 3 meV/nm). The additionally displayed two sublattice contributions (Fig. 10.14) reveal the well-known one- and two-fold antinodal structure for LL+1 as well as the two- and three-fold antinodal structure for LL-2, representing the chiral symmetry of graphene in analogy to the quantum dot solutions of Fig. 10.6. However, remarkably, the resulting peaks are different in height showing that the wave functions are not pure Landau gauge solutions, but the solutions are mixed LL wave functions due to the influence of the potential slope. The simplified model nicely reproduces peak distances and relative peak heights of the more complex tight binding simulations that include the detailed potential of the Poisson solver (blue lines in Fig. 10.14c,d) as well as the ones that

additionally consider the TIQD (orange lines in Fig. 10.14c,d). They also reproduce the trend of different peak heights as found in the experiment. We checked with the 1D tight binding model that potential slopes up to 3 meV/nm do not change the inter-peak distance by more than 1.5 nm and, thus, cannot explain the observed larger distances in the experiment.

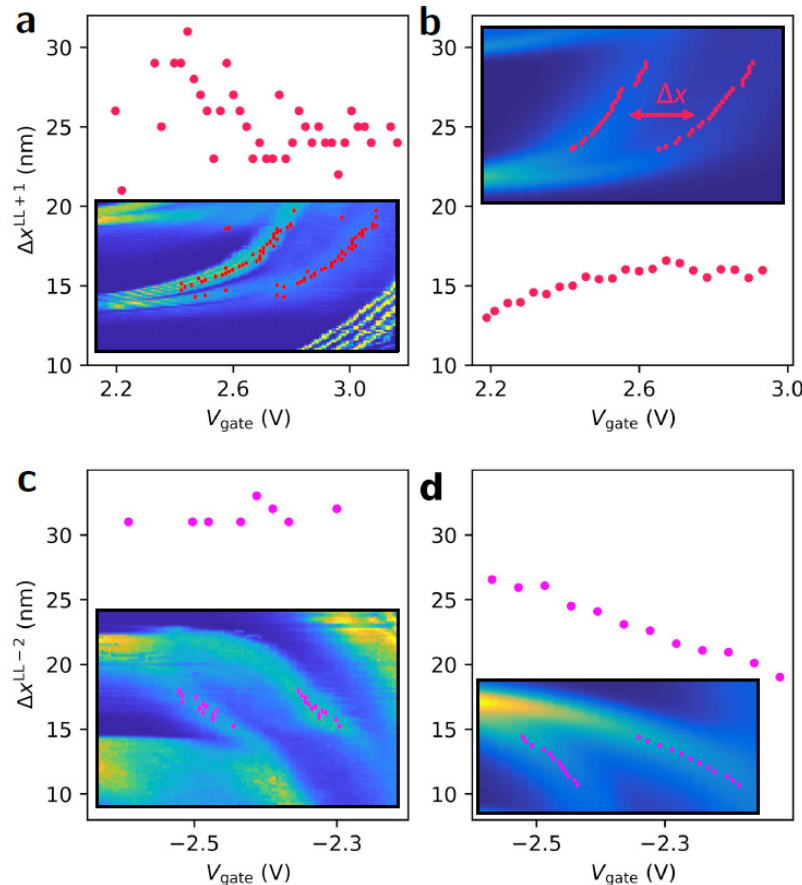


Fig. 10.13: Branching distances Δx as deduced from $dI/dV_{\text{sample}}(x_{\text{tip}}, V_{\text{gate}})$ of Fig. 10.2g, and LDOS($x_{\text{tip}}, V_{\text{gate}}$) of Fig. 10.9d. **a** Experimental branching distance of LL+1. **b** Simulated branching distance of LL+1. **c** Experimental branching distance of LL-2. **d** Simulated branching distance of LL-2. Insets show the parts of the images in Figs. 10.2 and 10.9 that are used to determine Δx with dots that mark the observed maxima in $dI/dV(x_{\text{tip}})$ lines, respectively LDOS(x_{tip}) lines. These maxima are used for distance determination indicated in b.

Discrepancies in relative intensities of anti-nodal peaks become, however, significant, if charging lines interfere (LL0 in Fig. 10.11e,f). While the peak distances in Fig. 10.11e still match reasonably well between green and orange lines, their relative peak intensities do not. More severely, the distances between the edge state peaks of LL+1 (LL+2) and LL0 (Fig. 10.11e (f)) are considerably reduced by the presence of the TIQD (blue vs. orange lines). This relates to a shift of the rightmost incompressible stripe towards the left by the superposed TIQD potential (Fig. 10.9c, upper frame). Nevertheless, the simulated shift of LL0 by the TIQD (orange) is in quantitative agreement with the experiment (green). The fact that the LL-1 feature in Fig. 10.11d strongly deviates from the simulated peak in terms of position and intensity

is likely related to the interfering charging lines (Fig. 10.2g) of a relatively shallow TIQD (Fig. 10.9c, lower frame, $x_{\text{tip}} > 40 \text{ nm}$). In such a shallow TIQD, individual charging events can strongly change the TIQD potential, an effect not captured by the simulations. Thus, imaging of the edge states works best if no charging lines are observed in the corresponding parameter regime and the TIQD is absent in the region of the lateral interface.

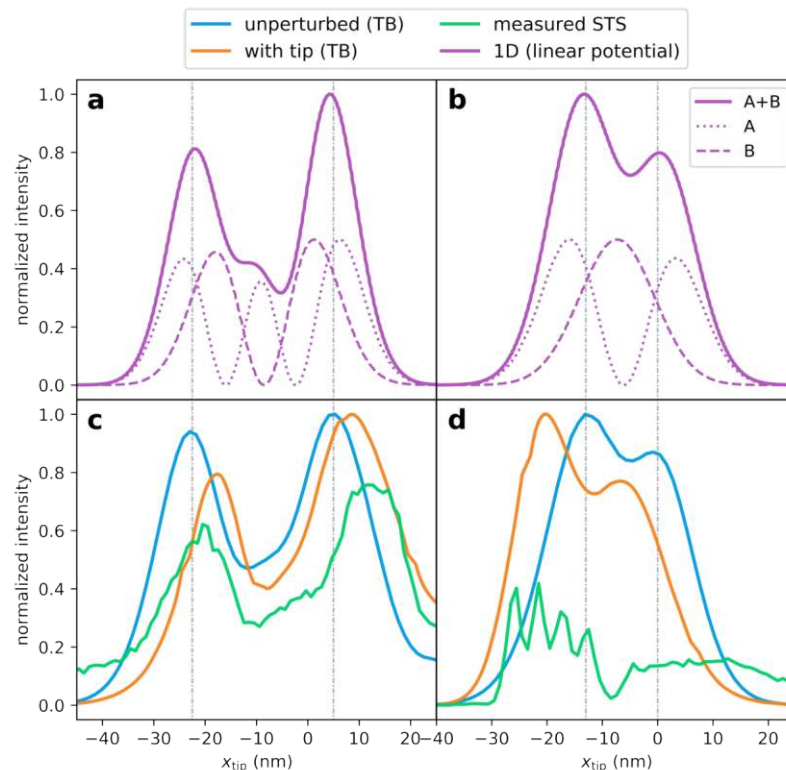


Fig. 10.14: **a** Numerical 1D TB solution of the squared graphene Landau level wave function belonging to LL-2 in a linear potential with slope -0.8 meV/nm (full line). The dashed and dotted curves are the sublattice contributions. **b** Same as subfigure a, but for LL+1 at a potential slope of $+0.8 \text{ meV/nm}$. **c, d** Zoom-ins of Fig. 10.11d, for the LL features belonging to LL-2 (c) and LL+1 (d). Vertical dashed lines highlight the agreement of distances between maxima.

To corroborate the generally good agreement of measured dI/dV_{sample} and simulated LDOS, we compare their dependence on V_{sample} and x_{tip} in Fig. 10.12a,b (see also Fig. D.20 in Appendix Chapter D). We again observe semi-quantitative agreement including the branching features of LL-2 and LL-3. At a slightly smaller V_{gate} , where only LL-1 crosses E_F at the interface, we map $dI/dV_{\text{sample}}(x_{\text{tip}})$ two-dimensionally at E_F (Fig. 10.12c). A bright line about 40 nm in width with some internal structure meanders along the lateral interface. Width and internal structure of this stripe are rather similar to the simulated LDOS(x_{tip}) of the LL-1 edge state (Fig. 10.12d, along red line) that itself turns out to be barely perturbed by the shallow TIQD (Fig. 10.12e). Hence, an imaging of an edge state with resolution well below the magnetic length $l_B = 10 \text{ nm}$ and only minor perturbations by the TIQD is achieved for the first time.

10.8 Conclusion

We conclude that quantum Hall edge states can be mapped without significant perturbations if one selects favorable parameter regimes. One attractive option to identify such regions is a direct comparison of dI/dV_{sample} across a gated lateral interface with TB simulations accounting for the TIQD. Crucially, reliable parameters for simulating the TIQD can be straightforwardly deduced from the measured charging lines in $dI/dV_{\text{sample}}(V_{\text{gate}}, V_{\text{sample}})$.

Current limitations of the method include neglecting confinement effects on the shape of the TIQD, which would require more time-consuming Poisson-Schrödinger simulations and, probably more severe, the assumption of a circularly symmetric TIQD. Trial and error-type control on the TIQD shape, however, can generally be achieved by mapping the capacitive charging of a point defect [386, 387]. Even with these limitations, the anti-nodal structure of the edge states could be mapped in a largely quantitative fashion, even revealing the influence of the potential gradient at the interface on the relative peak heights.

Plans for future experimental setups include an additional gate that can simultaneously tune the filling factor on the other side of the interface. This will eventually give access to multiple nearly unperturbed edge states including some that separate symmetry broken [388] or fractional QH phases.

We meanwhile have a working 3D Poisson solver based on *finite elemente* software by Joachim Schöberl et. al. [389]. Qualitative agreement with some experiments from the RWTH Aachen has been established. However, precise quantitative analysis will require an extension of the current implementation (based on local shifts of a constant density of states) towards a full Poisson-Schrödinger solver that accounts for confinement energies as well as charging energies. We aim to reach predictive accuracy to efficiently support sample design and fabrication of experimental collaborators.

Chapter 11

Quantum Hall conductivity of graphene-hBN moirés

“It is good to be a cynic — it is better to be a contented cat — and it is best not to exist at all.”

H.P. Lovecraft

This short chapter reports on efforts to calculate the quantum Hall conductivity σ_{xy} of graphene on aligned hBN employing a TB Hamiltonian of the entire moiré super cell derived from a set of ab-initio DFT calculations of multiple primitive unit cells. We treat realistic system sizes and calculate conductance from the bandstructure $E(k)$ in an efficient algorithm that scales with N_k^3 (size of the Krylov space in the Lanczos method) instead of N_a^3 (the much larger number of atomic sites). Both the ab-initio derived TB Hamiltonian as well as the efficient band structure calculation heavily rely on work by my doctoral predecessors L. Linhart [83] and T. Fabian [84]). We find that in order to compare with future experimental data from collaborators at the university of Manchester (Julien Barrier and the group of Prof. Gorbatchev) we will require a different approach that works over the entire energy range.

11.1 Technicalities

11.1.1 A realistic moiré TB Hamiltonian

Graphene on hBN has seen a lot of model Hamiltonians [390–392] that focus on quantitative analysis of the low energy bands for vanishing or small magnetic fields. Our approach combines an atomistic TB Hamiltonian parametrized from DFT calculations with a continuum elasticity model that accounts for lattice relaxation (see [83] for a much more detailed introduction). The 1.75% [393] difference in lattice constants of hBN and graphene can be described via a hexagonal supercell that encompasses 58×58 graphene unit cells and 57×57 hBN unit cells. The local stacking configuration of the two layers (parametrized via displacement vector \mathbf{d}) changes throughout this large super cell and can be used to map out the TB parameters of any local environment via a set of DFT calculations that involve only primitive unit cells of graphene and hBN with a relative shift of $\mathbf{d}(\mathbf{r})$ (see Fig. 11.1). This two-dimensional configuration space of the displacement vector \mathbf{d} is sampled on a grid involving 100 primitive

bilayer cells calculated in VASP [100–103] with LDA, 25×25 Monkhorst \mathbf{k} -space grid and plane wave cutoff of 380 eV. Atomic positions are relaxed in out-of-plane direction but fixed in-plane. We then project all Kohn-Sham orbitals onto one p_z orbital per carbon site (via Wannier90 [120, 124, 239, 240]) and thus capture all the influence of the hBN layer that is relevant for electronic transport close to the Fermi energy.

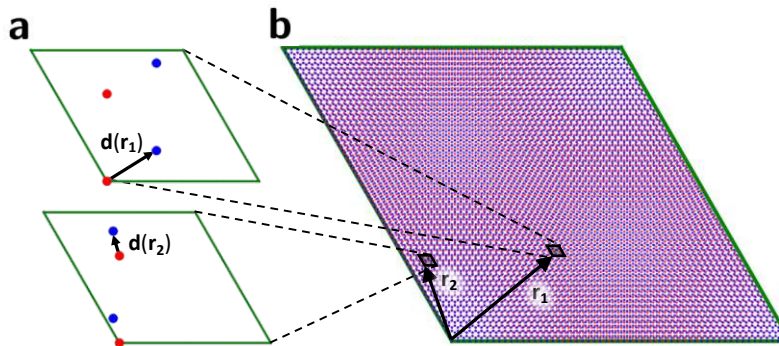


Fig. 11.1: **a** Primitive bilayer (red...hBN, blue...graphene) unit cells in the x-y plane with local displacement vector \mathbf{d} of two regions in the entire moiré super cell shown in **b**.

From this point on we can smoothly interpolate TB couplings γ_{ij} across the entire moiré super cell. However, we have yet to account for the significant strain fields of the real moiré super cell. We do so via exponential correction factors that depend on the local strain:

$$\gamma_{i,j}^{(\text{corr.})} = \gamma_{i,j} e^{-\Delta l_{ij} \alpha_{ij}} \quad (11.1)$$

where Δl_{ij} is the change in inter orbital distance due to mechanical relaxation and α_{ij} encodes the distance sensitivity of individual TB hopping parameters. We determine the α_{ij} from a set of DFT calculations on primitive unit cells of strained single layer graphene with subsequent Wannierization. Finally we determine the Δl_{ij} via an approach that resembles the elasticity models of Nam and Koshino [394]. Such an approach determines an equilibrium configuration that balances energy gain due to more favourable stacking fault energies with the elastic energy cost associated with in-plane displacements. The corresponding energy functional is of the form,

$$U_{\text{tot}} = U_E[\mathbf{u}_{\text{hBN}}] + U_E[\mathbf{u}_{\text{SLG}}] + U_B[\mathbf{u}_{\text{hBN}}, \mathbf{u}_{\text{SLG}}] \quad (11.2)$$

where $\mathbf{u}_{\text{hBN/SLG}}$ are the local displacement vectors in hBN and graphene respectively. The third, stacking dependent term is elegantly expressed via the first few Fourier components c_G of the generalized stacking fault energy:

$$U_B[\mathbf{u}_{\text{hBN}}, \mathbf{u}_G] = \int \sum_G c_G e^{i((\mathbf{d} + \mathbf{u}_{\text{hBN}} - \mathbf{u}_{\text{SLG}}) \cdot \mathbf{G})} d\mathbf{r} \quad (11.3)$$

with \mathbf{G} running over reciprocal lattice vectors. The interlayer contributions U_E of both layers ($m = \text{hBN}/\text{SLG}$) read,

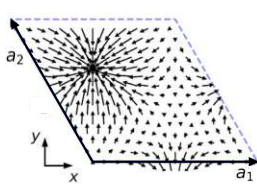


Fig. 11.2:
Reconstruction
of atomic position
following the elasticity
model in Eq. (11.2).
 $a_{1/2}$ are the moiré
super-cell lattice vectors.
Black arrows indicate
the relative displace-
ments throughout the
super-cell. Taken from
[84].

with Lamé parameters [390, 395] λ (SLG: $3.25 \text{ eV}\text{\AA}^{-2}$, hBN: $3.5 \text{ eV}\text{\AA}^{-2}$) and μ (SLG: $9.57 \text{ eV}\text{\AA}^{-2}$, hBN: $7.8 \text{ eV}\text{\AA}^{-2}$). We then solve the Euler Lagrange equations of the system following closely along the procedures in [394]. The main result of this relaxation is the proliferation of the energetically favourable AB stacking region in the upper left half of the moiré super cell (see Fig. 11.2).

11.1.2 Efficient band structure calculations on dense \mathbf{k} -grids

We wish to efficiently calculate the band structure of a ribbon of several of the — by themselves already quite sizable — moiré unit cells. Since we are only interested in the eigenvalues close to charge neutrality we may employ iterative methods to work on sparse matrices at each \mathbf{k} – point. We therefore solve $H(\mathbf{k})\Psi_n = E_n(\mathbf{k})\Psi_n$ via shift-and-invert in combination with the Lanczos method [396]. In order to partially avoid cubic scaling we perform several independent matrix factorizations around different energies to eventually cover the range $E \in [-0.25\text{eV}, 0.25\text{eV}]$. The accuracy of subsequent evaluations of the Hall conductivity depends on the sampling resolution in reciprocal space (no further improvements noticeable beyond $N_{kpt} > 3000$ in our system). Sampling at such high \mathbf{k} -point densities can be further optimized by exploiting the continuity of bands along small distances in \mathbf{k} -space. We avoid solving the Bloch eigenvalue problem at most of the N_{kpt} \mathbf{k} -points and instead span a Krylov space for a subset $N_{pillars}$ of “pillar” \mathbf{k} -points. Combining the Krylov spaces of two adjacent pillar points k_j and k_{j+1} generates a basis $\{\mathbf{b}_i\}$ on which to project for all intermediate \mathbf{k} -points k' ($k_j < k' < k_{j+1}$) and thus evaluate band energies. Main caveat of this approach is the emergence of unphysical eigenvalues due to the artificially enlarged size of the combined Krylov spaces. This can largely be remedied by evaluating the following error norm,

$$\delta_n = \sum_i |\phi_i[H(\mathbf{k}) - E_n(\mathbf{k})\mathbb{1}]\Psi_n|^2 \quad (11.5)$$

which sees the solutions projected onto a fixed set of randomly chosen vectors $\phi_i \in \mathbb{C}^N$ with $i \in [1, N_k]$. This error measure only vanishes for an eigenstate of the full problem and thus filters out the unphysical solutions. Matrix vector operations between the ϕ_i and H_0 or H_I do not depend on \mathbf{k} and thus need only be evaluated once. This procedure thus enables efficient sampling of a very dense \mathbf{k} -grid only a small subset of which is solved “rigorously”.

11.2 From bandstructure to quantum Hall conductivity

The Hall conductivity σ_{xy} of a material is represented by the off-diagonal components of its conductivity tensor used in Ohm's law $\mathbf{I} = \sigma\mathbf{E}$. It describes the emergence of a voltage difference (and therefore a current) transverse to both an applied electric field and an applied magnetic field perpendicular to the current [397]. A quantized analogue of this Hall effect can be observed in two dimensional electron systems for low temperatures and high magnetic field strengths [398, 399]. Deep into the Landau regime this effect sees the longitudinal ρ_{xx} and transverse (Hall) ρ_{xy} resistivity adopt very impressive characteristic shapes as a function of the perpendicular magnetic field strength. While ρ_{xx} exhibits sharp peaks whenever a Landau level passes through the Fermi surface the Hall resistivity ρ_{xy} concurrently jumps between well defined plateaus (staircase) of integer multiples of the conductance quantum e^2/h . This integer is called Thouless-Kohmoto-Nightingale-Nijs (TKNN, [400]) number (or the first Chern number C) and characterizes topological properties of the underlying Bloch bands.

$$\sigma_{xy} = \frac{-ie^2}{\hbar} \sum_{\alpha, E_\alpha < E_F} \sum_{\beta, E_\beta > E_F} \frac{\langle \alpha | \frac{\partial H}{\partial k_1} | \beta \rangle \langle \beta | \frac{\partial H}{\partial k_1} | \alpha \rangle - \langle \alpha | \frac{\partial H}{\partial k_2} | \beta \rangle \langle \beta | \frac{\partial H}{\partial k_1} | \alpha \rangle}{(E_\alpha - E_\beta)^2} \quad (11.6)$$

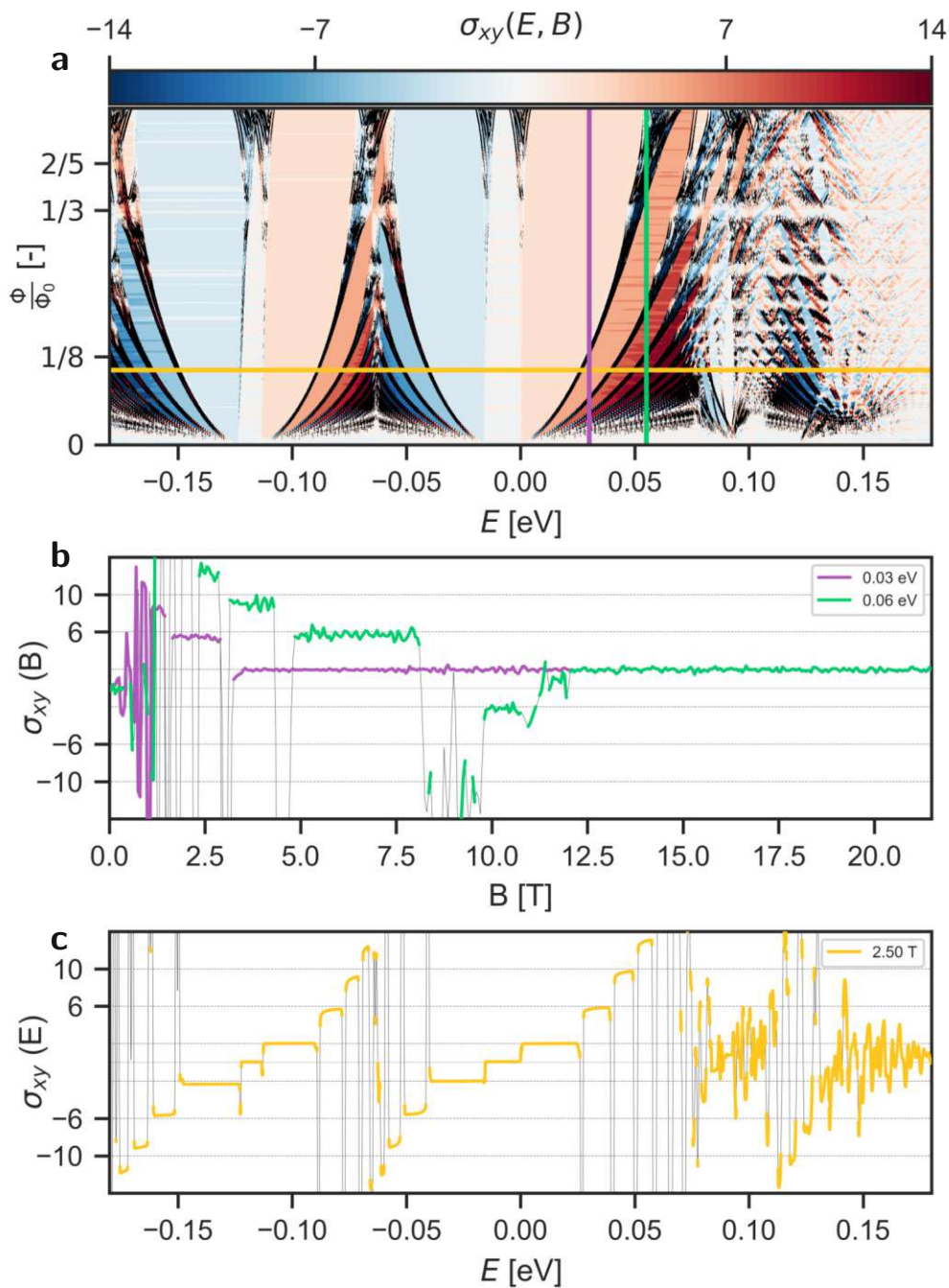
The Hall conductivity σ_{xy} (see Eq. (11.6), [401, 402]) is usually derived via the Kubo formula [403, 404] in the context of linear response theory (see [405] for an excellent modern introduction). Since the contribution of all occupied states is quantized the integer quantum Hall effect emerges whenever the Fermi energy lies in a gap. For this situation the Strěda formula [406] allows the reformulation of σ_{xy} in terms of a \mathbf{B} -field derivative of the charge carrier density $n(E, B)$:

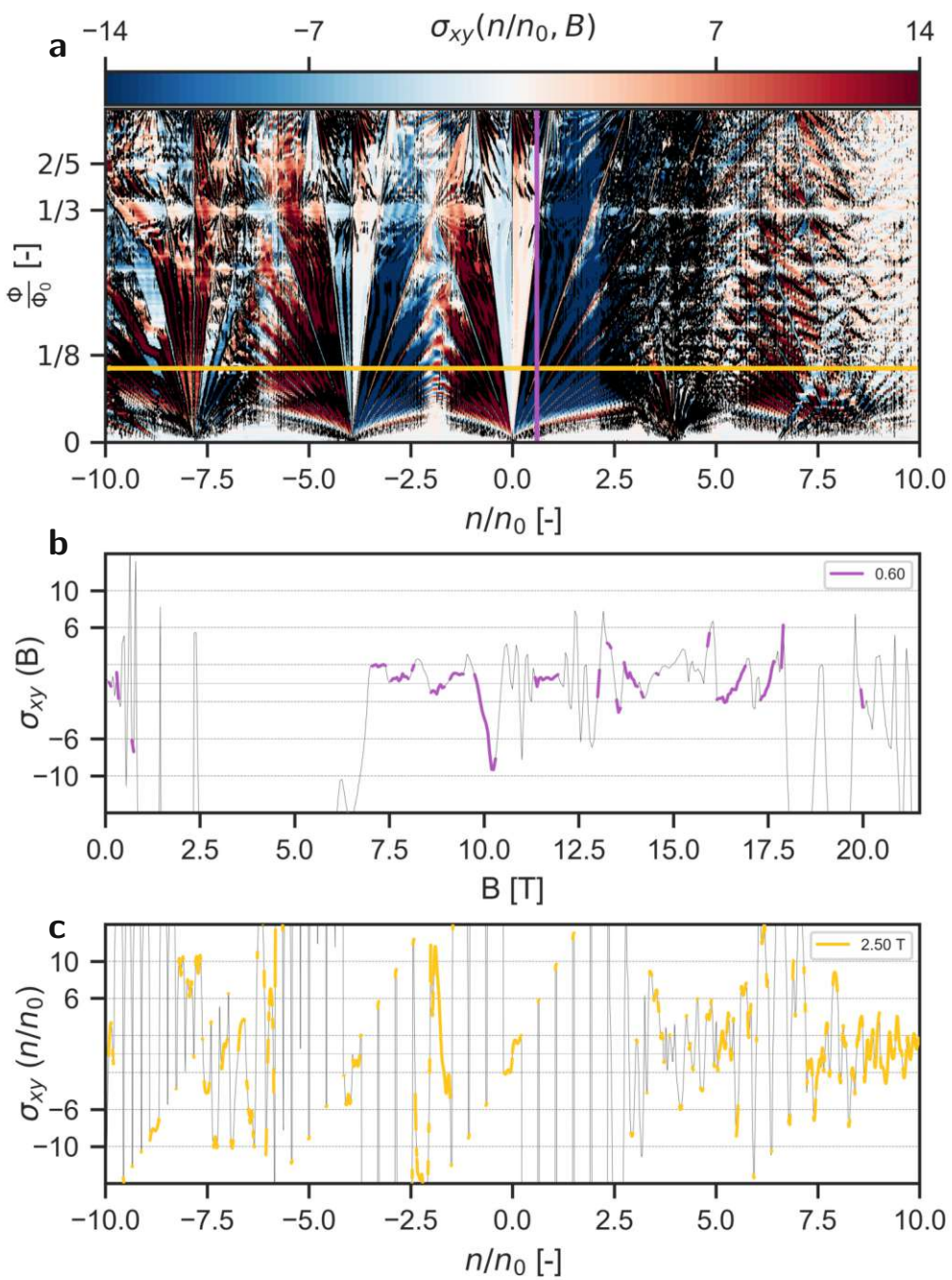
$$\sigma_{xy} = e \frac{\partial n}{\partial B}|_{E=E_F} = C \frac{e^2}{h} \quad (11.7)$$

with Chern number $C \in \mathbb{Z}$. Outside the band gaps one would additionally have to compute terms of the form,

$$\sigma_{xy}^{(\text{no gap})} = \frac{i\hbar e^2}{2} \text{Tr}[v_x G^+(E_F)v_y \delta(E_F - H) - v_x \delta(E_F - H)v_y G^-(E_F)] \quad (11.8)$$

where $G^\pm(E) = (E - H \pm i0)^{-1}$ are Greens functions and v_x/y are velocity operators. This is numerically unfeasible for ribbons consisting of several large moiré super cells. However, unlike earlier work that also omits the direct calculation of the energy spectrum (as required for Eq. (11.7)) for large twisted moiré systems (e.g. by constructing effective-mass wave functions for Landau levels [407]) we can use this expression Eq. (11.7) in combination with the extremely efficient band structure calculations that employ the ab-initio derived TB Hamiltonians.





We calculate band structures of ribbons consisting of several moiré unit cells and evaluate the energy dependent charge carrier density $n(E, B)$ before interpolating on a very dense energy grid. We sample the magnetic field axis with increments of 50 mT and then apply Strěda's formula via a symmetric numerical derivative at constant energy. The resulting quantum Hall conductivity $\sigma_{xy}(E, B)$ (see Fig. 11.3) displayed as a function of energy reveals familiar features. Regions where the Strěda formula does not apply (i.e. outside of bandgaps) are colored black in Fig. 11.3. Plateaus of constants Hall conductivity separated by openings of Landau levels are well visible over a large region of the magnetic field (the critical magnetic field where one full flux quantum is threaded through a single moiré unit cell is roughly 23.5 T). The plateaus close to the Dirac point (i.e. $E = 0$) do not quite match the values of the Hall conductivity plateaus in single layer graphene (i.e. 2, 6, 10) while higher plateaus increasingly fall short (see yellow features in Fig. 11.3c). Horizontal artifacts within these plateaus are most present to the right of the $E = 0$ Landau fan as well as to the left of the hole side satellite. These may arise due to “lost” states due to erroneously selected states within the two-fold enlarged Krylov space at interpolated \mathbf{k} -points. Since calculations at different magnetic fields are in principle entirely decoupled the identification of the $n = 0$ point on the energy axis also introduces an error margin that can cause slight horizontal misalignment of the individual 50 mT increments, thereby introducing artifacts in the numerical derivative.

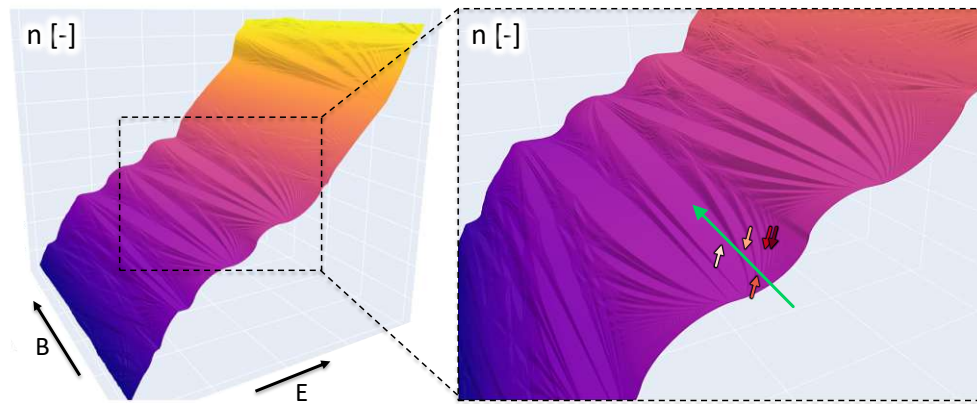


Fig. 11.5: Surface plot of the charge carrier density of the graphene/hBN ribbon as a function of both energy and magnetic field. Zoom-in illustrates the limits of the Strěda formula (see text). Green arrow indicates direction of magnetic field derivative. Short arrows point at ramps of constant slope and are color coded according to plateaus of σ_{xy} in Fig. 11.3a.

The satellite Dirac cones display distinct asymmetry between electron and hole side with the hole side rendered much cleaner. Regardless of energy all structure vanishes at low magnetic fields due to the finite ribbon width of roughly 750 nm. Transforming $\sigma_{xy}(E, B)$ to a density axis in units of moiré super cell fillings is usually the preferred way to compare to experimental (gate voltage dependent) data. This transformation first of all straightens the Landau fan but while readily viable from a numerical viewpoint also shrinks the gap plateaus while enlarging the regions that

are inaccessible with Eq. (11.7) (see black spotted and or clipped regions in Fig. 11.4a). Unambiguously identifying these regions and coloring them black is numerically difficult. $\partial n / \partial B|_{E=\text{const.}}$ in Eq. (11.7) erroneously produces large values of the wrong sign when applied in these regions. The plateaus of constant σ_{xy} in the Landau gaps translate to ramps of constant slope for $n(E, B)$ (see Fig. 11.5). Since all these curved ramps originate at the same value of $n(E = 0, B = 0)$, a derivative along the magnetic field axis will inevitably see steep steps in-between the ramps of constant slope (as illustrated in Fig. 11.5). These regions can thus (if not already colored black) also appear either dark blue or dark red depending on which side of the Landau fan they are located at. Employing Fig. 11.4 for comparison to experimental data (not shown) is therefore dubious at best. The only meaningful commonality of the in general much more washed out experimental data and my simulations is the asymmetry in the satellite structures between electron and hole side.

11.3 Outlook

With the help of efficient algorithms that have been developed in our group we have efficiently sampled band structures of moiré structures of realistic sizes (several hundred nanometers). We have sucessfully employed the simple yet elegant Strěda formula Eq. (11.7) to process our band structure data into quantum Hall conductivities of a graphene/hBN moire system. However, the inability of the current method to calculate σ_{xy} outside of band gaps results in extremely limited comparability to experimental data.

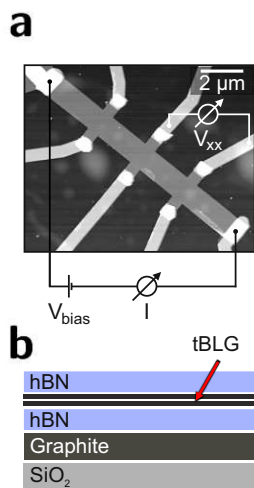
The desire for meaningful theoretical data of experimentally accessible moiré structures across the entire parameter space (E, B) warrants further investigation. The fact that our approach can in principle also extract full information on the underlying Bloch states of the band structure opens yet another efficient route to mitigate this issue. We are currently implementing an algorithm following the work of Imry et.al [408] that calculates chemical potential differences between upper and lower border of the ribbon via wave function amplitudes. This will allow us to produce a complete quantum Hall conductance map as a function of magnetic field and charge carrier density.

Chapter 12

Composite super-moiré lattices in twisted bilayer graphene on hexagonal boron nitride

“Physics is the only profession in which prophecy is not only accurate but routine.”

Neil deGrasse Tyson



Employing most of the numerical methods introduced in Chapter 11 in a collaboration with Alexander Rothstein from the group of C. Stampfer at the RWTH Aachen we study magneto transport of hBN-encapsulated twisted bilayer graphene (tBLG). Alignment of one of the hBN layers leads to additional Landau fans related to two competing moiré super lattices. Furthermore the presence of this additional moiré lattice results in pronounced asymmetry of the single particle band gaps in both theory and experiment. A. Rothstein performed measurements on several hBN/tBLG/hBN devices (see Fig. 12.1) while we provided magneto transport and bandstructure calculations of ab-initio derived TB ribbons for a commensurable configuration of both moiré super cells (as identified in the experiment). A manuscript of our findings intended for publication is currently in preparation.

12.1 Introduction

Fig. 12.1: **a** False-color atomic force microscopy image of the measured device. Overlay depicts schematic measurement setup for both two- and four-terminal measurements. **b** Schematic cross-section of the stacked devices.

Van-der-Waals heterostructures allow the fabrication of quantum materials with tailored properties [409]. Apart from the sequencing of the two-dimensional constituents in these layered materials, the relative orientation of the individual interfaces is another vital tuning knob for the final physical properties. Inducing a small orientation mismatch between the individual building blocks can create a moiré superlattice that significantly changes the characteristics of the structure. Prime example for the vast consequences of such superordinate patterns is twisted bilayer graphene. Close to the magic angle of 1.1° one finds a vast number of exotic quantum phenomena including superconductivity [11, 410–413] and correlated insulators [11, 410, 414–416]. Introducing a second, and thus competing superlattice can alter the physical properties of tBLG even further. Experimental evidence of an anomalous quantum Hall effect as well as orbital ferromagnetism at certain carrier densities in tBLG [417–419] is traced back to an additional hBN

alignment leading to the formation of a dual moiré effect and is supported by theoretical investigations [420, 421].

While one typically tries to avoid the creation of more than one superlattice in a van-der-Waals stack due to the arising complexity (e.g. via optical investigation of the orientation of crystallographic axes during the fabrication process), here, we want to investigate the effect of simultaneous alignment both within the BLG as well as to one of the hBN substrate layers. We have also become aware of studies on composite super moiré lattices in single layer graphene [422]. However, there the two moiré lattices are both of graphene/hBN origin.

12.2 Modelling two moiré superlattices in concert

In order to simulate magnetotransport in composite moiré systems we employ a tBLG tight-binding Hamiltonian derived via the same process introduced in Section 11.1.1. Several DFT calculations of displaced BLG unit cells wannierized are put together to form a state-of-the-art description of a mechanically relaxed bilayer moiré cell. While it might be worth to contemplate about a clever way to merge the ab-initio derived tBLG Hamiltonian with the ab-initio derived graphene/hBN Hamiltonian from Chapter 11 we omit this potentially error-prone challenge in favor of replacing the entire hBN layer by effective potentials. We utilize a combination of slowly varying background potentials V_i and short-range symmetry breaking potentials W_i [423]:

$$V_{\text{hBN}} = \sum_{i=I,III,V} V_i e^{-\frac{(r-R_i)^2}{2w_i^2}} \cdot \sigma_0 \otimes \tau_0 + \sum_{i=I,III,V} W_i e^{-\frac{(r-R_i)^2}{2w_i^2}} \cdot \sigma_z \otimes \tau_0 \quad (12.1)$$

where w_i are characteristic length scales, $\sigma_0(\sigma_z)$ represent unity (z-Pauli matrix) in sublattice space and τ_0 is the unity in valley space. While the V_i break particle-hole symmetry the W_i introduce sublattice asymmetry. Derived from DFT calculations [390, 424] these terms can accurately describe the effect of hBN alignment with respect to one of the graphene layers.

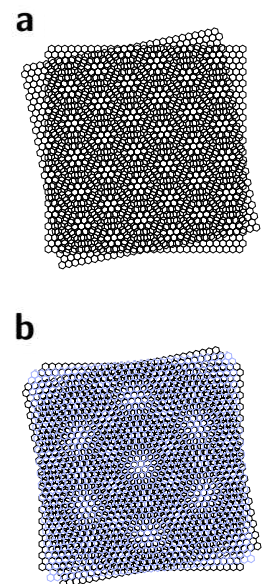


Fig. 12.2: Schematic representation of **a** a single moiré (tBLG) and **b** two superimposed moiré lattices (tBLG aligned with hBN).

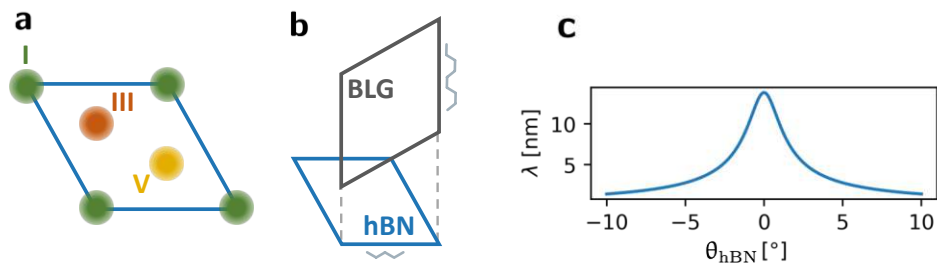


Fig. 12.3: **a** Schematic of the real space moiré super cell of the graphene/hBN system. Colored circles (I, II, V) correspond to centers of Gaussians used in the effective moiré potential in Eq. (12.1) as taken from [423]. **b** Schematic explanation of the superposition of the two moiré lattices. Light grey lines indicate edge character of the unit cells. Assuming a small graphene/hBN twist angle of $\theta_{\text{hBN}} \approx 0.7^\circ$ brings the two moiré cells to the same periodicity. **c** Moiré lattice constant of the graphene/hBN moiré as a function of their relative twist angle θ_{hBN} .

We partition the hBN moiré unit cell in five regions based on relative local alignment with the graphene layer (see Fig. 12.3). Assigning different amplitudes ($V_I = V_{III} = 0\text{meV}$, $V_V = 100\text{meV}$ [425], $W_I = 57\text{meV}$, $W_{III} = -34\text{meV}$, $W_V = -47\text{meV}$) and widths ($0.63w_I = w_{III} = w_V = 7\text{nm}$) to the Gaussians in Eq. (12.1) allows us to effectively model the influence of the hBN alignment and introduces the second moiré lattice length scale into the tBLG Hamiltonian in an elegant and easily adaptable manner. This adaptability is very important for us to create structures with feasible periodicity. The relaxed displacement-mapping method we use for the derivation of the tBLG TB Hamiltonian can only really be applied to commensurate twist-angles θ_{BLG} defined by [72, 426]:

$$\cos(\theta_{\text{BLG}}) = \frac{3m^2 + 3mr + \frac{r^2}{2}}{3m^2 + 3mr + r^2} \quad m, r \in \mathbb{N} \quad (12.2)$$

Having access to a set of different twist angles of tBLG Hamiltonians (as parametrized by L. Linhart [83]) we identify $\theta_{\text{BLG}} = 0.987^\circ$ as the closest one to the experimentally determined twist angles (see Section 12.3). The unit cell for this moiré system is spanned by the vectors $\mathbf{a}_1 = (14.3, 0)^\top \text{nm}$ and $\mathbf{a}_2 = (-7.1, 12.4)^\top \text{nm}$ and features armchair borders. The effective hBN potential of Eq. (12.1) is derived for a perfectly aligned graphene/hBN moiré cell ($\mathbf{b}_1 = (13.8, 0)^\top \text{nm}$, $\mathbf{b}_2 = (-6.9, 11.9)^\top \text{nm}$) that features zig-zag borders. Their difference in border character is easily reconciled via a rotation. However, this would result in a slightly different periodicity in x direction. We avoid cumbersome duplication to their least common multiple and instead assume a slight rotation of the graphene/hBN moiré. This bilayer of materials with unequal lattice constants also features an angle dependence ([76, 427–429], see Fig. 12.3c):

$$\lambda(\epsilon, \theta) = \frac{1 + \epsilon}{\sqrt{\epsilon^2 + 2(1 + \epsilon)(1 - \cos(\theta))}} \quad (12.3)$$

where ϵ is the relative mismatch of lattice constants ($\approx 1.8\%$ for graphene / hBN). A small twist angle $\theta_{\text{hBN}} \approx 0.5^\circ$ results in perfect agreement of x periodicity for the composite moiré system which we can then duplicate in y direction to describe ribbons of realistic width. The area ratio of the two moiré unit cells of $\sqrt{3}/2)^2 = 3/4$ will become important when discussing magneto transport in Section 12.4. Terminating the edges with σ_z potentials in sublattice space [39, 340] suppresses surface states. We again utilize the efficient algorithms introduced in Section 11.1.2 to compute band structures and obtain the group velocity of each Bloch state ψ_n via

$$v_g(n) = \frac{1}{\hbar} \frac{\partial E_n(k)}{\partial k} = \frac{i\Delta x}{\hbar} \psi_n^\dagger \left(H_I e^{ik\Delta x} - e^{-ik\Delta x} H_I^\dagger \right) \psi_n \quad (12.4)$$

The energy dependent conductance $G(E)$ is then easily obtain by weighting all right moving states with their respective group velocity and sampling the

entire Brillouin zone. We estimate the number of modes at a given energy $M(E)$ as,

$$M(E) \approx \sum_{m=1}^M \frac{\partial E}{\partial k} \frac{\Delta k}{\Delta E} \approx \frac{d}{dE} \sum_{n:E_n < E, v_g^{(n)} > 0} \hbar v_g^{(n)} \Delta k \quad (12.5)$$

with k -point spacing Δk [84].

12.3 Device characterization and band gap asymmetries

The investigated heterostructure (Fig. 12.1a) consists of tBLG encapsulated in hBN (thicknesses of the top and bottom flakes are approximately 24 nm and 32 nm, respectively) and a graphite back gate. After stack assembly (with a conventional dry PC/PDMS van-der-Waals pick-up technique) the entire heterostructure is placed on a $\text{Si}^{+++}/\text{SiO}_2$ substrate (see schematic cross-section in Fig. 12.1b). We create the tBLG superlattice following a convenient “laser-cut-and-stack” technique adjusting a twist angle of around 1.3° , slightly overshooting the target angle of 1.1° [430].

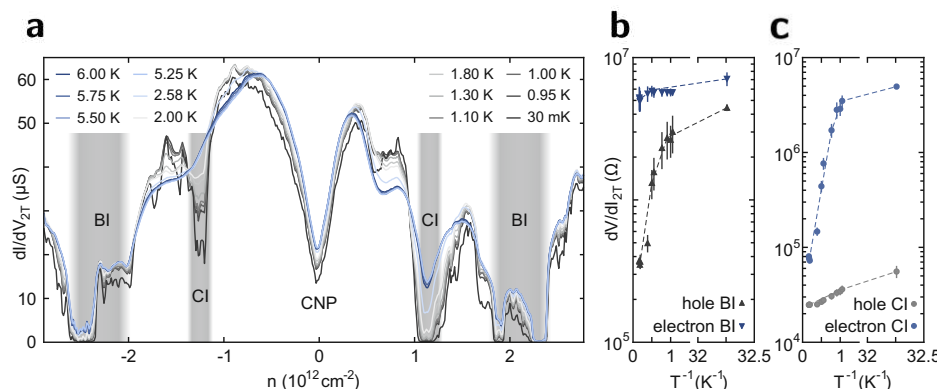


Fig. 12.4: **a** Two-terminal differential conductance dI/dV_{2T} as a function of the charge carrier density n for different temperatures measured along the entire Hall bar structure. **b** Arrhenius representation showing the differential resistance dV/dI_{2T} of the band insulating states as a function of the inverse temperature. The data is taken at charge carrier densities of $n \approx -2.4 \times 10^{12} \text{ cm}^{-2}$ and $n \approx 2.25 \times 10^{12} \text{ cm}^{-2}$ for the hole and electron insulating state, respectively. **c** Same as (b), but for the correlated insulating features at charge carrier densities of $n \approx -1.2 \times 10^{12} \text{ cm}^{-2}$ (hole doping) and $n \approx 1.1 \times 10^{12} \text{ cm}^{-2}$ (electron doping).

The composite supermoiré hBN/graphene lattice is created by aligning the crystallographic axes of an hBN flake with the tBLG area. Our colleagues at the RWTH Aachen perform each transfer step as slowly as possible to reduce the mechanical stress on the heterostructure. We utilize standard electron beam lithography and reactive ion etching (CF_4/O_2) to define ohmic contacts to the graphene [431] which are subsequently evaporated (Cr/Au , 5/50 nm). Additional lithography and metal evaporation steps define the lines to the etched contacts (Cr/Au , 5/50 nm). The Hall bar geometry is defined after hard mask evaporation (Al , 60 nm) by a reactive

ion etching step (SF_6/O_2). Finally, we remove the aluminium hard mask in $\text{N}(\text{CH}_3)_4^+\text{OH}^-$ (2.38% in de-ionized water). All measurements are performed in a ${}^3\text{He}/{}^4\text{He}$ dilution refrigerator (Oxford Kelvinox) at a base temperature of around 30 mK until otherwise noted, using standard low-frequency lock-in measurement techniques (Stanford SR830).

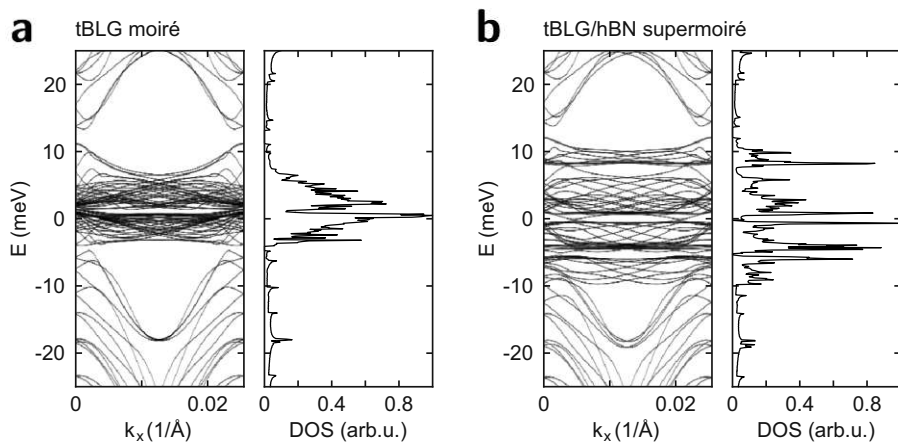


Fig. 12.5: Band structure and density of state for a ribbon with a width of 10 tBLG moiré unit cells of **a** just tBLG ($\theta_{\text{BLG}} \approx 0.987^\circ$) and **b** tBLG (same θ_{BLG}) with additional alignment ($\theta_{\text{hBN}} \approx 0.7^\circ$) to an hBN layer.

We initially characterize our device by measuring the two-terminal differential conductance dI/dV_{2T} as a function of the charge carrier density by applying an ac bias of $V_{\text{ac}} = 1$ V via an in-house build IV-converter (gain: 10^7) along the entire Hall bar structure (see Fig. 12.1a) and measuring the current in parallel for different temperatures (see Fig. 12.4a). We observe five dips in the differential conductance with decreasing temperature and identify the insulating features around $n \approx \pm 2 \cdot 10^{12} \text{ cm}^{-2}$ with the edges of the flat bands, corresponding to full filling of four holes/electrons of the tBLG moiré superlattice unit cell [414]. Note that these band insulator (BI) states exhibit a distorted shape rather than a clean gap opening: the band insulator at hole doping exhibits a plateau in differential conductance until the final pinch-off, while the band insulator at electron doping appears to be split into two separate insulating features. However, this behaviour is only visible in the two-terminal data and might be due to twist angle variations along the device. The strongly insulating parts of the band insulators around $n \approx \pm 2.4 \cdot 10^{12} \text{ cm}^{-2}$ display an asymmetry in their temperature dependence: while the hole-site band insulator shows a clear gap opening over the accessible temperature range, the band insulator at electron-doping does not show indications of thermal activation up to the maximum temperature of $T = 6$ K. This asymmetric behaviour between the two doping regimes becomes even clearer at the insulating features around $n \approx \pm 1.2 \cdot 10^{12} \text{ cm}^{-2}$ which we identify as the correlated insulator (CI) at half-filling of the moiré superlattice unit cell. These correlated insulators display a strong temperature dependence. However, complete pinch-off is only reached at electron doping.

The influence of the competing moiré superlattices becomes clearly visible in band structure calculations (see Fig. 12.5), where we show the non-aligned and aligned cases for a graphene twist-angle of 0.987° (additional BS calculations for different twist-angles can be found in Fig. G.2 in Appendix Chapter G). An intrinsic asymmetry between the gaps at electron and hole doping is already present in the non-aligned case (Fig. 12.5a). We extract a gap ratio of around $E_{\text{gap}}^e/E_{\text{gap}}^h \approx 2.66$. The presence of hBN alignment (Fig. 12.5b) induces a strong broadening of the flat bands around an energy of $E \approx 0 \text{ meV}$. In this case we observe an increase of the gap asymmetry, extracting a ratio of $E_{\text{gap}}^e/E_{\text{gap}}^h \approx 4.48$.

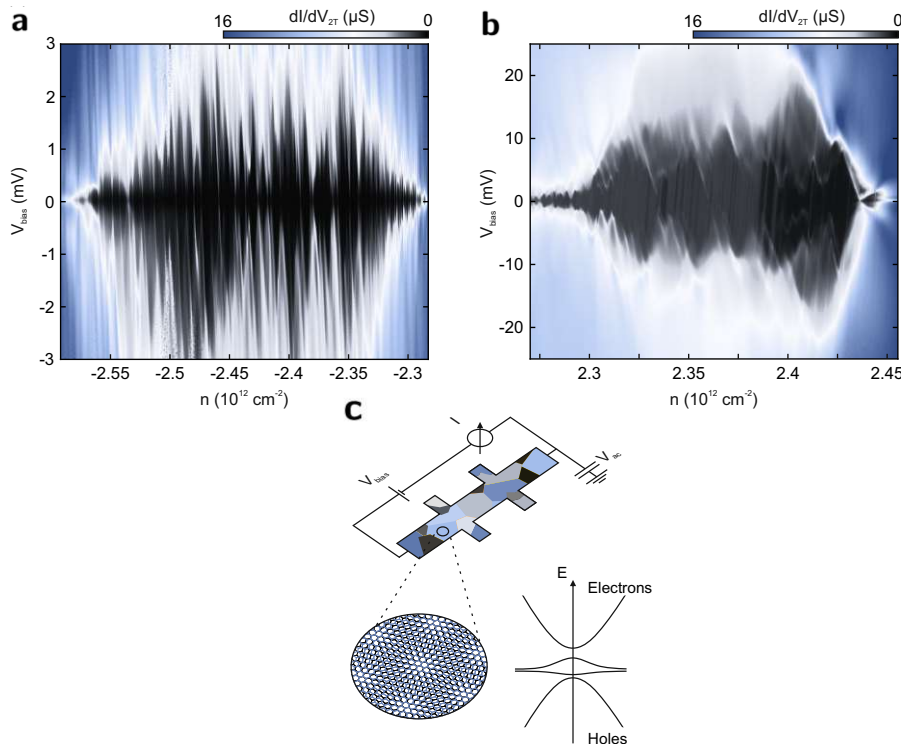


Fig. 12.6: **a** Finite bias spectroscopy measurement of the band insulating state at hole doping. Instead of a clean gap, we observe the formation of roughly 130 individual Coulomb diamonds indicating a disordered system. **b** Same as in (a) but for the band insulator at electron doping. Striking is the asymmetry in the applied bias compared to the hole-doped band insulator. **c** Schematic representation of the measurement. The Hall bar consists of individual areas of tBLG with slightly different twist angles.

To extract the gap sizes experimentally from transport experiments, we perform finite bias spectroscopy measurements at the carrier densities associated with the insulating features (see Fig. 12.6). Instead of a clean gap opening (which would be indicated by a large diamond structure of suppressed differential conductance), we observe disordered behaviour. In the case of the hole-doped band insulator (Fig. 12.6a) this behaviour is manifested by the presence of approximately 130 individual (but superimposed) Coulomb diamonds of suppressed differential conductance with addition energies in the low meV regime. Inhomogeneous twist-angle distributions over the probed area of the device or edge effects might be a plausible origin of this effect.

Interestingly, the band insulating state at electron doping exhibits a less complex substructure (Fig. 12.6b). Individual Coulomb diamonds cannot be identified as easily as in the hole-doped case and seem to be shifted inwards one another. This indicates a cleaner and more stable gap opening at electron doping. Striking is the stark difference in bias voltages between electron and hole sides associated with these unclean Coulomb diamonds. Clear energy gap estimation for comparison to the theory data is however not credible from this data.

12.4 Magnetotransport simulations

We now focus on the area of the device where the four-terminal magnetoresistance measurements were taken (Fig. 12.7). We can extract the local twist-angle in this area of the device by reading off the superlattice density $n_s \approx \pm 2.17 \cdot 10^{12} \text{ cm}^{-2}$ at which we observe Landau levels emerging from the band insulating states. Together with the small angle approximation [414]

$$n_s = \frac{8\theta^2}{\sqrt{3}a^2}, \quad (12.6)$$

where $a = 0.246 \text{ nm}$ is the lattice constant of graphene, we estimate the twist angle in this area to be $\theta \approx 0.97^\circ$. Comparing the magneto transport simulations of tBLG with those of tBLG with additional hBN alignment reveals additional Landau fan features emerging in the double moiré system. These lines (see red arrows in Fig. 12.7b) originate from fillings close to $\nu = 3$ which corresponds to the hBN moiré unit cell being three quarter the size of the tBLG moiré in (see Section 12.2 for modeling details). The derivative of the longitudinal resistance with respect to the magnetic field dR_{xx}/dB (Fig. 12.7c,d) as a function of the filling factor $\nu = 4n/n_s$ and the magnetic flux per moiré unit cell Φ_{uc}/Φ_0 normalised to the magnetic flux quantum $\Phi_0 = h/e$ (see also Fig. G.1 in Appendix Chapter G for a depiction without the derivative along the magnetic field) also shows similar novel features when aligned to hBN. Aside from Landau levels emerging from the charge-neutrality point (filling factor $\nu = 0$) and the band insulating states (filling factor $\nu = \pm 4$) we also observe a clear set of Landau levels from $\nu = 2$ associated with the CI and thus not captured by the single particle simulation. However, we also notice an additional set of lines emerging from non-integer filling factors around $\nu \approx \pm 2.5$ (see Fig. 12.7d,e), in line with theoretical expectations of an additional alignment with the hBN layer.

We are able to extract the twist angle of the hBN-graphene superlattice by exploiting the ratio between the superlattice unit cell areas given by

$$A_{hBN} = \frac{2.5}{4} A_{tBLG} \quad (12.7)$$

as well as the angle dependent superlattice wavelength Eq. (12.3), to be $\theta \approx 0.7^\circ$.

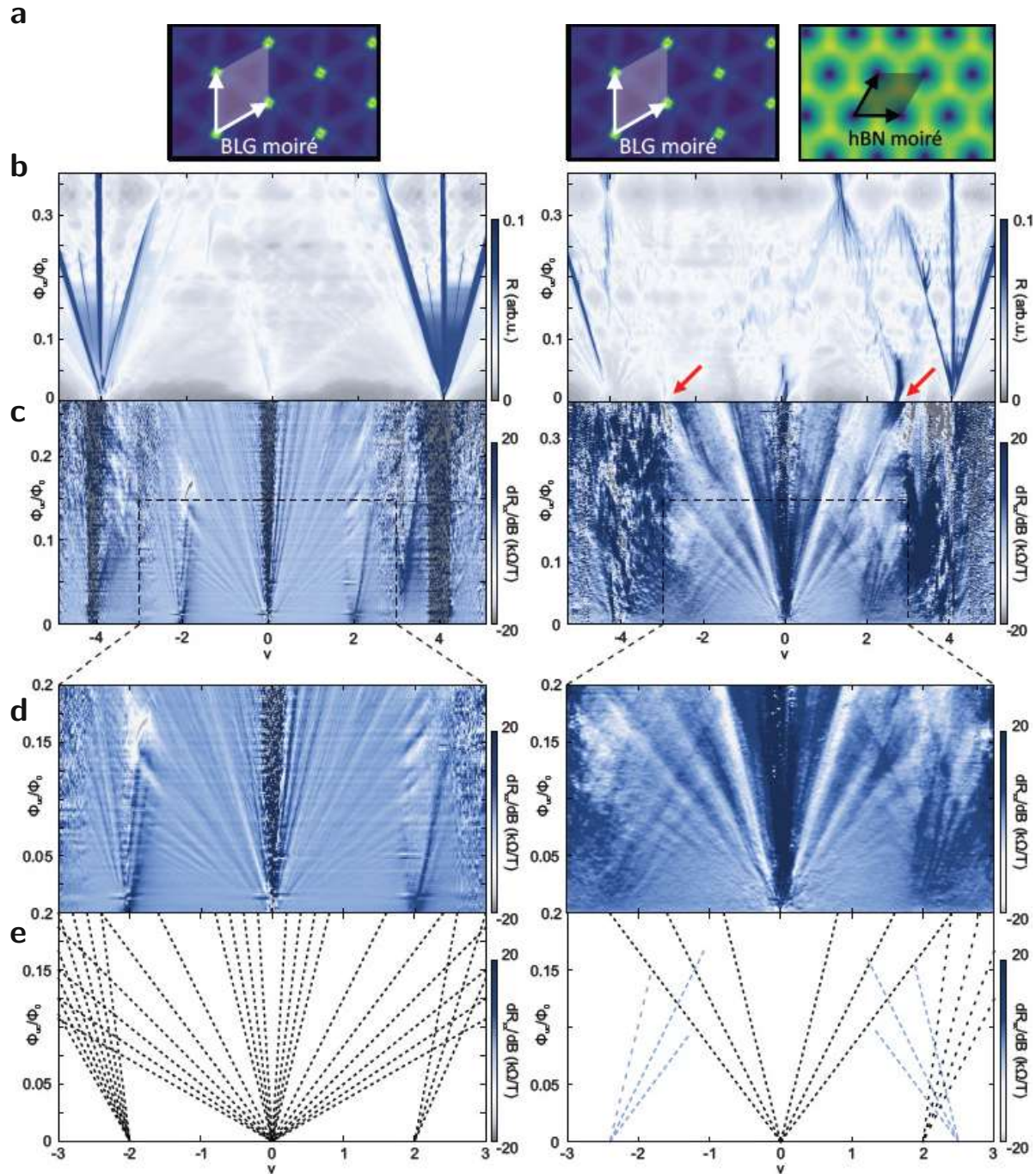


Fig. 12.7: **left column:** tBLG with non-aligned hBN, **right column:** tBLG with aligned hBN ($\theta_{hBN} \approx 0.7^\circ$). **a** Schematic of the onsite energy corresponding to the different moiré super lattices. (relative sizes are to scale!) **b** Magnetoconductance simulation of the tBLG/hBN system with a BLG-twist-angle θ_{BLG} of 0.987° . Landau levels emerge from the charge neutrality point ($v = 0$) and the single-particle band gaps at full filling of the BLG moiré superlattice unit cell ($v = 4$). Alignment with hBN introduces additional Landau level features at non-integer filling factors ($v \approx 2.5$). **c** Magnetotransport measurements showing the **B** derivative of the longitudinal resistance as a function of filling factor v and the normalized flux quantum per moiré super lattice unit cell of a tBLG moiré device ($\theta^{exp.} \approx 0.97^\circ$). Landau fans emerge from integer-values of the filling factor. For additional hBN alignment (right) we observe additional lines starting at non-integer fillings ($v \approx 2.5$). **d** Zoom-ins of (c) **e** Dashed black lines (integer fillings) and dashed blue lines (non-integer fillings) as guide to the eye for (d).

Our interpretation of hBN alignment is supported by the absence of any indications of superconductivity in our device which is in agreement with hBN-aligned twisted bilayer graphene devices reported in literature [417–419]. Although this could also be caused by our relatively low twist-angle we want to highlight that these indications were found at clearly lower angles than the one discussed here [432].

12.5 Conclusion

We studied a twisted bilayer graphene system at a twist angle of approximately 0.97° which exhibited additional alignment to hBN. Hereby, we were able to find evidence of this alignment from magnetotransport measurements which showed remarkable agreement with the theoretical prediction. Band structure calculations revealed that the competing superlattice reinforces an intrinsic electron-hole asymmetry twisted bilayer graphene. The presence of the additional superordinate moiré lattice introduces new Landau fan features at fillings corresponding to the relative size of the two moiré unit cells.

Chapter 13

Summary

“Common Sense is that which judges the things given to it by other senses.”

Leonardo da Vinci

Throughout this thesis we have studied the influence of various forms of lattice imperfections (point defects, grain boundaries, ...) on the electronic properties of two-dimensional materials. We have (among other things) calculated level spectra of quantum dots via large-scale tight-binding, simulated electronic transport in moiré systems and developed a machine learning algorithm to aid in the extraction of defect parametrizations from ab-initio band structures. I strongly encourage to look up the conclusion/outlook sections of each individual chapter but nevertheless provide concise summaries for the weary reader.

Manipulating quantum dots through nearby lattice defects We calculated the effect of lattice defects in single layer graphene on the level spectrum of smoothly confined quantum dots (Chapter 5). Different types of defect induce valley splittings Δ^τ of up to 12 meV. We showed that controlled motion of the quantum dot (generated via STM or electronic gates) allows for controlled transition dynamics that are well captured by Landau-Zener theory. Controlled breaking of the valley symmetry is a vital ingredient for building quantum logic gates based on graphene technology in the future.

Sparse TB parametrizations via machine learning We have explored various forms of modern machine learning concepts in order to aid in the extraction of tight-binding parametrizations for defect super cells calculated in ab-initio density functional codes (Chapter 6). We have identified neural networks as promising candidates and successfully applied a purely distance based algorithm to two point defects in single layer graphene. A proof-of-principle approach for generalization to discrete Slater-Koster maps allows studying a di-vacancy in WSe₂.

Two particle spectra in BLG quantum dots This chapter focused on our efforts to correctly reproduce two particle spectra measured in the Stampfer group at the RWTH Aachen (Chapter 7). We set up an elegant numerical apparatus to re-diagonalize a bare Coulomb kernel in a basis

of confined BLG wavefunctions. Missing the vital ingredient of short-range symmetry breaking perturbations we nevertheless learned a lot about efficiently evaluating four-orbital-integrals.

Strain enhanced photoluminescence in WSe₂ Collaborating with the group of S. Heeg in Berlin we provided theory support for photoluminescence measurements of strained WSe₂ in Chapter 8. A fairly simple model that correctly captures the influence of strain on the single-particle energies of a vacancy defect appears as the prime candidate to explain strong enhancement of emission encountered in the experiment. Improvement descriptions of the full defect cell open the door for future collaborations on time-resolved Kerr microscopy data.

Grain boundary induced valley polarization Studying the valley filtering properties of grain boundaries we map their energy and angle dependent transmission landscape in Chapter 9. Employing first class defect parametrizations we find qualitative agreement with old theory predictions. Interesting resonance behavior with bound defect states warrants additional investigation.

Probing quantum Hall edge states at an electrostatically define pn-junction in graphene Together with the group of Markus Morgenstern at the RWTH Aachen we carefully investigate edge states in the quantum Hall regime in Chapter 10. A partially covering back gate creates an artificial edge in single layer graphene. Meticulous extraction of parameters for Poisson and TB calculations reveal parameter regimes in which these edge states can be mapped via scanning tunneling microscopy with only minimal perturbations from the tip induced quantum dot.

Quantum Hall conductivity in graphene/hBN moirés We employ ab-initio derived models of real space moiré super cells of graphene/hBN systems and utilize efficient numerical methods to calculate quantum Hall conductance maps as a function of both magnetic field and charge carrier density (Chapter 11). The current approach based on evaluating magnetic field derivatives prevents us from meaningful experimental comparison as it only applies to the gapped part of the spectrum.

Competing moirés in encapsulated tBLG Modeling two moiré lattices in concert we corroborate experimental data from the Stampfer group at the RWTH Aachen in Chapter 12. The presence of two superordinate length scales in these systems leads to the emergence of additional Landau fan features at filling ratios defined by the relative areas of the moiré super cells.

In the course of my thesis I worked on several projects that, to varying extent, focus on the influence of lattice defects (point defects, grain boundaries and “artificial” defects in the form of potential steps) on the physical properties of their host system. While the constant ambition to improve predictive aspects of theoretical defect models inevitably also increases model complexity we find that in some instances simple models also provide surprisingly good agreement with experimental data. I have explored the prospects of employing machine learning algorithms to generate accurate tight-binding parametrizations for defects. While our algorithm is not yet general enough to avoid the Wannier formalism altogether we nevertheless took an important first step in its conceptualization and application.

We also developed state-of-the-art algorithms to study quantum transport of large (small twist angle) bilayer systems in the context of moiré physics. The recent and rightfully exciting observations of correlated physics in these systems call for careful analysis of features that may already be explained via mean-field physics. Graphene offers a seemingly shallow entrance into open questions of solid state physics. It provides a platform to study complicated things such as high-temperature superconductivity, (proximity induced) spin-orbit textures of highly mobile electrons (spintronics) and possibly magnetic phases in a fiendishly simple material that merely consists of the very same carbon atoms that make up pencil lead.

The relentless improvement in sample quality and system control in bilayer graphene systems among experimental groups (e.g. RWTH Aachen) continues to challenge theory to provide not only retrospective understanding but aid in sample design via realistic simulations (e.g. Poisson-Schrödinger solver for optimal gate design).

Appendices

Acknowledgements

The computational results presented, have been achieved [in part] using the Vienna Scientific Cluster (VSC3, VSC4 and VSC5).

I would like to thank all the people without whom this thesis would have never been possible:

Starting with my supervisor Prof. Florian Libisch, who not only always found a few minutes to answer questions but whose various connections to excellent physicists around the world has lead to lots of interesting collaborations with experimental groups. Despite Covid wreaking havoc on working environment throughout essentially most of my PhD time he managed to establish a stress-free environment to work and study in. Talking to other PhD students in larger groups always reveals that interacting with your supervisor in a friendly, informal and nonchalant manner the way Florian encourages it, is in no way common.

My examiners for the time and patience required to read and grade this thesis.

Prof. Joachim Burgdörfer for his profound insights in physics, global politics and history which he (to the delight of me and my fellow PhD students) freely shares so long as chocolate is present during coffee brakes. Furthermore for granting me the possibility to partake in the teaching side of research in the analytical mechanics lectures.

My colleagues, Valerie Smejkal, Lukas Linhart, Thomas Fabian, Isabella Floss, Stefan Donsa, Iva Hunger-Brezinova, Fabian Lackner, Christoph Lemell, Felix Hummel, Siyar Duman, Tobias Jawecki, Nina Girotto and the students whom I supervised during their projects at the institute.

All the collaborators (especially the groups of Prof. Morgenstern, Prof. Stampfer and Prof. Rinke) with whom I had the pleasure to work, publish or discuss interesting physics.

The administrative group of Heike Höller, Silvia Riedler, Ingrid Unger, Almaz Murshudova and Prof. Kahl that keep the institute for theoretical physics running.

My Family and friends. Especially my parents whose unconditional love and support have helped me throughout my entire life and never once questioned my academic choices. Thank you for everything!

My wife, Lili, for always understanding and supporting me. I could not have faced the various troubles and adversities that come with pursuing a PhD without her. Thank you for being the lighthouse of my universe!

Appendix A

Band structure reconstruction for the sparse ML models

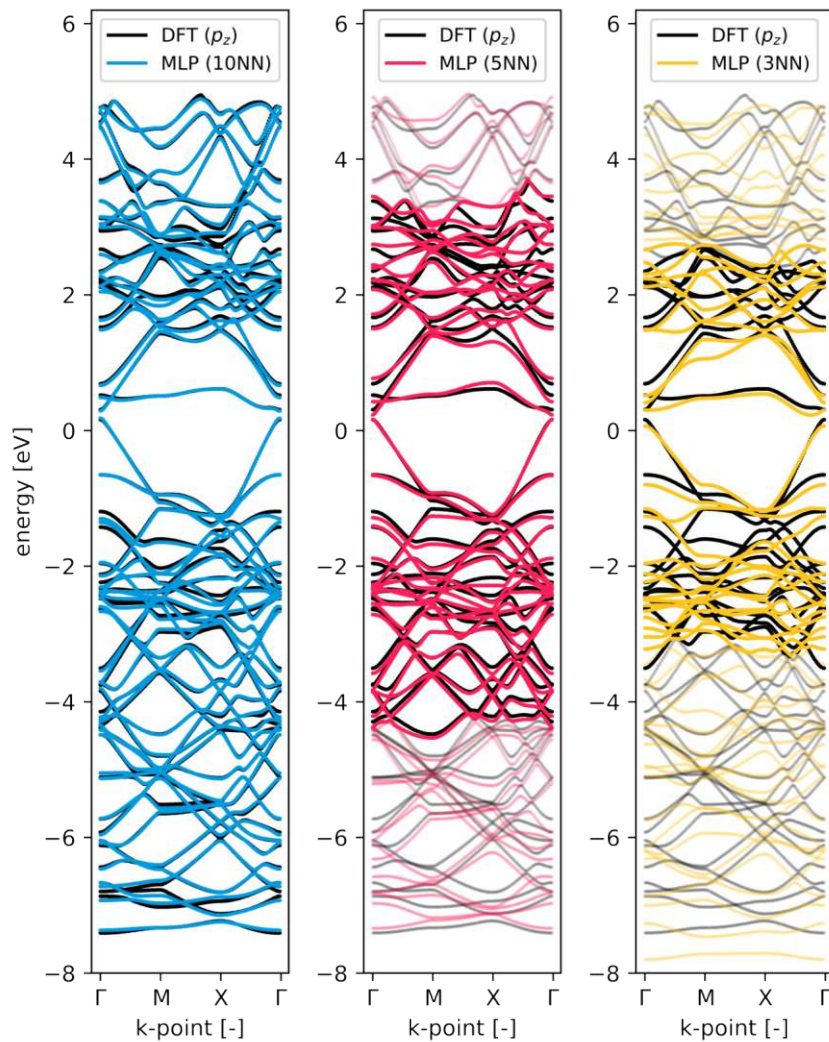


Fig. A.1: BS comparison for ML parametrizations (double vacancy) of different sparsity (indicated as xNN) with DFT BS as reference. Bands that are not explicitly part of the loss function \mathcal{L}_e are drawn in a fainter color.

Following the main text in Section 6.6.1 we present additional plots for the comparison of ML models with different sparsity regarding BS approximation accuracy and LDOS similarity. The desired sparseness and the number of

input bands accounted for in the loss function \mathcal{L}_e are a priori independent in our algorithm. However, very sparse models that aim to evenly minimize BS loss across all bands tend to reproduce very low/high bands slightly more accurately at the cost of performing much worse for bands around the Dirac point (i.e. $E = 0$). Since in graphene these are the bands relevant for transport we exclude a subset of extremal bands (i.e. low or high in energy, fainter lines in Fig. A.1 and Fig. A.2) from the loss function. This slightly improves accuracy for the bands of interest and also reduces model complexity but comes at the cost of larger errors in reproducing the extremal bands (this appears to be more pronounced for the flower defect).

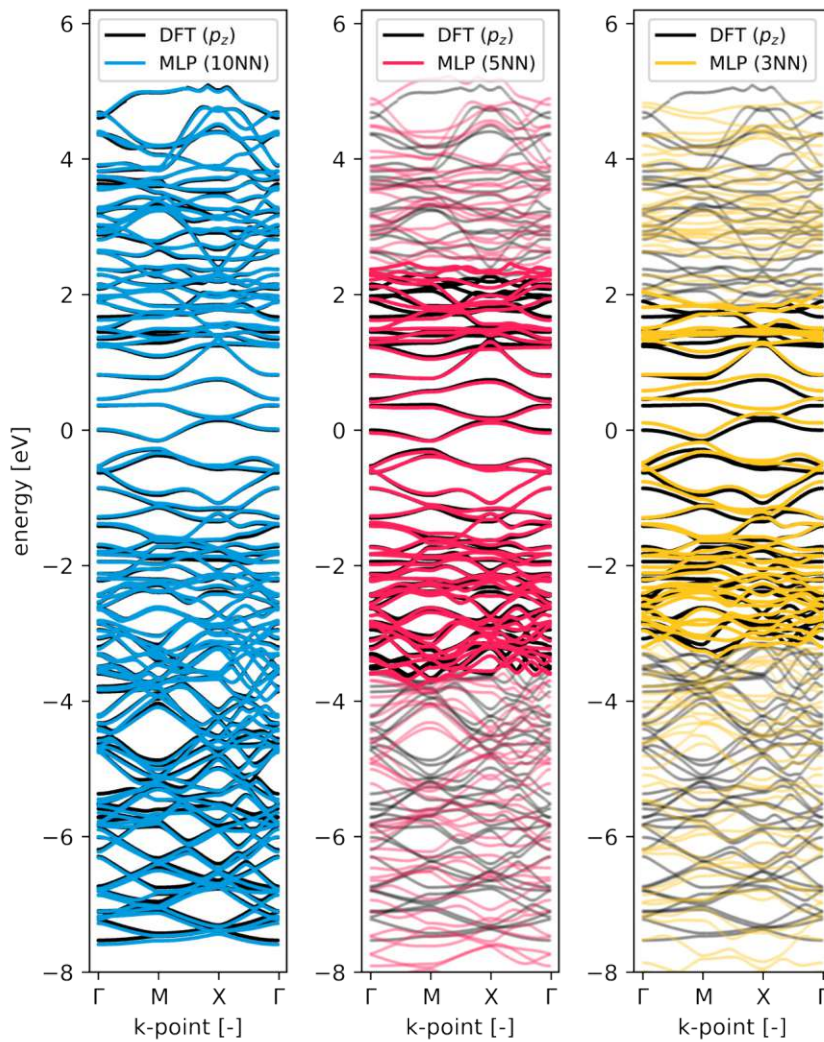


Fig. A.2: BS comparison for ML parametrizations (flower defect) of different sparsity (indicated as xNN) with DFT BS as reference. Bands that are not explicitly part of the loss function \mathcal{L}_e are drawn in a fainter color.

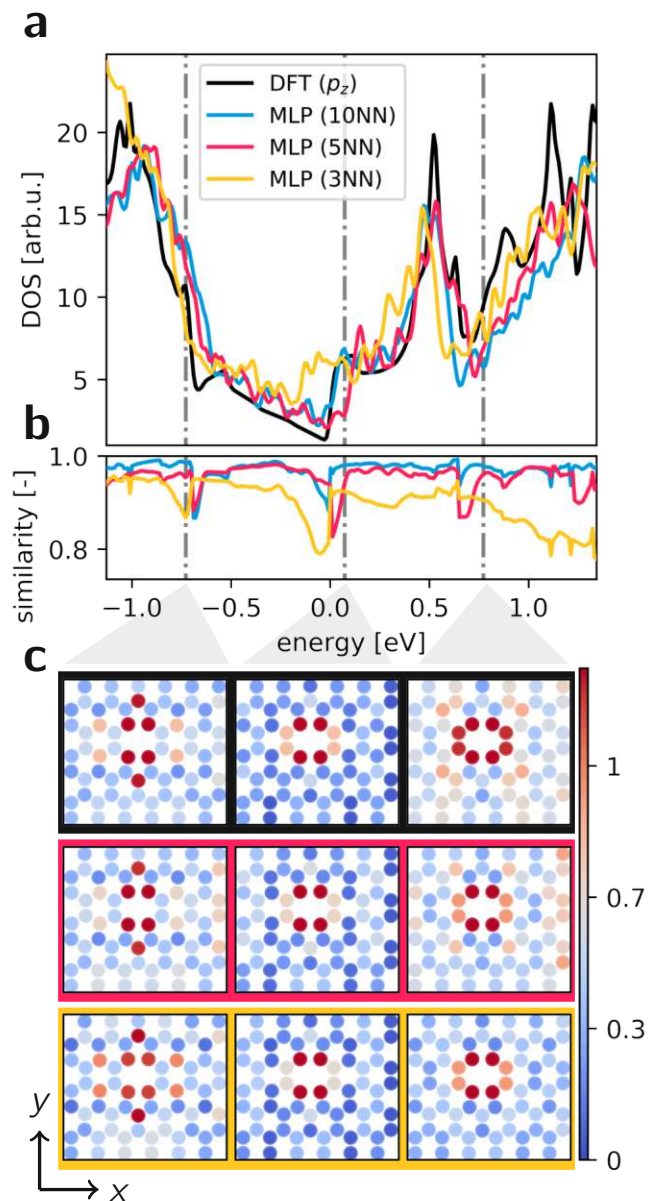


Fig. A.3: DFT results vs. double vacancy ML parametrizations of different sparsity (sparsity indicated by xNN and line colors). **a** DOS over a limited energy range **b** Cosine similarity of the **c** LDOS distribution within the supercell.

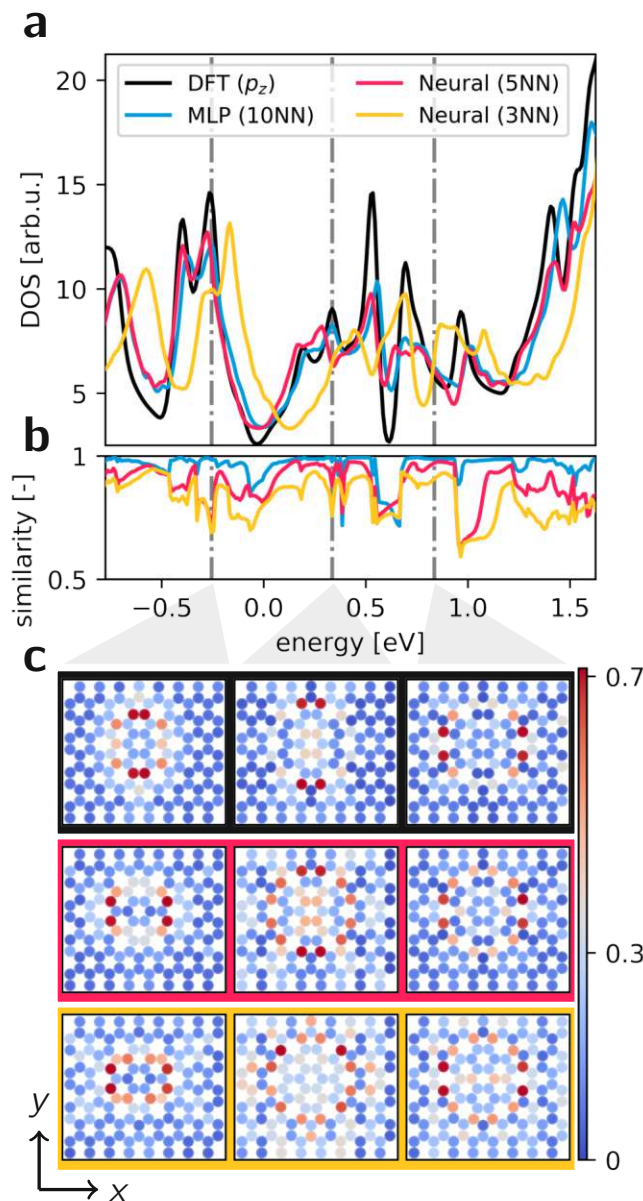


Fig. A.4: DFT results vs. flower defect ML parametrizations of different sparsity (sparsity indicated by xNN and line colors). **a** DOS over a limited energy range **b** Cosine similarity of the **c** LDOS distribution within the supercell.

Appendix B

Sample fabrication and measurement details

All devices are fabricated by transferring [433] mechanically exfoliated WSe₂ monolayers onto a circular hole (diameter $\sim 5\mu\text{m}$) etched 700nm into Au/Cr/SiO₂/Si (70 nm/3 nm/1500 nm/300 μm) substrates. The large thickness of SiO₂ allows applying voltages of up to ± 280 V before the dielectric rupture of the sample, but measurements are typically limited to ± 235 V for sample protection. The monolayers are many times larger than the hole to ensure device stability. Room temperature PL mapping of the finished device is used to confirm that the monolayer uniformly covers the hole area. The devices are measured in vacuum inside a cryostat with the base temperature of 4 K. To avoid damage to the suspended WSe₂ during pump-down of the cryostat, a pressure relief channel is fabricated in SiO₂. Temperature at the sample is detected via an on-sample temperature sensor and confirmed by tracking the energetic blueshift and linewidth narrowing of the (bright) neutral exciton. PL measurements are carried out in a homebuilt setup using a tightly focused laser (diameter $\sim 1\mu\text{m}$) placed at the centre of the device. We excite the membranes with a linearly polarized, CW laser with $\lambda = 532\text{nm}$ and power $\sim 10\mu\text{W}$ (power density 500 Wcm^{-2}) and in the range $100\text{ nW} - 4.5\mu\text{W}$ to quantify the character of excitonic states (power densities $5\text{ W/cm}^2 - 250\text{ W/cm}^2$). Additionally, from power-dependent measurements we estimate the defect concentration on our samples to be in the order of 10^{10}cm^{-1} (see Fig. B.1) [434]. Photoluminescence excitation spectroscopy in the range $570\text{ nm} - 675\text{ nm}$ with a pulsed laser source (femtosecond Ti:Sa Chameleon Ultra II + OPO-VIS) is used to quantify the contribution of interference effects in our data. We ascribe strain values to each spectrum by measuring energetic shifts for excitonic species and assuming the shift rate $95\text{meV}/\%$ [322] for all free excitons. This analysis is confirmed through separate interferometric measurements capable of directly measuring membrane displacement with nanometer resolution. To identify excitonic species in our PL data, we compare their energy position and the binding energy (measured with respect to the X_0 position) with detailed measurement of excitonic species in high-quality unstrained devices encapsulated in hBN [315, 317, 435, 436]. While the difference in electrostatic screening between suspended and encapsulated devices leads to noticeable changes in the binding energy of the excitons, in most cases the identification is possible.

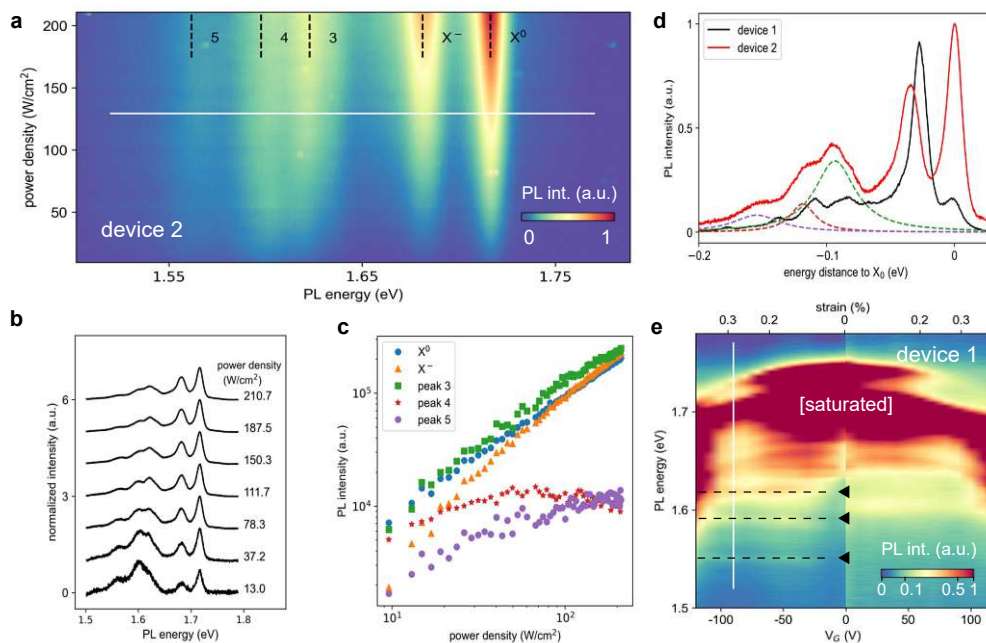


Fig. B.1: In Fig. 8.3 of the main text we observe strain-independent lines in the PL energy range between 1.55 – 1.6 eV that we assign to defect-related excitons. This assignment is supported by the detailed analysis of excitation power and V_G dependence of PL spectra. **a** PL vs. excitation power for an unstrained membrane ($V_G = 0$) measured on device 2 at 77 K. We identify neutral (X^0) and charged exciton (X^-) and three other peaks labelled 3 – 5 in decreasing energy order (black dashed lines). **b** PL spectra at selected excitation power densities. Spectra are normalized and offset for clarity. Peaks 3 – 5 dominate the PL spectrum at lower excitation powers while X^0 and X^- dominate at higher powers. **c** PL integrated intensities of the five peaks marked with dashed lines in (a) as a function of excitation power density. PL intensities are obtained by fitting the PL spectra to five Lorentzians. X^0 and X^- show an approximately linear dependence with excitation power. This behaviour is typical for free excitons [324]. PL intensities of peaks 3, 4 and 5 saturate with power indicating the defect-related character of the emission at those energies. **d** PL spectra of devices 1 and 2 featuring the same set of defect peaks, confirming their reproducibility. Spectra for device 1 (black) and device 2 (red) are extracted from the white lines in (e) and (d), respectively. Typically fitted spectra for device 2 corresponding to peaks 3 – 5 shown in (a)-(c) are plotted with dashed lines. **e** PL spectra vs. V_G for device 1. The energies of defect-related states are almost strain-independent, as expected from theory. (a)–(e) are measured at excitation 532 nm. (d) and (e) are measured at excitation power density 250 W cm⁻².

Strain response of excitonic states in WSe₂ at 100K and 10K

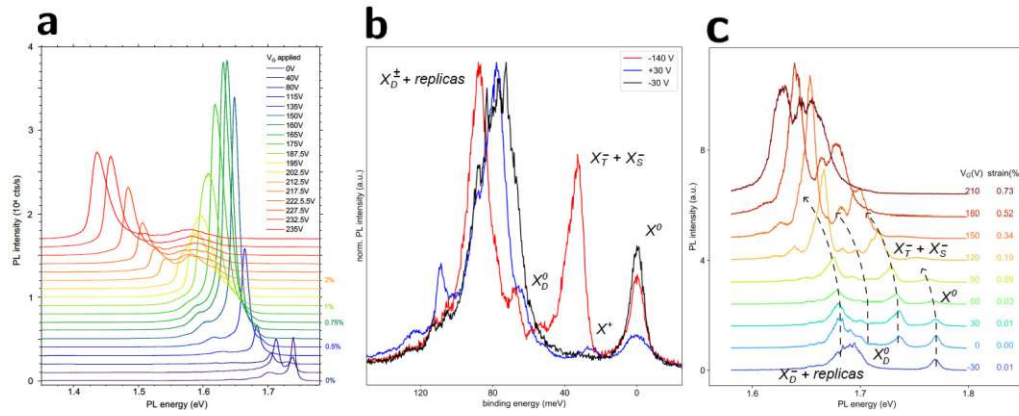


Fig. B.2: **a** PL spectra of the suspended WSe₂ monolayer (device 1) at T = 100 K and positive V_G . Here the spectra are offset for clarity to allow for tracking individual peaks as a function of gate voltage / strain. In **b** Normalized PL spectra measured at T = 10 K (device 1) in the electron doping (red line), hole doping (blue) and charge neutrality (black) regimes under negligible strain. We identify a bright neutral exciton (X^0) at 1.769 eV, positive (X^+ , binding energy 29 meV) and negative trions (X_T^- and X_S^- , 32 and 38 meV) and a dark neutral exciton (X_D^0 , 17 meV below X_S^-). We observe a lower energy PL band peaking at 80 meV and 87 meV below (X^0) for hole and electron doping, respectively. We assign this PL band to dark trions (X_D^\pm) and their phonon replicas. **c** Selected PL spectra measured at T = 10 K (device 1) at different voltages (strain values), offset for clarity. We mark the excitonic species identified in (a) with dashed lines and track their PL signatures upon increasing voltage. PL intensity of dark trions and their replicas and dark neutral exciton increase 6 and 20 times, respectively, as compared to their unstrained values when their energies approach the D1 hybridization energy 1.52 eV.

Confirmation of strain extraction and mechanical constants from optical measurements

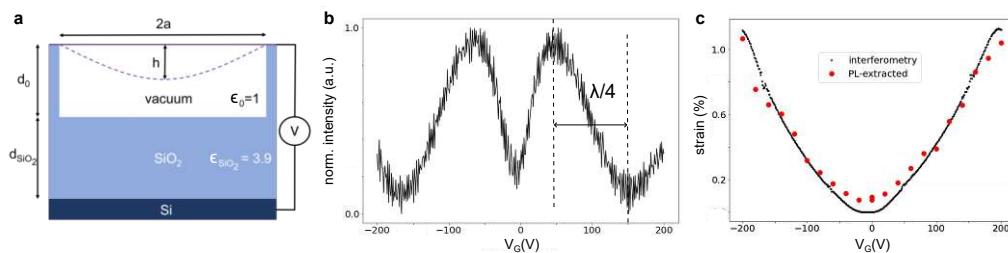


Fig. B.3: In the main text, we obtain strain at each gate voltage by measuring the shift in the energy position of the neutral exciton compared to its unstrained position. Here, we confirm the assignment of strain via an independent interferometric measurement. **a** Schematic of the device used in the main manuscript seen as an interferometric cavity. A circular monolayer WSe₂ membrane of radius $a = 2.5\mu\text{m}$ is suspended over a hole in SiO₂ and actuated (displacement h) by applying gate voltage V_G between WSe₂ and a Si substrate underneath (see Methods for details). The device is measured at room temperature by recording the reflected laser intensity of the laser beam ($\lambda = 633\text{nm}$, $P = 10\mu\text{W}$) focused on the membrane's center vs. V_G **b**. The interference of the laser beam in the optical cavity consisting of vacuum, SiO₂ and Si results in the changes of absorption by the membrane. With increasing $|V_G|$, the membrane moves downwards and the reflected intensity changes depending on the position of the membrane with respect to the nodes of the interference pattern. Quantitatively, a displacement of the membrane by $\lambda/4$ produces a change of π (half a period) in the phase of the sinusoidal modulation of the reflected signal. In this way we extract the position of the membrane's center h vs. V_G from the observed intensity of reflected light. Next, we convert the displacement into mechanical strain using the formula $\varepsilon = \frac{2h^2}{3a^2}$ obtained from the analysis of the system's geometry [332]. The resulting data are plotted in **c** as black dots. For comparison, in the same graph we plot as red circles the values of strain obtained from the photoluminescence energetic shift of the excitonic peaks following the same procedure as in the main text. Both approaches to estimate strain produce very similar strain values.

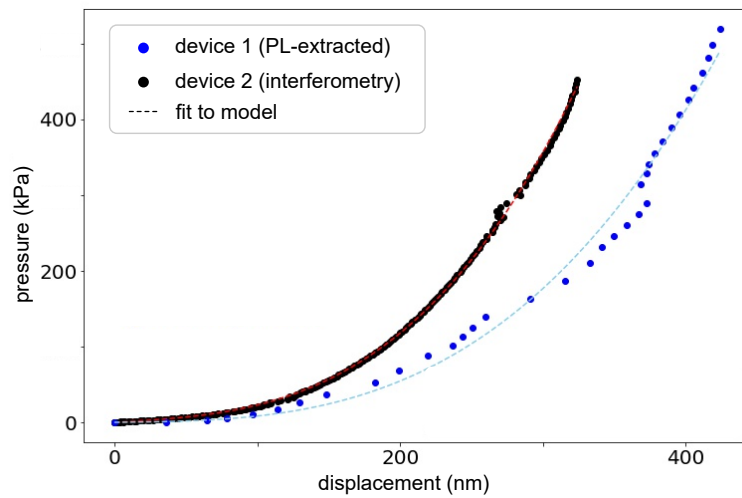


Fig. B.4: To confirm the validity of the model of strain induced by electrostatic force used in the main text, we extract the mechanical constants of WSe₂ from PL measurements at room temperature. To do this, we first calculate the electrostatic pressure P acting on the suspended WSe₂ at a particular gate voltage. Modelling the system as a parallel plate capacitor (WSe₂/Si) with two media inside of it (vacuum, SiO₂), we obtain $P = \frac{\epsilon_0 \epsilon_{\text{SiO}_2}^2}{(\epsilon_0 d_{\text{SiO}_2} + \epsilon_{\text{SiO}_2} d_0)^2} \frac{V_G^2}{2}$. We then calculate the displacement of the central point of the membrane h from strain obtained via PL measurements using $\epsilon = \frac{2h^2}{3a^2}$, where a is the radius of the membrane. Finally, $P(h)$ data obtained this way is plotted for two different devices (1 and 2). This data is fitted using an analytical model for $P(h)$ that is based on the well-known bulge-test equation in thin-film mechanics [332, 437]. This model describes the deflection of a uniform circular membrane under uniform pressure using Young modulus E_{2D} and built-in strain ϵ_0 as free parameters as $P = \frac{4E_{2D}\epsilon_0}{a^2} h + \frac{8E_{2D}}{3(1-\nu)a^4} h^3$, where $\nu = 0.2$ is the Poisson ratio for WSe₂ [438]. All data points agree quite well with the analytical fits (dashed lines). We obtained $E_{2D} \sim 74$ N/m and $\epsilon_0 = 0.04$ % for device 1 and $E_{2D} \sim 140$ N/m and $\epsilon_0 = 0.12$ % for device 2. The values are consistent with the mechanical constants typically reported for WSe₂ at room temperature [319].

Appendix C

Valley character of QDOT states in SLG

The preliminary analysis of radial and angular quantum number of quantum dot (QDOT) states in single layer graphene (SLG) calculated in the Green's code [199, 247] within a tight-binding framework necessitates correction of the phase $e^{ik \cdot r}$, the wave function acquires depending on its localization in \mathbf{k} -space.

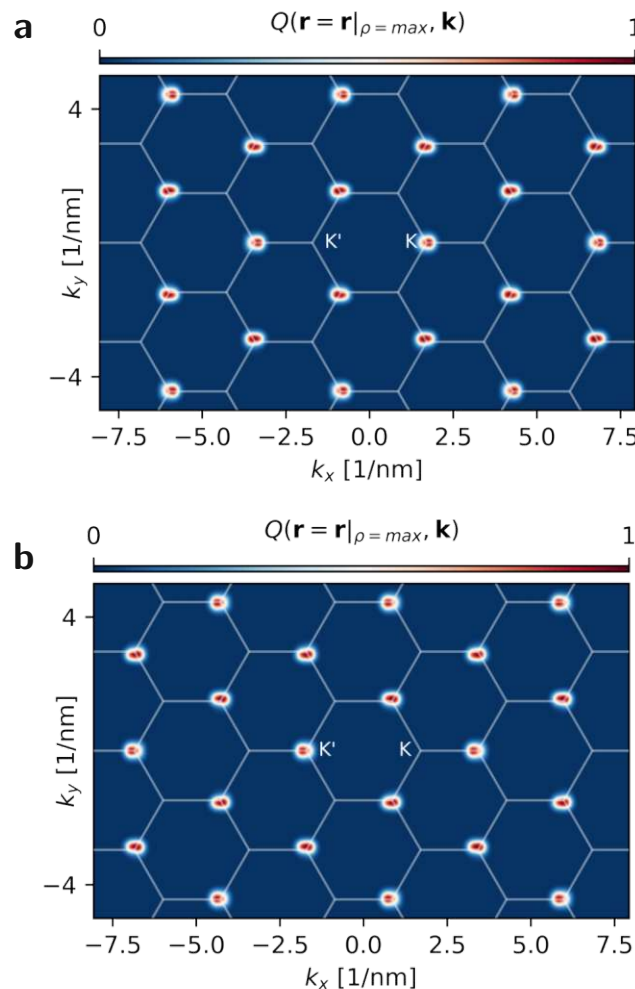


Fig. C.1: Husimi distributions $Q(\mathbf{r}, \mathbf{k})$ for the third **(a)** and fourth **(b)** eigenstate of the first Landau level, averaged over several positions of maximal real space probability density $\rho(\mathbf{r}) = |\psi|^2$ (indicated as $\mathbf{r}|_{\rho=\max}$).

Instead of just assuming that the smooth confinement potential Eq. (10.3) of our tip-induced QDOT does not induce valley mixing we verify the valley character by calculating the Husimi distribution [439] of the calculated TB wavefunctions. This quasi-probability density can be understood as a phase space distribution constructed in a basis of minimum uncertainty states:

$$Q(q, p; \sigma) = \frac{1}{2\pi\hbar} \langle q, p | \hat{\rho} | q, p \rangle \quad (C.1)$$

with

$$|q, p\rangle \stackrel{\{x\}}{=} \frac{1}{2\pi\sigma^2} e^{-\frac{(x-q)^2}{4\sigma^2}} e^{i\frac{px}{\hbar}}. \quad (C.2)$$

The code for evaluating this function at fixed real space coordinates (specified to the position of density maxima in real space) has been provided by friend of the group G. Datseris [440, 441]. We find that the two-fold degenerate QDOT orbitals are clearly localized in the respective valleys (see Fig. C.1) and thus confirm our fairly simple phase correction for determining the m quantum number (Section 10.4) as valid.

Appendix D

LDOS maps of the QDOT - PN system

This section presents additional LDOS maps for the PN - QDOT junction discussed in Chapter 10.

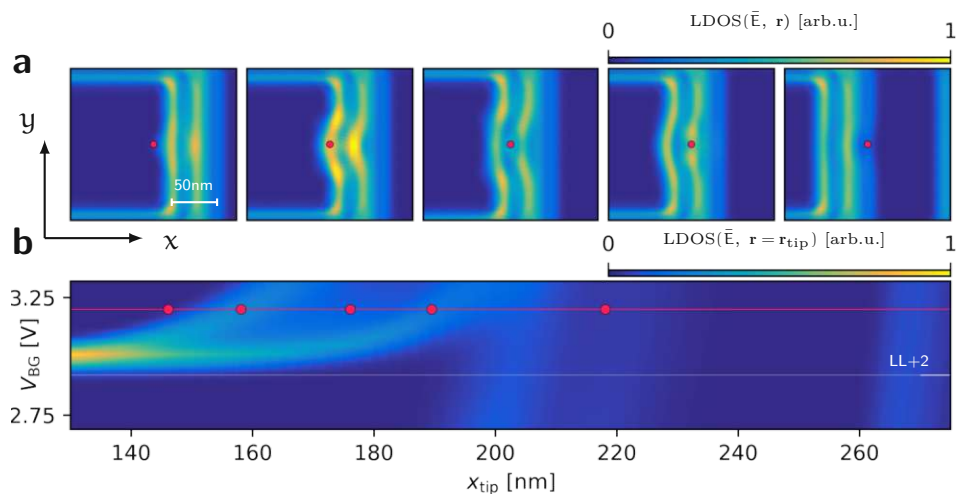


Fig. D.1: **a** Array of calculated LDOS colormaps across a zoom-in of the graphene flake for different x_{tip} (as indicated by red dots). **b** Zoom-in of Fig. 10.9d near LL+2 with coordinates ($V_{\text{BG}}, x_{\text{tip}}$) corresponding to panels in **a** again indicated as red dots.

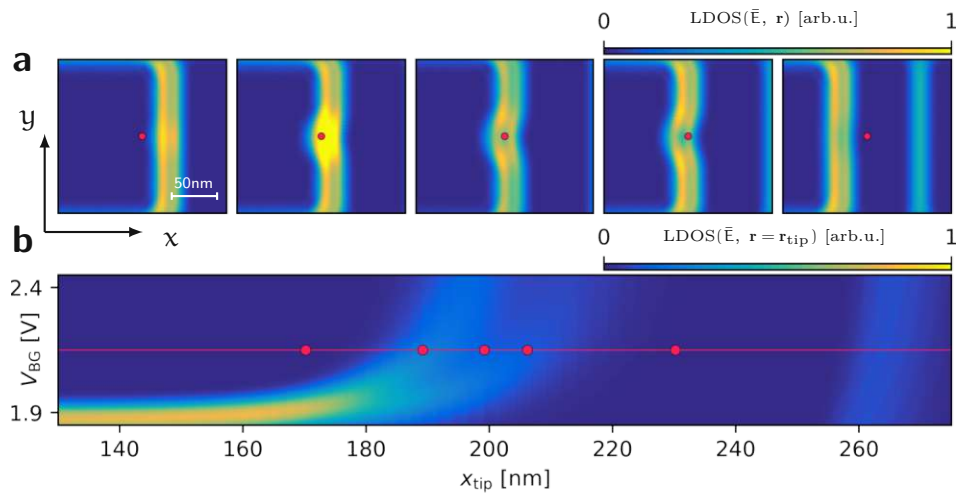


Fig. D.2: **a** Array of calculated LDOS colormaps across a zoom-in of the graphene flake for different x_{tip} (as indicated by red dots). **b** Zoom-in of Fig. 10.9d near LL+1 with coordinates ($V_{\text{BG}}, x_{\text{tip}}$) corresponding to panels in **a** again indicated as red dots.

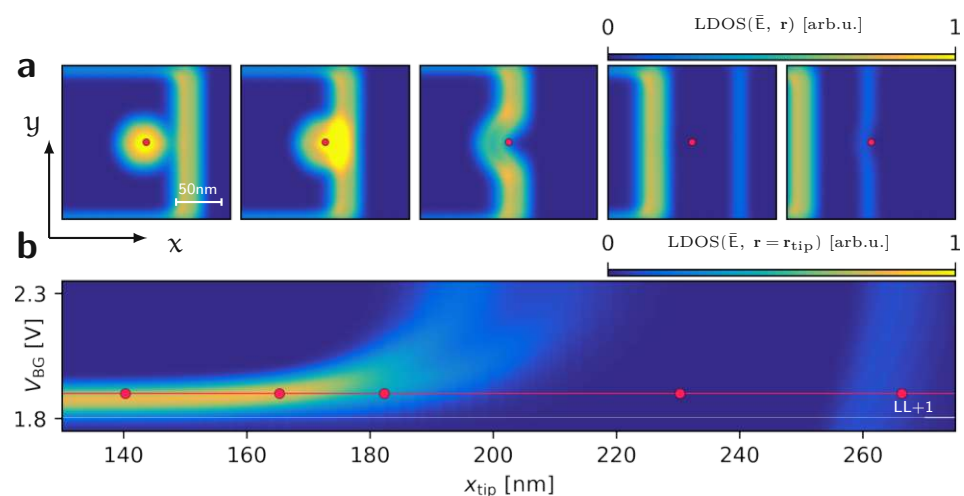


Fig. D.3: **a** Array of calculated LDOS colormaps across a zoom-in of the graphene flake for different x_{tip} (as indicated by red dots). **b** Zoom-in of Fig. 10.9d near LL+1 with coordinates (V_{BG} , x_{tip}) corresponding to panels in **a** again indicated as red dots.

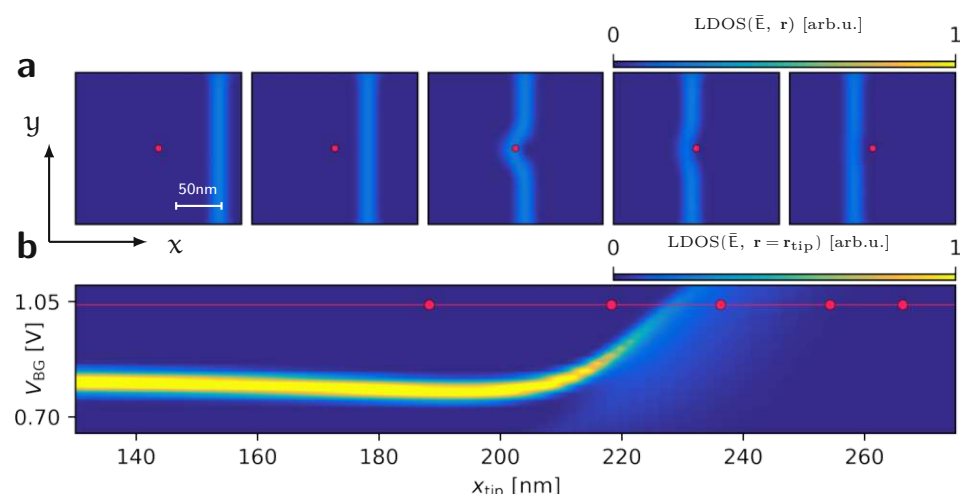


Fig. D.4: **a** Array of calculated LDOS colormaps across a zoom-in of the graphene flake for different x_{tip} (as indicated by red dots). **b** Zoom-in of Fig. 10.9d near LL-1 with coordinates (V_{BG} , x_{tip}) corresponding to panels in **a** again indicated as red dots.

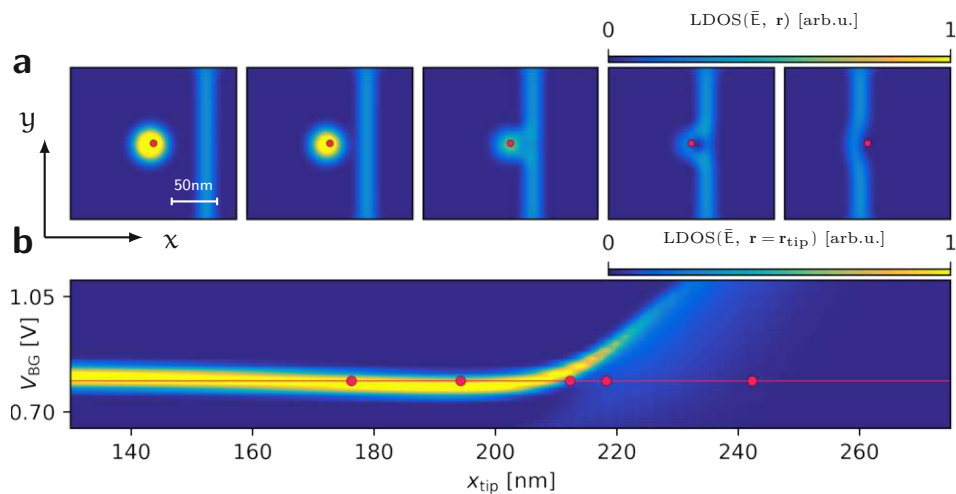


Fig. D.5: **a** Array of calculated LDOS colormaps across a zoom-in of the graphene flake for different x_{tip} (as indicated by red dots). **b** Zoom-in of Fig. 10.9d near LL0 with coordinates (V_{BG} , x_{tip}) corresponding to panels in **a** again indicated as red dots.

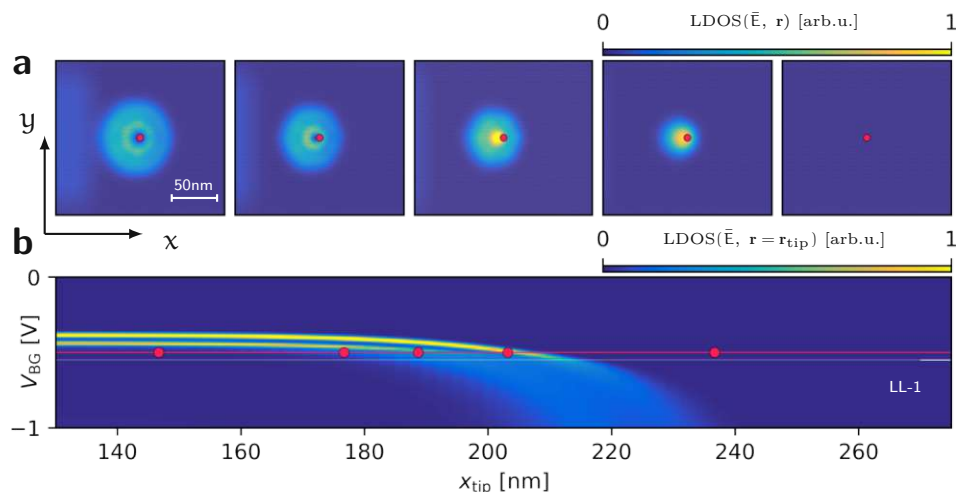


Fig. D.6: **a** Array of calculated LDOS colormaps across a zoom-in of the graphene flake for different x_{tip} (as indicated by red dots). **b** Zoom-in of Fig. 10.9d near LL-1 with coordinates (V_{BG} , x_{tip}) corresponding to panels in **a** again indicated as red dots.

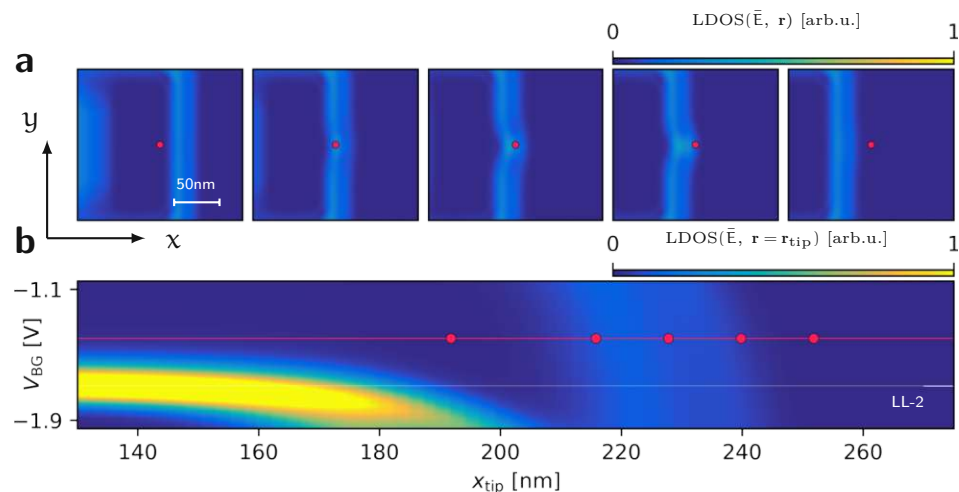


Fig. D.7: **a** Array of calculated LDOS colormaps across a zoom-in of the graphene flake for different x_{tip} (as indicated by red dots). **b** Zoom-in of Fig. 10.9d near LL-1 with coordinates ($V_{\text{BG}}, x_{\text{tip}}$) corresponding to panels in **a** again indicated as red dots.

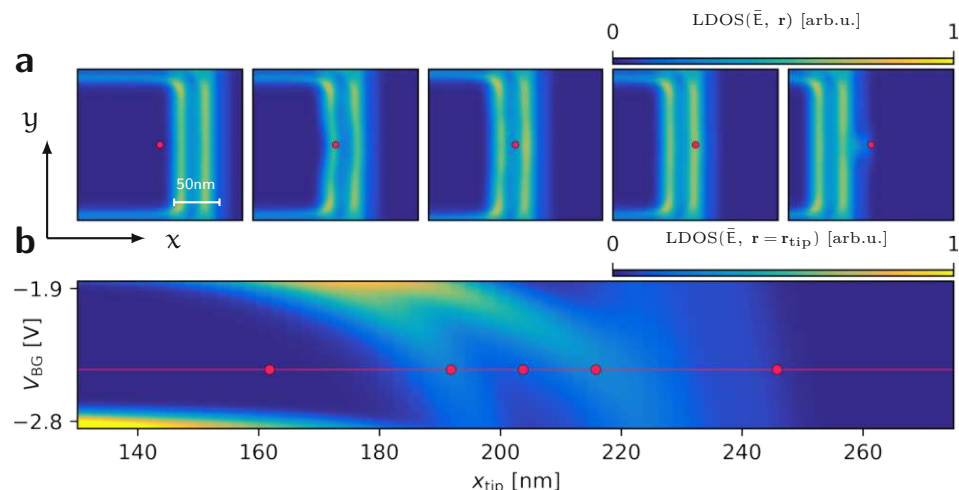


Fig. D.8: **a** Array of calculated LDOS colormaps across a zoom-in of the graphene flake for different x_{tip} (as indicated by red dots). **b** Zoom-in of Fig. 10.9d near LL-2 with coordinates ($V_{\text{BG}}, x_{\text{tip}}$) corresponding to panels in **a** again indicated as red dots.

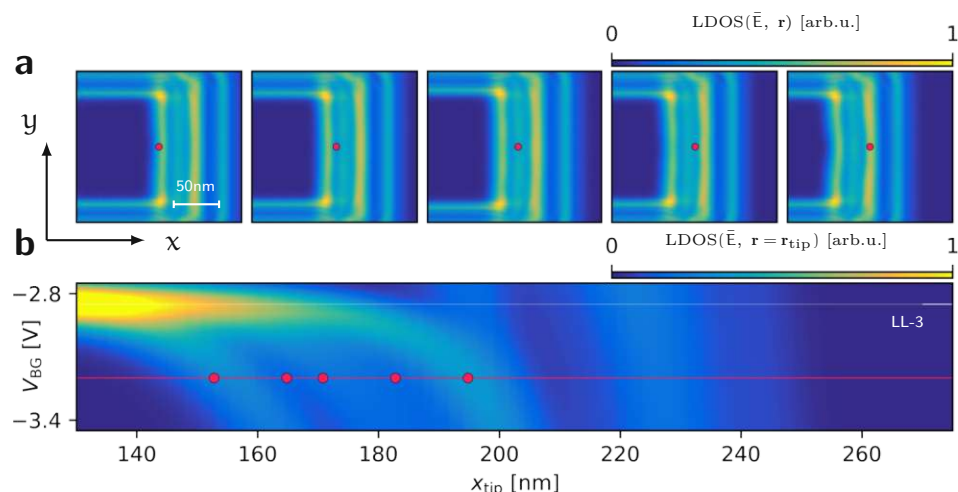


Fig. D.9: **a** Array of calculated LDOS colormaps across a zoom-in of the graphene flake for different x_{tip} (as indicated by red dots). **b** Zoom-in of Fig. 10.9d near LL-3 with coordinates (V_{BG} , x_{tip}) corresponding to panels in **a** again indicated as red dots.

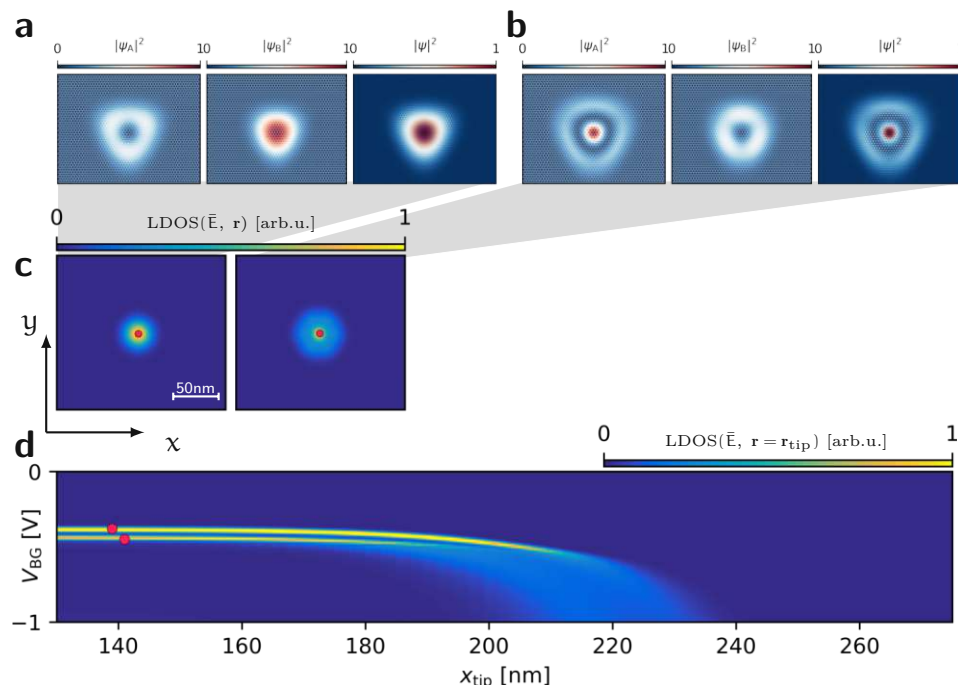


Fig. D.10: **a,b** Square amplitude of the state with the largest contribution to the LDOS in **c** (cohesiveness indicated with grey shading). States are valley degenerate and feature pronounced sub lattice structure. The degenerate partner states (not shown) feature inverted triangular shapes that sum to fairly spherical LDOS signatures in **c**. **c** Array of calculated LDOS colormaps across a zoom-in of the graphene flake for different x_{tip} (as indicated by red dots). **d** Zoom-in of Fig. 10.9d near the branching of LL-1 with coordinates (V_{BG} , x_{tip}) corresponding to panels in **c** again indicated as red dots.

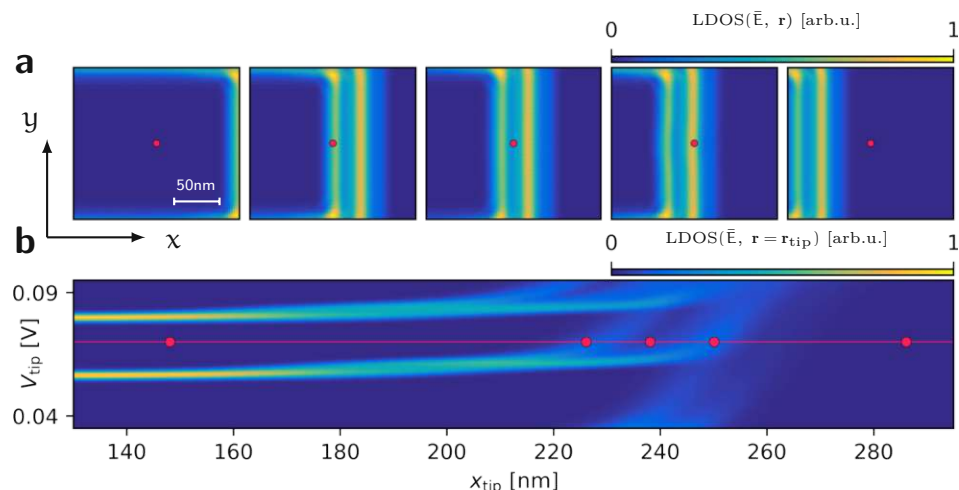


Fig. D.11: **a** Array of calculated LDOS colormaps across a zoom-in of the graphene flake for different x_{tip} (as indicated by red dots). **b** Zoom-in of Fig. 10.12a for fixed V_{BG} with coordinates (V_{tip} , x_{tip}) corresponding to panels in **a** again indicated as red dots.

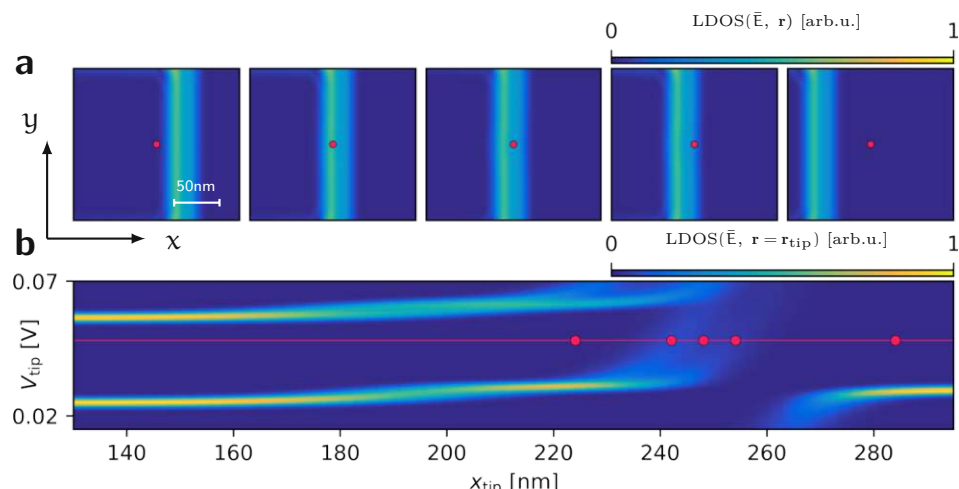


Fig. D.12: **a** Array of calculated LDOS colormaps across a zoom-in of the graphene flake for different x_{tip} (as indicated by red dots). **b** Zoom-in of Fig. 10.12a for fixed V_{BG} with coordinates (V_{tip} , x_{tip}) corresponding to panels in **a** again indicated as red dots.

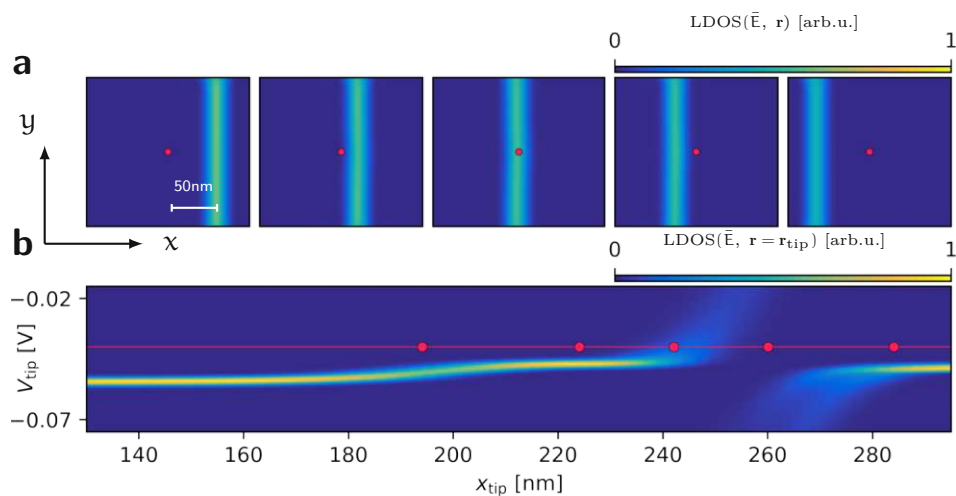


Fig. D.13: **a** Array of calculated LDOS colormaps across a zoom-in of the graphene flake for different x_{tip} (as indicated by red dots). **b** Zoom-in of Fig. 10.12a for fixed V_{BG} with coordinates (V_{tip} , x_{tip}) corresponding to panels in **a** again indicated as red dots.

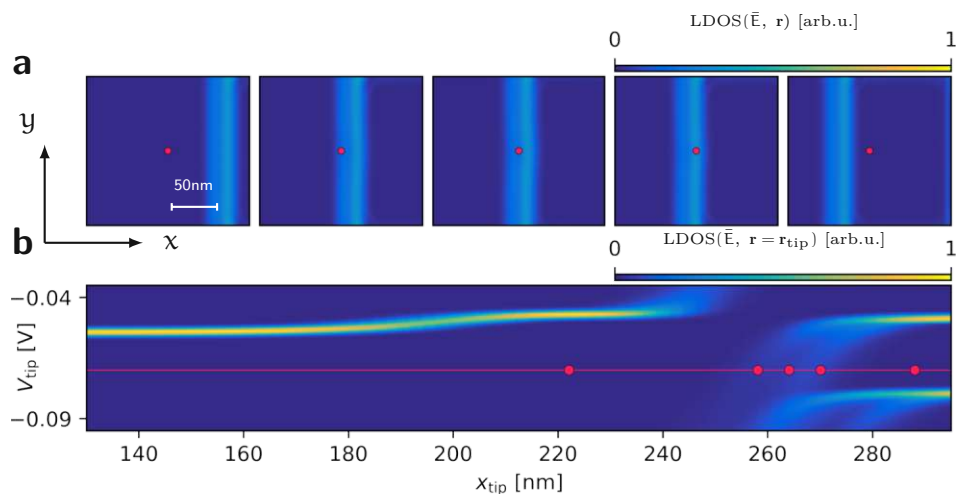


Fig. D.14: **a** Array of calculated LDOS colormaps across a zoom-in of the graphene flake for different x_{tip} (as indicated by red dots). **b** Zoom-in of Fig. 10.12a for fixed V_{BG} with coordinates (V_{tip} , x_{tip}) corresponding to panels in **a** again indicated as red dots.

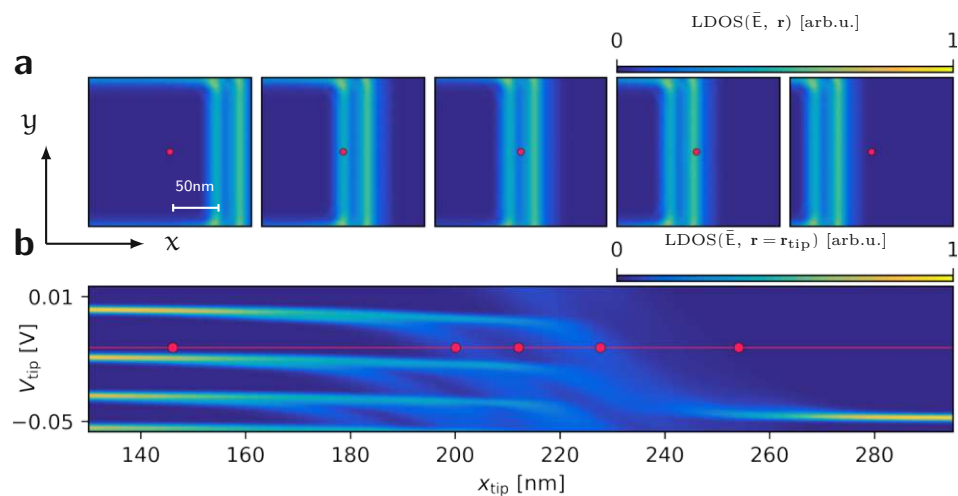


Fig. D.15: **a** Array of calculated LDOS colormaps across a zoom-in of the graphene flake for different x_{tip} (as indicated by red dots). **b** Zoom-in of Fig. 10.12b for fixed V_{BG} with coordinates (V_{tip} , x_{tip}) corresponding to panels in **a** again indicated as red dots.

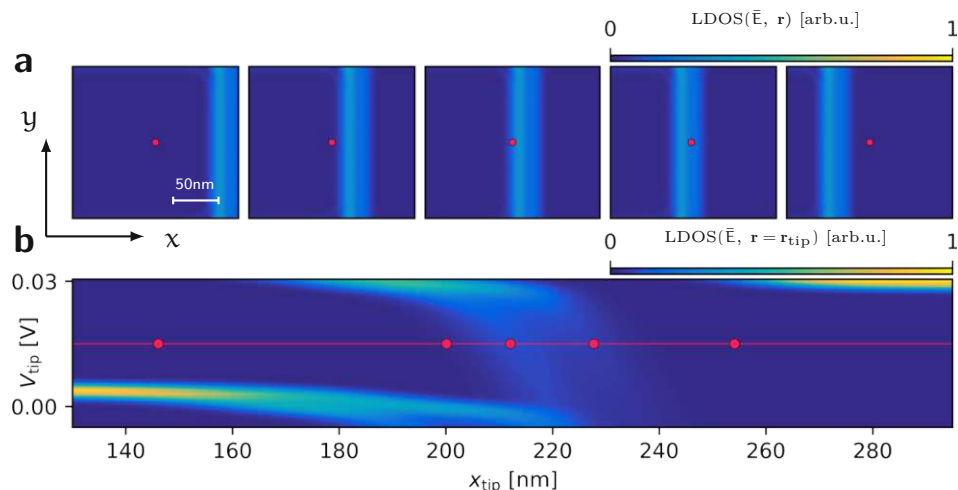


Fig. D.16: **a** Array of calculated LDOS colormaps across a zoom-in of the graphene flake for different x_{tip} (as indicated by red dots). **b** Zoom-in of Fig. 10.12b for fixed V_{BG} with coordinates (V_{tip} , x_{tip}) corresponding to panels in **a** again indicated as red dots.

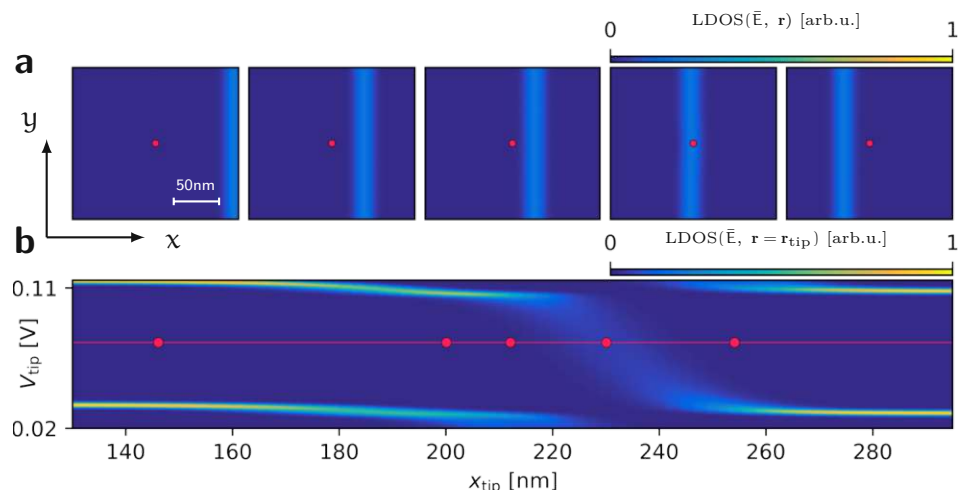


Fig. D.17: **a** Array of calculated LDOS colormaps across a zoom-in of the graphene flake for different x_{tip} (as indicated by red dots). **b** Zoom-in of Fig. 10.12b for fixed V_{BG} with coordinates $(V_{\text{tip}}, x_{\text{tip}})$ corresponding to panels in **a** again indicated as red dots.

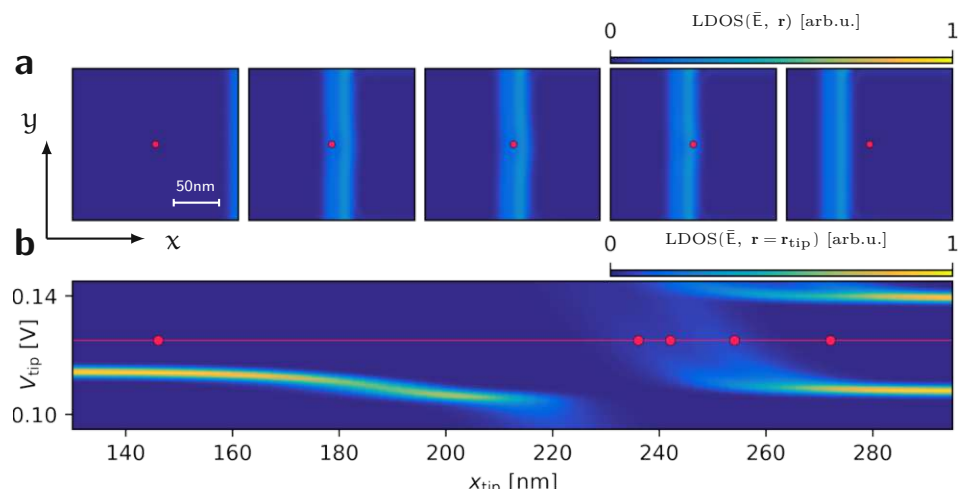


Fig. D.18: **a** Array of calculated LDOS colormaps across a zoom-in of the graphene flake for different x_{tip} (as indicated by red dots). **b** Zoom-in of Fig. 10.12b for fixed V_{BG} with coordinates $(V_{\text{tip}}, x_{\text{tip}})$ corresponding to panels in **a** again indicated as red dots.

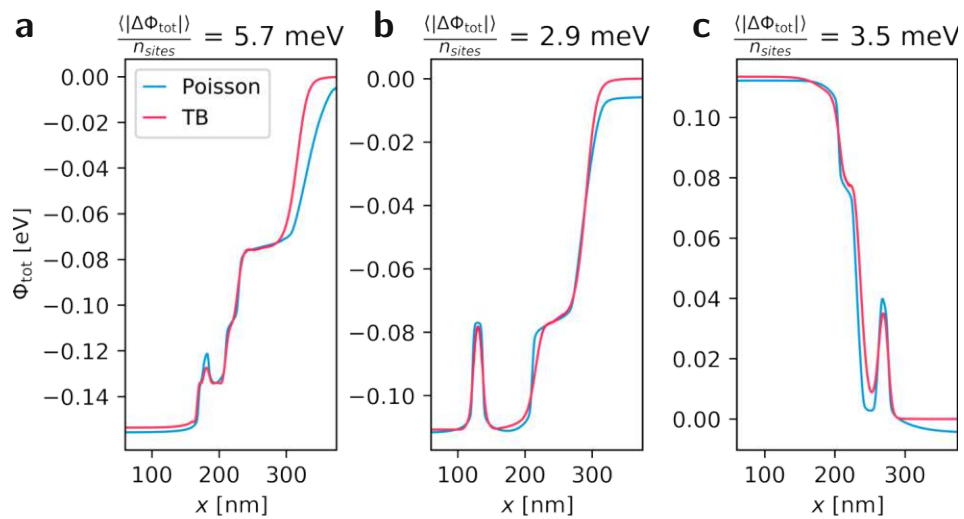


Fig. D.19: Detailed comparison of the potentials calculated with the 1D Poisson solver and the analytic fits used for the 2D TB calculations for three representative configurations of $(V_{\text{BG}}, x_{\text{tip}})$ **a** $\eta = -0.41$, $x_{\text{tip}} = 180\text{nm}$, **b** $\eta = -0.31$, $x_{\text{tip}} = 130\text{nm}$, **c** $\eta = 0.32$, $x_{\text{tip}} = 270\text{nm}$. The mean absolute difference of the two potentials $\frac{\langle |\Delta\Phi_{\text{tot}}| \rangle}{n_{\text{sites}}}$ per TB site is shown as well.

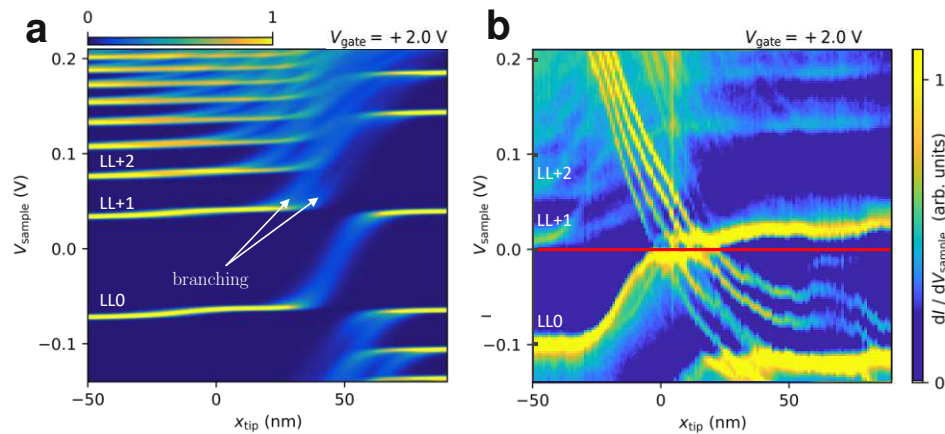


Fig. D.20: **a** Simulated LDOS(V_{sample} , x_{tip}) across the lateral interface, while including the TIQD, $V_{\text{gate}} = 2.0 \text{ V}$. **b** Measured dI/dV_{sample} (V_{sample} , x_{tip}), $V_{\text{gate}} = 2.0 \text{ V}$, $I_{\text{stab}} = 200 \text{ pA}$, $V_{\text{stab}} = -250 \text{ mV}$.

Appendix E

Charging lines in scanning tunneling spectroscopy

This section presents additional zooms into the $dI/dV_{\text{sample}}(V_{\text{gate}}, V_{\text{sample}})$ map of Fig. 10.2a,b in Chapter 10. The zoom in the lower right showcases Coulomb diamonds that appear when the different m states cross E_F (red line). The zooms in the lower left and the upper right of Fig. E.1 feature the kinks in the LDOS lines of $m = 0$ states away from E_F ($V_{\text{sample}} = 0 \text{ V}$) that appear whenever a charging line is crossing.

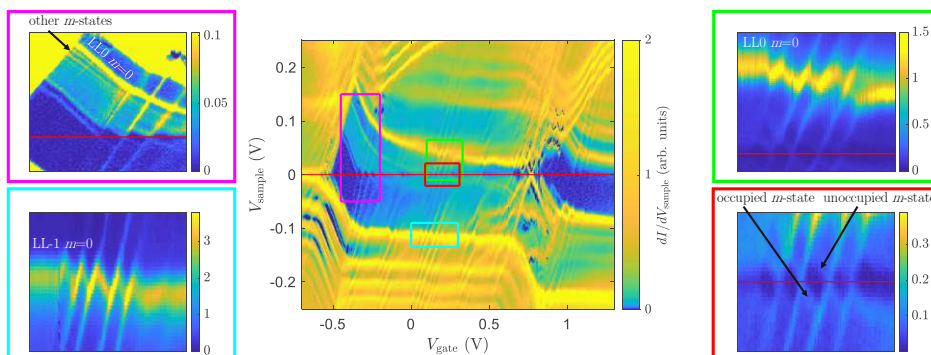


Fig. E.1: Zooms into dI/dV_{sample} ($V_{\text{gate}}, V_{\text{sample}}$) around the LL0 plateau at E_F at fixed position $x_{\text{tip}} \ll 0 \text{ nm}$ (same data as Fig. 10.2a,b in Chapter 10), $I_{\text{stab}} = 1 \text{ nA}$, $V_{\text{stab}} = -250 \text{ mV}$. The areas of the four zooms are marked in the central image by a frame of the same color. Magenta frame: LDOS lines of the various m states that belong to LL0. Cyan frame: Kinks in the LDOS line belonging to LL-1 that appear each time when a charging line is crossing. Green frame: same as cyan frame for the LDOS line belonging to the $m = 0$ state of LL0. Red frame: Coulomb diamonds at E_F belonging to a higher m state of LL0. The occupied and unoccupied version of the same m state is marked.

The upper right zoom, moreover, features a quadruplet of rather equidistant charging lines. The four rightmost ones have a similar mutual distance, while the fifth one exhibits a larger distance to the fourth one. This fourfold bunching is caused by the fourfold spin and valley degeneracy of each m state in graphene. By following the charging lines down to E_F (red line) and comparison with the central image, it is also apparent that these charging lines mark the charging of a higher m state of LL0.

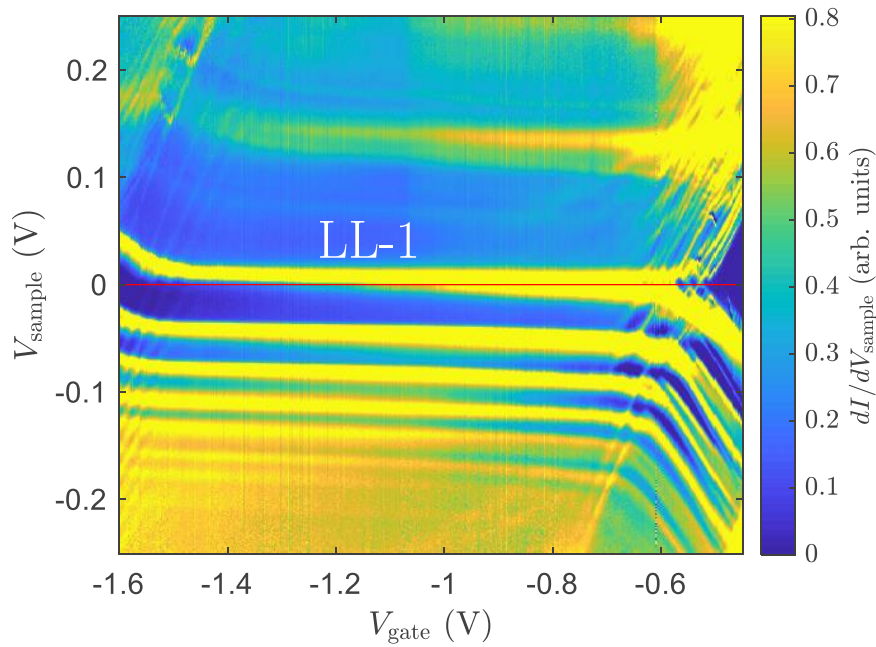


Fig. E.2: dI/dV_{sample} ($V_{\text{gate}}, V_{\text{sample}}$) (zoom into Fig. 10.2a in Chapter 10), $x_{\text{tip}} \ll 0$ nm, $I_{\text{stab}} = 1$ nA, $V_{\text{stab}} = -250$ mV. The LL-1 plateau and its charging lines starting from the right end of the plateau are visible.

Fig. E.2 features the plateau at E_F of the LDOS line belonging to LL-1. The most bright charging lines appear on the right end of the plateau followed by weaker charging lines towards the left. As explained in the main text, this supports our classification of the TIQD as a hole-type dot. The ($m = 0$)-state is the one with the highest probability density in the center of the quantum dot and, hence, leads to the strongest charging line by its strongest Coulomb repulsion acting on the states that are probed by the tip. The fact that this ($m = 0$)-state is charged at the largest V_{gate} further corroborates the assignment of the TIQD to a hole-type band bending. Notice that additional bright charging lines appear in the upper left corner of Fig. E.2. They are likely caused by the charging of the ($m = 0$)-state of LL-2.

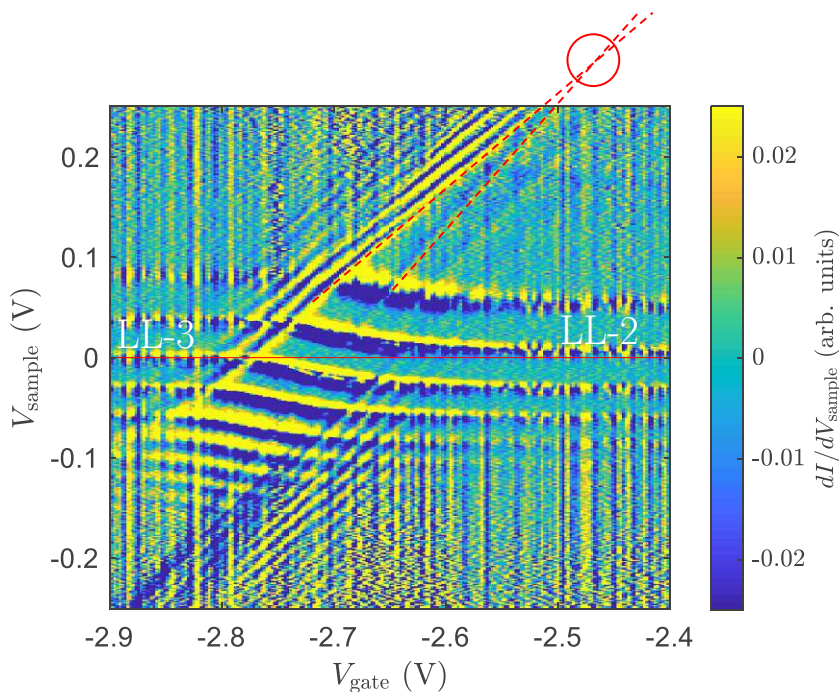


Fig. E.3: $d^2I/dV_{\text{sample}}dV_{\text{gate}}(V_{\text{gate}}, V_{\text{sample}})$ for the transition between LL-3 to LL-2 at E_F (full red line), $I_{\text{stab}} = 1 \text{ nA}$, $V_{\text{stab}} = -250 \text{ mV}$. The crossing point of the first charging line of LL-3 with the last charging line belonging to LL-2 is marked (red circle) via extrapolation of the two charging lines (dashed red lines).

The following plots explain the selection of Poisson parameters ΔV_{gate} and ΔV_{sample} from two crossing points of charging lines between two pairs of LL_n features (Fig. E.3 and Fig. 10.9a). Practically, we firstly measure the experimental voltage differences between the two crossing points, $\delta V_{\text{gate}} = 0.95 \text{ V}$ in V_{gate} direction and $\delta V_{\text{sample}} = 0.15 \text{ V}$ in V_{sample} direction. Then, we determine the depth of the TIQD potential from the Poisson simulations at varying Φ_{tip} and Φ_{gate} (Fig. E.4a) using circular symmetric coordinates. Afterwards, we select all $(\Phi_{\text{tip}}, \Phi_{\text{gate}})$ that exhibit the potential depths as present during the crossing points in the experiment (Fig. E.4b). Subsequently, we find pairs of $(\Phi_{\text{gate}}, \Phi_{\text{tip}})$ that feature the two TIQD depths at the two crossing points (38.9 meV, 30.5 meV) and, at the same time, the energetic distances in Φ_{gate} and Φ_{tip} that are identical to the voltage distances between the two crossing points ($\delta V_{\text{gate}} = 0.95 \text{ V}$, $\delta V_{\text{sample}} = 0.15 \text{ V}$). The pairs are marked as symbols of the same color in Fig. E.4. We then select the combination such that the calculated LDOS map from the Poisson simulation best matches experimental observations (Fig. E.5).

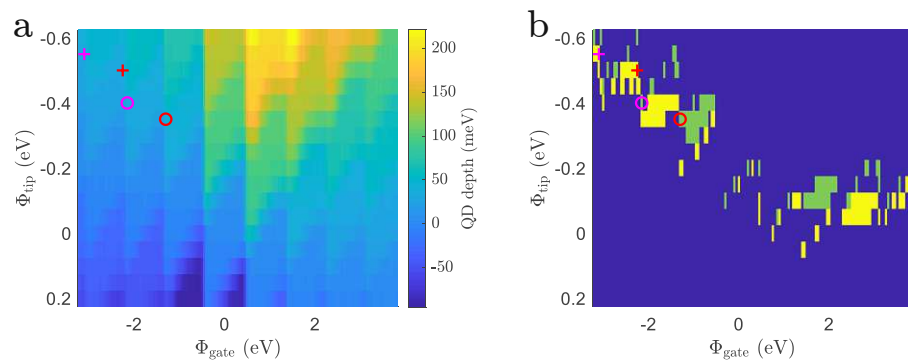


Fig. E.4: **a** Potential depth of the hole-type TIQD for varying external potentials Φ_{gate} and Φ_{tip} , $r_{\text{tip}} = 25 \text{ nm}$. **b** Selection of the potential depth values from a that are in accordance with the crossing points of charging lines in the experiment. green: TIQD depth $= 39.8 \pm 2.5 \text{ meV}$, yellow: TIQD depth $= 30.5 \pm 2.5 \text{ meV}$, blue: all other TIQD depths. Pairs of circle and cross of the same color are separated by $e\delta V_{\text{gate}} = 0.95 \text{ eV}$ along Φ_{gate} and by $e\delta V_{\text{sample}} = 0.15 \text{ eV}$ along Φ_{tip} , such as the two crossing points of charging lines in Fig. E.3 and Fig. 10.9a from the main text. Only two pairs are found to match the required conditions that the circle is on a green area, while the corresponding cross is on a yellow area.

We eventually plot a simulated LDOS(V_{gate} , V_{sample}) derived from the LDOS of graphene directly below the tip center at the energy with respect to the Fermi level of the sample that matches V_{sample} . This enables a comparison with the measured dI/dV_{sample} (V_{gate} , V_{sample}) (Fig. E.5)

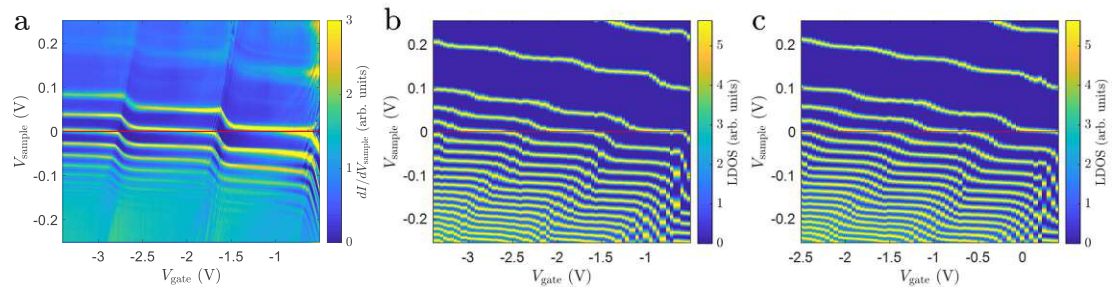


Fig. E.5: **a** dI/dV_{sample} (V_{gate} , V_{sample}) recorded at a position $x_{\text{tip}} \ll 0 \text{ nm}$, $I_{\text{stab}} = 1 \text{ nA}$, $V_{\text{stab}} = -250 \text{ mV}$. **b** LDOS(V_{gate} , V_{sample}) resulting from the Poisson simulations with optimized parameters, $\Delta V_{\text{gate}} = -200 \text{ mV}$, $\Delta V_{\text{sample}} = -180 \text{ mV}$, $r_{\text{tip}} = 25 \text{ nm}$. **c** LDOS(V_{gate} , V_{sample}) resulting from the Poisson simulations with less favorable parameters, $\Delta V_{\text{gate}} = +650 \text{ mV}$, $\Delta V_{\text{sample}} = -230 \text{ mV}$, $r_{\text{tip}} = 25 \text{ nm}$. Note the shifted V_{gate} axis in c.

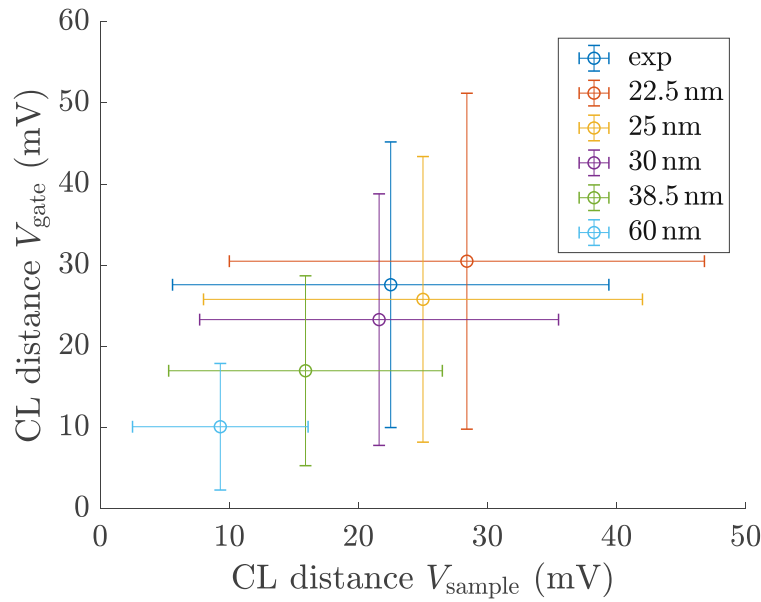


Fig. E.6: Comparison of the averaged distance between charging lines in the experiment (dark blue) with the ones deduced from the Poisson simulations at different r_{tip} as labelled, $\Delta V_{\text{gate}} = -200 \pm 50 \text{ mV}$, $\Delta V_{\text{sample}} = -180 \pm 50 \text{ mV}$. The error bars of the experiment result from the variance of the averages from different regularly spaced groups of charging lines (see text). The error bars of the simulations result from the variance in $\Delta \Phi_{\text{gate}}/\Delta Q_{\text{QD}}$ and $\Delta \Phi_{\text{tip}}/\Delta Q_{\text{QD}}$, respectively, within the simulation range of $\Phi_{\text{tip}} \in [-0.6, 0] \text{ eV}$ and $\Phi_{\text{gate}} \in [-3.2, 0] \text{ eV}$. Note that the error bars indicate the same variance in experiment and simulation, but do not provide the statistical uncertainty of the mean values.

Appendix F

Strain influence on the branching features

One might wonder, if the presence of the step edge visible in Fig. 10.9d leads to strain that eventually causes the branching of the LL features in $dI/dV_{\text{sample}}(x_{\text{tip}})$. To exclude such a scenario, we estimate the strain in the following. The step edge visible in Fig. 10.9d has a height of 2.1 nm and a width of ~ 70 nm according to its line profile (Fig. E.1a). The line profile exhibits a continuous curvature with nearly Gaussian shape across the edge. The smooth shape suggests a direct contact of the graphene to the underlying hBN. The graphene is deposited in a separate step after the hBN, such that the hBN already covers the graphite edge prior to graphene transfer. Hence, there is no obvious reason that the graphene should be particularly stretched at the step edge. During transfer, the graphene just sees a minimally bended hBN below. But even if one assumes that the graphene profile develops from a relaxed, initially flat graphene exactly parallel to the SiO_2 substrate (red line in Fig. E.1a), the resulting strain from stretching it to the measured profile line would be below 0.05 % only. This is roughly the same magnitude as the typical strain fluctuations for graphene samples on flat hBN that exhibit a rms value of 0.05 % as well [442, 443]. Hence, if strain of this small magnitude would cause a peak splitting, such a splitting would appear everywhere, not only at the step edge, in clear contrast to the experiment.

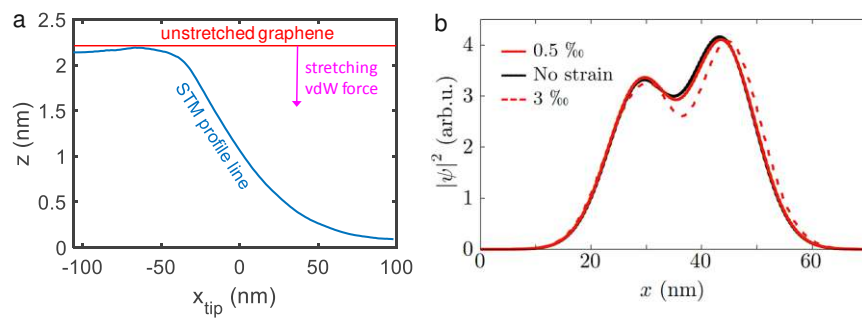


Fig. F.1: **a** Blue line: profile line across the step edge due to the graphite gate as measured by STM (see also Fig. 10.9c–d). Red line: tentative position of relaxed graphene directly prior to contact with the hBN. Pink arrow: Force that pulls the graphene downwards to the hBN. **b** Wave function corresponding to LL1 determined by a tight binding calculation without strain (black), with a Gaussian strain profile of amplitude 0.05 % and FWHM 60 nm (red full line), and with amplitude 0.3 % and FWHM 60 nm (red dashed line).

To quantitatively assess the influence of strain on the LL wave functions we consider a strain of 0.05 % as a maximum of a Gaussian profile with full width at half maximum (FWHM) of 60 nm. We modify the hopping parameters accordingly in the TB simulation. We find only minimal changes in the two component Landau level wave function (see Fig. E.1b, black vs. red line). The double peak structure barely changes due to this strain. To asses the effect of even larger strain, we increased the strain in the calculation by a factor of six and still found only minor qualitative changes (dashed line, Fig. E.1b). For the 1D step edge, we only expect a strain gradient perpendicular to the edge, and thus no pseudomagnetic field that requires a two-dimensional strain distribution [444]. However, even if one assumes a circular symmetric Gaussian bump of the same profile as the step, the pseudomagnetic field would be 200 mT only [444, 445], much smaller than the externally applied magnetic field (7 T). The difference in Landau quantization due to such a small pseudo-magnetic field would result in an energy splitting between the two Dirac cones of ~ 2 meV.[444] This unrealistic strain scenario, thus, would still be significantly too small to explain the observed splittings during branching of about 25 meV. Consequently, we can safely exclude that strain is a major factor for the observed branching of LDOS features at the lateral interface.

Appendix G

Magnetotransport in a composite moiré system

The conversion from the applied back gate voltage to the adjusted carrier density is performed by extracting the lever arm from the four-terminal magnetotransport data. We are extracting the lever arm of the graphite back gate α from the slopes of the visible Landau levels emerging from charge neutrality. From quantum Hall effect measurements (data not shown) we can identify a Landau level filling factor of $v_{LL} = \pm 4$ for the first visible Landau level. We therefore assume a Landau level filling sequence of $v_{LL} = \pm 4, \pm 8, \pm 12$ for the extraction of the lever arm. This proceeding results in a numerical value of $\alpha = (5.148 \pm 0.129) \cdot 10^{15} \text{ V}^{-1} \text{ m}^{-2}$. This value is in quantitative agreement with the geometric lever arm expected from a simple plate capacitor model

$$\alpha_g = \epsilon_0 \epsilon_{\text{hBN}} \frac{1}{ed}, \quad (\text{G.1})$$

which yields a value of $\alpha_g \approx 5.872 \cdot 10^{15} \text{ V}^{-1} \text{ m}^{-2}$. Here, we used $\epsilon_{\text{hBN}} = 3.4$ and a thickness of $d = 32 \text{ nm}$ for the bottom hBN flake which was extracted via atomic force microscopy [446, 447]. We note, that we observed an intrinsic doping in our device leading to a shift of the charge neutrality point away from $V_{\text{gate}} = 0 \text{ V}$. During the data analysis we corrected for this intrinsic shift by fitting according to $n = \alpha \cdot (V_{\text{gate}} - V_{\text{gate,off}})$ with $V_{\text{gate,off}} = 112 \text{ mV}$.

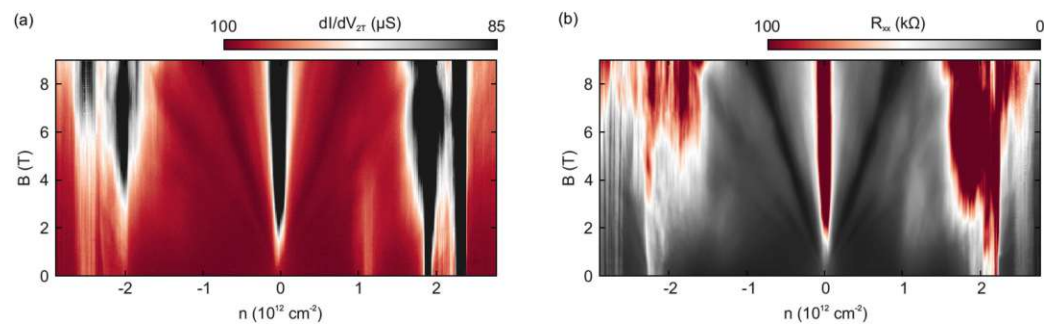


Fig. G.1: **a** Two-terminal differential conductance as a function of magnetic field and carrier density measured along the entire Hall bar structure. **b** Four-terminal longitudinal resistance as a function of magnetic field and carrier density.

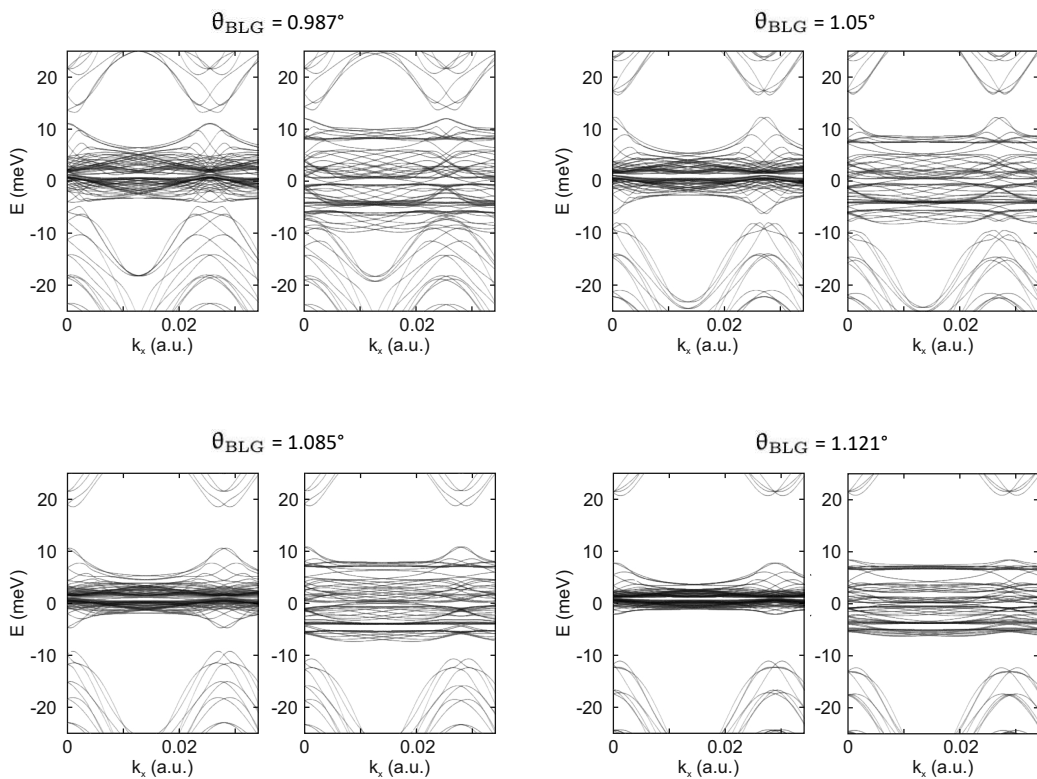


Fig. G.2: Band structure of a ribbon of (left) tBLG (right) tBLG with hBN alignment.

List of Figures

2.1	Schematic honey comb lattice of graphene (black carbon atoms with grey bonds) in a x,y plane (including the Wigner Seitz cell - blue rhombus) and b x,z plane. c Unit cell employed throughout this thesis (see also a). d Reciprocal unit cell spanned by \mathbf{G}_1 and \mathbf{G}_2 . The black hexagon represents the 1 st Brillouin zone of graphene. High symmetry points of the hexagonal lattice including the k-point path for the band structure plots are indicated. e Band structure of single layer graphene (computed along the path shown in d) including zoom-in of the Dirac cone close to the Fermi energy.	7
2.2	Schematic structure of Bernal stacked bilayer graphene (bottom layer slightly opaque) in a x,y plane and b x,z plane. c Unit cell with 4 atoms (two of them congruent in z view). d Bandstructure along $\Gamma K M \Gamma$ including zoom-in close to the Fermi energy highlighting the now quadratic dispersion.	9
2.3	Illustration of the spin-valley texture of WSe ₂ in K and K'.	11
2.4	Schematic lattice of tungsten-diselenide (WSe ₂) (blue tungsten atoms and orange selen atoms, bonds indicated in grey) in a z,y plane b x,y plane and c x,z plane. d Unit cell employed throughout this thesis (see also b). e Reciprocal unit cell spanned by \mathbf{G}_1 and \mathbf{G}_2 . The black hexagon represents the 1 st Brillouin zone of WSe ₂ . High symmetry points of the lattice including the k-point path for the band structure plots are indicated. f Band structure of WSe ₂ (computed along the path shown in e). Colorscale indicates spin character of the respective band in \mathbf{k} -space.	13
2.5	Illustration of commensurable moiré unit cells (green) for twisted bilayers (top layer - red, bottom layer - blue) for a m=1, r=2 ($\theta \approx 32^\circ$) b m=1, r=1 ($\theta \approx 21^\circ$) c m=1, r=4 ($\theta \approx 42^\circ$)	15
3.1	Sketch of the NN neighbour sites in the graphene lattice.	21
3.2	a p _z bands of graphene calculated from TB models with different numbers of neighbour interactions. b , c , d Periodic Hamiltonians $H^{(\lambda_1, \lambda_2, 0)}$ for TB models of SLG with 3, 5 and 10 NN interactions respectively with labels for $(\lambda_1, \lambda_2, 0)$	22
3.3	Sketch of the periodic neighbour unit cells in graphene.	23
3.4	(top) Unit cell of WSe ₂ (tungsten atom in blue, two selenium atoms stacked along the z direction in orange). Wannier band structure projected onto tungsten orbitals (center) and selenium atoms (bottom).	25

3.5 Wannier band structure of pristine WSe ₂ with color scale indicating the contribution of the different d-type orbitals (a - d _{z²} , b - d _{xz,yz} , c - d _{x²-y²,xy}) of W. Insets represent schematics of the corresponding spherical harmonics. d DFT band structure (solid black lines) of pristine WSe ₂ with Wannier band structure on top (dashed blue lines). Shaded regions represent energy windows (inner - green, outer - red) for the disentanglement process of wannier90.	27
4.1 Schematic ML time line.	28
4.2 Explanatory sketches for the different types of tasks.	29
4.3 Schematic layout of a simple fully-connected feed-forward neural network layout with two hidden layers (associated neurons in blue) that processes three input values (pink input neurons) to a result stored in two output neurons (purple). Inset to the left sketches an artificial neuron with inputs a _i , weights w _i , bias b and activation function θ.	30
4.4 Typical activation functions θ(x).	31
4.5 Information flow schematic in neural networks.	33
4.6 Typical learning curves of unregularized and a regularized network.	34
4.7 Schematic explanation of slimming networks by randomly dropping nodes.	35
4.8 Diagrammatic structure of a convolutional network with two convolutional layers (shape and number of filter kernels indicated for each layer) connected to fully-connected layers on the output side.	36
4.9 Exemplary depiction of different pooling prescriptions. . . .	37
4.10 One dimensional Gaussian with exemplary means and variances.	37
4.11 Contour plots of two dimensional Gaussian distributions labeled with percentiles. Subplots correspond to different Covariance matrices.	38
4.12 Colors correspond to different degrees of correlation in the covariance matrix similar to Fig. 4.11. a Three random vectors x sampled from a 40 dimensional Gaussian. b Interpolated mean and 1 σ intervals (light grey area between dashed lines). c Three random vectors x sampled from a 40 dimensional Gaussian conditioned to four training data points (marked as black diamonds). d Interpolated mean and 1 σ intervals for the conditioned Gaussian.	39
5.1 a Schematic setup of STM tip and graphene flake on an hBN substrate. b Achieving confinement within the first Landau gap	45

5.2	a Schematic depiction of the model graphene-flake with red marker indicating the embedding position for defects (flake center) and the green circle representing the GQD (possibly shifted relative to the defect by $\mathbf{R}_T = (X_T, Y_T)$). b sequence of eigenenergies (real part) around the Dirac point for different values of tip voltage (and thus “depth” of the GQD potential) filtered for localized (low imaginary parts $\Gamma_{i,\tau}$, blue dots) and delocalized states (high imaginary parts $\Gamma_{i,\tau}$, grey dots). Landau level energies (horizontal dot-dashed green lines) as well as the Fermi level for defining occupied GQD states are indicated (red line). c Energy level diagram for the lowest two orbitals of a GQD with orbital splitting Δ_l^O , valley splitting Δ_l^V and spin splitting Δ^σ indicated.	47
5.3	Probability density of the first six (one valley pair per row) GQD eigenstates as well as their sublattice projected density (A/B insets) for the pristine system.	49
5.4	Level spacing landscape for different embedding methods of the double vacancy defect for GQD displacement in x-direction.	50
5.5	Displacement dependent level spectrum for the lowest GQD states (first three valley pairs) in the presence of a double vacancy defect at the indicated position (red marker in flake schematic) for GQD displacement in a x-direction and b y-direction. The color scale represents the squared overlap between defect and pristine wavefunctions P_τ as defined in Eq. (5.9).	52
5.6	Probability density in the presence of a double vacancy for $\mathbf{R}_T = (0, 0)$. The panels show the first six (one valley pair per row) GQD eigenstates as well as their sublattice projected density (A/B insets)	53
5.7	GQD energies as function of quantum dot position $\mathbf{R}_T = (X_T, Y_T)$ relative to a a flower defect and b a Si substitution defect for GQD displacement in y-direction.	54
5.8	Level spectrum landscapes for the double vacancy defect (with GQD displacement in x-direction) in the presence of correlated disorder (dashed black lines correspond to vanishing disorder). The subplots are labelled with values for both $\sqrt{\langle V_D^2 \rangle}$ and l_{corr} . Each subplot is additionally referenced by a sketch of the total onsite potential s_i [eV] throughout the graphene flake ($120 \times 100 \text{ nm}^2$) to put the included disorder into perspective.	55

5.9	a Schematic overview of the graphene flake with initial and final y -coordinate of the GQD center indicated by lines labelled "A" and "B". b Level spectrum landscape of the double vacancy defect with the avoided crossing between levels 3 and 4 centered between lines "A" and "B" which correspond to the ones in a). c Squared projections (as labelled) of the propagated state as a function of y -coordinate. d Final values of the projections in c) superposed onto the analytical function for the diabatic transition probability.	58
6.1	Lattice geometry of double vacancy (top) and flower defect (bottom) in single layer graphene.	60
6.2	Interaction of a defect supercell with its periodic images (defect region highlighted in orange). The center cell itself is described by $\mathcal{H}^{(0,0)}$, the interactions to its neighboring cells by $\mathcal{H}^{(\lambda_x, \lambda_y)}$ — for large super cells such as this only the nearest-neighbor interactions between cells, i.e., $\lambda_x, \lambda_y \in \{-1, 0, 1\}$ are non-zero.	62
6.3	Distance-hopping map for all entries of a Wannier parametrization for the double vacancy defect in SLG (black dots) with both a Slater-Koster based initialization (taken from [210]) $\gamma^{(SK)}(\delta r)$ (dashed green line) as well as another initialization $\gamma^{(0)}(\delta r)$ defined as spline interpolation between the 10 th -NN distance-hopping values of a bulk singler layer graphene cell (red crosses). The hoppings at distance zero represent the onsite energies s_i	63
6.4	Non complete selection of representative distance classes with the symmetry related interactions highlighted in red (defect super cell indicated in blue).	64
6.5	Schematic of the inverse BS problem: for a given Hamiltonian, calculating a BS is trivial. By contrast, there is no constructive algorithm to obtain a Hamiltonian from a BS. Using ML, we aim to find such an inverse mapping from BS data (scalar energy values $\epsilon_{b,k}$ for each band b and k -point k) to a minimal list of TB parameters $\{\gamma_l, s_i\}$ (for each distance and onsite class l) which describes a full TB Hamiltonian \mathcal{H}	66
6.6	DFT band structure for the double vacancy defect. Color map represents the projection of the corresponding Bloch states onto atomic p_z orbitals.	66
6.7	2D schematic of the high dimensional search via the GLD algorithm. Initial parameter set (red dot) and its vicinity (red-grey circle) followed by successively improved (orange, yellow) parameter sets with their respective n -balls	68
6.8	Contour plot of the probability to add a sample to the training data (i.e. acquisition function $A(\mathcal{L}_e, \sigma_e)$) depending on both GP predicted BS error as well as GP uncertainty.	69

6.9	Convergence of (top) length scale l of the RBF kernel in the GP, (center) batch-averaged band structure approximation error and (bottom) batch-averaged uncertainty of the GP queries.	69
6.10	Schematic flow chart of the active learning approach via Gaussian Process and an acquisition function. The right branch represents preliminary sampling that allows for an initial fit of the GP. The left branch describes the main algorithm that then employs and successively improves the GP.	70
6.11	Visualization of the input form of the band structure data into the CNN.	71
6.12	Convergence study for the network performance (i.e. the quality of its produced band structure) depending on the size of the training set.	73
6.13	Schematic flow chart of the steps to produce a machine learned TB parametrization of a defect system. The hued section on the right can be replaced with an initial $\gamma^{(\text{SK})}$ from Slater-Koster theory for materials with challenging bulk cells. Cornered green nodes represent calculation processes and rounded blue nodes represent data.	74
6.14	Convergence study for the network performance (i.e. the quality of its produced band structure) depending on a_e	75
6.15	a BS of the SLG double vacancy supercell along $\Gamma\text{M}\bar{\chi}\Gamma$ of both DFT calculation and MLP TB-model. b p_z -projected density of states of the supercell. c Cosine similarity of the local density of states between different TB models and the DFT result. d LDOS at the three energies (left to right) indicated by vertical dash-dotted grey lines in b,c) for DFT, Wannier, MLP respectively (top to bottom, colored boxes match line colors in b,c).	77
6.16	a BS of the SLG flower defect supercell along $\Gamma\text{M}\bar{\chi}\Gamma$ of both DFT calculation and MLP TB-model. b p_z -projected density of states of the supercell. c Cosine similarity of the local density of states between different TB models and the DFT result. d LDOS at the three energies (left to right) indicated by vertical dash-dotted grey lines in b,c) for DFT, Wannier, MLP respectively (top to bottom).	78
6.17	Energy dependent transmission $T(E)$ for different TB parametrizations of the a double vacancy and c flower defect in SLG (vertically offset for clarity). b Scattering density plots for the three lowest modes at $E = 0.7\text{eV}$ in the double vacancy setup with ribbon-width and embedded defect positions indicated.	79

6.18 Level spectrum landscapes calculated with different TB parametrizations of the double vacancy in SLG compared against the Wannier parametrization [a MLP(10NN), b Slater-Koster, c MLP(5NN), d MLP(3NN)]. Inset shows schematic sketch of the underlying system: We calculate the level spectrum (orbital and valley quantum number, spin is omitted) as a function of the position of an STM-tip (brown) induced (smoothly confined) GQD relative to an embedded defect in a large graphene flake (grey rectangle). Dotted grey lines represent the level structure of a pristine GQD with doubly degenerate orbitals.	81
6.19 Level spectrum landscapes calculated with different TB parametrizations of the flower defect in SLG compared against the Wannier parametrization [a MLP(10NN), b Slater-Koster, c MLP(5NN), d MLP(3NN)].	82
6.20 Relaxed 6×6 super cell of a selenium divacancy in WSe ₂	83
6.21 a Table for the SK parameters for the pristine system optimized for the system without spin degree of freedom (starting from [249]). b Corresponding band structure of the pristine system (DFT in blue, SK for the lowest conduction and highest valence band in red).	84
6.22 Grouping of hoppings into 2NN (in this context first neighbour of a W atom being a Se and the second neighbour being another W irrespective of distance class) SK distance maps (line colors correspond to different distance classes l , see Eq. (6.15)) for (left) tungsten-tungsten bonds, (center) tungsten-selenium bonds, (right) selenium-selenium bonds. Periodic unit cell borders are drawn in dark green.	85
6.23 Relevant bands around E_F for the 6×6 Se divacancy super cell of WSe ₂ for a a *poorman's Wannier description (i.e. vacancy with pristine wannier parametrization, b Slater Koster parametrization (from the pristine system), c machine-learned parametrization based on discrete Slater Koster maps with r_{NN} cutoff that allows for up to 3NN interactions between kindred atoms (i.e. W - W or Se - Se).	86
6.24 DOS (including analysis of orbital contributions, see color scheme) near E_F for the 6×6 Se divacancy super cell of WSe ₂ . a DFT result vs. tight-binding DOS for the MLP Slater Koster map parametrization of Fig. 6.23c. b Zoom-ins of the midgap defect states D1, D2, D3.	87
7.1 Absolute value of the differential conductance $ dI/dV_{fg} $ as a function of both V_{fg} and B_\perp measured across the a $N = 2$ coulomb peak and b $N = 1$ coulomb peak. See Fig. 7.2 for a sketch of the experimental setup. (These impressive measurements were performed by S. Möller et. al. in the group of C. Stampfer at the RWTH Aachen.)	90

7.2	Sketch of the experimental system (as imagined by a theorist) used for the measurements (see Fig. 7.1) in the group of C. Stampfer. FG...finger gate, SG...side gates, S...source, D...drain.	91
7.3	Single particle spectrum in a BLG quantum dot ($r \approx 50\text{nm}$) as a function of total angular momentum $j = m + \tau$ at $B = 0$	92
7.4	Evolution of single particle energy levels in a BLG quantum dot with perpendicular magnetic field B . Valleys K and K' are colored blue and red respectively. Yellow curves show analytic solutions (following [268]) of Landau levels in an infinite BLG system.	92
7.5	a Single particle energies for states of the lowest radial quantum number n . b Energy $E_1 + E_2$ for the non-interacting singlet and triplet states introduced in Eqs. (7.15) and (7.16).	94
7.6	a Interacting two-particle spectrum for an effective dot radius of about 30nm using $\epsilon_{hBN} = 3.6$ to account for screening. b same as a but now with the lowest single particle energy subtracted (as a function of magnetic field, see Fig. 7.5).	95
8.1	a Schematic of the device and measurement scheme. Applying a voltage V_G between a suspended WSe ₂ monolayer suspended and the backgate introduces strain. We record PL spectra at the center of the suspended WSe ₂ where the strain is spatially homogeneous and biaxial in nature. b Microscope image of a typical device. Inset: Room temperature PL map of the neutral exciton at 1.66eV in the unstrained ($V_G = 0\text{V}$) membrane.	97
8.2	a PL spectra as a function of V_G at $T = 100\text{K}$. b Cuts of (a) for fixed V_G . Neutral exciton (X^0 , 1.738eV), positively charged trion (X^+ , 1.713eV), negatively charged intervalley trion (X_T^- , 1.708eV), and negatively charged intravalley trion (X_S^- , 1.701eV) appear at the energies close to what is reported in literature for high-quality hBN encapsulated devices [315–318]. The near-zero charge neutrality point and the disappearance of the X^0 peak outside of the $-50\text{V} < V_g < +10\text{V}$ region confirm the good optical quality of our samples.	99
8.3	a PL map (device 1) at $T = 100\text{K}$ with individual spectra shown in b . Free excitonic states X^0 , $X^{+/-}$, X_d^0 red-shift with increasing strain (black, dashed lines as a guide to the eye). The state X_d^0 develops strong intensity maxima at energies 1.63eV (D1) and 1.45eV (D2). The strain-independent states close to the position of D1 associate with defects are marked with a dotted line. See Fig. B.2a in Appendix chapter Chapter B for an offset plot of the PL spectra. c High-resolution map of the region I (device 2). The state X^- disappears with increasing strain while the state X_d^0 arises ~ 14 meV below it. d Detailed map of the region II (marked with white dashed lines in (a)) from device 1.	100

8.8	Composition of the wavefunction at the K- and Q-valley minima of the conduction band as calculated by our Wannier model. Unlike the strongly strain-dependent K-valley band minimum, composed of only dz^2 orbitals, the band minimum at Q features many different orbitals whose strain dependencies could be thought to cancel each other out, explaining the weak strain dependence of the Q-valley.	104
8.9	Tight binding band structure along Γ KM Γ and lattice plots for 7×7 super cells of tungsten diselenide for a pristine reference, b selenium di-vacancy defect, c selenium mono-vacancy defect, d tungsten vacancy. Horizontal dotted lines serve as guide to the eye for the pristine band gap with scissor correction applied.	105
8.10	a Schematic illustration of the K and K' valley bandstructure of WSe ₂ at several different strain levels. Filled and empty arrows denote spin. b Corresponding bandstructure calculated via maximally localized Wannier functions. The color scale of the bands denotes their degree of localization in the immediate vicinity \mathcal{V} of the defect site. Dark excitonic states X_d^0 associated with the K point becomes resonant with excitons related to defect-related mid-gap states D1 and D2 at 1.2% and 2.4% strain. The resonance between X_d^0 and D1/D2 is determined by the total strain. Since intrinsic strain is temperature-dependent due to the thermal extension of involved materials as well as other effects [329], strain values at which the hybridization occurs also depend on temperature, as discussed in detail in Section 8.7.	106
8.11	Modeled PL intensity for a 17×17 Se single vacancy super cell in WSe ₂ (i.e. the expression of transition matrix elements in Eq. (8.6) evaluated at K and K') plotted as a function of strain ϵ and PL energy. a no relative weighting of bright and dark feature, b bright feature suppressed by a factor of $e^{-(36\text{meV}/8.6\text{meV})} \approx 1/66$ (to account for thermal population differences). We include a Gaussian smearing of width 10 meV for all energies.	107
8.12	Experimental (a) and modelled (b) PL spectra map of WSe ₂ vs. strain. Different shift rates vs. strain for the defect-related states D1,D2 and a dark excitonic state X_d^0 are evident. When X_d^0 is energetically resonant with either D1 (around $\epsilon \sim 1.2\%$) or D2 (around $\epsilon \sim 2.4\%$) a strong increase in oscillator strength and avoided-crossing type behaviour occur. Insets show on- and off- resonant alignment between dark- and defect-related excitons.	108

- 8.13 One artefact that can produce non-monotonous changes in the PL intensity vs. V_G — and hence appear similar to the signatures observed — arises due to optical interference. We expect the total PL intensity – by which we mean the integrated intensity of all PL peaks peaks in a spectrum – to vary proportional to the membrane displacement. Here, we quantify the possible contribution of this effect. We examine the integrated PL intensity vs. V_G (empty symbols) for different excitation wavelengths (570, 600, 645, 675 nm) on device 5 at room temperature. Room temperature PL intensity in this range of V_G is roughly constant with most changes likely arising from interference effects. Indeed, we see that for all excitations, the variation in the signal remains small, but its phase shifts, as expected for interference. Furthermore, the signal matches the calculated laser intensity at the position of the device vs. V_G for same wavelengths using a simple model based on transfer matrices that captures interference effects (solid lines). In addition, we also plot the normalized reflectivity vs. V_G (curves are upshifted for clarity). As expected, this data is similar to the PL intensity data as the reflectivity maxima coincide with the maxima in absorption. We therefore ascribe the modulations seen in the figure to interference effects. Note that the maximum modulation due to interference is found for 645 nm (green empty symbols) and it is smaller than a 30 % of the average intensity. This allows us to set 30 % as an upper boundary for the effect of interference in the experimental data. 110
- 8.14 PL spectra vs. strain maps acquired at **a** T=10 K, **b** 100 K, **c** 300 K. An individual spectrum at 10K measured under 0.25% strain (-140 V) and marked with a white, solid line is shown in the inset of (a). While the energy of the unstrained, free excitonic states (X^0 , X^+ , X_d^0 , the corresponding spectral lines are marked with dashed lines) blueshifts with lowering temperature, the features D1 and D2 associated with the corresponding defects stay roughly energy-independent. Due to the temperature-related changes in mechanical constants, only the D1 state is resolved at 10 K within our accessible V_G range. In contrast, we resolve the hybridization with both states D1 and D2 at 100 K and 300 K. As opposed to the T=10 K data in (a) that is symmetric with respect to p- and n- doping, the intensity of the n-branch at 300 K in (c) is roughly 30 times lower than that for the p-branch. Note that the voltage scales in (a-c) are not linear. 112

9.1	a Relaxed pentagon/octagon (indicated in blue and green respectively) geometry of a 5-8-5 line defect resulting from two graphene flakes shoved into each other along the arm chair direction. Grain boundary adjacent atoms are colored red. Dashed orange lines indicate periodicity in y direction. b Relaxed pentagon/heptagon (indicated in blue and green respectively) geometry of a tilt line defect (classified via grain boundary indices $m = 1$, $n = 2$ according to [341]) resulting from two graphene flakes rotated by $\theta = 21.8^\circ$ (arm chair orientation of both sides indicated by dotted grey lines). Grain boundary adjacent atoms are colored red. Dashed orange lines indicate periodicity in y direction.	116
9.2	a Top view schematic of the zig-ac-zig geometry employed for transport calculations through the 5-8-5 line defect (see Fig. 9.1a). The line defect is oriented along the brown, dot-dashed line. The half-infinite zig-zag edged leads are attached at the left and right ends. Dashed lines (red, orange, yellow) represent the center of the guiding potential used for manipulating the angle of incidence α . b Perspective view of the same geometry as in a with a schematic cross section of the guiding potential Eq. (9.9)	118
9.3	Transmitted (top) and reflected (bottom) valley polarization $P_{T/R}$ for the pristine benchmark geometry (no line defect embedded but otherwise identical) as a function of energy and angle of incidence α . Vertical, dotted, grey lines indicate the angle range in which the pristine geometry does not produce finite valley polarization. For $\alpha < -20^\circ$ the guiding potential clashes with the zz edge of the graphene flake in an unintended and non-physical manner.	118
9.4	Exemplary scattering densities in the pristine reference geometry at $E = 0.5\text{eV}$ (color scale from black to red) for (top) zero node mode, $\alpha = 30^\circ$, (center) zero node mode, $\alpha = -15^\circ$, (bottom) single node mode, $\alpha = -4^\circ$	119
9.5	a Transmitted valley polarization $P_T(E, \alpha)$ Eq. (9.11) for the 5-8-5 linedefect geometry presented in Fig. 9.2. Curly brackets indicate energy regions I-IV referred to in the discussion. Dashed lines indicate coordinates of cuts presented in panels b-d. b Constant angle cut of panel a ($\alpha = 17^\circ$). Dotted, vertical lines separate qualitatively different behaviour (I . . . isolated peaks, II . . . emerging background, III . . . pronounced background with sharp “Fano-like” resonances, IV . . . monotonic decline before mode opening). c Constant energy cuts of panel a (A . . . 0.18eV, B . . . 0.163eV, C . . . 0.154eV). Grey, dashed line plots $\sin \alpha$ for visual comparison. d Constant energy cuts of panel a (D . . . 0.18eV, E . . . 0.163eV, F . . . 0.154eV). Grey, dashed line plots $\sin \alpha$ for visual comparison.	120

- 9.6 Scattering density at **a** a generic energy with no significant valley polarization P_T and **b** at a polarization resonance. (see respective energies in panel c). **c** P_T for the 5-8-5 defect geometry (see also panel b in Fig. 9.5). **d** Probability density for bound states at the energies indicated in panel c. Resonances in transmitted valley polarization correspond to the existence of bound defect states. 121
- 9.7 **a** Reflected valley polarization $P_R(E, \alpha)$ Eq. (9.10) for the 5-8-5 linedefect geometry presented in Fig. 9.2. Curly brackets indicate energy regions I-IV referred to in the discussion. Dashed lines indicate coordinates of cuts presented in panels b-d. **b** Constant angle cut of panel a ($\alpha = 17^\circ$). Dotted, vertical lines separate qualitatively different behaviour (I ... isolated peaks, II ... emerging background, III ... pronounced background with sharp “Fano-like” resonances, IV ... monotonic decline before mode opening). **c** Constant energy cuts of panel a (A...0.18eV, B...0.163eV, C...0.154eV). Grey, dashed line plots $\sin \alpha$ for visual comparison. **d** Constant energy cuts of panel a (D...0.18eV, E...0.163eV, F...0.154eV). Grey, dashed line plots $\sin \alpha$ for visual comparison. 123
- 10.1 (top) Optical image of the finalized sample with different areas marked. The graphene area is encircled (red line) as determined by atomic force microscopy (AFM). The graphene has been ruptured during the transfer, such that the trenches within the graphite are not used. The studied lateral interface is marked (blue line) separating the graphite gate area on the left and an area without graphite gate on the right. (bottom) AFM image acquired in tapping mode at ambient conditions, Si-cantilever, $f_{\text{res}} = 325$ kHz. The rim of the contacted graphene flake is marked by a red line. The circle indicates the intended landing position of the STM tip. . . 125

10.2 a $dI/dV_{\text{sample}}(V_{\text{gate}}, V_{\text{sample}})$ on a graphene area far away from the lateral interface. Landau level features LL n are marked. The tip-sample distance is stabilized at current $I_{\text{stab}} = 1 \text{ nA}$ and voltage $V_{\text{stab}} = -250 \text{ mV}$. b Zoom into the area where the LL0 lines cross E_F ($V_{\text{sample}} = 0 \text{ V}$). The marked bright line above E_F corresponds to the ($m = 0$)-orbital of LL0 confined in the TIQD. The replica of this line at lower V_{sample} are other confined m -states of LL0. Charging lines run from the lower left to the upper right. The ones that cross an m -state at E_F are caused by the charging of exactly this m -state. Quadruplets of charging lines showcase the spin and valley degeneracy of graphene. c Sample layout with circuitry, graphite thickness: 3 nm, hBN: 23 nm, SiO ₂ : 300 nm. The graphite is used to partially gate the graphene. d STM topography of graphene with a step marking the onset of the underlying graphite defined as $x_{\text{tip}} = 0 \text{ nm}$ (white line), $I = 200 \text{ pA}$, $V_{\text{sample}} = -500 \text{ mV}$. e STM topography of graphene with atomic resolution and moiré lattice due to a mutual rotation of the graphene and the underlying hBN by 11.1° , $I = 1 \text{ nA}$, $V_{\text{sample}} = -250 \text{ mV}$, $V_{\text{gate}} = 3.5 \text{ V}$. f $dI/dV_{\text{sample}}(x_{\text{tip}}, V_{\text{sample}})$ across the lateral interface, $I_{\text{stab}} = 200 \text{ pA}$, $V_{\text{stab}} = -500 \text{ mV}$, $V_{\text{gate}} = 3.5 \text{ V}$. g $dI/dV_{\text{sample}}(x_{\text{tip}}, V_{\text{gate}})$ across the lateral interface, $I_{\text{stab}} = 1 \text{ nA}$, $V_{\text{stab}} = -250 \text{ mV}$, $V_{\text{sample}} = 0 \text{ V}$	127
10.3 a Top view of the simulated graphene sheet (scaled by a factor 10) with edge types and center position of the QDOT potential indicated. b Eigen-energies of the finite graphene sheet in a at a magnetic field of 7T. Horizontal grey lines indicate analytical Landau level energies (Eq. (5.1)). c Electrostatic potential imprinted on the graphene sheet by a hovering STM tip (resulting from a fit in [14, 180] and taken unaltered for shallow potentials).	129
10.4 Total density of states of the graphene flake pictured in Fig. 10.3 at $B = 7\text{T}$ for relevant energies.	130
10.5 a 2D Cartesian geometry as used for the Poisson simulations including the lateral interface. The potentials Φ_{tip} and Φ_{gate} are applied to the tip and the graphite gate, respectively. b Cylindrical geometry as used for simulations of the TIQD without lateral interface (i.e. the graphite gate covers the entire area).	131
10.6 In depth analysis of four QDOT states (a LL0 #0, b LL0 #4, c LL1 #2, d LL2 #4) including 2D color plots of sub lattice densities $ \psi_{A/B} ^2$, radial density distribution and overlap (within an annulus close to the density maximum) with azimuthal test functions of the form $ e^{im\phi}\rangle$ (top, center and bottom subplots for each panel a , b , c , d).	131

10.7 a Band bending of two adjacent LLn due to the TIQD potential. The probability density of the confined states of LL-2 are added at their confinement energy and labeled with its azimuthal quantum number m . b Same as (a) with added E_F line . The blue shaded areas mark the onset of the insulating surrounding. c E_F at the charging position of the last state from LL-1. Tunnel barrier indicated in grey. d Sketch with two states at E_F enabling simultaneous charging of both LL.	132
10.8 a Potential calculated with a Poisson solver along a 1D trajectory (evaluated for varying x at fixed z_{graphene}) perpendicular to the PN junction for different values of V_{gate} (from $-3V$ to $+3.5V$ in $0.5V$ increments). b 2D analytical potential (i.e. true function of x and y) given in Eq. (10.7) used for the TB system sketched in Fig. 10.3a evaluated along the center line in zig-zag direction for different values of η with fixed λ . Columns in both subplots correspond to different tip positions (as indicated by vertical black lines).	133
10.9 a $d^2I/dV_{\text{sample}}dV_{\text{gate}}(V_{\text{gate}}, V_{\text{sample}})$ at the transition from LL-2 to LL-1 being located at E_F (red line), $I_{\text{stab}} = 1 \text{ nA}$, $V_{\text{stab}} = -250 \text{ mV}$. The crossing point of the first ($m = 0$)-charging line of LL-2 with the last charging line belonging to LL-1 is marked (red circle). Such crossings for various adjacent LLn are used to determine ΔV_{sample} and ΔV_{gate} as input parameters for the Poisson calculations. b Potential of the TIQD without lateral interface for the marked V_{sample} , V_{gate} as resulting from the Poisson simulations. c Profile line through the potential of superposed TIQD and lateral interface, $V_{\text{sample}} = 0 \text{ V}$, $x_{\text{tip}} \in [-130, +100] \text{ nm}$ with increments of 20 nm (blue to red), V_{gate} as marked. The potentials are used as input for the TB simulations. d LDOS($x_{\text{tip}}, V_{\text{gate}}$) at $V_{\text{sample}} = 0 \text{ V}$ as resulting from the TB simulations. The LDOS is averaged over a circular region (radius $\approx 1.5 \text{ nm}$) around the vector x_{tip} describing the position of the tip center. White horizontal lines on the left mark the bulk LLn. The marked branching of various LLn states around $x_{\text{tip}} = 0 \text{ nm}$ qualitatively matches the experimental ones (Fig. 10.2g). Red lines with red dots mark V_{gate} and x_{tip} , respectively, as used in e-g. e LDOS as a function of real space coordinates x, y , $V_{\text{gate}} = 2.15 \text{ V}$. The columns are for different x_{tip} marked by red dots (also in d). f Same as e, $V_{\text{gate}} = 1.05 \text{ V}$. g Same as e, $V_{\text{gate}} = -2.45 \text{ V}$.	135
10.10 Array of 3D surface plots of Φ_{tot} for varying x_{tip} (indicated in nm) and fixed $\eta = -0.4$.	138

10.11a Same data set as in Fig. 10.9d with different red lines and dots according to b–c and additional dashed orange lines indicating V_{gate} of the line profiles in d–f. b, c LDOS(x, y) as marked in a and x_{tip} marked by the red dot in each panel as well as in a. d–f Profile lines along the dashed lines in a (orange), across the calculated LDOS at the same V_{gate} , but without the TIQD (blue) and across the experimental data of Fig. 10.2 at the same V_{gate} (green). The experimental profiles have been horizontally shifted by +5 nm (d), +20 nm (e), +10 nm (f) to ease the comparison. Additional intensity adjustments as marked are used to compensate for the strong charging lines that are not included in the simulation. The peak fine structure is a fingerprint of the charging lines (compare Fig. 10.2g)	138
10.12a Simulated LDOS($x_{\text{tip}}, V_{\text{sample}}$) across the lateral interface, while including the TIQD, $V_{\text{gate}} = -1.9$ V. b Measured $dI/dV_{\text{sample}}(x_{\text{tip}}, V_{\text{sample}})$, $V_{\text{gate}} = -2.0$ V, $I_{\text{stab}} = 200$ pA, $V_{\text{stab}} = -250$ mV. c $dI/dV_{\text{sample}}(x_{\text{tip}})$ along the lateral interface (y direction) featuring the LL-1 edge state at E_F , $V_{\text{gate}} = -1.6$ V, $V_{\text{sample}} = 0$ V, $I_{\text{stab}} = 1$ nA, $V_{\text{stab}} = -250$ mV. Filling factors ν are marked on both sides of the interface. d Zoom into Fig. 10.11a (simulated LDOS, $V_{\text{sample}} = 0$ V) at larger contrast to visualize the internal structure of the LL-1 edge state. e Simulated LDOS(x, y) across the interface for various x_{tip} marked by red dots (also in d), $V_{\text{gate}} = -1.4$ V (red line in d)	140
10.13 Branching distances Δx as deduced from $dI/dV_{\text{sample}}(x_{\text{tip}}, V_{\text{gate}})$ of Fig. 10.2g, and LDOS($x_{\text{tip}}, V_{\text{gate}}$) of Fig. 10.9d. a Experimental branching distance of LL+1. b Simulated branching distance of LL+1. c Experimental branching distance of LL-2. d Simulated branching distance of LL-2. Insets show the parts of the images in Figs. 10.2 and 10.9 that are used to determine Δx with dots that mark the observed maxima in $dI/dV(x_{\text{tip}})$ lines, respectively LDOS(x_{tip}) lines. These maxima are used for distance determination indicated in b.	141
10.14a Numerical 1D TB solution of the squared graphene Landau level wave function belonging to LL-2 in a linear potential with slope -0.8 meV/nm (full line). The dashed and dotted curves are the sublattice contributions. b Same as subfigure a, but for LL+1 at a potential slope of $+0.8$ meV/nm. c, d Zoom-ins of Fig. 10.11d, for the LL features belonging to LL-2 (c) and LL+1 (d). Vertical dashed lines highlight the agreement of distances between maxima.	142
11.1 a Primitive bilayer (red...hBN, blue...graphene) unit cells in the x-y plane with local displacement vector d of two regions in the entire moiré super cell shown in b	145

11.2 Reconstruction of atomic position following the elasticity model in Eq. (11.2). a _{1/2} are the moiré supercell lattice vectors. Black arrows indicate the relative displacements throughout the supercell. Taken from [84].	146
11.3 a Quantum Hall conductivity σ_{xy} (in units of [e^2/h]) of a graphene on hBN ribbon (of a width of 30 super cells ≈ 750 nm) as a function of perpendicular magnetic field and Fermi energy as calculated via Eq. (11.7). Regions where the Strěda formula does not apply are colored black. Green, purple and yellow lines indicate cuts in subsequent panels. b Constant energy cuts of panel a). c Constant B -field cuts of panel a). Regions where the Strěda formula does not apply are indicated by thin black lines in panels b) and c).	148
11.4 a Quantum Hall conductivity σ_{xy} (in units of [e^2/h]) of a graphene on hBN ribbon (of a width of 30 super cells ≈ 750 nm) as a function of perpendicular magnetic field and filling factor n/n_0 of the super lattice as calculated via Eq. (11.7). Apart from x-axis rescaling identical data to Fig. 11.3. Regions where the Strěda formula does not apply are colored black. Green, purple and yellow lines indicate cuts in subsequent panels. b Constant energy cuts of panel a). c Constant B -field cuts of panel a). Regions where the Strěda formula does not apply are indicated by thin black lines in panels b) and c).	149
11.5 Surface plot of the charge carrier density of the graphene/hBN ribbon as a function of both energy and magnetic field. Zoom-in illustrates the limits of the Strěda formula (see text). Green arrow indicates direction of magnetic field derivative. Short arrows point at ramps of constant slope and are color coded according to plateaus of σ_{xy} in Fig. 11.3a.	150
12.1 a False-color atomic force microscopy image of the measured device. Overlay depicts schematic measurement setup for both two- and four-terminal measurements. b Schematic cross-section of the stacked devices.	152
12.2 Schematic representation of a a single moiré (tBLG) and b two superimposed moiré lattices (tBLG aligned with hBN).	153
12.3 a Schematic of the real space moiré super cell of the graphene/hBN system. Colored circles (I,II,V) correspond to centers of Gaussians used in the effective moiré potential in Eq. (12.1) as taken from [423]. b Schematic explanation of the superposition of the two moiré lattices. Light grey lines indicate edge character of the unit cells. Assuming a small graphene/hBN twist angle of $\theta_{hBN} \approx 0.7^\circ$ brings the two moiré cells to the same periodicity. c Moiré lattice constant of the graphene/hBN moiré as a function of their relative twist angle θ_{hBN}	153

12.4 a Two-terminal differential conductance dI/dV_{2T} as a function of the charge carrier density n for different temperatures measured along the entire Hall bar structure. b Arrhenius representation showing the differential resistance dV/dI_{2T} of the band insulating states as a function of the inverse temperature. The data is taken at charge carrier densities of $n \approx -2.4 \times 10^{12} \text{ cm}^{-2}$ and $n \approx 2.25 \times 10^{12} \text{ cm}^{-2}$ for the hole and electron insulating state, respectively. c Same as (b), but for the correlated insulating features at charge carrier densities of $n \approx -1.2 \times 10^{12} \text{ cm}^{-2}$ (hole doping) and $n \approx 1.1 \times 10^{12} \text{ cm}^{-2}$ (electron doping).	155
12.5 Band structure and density of state for a ribbon with a width of 10 tBLG moire unit cells of a just tBLG ($\theta_{BLG} \approx 0.987^\circ$) and b tBLG (same θ_{BLG}) with additional alignment ($\theta_{hBN} \approx 0.7^\circ$) to an hBN layer.	156
12.6 a Finite bias spectroscopy measurement of the band insulating state at hole doping. Instead of a clean gap, we observe the formation of roughly 130 individual Coulomb diamonds indicating a disordered system. b Same as in (a) but for the band insulator at electron doping. Striking is the asymmetry in the applied bias compared to the hole-doped band insulator. c Schematic representation of the measurement. The Hall bar consists of individual areas of tBLG with slightly different twist angles.	157
12.7 left column: tBLG with non-aligned hBN, right column: tBLG with aligned hBN ($\theta_{hBN} \approx 0.7^\circ$). a Schematic of the onsite energy corresponding to the different moiré super lattices. (relative sizes are to scale!) b Magnetoresistance simulation of the tBLG/hBN system with a BLG-twist-angle θ_{BLG} of 0.987° . Landau levels emerge from the charge neutrality point ($\nu = 0$) and the single-particle band gaps at full filling of the BLG moiré superlattice unit cell ($\nu = 4$). Alignment with hBN introduces additional Landau level features at non-integer filling factors ($\nu \approx 2.5$). c Magnetotransport measurements showing the B derivative of the longitudinal resistance as a function of filling factor ν and the normalized flux quantum per moiré super lattice unit cell of a tBLG moiré device ($\theta^{\exp.} \approx 0.97^\circ$). Landau fans emerge from integer-values of the filling factor. For additional hBN alignment (right) we observe additional lines starting at non-integer fillings ($\nu \approx 2.5$). d Zoom-ins of (c) e Dashed black lines (integer fillings) and dashed blue lines (non-integer fillings) as guide to the eye for (d).	159
A.1 BS comparison for ML parametrizations (double vacancy) of different sparsity (indicated as xNN) with DFT BS as reference. Bands that are not explicitly part of the loss function \mathcal{L}_e are drawn in a fainter color.	168

A.2 BS comparison for ML parametrizations (flower defect) of different sparsity (indicated as xNN) with DFT BS as reference. Bands that are not explicitly part of the loss function \mathcal{L}_e are drawn in a fainter color.	169
A.3 DFT results vs. double vacancy ML parametrizations of different sparsity (sparsity indicated by xNN and line colors). a DOS over a limited energy range b Cosine similarity of the c LDOS distribution within the supercell.	170
A.4 DFT results vs. flower defect ML parametrizations of different sparsity (sparsity indicated by xNN and line colors). a DOS over a limited energy range b Cosine similarity of the c LDOS distribution within the supercell.	171
B.1 In Fig. 8.3 of the main text we observe strain-independent lines in the PL energy range between 1.55 – 1.6eV that we assign to defect-related excitons. This assignment is supported by the detailed analysis of excitation power and V_G dependence of PL spectra. a PL vs. excitation power for an unstrained membrane ($V_G = 0$) measured on device 2 at 77 K. We identify neutral (X^0) and charged exciton (X^-) and three other peaks labelled 3 – 5 in decreasing energy order (black dashed lines). b PL spectra at selected excitation power densities. Spectra are normalized and offset for clarity. Peaks 3 – 5 dominate the PL spectrum at lower excitation powers while X^0 and X^- dominate at higher powers. c PL integrated intensities of the five peaks marked with dashed lines in (a) as a function of excitation power density. PL intensities are obtained by fitting the PL spectra to five Lorentzians. X^0 and X^- show an approximately linear dependence with excitation power. This behaviour is typical for free excitons [324]. PL intensities of peaks 3, 4 and 5 saturate with power indicating the defect-related character of the emission at those energies. d PL spectra of devices 1 and 2 featuring the same set of defect peaks, confirming their reproducibility. Spectra for device 1 (black) and device 2 (red) are extracted from the white lines in (e) and (d), respectively. Typically fitted spectra for device 2 corresponding to peaks 3 – 5 shown in (a)-(c) are plotted with dashed lines. e PL spectra vs. V_G for device 1. The energies of defect-related states are almost strain-independent, as expected from theory. (a)–(e) are measured at excitation 532nm. (d) and (e) are measured at excitation power density 250Wcm^{-2}	173

B.3 In the main text, we obtain strain at each gate voltage by measuring the shift in the energy position of the neutral exciton compared to its unstrained position. Here, we confirm the assignment of strain via an independent interferometric measurement. **a** Schematic of the device used in the main manuscript seen as an interferometric cavity. A circular monolayer WSe₂ membrane of radius $a = 2.5\mu\text{m}$ is suspended over a hole in SiO₂ and actuated (displacement h) by applying gate voltage V_G between WSe₂ and a Si substrate underneath (see Methods for details). The device is measured at room temperature by recording the reflected laser intensity of the laser beam ($\lambda = 633\text{nm}$, $P = 10\mu\text{W}$) focused on the membrane's center vs. V_G **b**. The interference of the laser beam in the optical cavity consisting of vacuum, SiO₂ and Si results in the changes of absorption by the membrane. With increasing $|V_G|$, the membrane moves downwards and the reflected intensity changes depending on the position of the membrane with respect to the nodes of the interference pattern. Quantitatively, a displacement of the membrane by $\lambda/4$ produces a change of π (half a period) in the phase of the sinusoidal modulation of the reflected signal. In this way we extract the position of the membrane's center h vs. V_G from the observed intensity of reflected light. Next, we convert the displacement into mechanical strain using the formula $\epsilon = \frac{2h^2}{3a^2}$ obtained from the analysis of the system's geometry [332]. The resulting data are plotted in **c** as black dots. For comparison, in the same graph we plot as red circles the values of strain obtained from the photoluminescence energetic shift of the excitonic peaks following the same procedure as in the main text. Both approaches to estimate strain produce very similar strain values.

- B.4 To confirm the validity of the model of strain induced by electrostatic force used in the main text, we extract the mechanical constants of WSe₂ from PL measurements at room temperature. To do this, we first calculate the electrostatic pressure P acting on the suspended WSe₂ at a particular gate voltage. Modelling the system as a parallel plate capacitor (WSe₂/Si) with two media inside of it (vacuum, SiO₂), we obtain $P = \frac{\epsilon_0 \epsilon_{\text{SiO}_2}^2}{(\epsilon_0 d_{\text{SiO}_2} + \epsilon_{\text{SiO}_2} d_0)^2} \frac{V_G^2}{2}$. We then calculate the displacement of the central point of the membrane h from strain obtained via PL measurements using $\epsilon = \frac{2h^2}{3a^2}$, where a is the radius of the membrane. Finally, $P(h)$ data obtained this way is plotted for two different devices (1 and 2). This data is fitted using an analytical model for $P(h)$ that is based on the well-known bulge-test equation in thin-film mechanics [332, 437]. This model describes the deflection of a uniform circular membrane under uniform pressure using Young modulus E_{2D} and built-in strain ϵ_0 as free parameters as $P = \frac{4E_{2D}\epsilon_0}{a^2} h + \frac{8E_{2D}}{3(1-\nu)a^4} h^3$, where $\nu = 0.2$ is the Poisson ratio for WSe₂ [438]. All data points agree quite well with the analytical fits (dashed lines). We obtained $E_{2D} \sim 74$ N/m and $\epsilon_0 = 0.04$ % for device 1 and $E_{2D} \sim 140$ N/m and $\epsilon_0 = 0.12$ % for device 2. The values are consistent with the mechanical constants typically reported for WSe₂ at room temperature [319]. 176
- C.1 Husimi distributions $Q(\mathbf{r}, \mathbf{k})$ for the third (**a**) and fourth (**b**) eigenstate of the first Landau level, averaged over several positions of maximal real space probability density $\rho(\mathbf{r}) = |\Psi|^2$ (indicated as $\mathbf{r}|_{\rho=\max}$). 177
- D.1 **a** Array of calculated LDOS colormaps across a zoom-in of the graphene flake for different x_{tip} (as indicated by red dots).
b Zoom-in of Fig. 10.9d near LL+2 with coordinates (V_{BG} , x_{tip}) corresponding to panels in **a** again indicated as red dots. 179
- D.2 **a** Array of calculated LDOS colormaps across a zoom-in of the graphene flake for different x_{tip} (as indicated by red dots).
b Zoom-in of Fig. 10.9d near LL+1 with coordinates (V_{BG} , x_{tip}) corresponding to panels in **a** again indicated as red dots. 179
- D.3 **a** Array of calculated LDOS colormaps across a zoom-in of the graphene flake for different x_{tip} (as indicated by red dots).
b Zoom-in of Fig. 10.9d near LL+1 with coordinates (V_{BG} , x_{tip}) corresponding to panels in **a** again indicated as red dots. 180
- D.4 **a** Array of calculated LDOS colormaps across a zoom-in of the graphene flake for different x_{tip} (as indicated by red dots).
b Zoom-in of Fig. 10.9d near LL-1 with coordinates (V_{BG} , x_{tip}) corresponding to panels in **a** again indicated as red dots. 180

- D.5 **a** Array of calculated LDOS colormaps across a zoom-in of the graphene flake for different x_{tip} (as indicated by red dots).
b Zoom-in of Fig. 10.9d near LL0 with coordinates (V_{BG} , x_{tip}) corresponding to panels in **a** again indicated as red dots. 181
- D.6 **a** Array of calculated LDOS colormaps across a zoom-in of the graphene flake for different x_{tip} (as indicated by red dots).
b Zoom-in of Fig. 10.9d near LL-1 with coordinates (V_{BG} , x_{tip}) corresponding to panels in **a** again indicated as red dots. 181
- D.7 **a** Array of calculated LDOS colormaps across a zoom-in of the graphene flake for different x_{tip} (as indicated by red dots).
b Zoom-in of Fig. 10.9d near LL-1 with coordinates (V_{BG} , x_{tip}) corresponding to panels in **a** again indicated as red dots. 182
- D.8 **a** Array of calculated LDOS colormaps across a zoom-in of the graphene flake for different x_{tip} (as indicated by red dots).
b Zoom-in of Fig. 10.9d near LL-2 with coordinates (V_{BG} , x_{tip}) corresponding to panels in **a** again indicated as red dots. 182
- D.9 **a** Array of calculated LDOS colormaps across a zoom-in of the graphene flake for different x_{tip} (as indicated by red dots).
b Zoom-in of Fig. 10.9d near LL-3 with coordinates (V_{BG} , x_{tip}) corresponding to panels in **a** again indicated as red dots. 183
- D.10 **a,b** Square amplitude of the state with the largest contribution to the LDOS in **c** (cohesiveness indicated with grey shading). States are valley degenerate and feature pronounced sub lattice structure. The degenerate partner states (not shown) feature inverted triangular shapes that sum to fairly spherical LDOS signatures in **c**. **c** Array of calculated LDOS colormaps across a zoom-in of the graphene flake for different x_{tip} (as indicated by red dots). **d** Zoom-in of Fig. 10.9d near the branching of LL-1 with coordinates (V_{BG} , x_{tip}) corresponding to panels in **c** again indicated as red dots. 183
- D.11 **a** Array of calculated LDOS colormaps across a zoom-in of the graphene flake for different x_{tip} (as indicated by red dots).
b Zoom-in of Fig. 10.12a for fixed V_{BG} with coordinates (V_{tip} , x_{tip}) corresponding to panels in **a** again indicated as red dots. 184
- D.12 **a** Array of calculated LDOS colormaps across a zoom-in of the graphene flake for different x_{tip} (as indicated by red dots).
b Zoom-in of Fig. 10.12a for fixed V_{BG} with coordinates (V_{tip} , x_{tip}) corresponding to panels in **a** again indicated as red dots. 184
- D.13 **a** Array of calculated LDOS colormaps across a zoom-in of the graphene flake for different x_{tip} (as indicated by red dots).
b Zoom-in of Fig. 10.12a for fixed V_{BG} with coordinates (V_{tip} , x_{tip}) corresponding to panels in **a** again indicated as red dots. 185
- D.14 **a** Array of calculated LDOS colormaps across a zoom-in of the graphene flake for different x_{tip} (as indicated by red dots).
b Zoom-in of Fig. 10.12a for fixed V_{BG} with coordinates (V_{tip} , x_{tip}) corresponding to panels in **a** again indicated as red dots. 185

D.15 a Array of calculated LDOS colormaps across a zoom-in of the graphene flake for different x_{tip} (as indicated by red dots). b Zoom-in of Fig. 10.12b for fixed V_{BG} with coordinates (V_{tip} , x_{tip}) corresponding to panels in a again indicated as red dots.	186
D.16 a Array of calculated LDOS colormaps across a zoom-in of the graphene flake for different x_{tip} (as indicated by red dots). b Zoom-in of Fig. 10.12b for fixed V_{BG} with coordinates (V_{tip} , x_{tip}) corresponding to panels in a again indicated as red dots.	186
D.17 a Array of calculated LDOS colormaps across a zoom-in of the graphene flake for different x_{tip} (as indicated by red dots). b Zoom-in of Fig. 10.12b for fixed V_{BG} with coordinates (V_{tip} , x_{tip}) corresponding to panels in a again indicated as red dots.	187
D.18 a Array of calculated LDOS colormaps across a zoom-in of the graphene flake for different x_{tip} (as indicated by red dots). b Zoom-in of Fig. 10.12b for fixed V_{BG} with coordinates (V_{tip} , x_{tip}) corresponding to panels in a again indicated as red dots.	187
D.19 Detailed comparison of the potentials calculated with the 1D Poisson solver and the analytic fits used for the 2D TB calculations for three representative configurations of (V_{BG} , x_{tip}) a $\eta = -0.41$, $x_{\text{tip}} = 180\text{nm}$, b $\eta = -0.31$, $x_{\text{tip}} = 130\text{nm}$, c $\eta = 0.32$, $x_{\text{tip}} = 270\text{nm}$. The mean absolute difference of the two potentials $\frac{\langle \Delta\Phi_{\text{tot}} \rangle}{n_{\text{sites}}}$ per TB site is shown as well.	188
D.20 a Simulated LDOS(V_{sample} , x_{tip}) across the lateral interface, while including the TIQD, $V_{\text{gate}} = 2.0\text{ V}$. b Measured $dI/dV_{\text{sample}}(V_{\text{sample}}, x_{\text{tip}})$, $V_{\text{gate}} = 2.0\text{ V}$, $I_{\text{stab}} = 200\text{ pA}$, $V_{\text{stab}} = -250\text{ mV}$	188
E.1 Zooms into $dI/dV_{\text{sample}}(V_{\text{gate}}, V_{\text{sample}})$ around the LL0 plateau at E_F at fixed position $x_{\text{tip}} \ll 0\text{ nm}$ (same data as Fig. 10.2a,b in Chapter 10), $I_{\text{stab}} = 1\text{ nA}$, $V_{\text{stab}} = -250\text{ mV}$. The areas of the four zooms are marked in the central image by a frame of the same color. Magenta frame: LDOS lines of the various m states that belong to LL0. Cyan frame: Kinks in the LDOS line belonging to LL-1 that appear each time when a charging line is crossing. Green frame: same as cyan frame for the LDOS line belonging to the $m = 0$ state of LL0. Red frame: Coulomb diamonds at E_F belonging to a higher m state of LL0. The occupied and unoccupied version of the same m state is marked.	189
E.2 $dI/dV_{\text{sample}}(V_{\text{gate}}, V_{\text{sample}})$ (zoom into Fig. 10.2a in Chapter 10), $x_{\text{tip}} \ll 0\text{ nm}$, $I_{\text{stab}} = 1\text{ nA}$, $V_{\text{stab}} = -250\text{ mV}$. The LL-1 plateau and its charging lines starting from the right end of the plateau are visible.	190
E.3 $d^2I/dV_{\text{sample}}dV_{\text{gate}}(V_{\text{gate}}, V_{\text{sample}})$ for the transition between LL-3 to LL-2 at E_F (full red line), $I_{\text{stab}} = 1\text{ nA}$, $V_{\text{stab}} = -250\text{ mV}$. The crossing point of the first charging line of LL-3 with the last charging line belonging to LL-2 is marked (red circle) via extrapolation of the two charging lines (dashed red lines).	191

E.4	a Potential depth of the hole-type TIQD for varying external potentials Φ_{gate} and Φ_{tip} , $r_{\text{tip}} = 25 \text{ nm}$. b Selection of the potential depth values from a that are in accordance with the crossing points of charging lines in the experiment. green: TIQD depth = $39.8 \pm 2.5 \text{ meV}$, yellow: TIQD depth = $30.5 \pm 2.5 \text{ meV}$, blue: all other TIQD depths. Pairs of circle and cross of the same color are separated by $e\delta V_{\text{gate}} = 0.95 \text{ eV}$ along Φ_{gate} and by $e\delta V_{\text{sample}} = 0.15 \text{ eV}$ along Φ_{tip} , such as the two crossing points of charging lines in Fig. E.3 and Fig. 10.9a from the main text. Only two pairs are found to match the required conditions that the circle is on a green area, while the corresponding cross is on a yellow area.	192
E.5	a dI/dV_{sample} ($V_{\text{gate}}, V_{\text{sample}}$) recorded at a position $x_{\text{tip}} \ll 0 \text{ nm}$, $I_{\text{stab}} = 1 \text{ nA}$, $V_{\text{stab}} = -250 \text{ mV}$. b LDOS($V_{\text{gate}}, V_{\text{sample}}$) resulting from the Poisson simulations with optimized parameters, $\Delta V_{\text{gate}} = -200 \text{ mV}$, $\Delta V_{\text{sample}} = -180 \text{ mV}$, $r_{\text{tip}} = 25 \text{ nm}$. c LDOS($V_{\text{gate}}, V_{\text{sample}}$) resulting from the Poisson simulations with less favorable parameters, $\Delta V_{\text{gate}} = +650 \text{ mV}$, $\Delta V_{\text{sample}} = -230 \text{ mV}$, $r_{\text{tip}} = 25 \text{ nm}$. Note the shifted V_{gate} axis in c.	192
E.6	Comparison of the averaged distance between charging lines in the experiment (dark blue) with the ones deduced from the Poisson simulations at different r_{tip} as labelled, $\Delta V_{\text{gate}} = -200 \pm 50 \text{ mV}$, $\Delta V_{\text{sample}} = -180 \pm 50 \text{ mV}$. The error bars of the experiment result from the variance of the averages from different regularly spaced groups of charging lines (see text). The error bars of the simulations result from the variance in $\Delta\Phi_{\text{gate}}/\Delta Q_{\text{QD}}$ and $\Delta\Phi_{\text{tip}}/\Delta Q_{\text{QD}}$, respectively, within the simulation range of $\Phi_{\text{tip}} \in [-0.6, 0] \text{ eV}$ and $\Phi_{\text{gate}} \in [-3.2, 0] \text{ eV}$. Note that the error bars indicate the same variance in experiment and simulation, but do not provide the statistical uncertainty of the mean values.	193
F.1	a Blue line: profile line across the step edge due to the graphite gate as measured by STM (see also Fig. 10.9c–d). Red line: tentative position of relaxed graphene directly prior to contact with the hBN. Pink arrow: Force that pulls the graphene downwards to the hBN. b Wave function corresponding to LL1 determined by a tight binding calculation without strain (black), with a Gaussian strain profile of amplitude 0.05 % and FWHM 60 nm (red full line), and with amplitude 0.3 % and FWHM 60 nm (red dashed line).	194
G.1	a Two-terminal differential conductance as a function of magnetic field and carrier density measured along the entire Hall bar structure. b Four-terminal longitudinal resistance as a function of magnetic field and carrier density.	196
G.2	Band structure of a ribbon of (left) tBLG (right) tBLG with hBN alignment.	197

List of Tables

2.1	Name, coordinates and symmetry groups (Schönflies notation) for the high symmetry points of the hexagonal lattice in reciprocal space.	7
2.2	Measured and calculated band gaps (ΔE_{KK}) for prominent TMDs. ^a [42], ^b [43], ^c [44], ^d [45], ^e [46]	11
4.1	Common loss functions \mathcal{L} in regression and classification problems.	31
4.2	Comparison of the number of trainable parameters necessary for connecting two layers of a neural network of type dense or convolutional.	36
4.3	Common kernels/covariance functions (if stationary: $k(\mathbf{x}, \mathbf{x}') = k(\Delta\mathbf{x})$) with representative functions sampled from the prior distribution (zero mean and variance indicated in black and grey respectively).	41
6.1	Comparison of both performance [in terms of BS error δ_ε , see Eq. (6.5)] and time efficiency of several ML approaches to the inverse BS problem of the double vacancy in SLG. While the underlying data sets are not necessarily equal for the different optimization algorithms we still find this to be a legitimate comparison.	67
6.2	Convolutional neural network setup used in Table 6.1 containing 668 839 trainable parameters for the double vacancy defect. The CNNs we considered are made up of feature selection blocks (convolutional layers + pooling) followed by a shallow dense network.	72
6.3	Structure of the multilayer perceptron architecture used for the double vacancy defect.	73
6.4	Number of independent TB parameters for a given sparseness in both defect structures under consideration.	76
10.1	Fit parameters used for the quenching function $q(f)$ defined in Eq. (10.8).	136
10.2	Average Δx values from experimental data (STM) and TB simulations (LDOS) of selected edge states. See Fig. 10.13 for individual data points.	140

Bibliography

1. Chidambaram, P., Bowen, C., Chakravarthi, S., Machala, C. & Wise, R. Fundamentals of silicon material properties for successful exploitation of strain engineering in modern CMOS manufacturing. *IEEE Transactions on Electron Devices* **53**, 944–964 (May 2006).
2. Shi, Z. *et al.* Deep elastic strain engineering of bandgap through machine learning. *Proceedings of the National Academy of Sciences* **116**, 4117–4122 (Feb. 2019).
3. Yeh, C.-C. *et al.* A low operating power FinFET transistor module featuring scaled gate stack and strain engineering for 32/28nm SoC technology in 2010 International Electron Devices Meeting (2010), 34.1.1–34.1.4. doi:10.1109/IEDM.2010.5703473.
4. Tao, L. *et al.* Recent advances in mechanical strain engineering of low-dimensional semiconductors and their applications in high-performance quantum emitters. *Semiconductor Science and Technology* **35**, 103002 (Sept. 2020).
5. Thompson, S. *et al.* A logic nanotechnology featuring strained-silicon. *IEEE Electron Device Letters* **25**, 191–193 (2004).
6. Novoselov, K. S. *et al.* Electric Field Effect in Atomically Thin Carbon Films. *Nature* **306**, 666–669 (Oct. 2004).
7. Gupta, A., Sakthivel, T. & Seal, S. Recent development in 2D materials beyond graphene. *Progress in Materials Science* **73**, 44–126 (Aug. 2015).
8. Lei, Y. *et al.* Graphene and Beyond: Recent Advances in Two-Dimensional Materials Synthesis, Properties, and Devices. *ACS Nanoscience Au* **2**, 450–485 (Sept. 2022).
9. Möller, S. *et al.* Probing Two-Electron Multiplets in Bilayer Graphene Quantum Dots. *Phys. Rev. Lett.* **127**, 256802 (25 2021).
10. Azzam, S. I., Parto, K. & Moody, G. Prospects and challenges of quantum emitters in 2D materials. *Applied Physics Letters* **118**, 240502 (June 2021).
11. Cao, Y. *et al.* Unconventional superconductivity in magic-angle graphene superlattices - Nature. *Nature* **556**, 43–50 (2018).
12. Schmitz, M *et al.* Fractional quantum Hall effect in CVD-grown graphene. *2D Materials* **7**, 041007 (Sept. 2020).
13. Bolotin, K. I., Ghahari, F., Shulman, M. D., Stormer, H. L. & Kim, P. Observation of the fractional quantum Hall effect in graphene. *Nature* **462**, 196–199 (Nov. 2009).

14. Freitag, N. M. *et al.* Electrostatically Confined Monolayer Graphene Quantum Dots with Orbital and Valley Splittings. *Nano Letters* **16**, 5798–5805 (2016).
15. Gunlycke, D. & White, C. T. Graphene Valley Filter Using a Line Defect. *Physical Review Letters* **106** (Mar. 2011).
16. Boehm, H. P., Clauss, A., Fischer, G. O. & Hofmann, U. Das Adsorptionsverhalten sehr d?nnner Kohlenstoff-Folien. **316**, 119–127 (July 1962).
17. Gjerding, M. N. *et al.* Recent progress of the computational 2D materials database (C2DB). *2D Materials* **8**, 044002 (July 2021).
18. Haastrup, S. *et al.* The Computational 2D Materials Database: high-throughput modeling and discovery of atomically thin crystals. *2D Materials* **5**, 042002 (Sept. 2018).
19. McCann, E. in *Graphene Nanoelectronics* 237–275 (Springer Berlin Heidelberg, 2011). doi:10.1007/978-3-642-22984-8_8.
20. Novoselov, K. S. *et al.* Two-dimensional gas of massless Dirac fermions in graphene. *Nature* **438**, 197–200 (Nov. 2005).
21. Goerbig, M. & Montambaux, G. in *Dirac Matter* (eds Duplantier, B., Rivasseau, V. & Fuchs, J.-N.) 25–53 (Springer International Publishing, Cham, 2017). doi:10.1007/978-3-319-32536-1_2.
22. Chelikowsky, J. R. & Cohen, M. L. Electronic Structure of GaAs. *Phys. Rev. Lett.* **32**, 674–677 (12 1974).
23. Castro Neto, A. H., Guinea, F., Peres, N. M. R., Novoselov, K. S. & Geim, A. K. The electronic properties of graphene. *Rev. Mod. Phys.* **81**, 109–162 (1 2009).
24. Lee, C., Wei, X., Kysar, J. W. & Hone, J. Measurement of the Elastic Properties and Intrinsic Strength of Monolayer Graphene. *Science* **321**, 385–388 (July 2008).
25. Guinea, F., Geim, A. K., Katsnelson, M. I. & Novoselov, K. S. Generating quantizing pseudomagnetic fields by bending graphene ribbons. *Phys. Rev. B* **81**, 035408 (3 2010).
26. Levy, N. *et al.* Strain-Induced Pseudo-Magnetic Fields Greater Than 300 Tesla in Graphene Nanobubbles. *Science* **329**, 544–547 (July 2010).
27. Masir, M. R., Moldovan, D. & Peeters, F. Pseudo magnetic field in strained graphene: Revisited. *Solid State Communications* **175-176**, 76–82 (Dec. 2013).
28. Kang, D.-H. *et al.* Pseudo-magnetic field-induced slow carrier dynamics in periodically strained graphene. *Nature Communications* **12**. doi:10.1038/s41467-021-25304-0 (Aug. 2021).
29. Guinea, F., Katsnelson, M. I. & Geim, A. K. Energy gaps and a zero-field quantum Hall effect in graphene by strain engineering. *Nature Physics* **6**, 30–33 (Sept. 2009).

30. Mohiuddin, T. M. G. *et al.* Uniaxial strain in graphene by Raman spectroscopy: G peak splitting, Grüneisen parameters, and sample orientation. *Phys. Rev. B* **79**, 205433 (20 2009).
31. Tsoukleri, G. *et al.* Subjecting a Graphene Monolayer to Tension and Compression. *Small* **5**, 2397–2402 (Nov. 2009).
32. Huang, M. *et al.* Phonon softening and crystallographic orientation of strained graphene studied by Raman spectroscopy. *Proceedings of the National Academy of Sciences* **106**, 7304–7308 (May 2009).
33. Graf, D. *et al.* Spatially Resolved Raman Spectroscopy of Single- and Few-Layer Graphene. *Nano Letters* **7**, 238–242 (Jan. 2007).
34. Oh, M. *et al.* Evidence for unconventional superconductivity in twisted bilayer graphene. *Nature* **600**, 240–245 (Oct. 2021).
35. McCann, E. Asymmetry gap in the electronic band structure of bilayer graphene. *Phys. Rev. B* **74**, 161403 (16 2006).
36. McCann, E. & Fal'ko, V. I. Landau-Level Degeneracy and Quantum Hall Effect in a Graphite Bilayer. *Phys. Rev. Lett.* **96**, 086805 (8 2006).
37. Zhang, Y. *et al.* Direct observation of a widely tunable bandgap in bilayer graphene. *Nature* **459**, 820–823 (June 2009).
38. Knothe, A. & Fal'ko, V. Influence of minivalleys and Berry curvature on electrostatically induced quantum wires in gapped bilayer graphene. *Phys. Rev. B* **98**, 155435 (15 2018).
39. Berry M. V., M. R. J. Neutrino billiards: time-reversal symmetry-breaking without magnetic fields. *Proceedings of the Royal Society of London. A. Mathematical and Physical Sciences* **412**, 53–74 (July 1987).
40. Liu, G.-B., Shan, W.-Y., Yao, Y., Yao, W. & Xiao, D. Three-band tight-binding model for monolayers of group-VIB transition metal dichalcogenides. *Phys. Rev. B* **88**, 085433 (8 2013).
41. Fang, S. *et al.* Ab initio tight-binding Hamiltonian for transition metal dichalcogenides. *Phys. Rev. B* **92**, 205108 (20 2015).
42. Klots, A. R. *et al.* Probing excitonic states in suspended two-dimensional semiconductors by photocurrent spectroscopy. *Scientific Reports* **4**. doi:10.1038/srep06608 (Oct. 2014).
43. Kormányos, A. *et al.* $k \cdot p$ theory for two-dimensional transition metal dichalcogenide semiconductors. *2D Materials* **2**, 022001 (Apr. 2015).
44. Ugeda, M. M. *et al.* Giant bandgap renormalization and excitonic effects in a monolayer transition metal dichalcogenide semiconductor. *Nature Materials* **13**, 1091–1095 (Aug. 2014).
45. Jo, S., Ubrig, N., Berger, H., Kuzmenko, A. B. & Morpurgo, A. F. Mono- and Bilayer WS₂ Light-Emitting Transistors. *Nano Letters* **14**, 2019–2025 (Mar. 2014).

46. Chiu, M.-H. *et al.* Determination of band alignment in the single-layer MoS₂/WSe₂ heterojunction. *Nature Communications* **6**. doi:10.1038/ncomms8666 (July 2015).
47. Molina-Sánchez, A. & Wirtz, L. Phonons in single-layer and few-layer MoS₂ and WS₂. *Phys. Rev. B* **84**, 155413 (15 2011).
48. Cappelluti, E., Roldán, R., Silva-Guillén, J. A., Ordejón, P. & Guinea, F. Tight-binding model and direct-gap/indirect-gap transition in single-layer and multilayer MoS₂. *Phys. Rev. B* **88**, 075409 (7 2013).
49. Ernandes, C. *et al.* Indirect to direct band gap crossover in two-dimensional WS₂(1-x)Se_{2x} alloys. *npj 2D Materials and Applications* **5**. doi:10.1038/s41699-020-00187-9 (Jan. 2021).
50. Hsu, W.-T. *et al.* Evidence of indirect gap in monolayer WSe₂. *Nature Communications* **8**. doi:10.1038/s41467-017-01012-6 (Oct. 2017).
51. Perdew, J. P. & Zunger, A. Self-interaction correction to density-functional approximations for many-electron systems. *Phys. Rev. B* **23**, 5048–5079 (10 1981).
52. Levine, Z. H. & Allan, D. C. Linear optical response in silicon and germanium including self-energy effects. *Phys. Rev. Lett.* **63**, 1719–1722 (16 1989).
53. Blundo, E. *et al.* Evidence of the direct-to-indirect band gap transition in strained two-dimensional WS₂, MoS₂, and WSe₂. *Phys. Rev. Research* **2**, 012024 (1 2020).
54. Hanbicki, A., Currie, M., Kioseoglou, G., Friedman, A. & Jonker, B. Measurement of high exciton binding energy in the monolayer transition-metal dichalcogenides WS₂ and WSe₂. *Solid State Communications* **203**, 16–20 (2015).
55. Wang, G. *et al.* Colloquium: Excitons in atomically thin transition metal dichalcogenides. *Rev. Mod. Phys.* **90**, 021001 (2 2018).
56. Cudazzo, P., Tokatly, I. V. & Rubio, A. Dielectric screening in two-dimensional insulators: Implications for excitonic and impurity states in graphane. *Phys. Rev. B* **84**, 085406 (8 2011).
57. Wang, Y. *et al.* Spin-Valley Locking Effect in Defect States of Monolayer MoS₂. *Nano Letters* **20**, 2129–2136 (Feb. 2020).
58. Cao, T. *et al.* Valley-selective circular dichroism of monolayer molybdenum disulphide. *Nature Communications* **3**. doi:10.1038/ncomms1882 (Jan. 2012).
59. Mak, K. F., He, K., Shan, J. & Heinz, T. F. Control of valley polarization in monolayer MoS₂ by optical helicity. *Nature Nanotechnology* **7**, 494–498 (June 2012).
60. Mermin, N. D. The topological theory of defects in ordered media. *Rev. Mod. Phys.* **51**, 591–648 (3 1979).
61. Kröger, F. & Vink, H. in *Solid State Physics* 307–435 (Elsevier, 1956). doi:10.1016/s0081-1947(08)60135-6.

62. Kröner, E. in *Trends in Applications of Pure Mathematics to Mechanics* 281–294 (Springer-Verlag). doi:10.1007/bfb0016397.
63. Kittel, C. & McEuen, P. *Introduction to Solid State Physics* en (John Wiley & Sons, 2018).
64. Bonaccorso, F. *et al.* Production and processing of graphene and 2d crystals. *Materials Today* **15**, 564–589 (Dec. 2012).
65. Banszerus, L. *et al.* Ultrahigh-mobility graphene devices from chemical vapor deposition on reusable copper. *Science Advances* **1**, e1500222 (July 2015).
66. Tian, W., Li, W., Yu, W. & Liu, X. A Review on Lattice Defects in Graphene: Types, Generation, Effects and Regulation. *Micromachines* **8**, 163 (May 2017).
67. Kim, N. *et al.* Lattice Engineering to Simultaneously Control the Defect/Stacking Structures of Layered Double Hydroxide Nanosheets to Optimize Their Energy Functionalities. *ACS Nano* **15**, 8306–8318 (Apr. 2021).
68. Lang, D. V. Deep-level transient spectroscopy: A new method to characterize traps in semiconductors. *Journal of Applied Physics* **45**, 3023–3032 (July 1974).
69. Dobaczewski, L., Kaczor, P., Hawkins, I. D. & Peaker, A. R. Laplace transform deep-level transient spectroscopic studies of defects in semiconductors. *Journal of Applied Physics* **76**, 194–198 (July 1994).
70. Andrei, E. Y. *et al.* The marvels of moiré materials. *Nature Reviews Materials* **6**, 201–206 (Mar. 2021).
71. Lopes dos Santos, J. M. B., Peres, N. M. R. & Castro Neto, A. H. Continuum model of the twisted graphene bilayer. *Phys. Rev. B* **86**, 155449 (15 2012).
72. Lucignano, P., Alfè, D., Cataudella, V., Ninno, D. & Cantele, G. Crucial role of atomic corrugation on the flat bands and energy gaps of twisted bilayer graphene at the magic angle $\theta \sim 1.08^\circ$. *Phys. Rev. B* **99**, 195419 (19 2019).
73. Liao, M. *et al.* Precise control of the interlayer twist angle in large scale MoS₂ homostructures. *Nature Communications* **11**. doi:10.1038/s41467-020-16056-4 (May 2020).
74. Andrei, E. Y. & MacDonald, A. H. Graphene bilayers with a twist. *Nature Materials* **19**, 1265–1275 (Nov. 2020).
75. Nimbalkar, A. & Kim, H. Opportunities and Challenges in Twisted Bilayer Graphene: A Review. *Nano-Micro Letters* **12**. doi:10.1007/s40820-020-00464-8 (June 2020).
76. Moon, P. & Koshino, M. Electronic properties of graphene/hexagonal-boron-nitride moiré superlattice. *Phys. Rev. B* **90**, 155406 (15 2014).
77. Kerelsky, A. *et al.* Maximized electron interactions at the magic angle in twisted bilayer graphene. *Nature* **572**, 95–100 (July 2019).

78. Carr, S., Fang, S. & Kaxiras, E. Electronic-structure methods for twisted moiré layers. *Nature Reviews Materials* **5**, 748–763 (July 2020).
79. Correa, J. D., Pacheco, M. & Morell, E. S. Optical absorption spectrum of rotated trilayer graphene. *Journal of Materials Science* **49**, 642–647 (Sept. 2013).
80. Kang, P. *et al.* Moiré impurities in twisted bilayer black phosphorus: Effects on the carrier mobility. *Phys. Rev. B* **96**, 195406 (19 2017).
81. Uchida, K., Furuya, S., Iwata, J.-I. & Oshiyama, A. Atomic corrugation and electron localization due to Moiré patterns in twisted bilayer graphenes. *Phys. Rev. B* **90**, 155451 (15 2014).
82. Kang, J., Li, J., Li, S.-S., Xia, J.-B. & Wang, L.-W. Electronic Structural Moiré Pattern Effects on MoS₂/MoSe₂ 2D Heterostructures. *Nano Letters* **13**, 5485–5490 (Oct. 2013).
83. Linhart, L. *On emergent mesoscopic effects in 2D materials* PhD thesis (TU Wien, 2020).
84. Fabian, T., Kausel, M., Linhart, L., Burgdörfer, J. & Libisch, F. Half-integer Wannier diagram and Brown-Zak fermions of graphene on hexagonal boron nitride. *Phys. Rev. B* **106**, 165412 (16 2022).
85. Bloch, F. Über die Quantenmechanik der Elektronen in Kristallgittern. *Zeitschrift für Physik* **52**, 555–600 (July 1929).
86. Thomas, L. H. The calculation of atomic fields. *Mathematical Proceedings of the Cambridge Philosophical Society* **23**, 542?548 (1927).
87. Lieb, E. H. & Simon, B. The Thomas-Fermi theory of atoms, molecules and solids. *Advances in Mathematics* **23**, 22–116 (Jan. 1977).
88. Hohenberg, P. & Kohn, W. Inhomogeneous Electron Gas. *Phys. Rev.* **136**, B864–B871 (3B 1964).
89. Kohn, W. & Sham, L. J. Self-Consistent Equations Including Exchange and Correlation Effects. *Phys. Rev.* **140**, A1133–A1138 (4A 1965).
90. Vignale, G. & Rasolt, M. Density-functional theory in strong magnetic fields. *Phys. Rev. Lett.* **59**, 2360–2363 (20 1987).
91. Capelle, K., Ullrich, C. A. & Vignale, G. Degenerate ground states and nonunique potentials: Breakdown and restoration of density functionals. *Phys. Rev. A* **76**, 012508 (1 2007).
92. Levy, M. Universal variational functionals of electron densities, first-order density matrices, and natural spin-orbitals and solution of the v-representability problem. *Proceedings of the National Academy of Sciences* **76**, 6062–6065 (Dec. 1979).
93. Mardirossian, N. & Head-Gordon, M. Thirty years of density functional theory in computational chemistry: an overview and extensive assessment of 200 density functionals. *Molecular Physics* **115**, 2315–2372 (June 2017).

94. Borlido, P. *et al.* Exchange-correlation functionals for band gaps of solids: benchmark, reparametrization and machine learning. *npj Computational Materials* **6**. doi:10.1038/s41524-020-00360-0 (July 2020).
95. Ceperley, D. M. & Alder, B. J. Ground State of the Electron Gas by a Stochastic Method. *Phys. Rev. Lett.* **45**, 566–569 (7 1980).
96. Perdew, J. P. Accurate Density Functional for the Energy: Real-Space Cutoff of the Gradient Expansion for the Exchange Hole. *Phys. Rev. Lett.* **55**, 1665–1668 (16 1985).
97. Lignères, V. L. & Carter, E. A. in *Handbook of Materials Modeling* 137–148 (Springer Netherlands, 2005). doi:10.1007/978-1-4020-3286-8_9.
98. Gandus, G., Valli, A., Passerone, D. & Stadler, R. Smart local orbitals for efficient calculations within density functional theory and beyond. *The Journal of Chemical Physics* **153**, 194103 (Nov. 2020).
99. Pathak, S. *et al.* Accurate Hellmann Feynman forces from density functional calculations with augmented Gaussian basis sets. *The Journal of Chemical Physics* **158**, 014104 (Jan. 2023).
100. Kresse, G. & Furthmüller, J. Efficient iterative schemes for ab initio total-energy calculations using a plane-wave basis set. *Phys. Rev. B* **54**, 11169–11186 (16 1996).
101. Kresse, G. & Furthmüller, J. Efficiency of ab-initio total energy calculations for metals and semiconductors using a plane-wave basis set. *Computational Materials Science* **6**, 15–50 (July 1996).
102. Kresse, G. & Hafner, J. Ab initio molecular dynamics for liquid metals. *Phys. Rev. B* **47**, 558–561 (1 1993).
103. Kresse, G. & Hafner, J. Ab initio molecular-dynamics simulation of the liquid-metal–amorphous-semiconductor transition in germanium. *Phys. Rev. B* **49**, 14251–14269 (20 1994).
104. Mortensen, J. J., Hansen, L. B. & Jacobsen, K. W. Real-space grid implementation of the projector augmented wave method. *Phys. Rev. B* **71**, 035109 (3 2005).
105. Enkovaara, J *et al.* Electronic structure calculations with GPAW: a real-space implementation of the projector augmented-wave method. *Journal of Physics: Condensed Matter* **22**, 253202 (June 2010).
106. Larsen, A. H., Vanin, M., Mortensen, J. J., Thygesen, K. S. & Jacobsen, K. W. Localized atomic basis set in the projector augmented wave method. *Phys. Rev. B* **80**, 195112 (19 2009).
107. Ernzerhof, M. & Scuseria, G. E. Assessment of the Perdew–Burke–Ernzerhof exchange-correlation functional. *The Journal of Chemical Physics* **110**, 5029–5036 (Mar. 1999).
108. Goringe, C. M., Bowler, D. R. & Hernández, E. Tight-binding modelling of materials. *Reports on Progress in Physics* **60**, 1447–1512 (Dec. 1997).

109. Harrison, W. *Electronic Structure and the Properties of Solids: The Physics of the Chemical Bond* (Dover Publications, 1989).
110. Ashcroft, N. W. & Mermin, N. D. *Solid State Physics* (Holt-Saunders, 1976).
111. Bena, C. & Montambaux, G. Remarks on the tight-binding model of graphene. *New Journal of Physics* **11**, 095003 (Sept. 2009).
112. Linhart, L., Burgdörfer, J. & Libisch, F. Accurate modeling of defects in graphene transport calculations. *Phys. Rev. B* **97**, 035430 (3 2018).
113. Büttiker, M. Absence of backscattering in the quantum Hall effect in multiprobe conductors. *Phys. Rev. B* **38**, 9375–9389 (14 1988).
114. Fabian, T. *Simulation of Electronic Transport in Graphene Systems* PhD thesis (TU Wien, 2021).
115. Sanvito, S. *Giant Magnetoresistance and Quantum Transport in Magnetic Hybrid Nanostructures* PhD thesis (Lancaster University, 1999).
116. Libisch, F. *Electronic structure and transport in mesoscopic devices* PhD thesis (Technological University of Vienna, 2009).
117. Roach, G. F. *Green's Functions* 2nd ed. (Cambridge University Press, Cambridge, England, May 1982).
118. Dyson, F. J. The S Matrix in Quantum Electrodynamics. *Phys. Rev.* **75**, 1736–1755 (11 1949).
119. Landauer, R. Spatial variation of currents and fields due to localized scatterers in metallic conduction (and comment). *Journal of Mathematical Physics* **37**, 5259–5268 (Oct. 1996).
120. Marzari, N., Mostofi, A. A., Yates, J. R., Souza, I. & Vanderbilt, D. Maximally localized Wannier functions: Theory and applications. *Rev. Mod. Phys.* **84**, 1419–1475 (4 2012).
121. Aufderheide, K. H. Localized atomic orbitals for atoms in molecules. I. Methodology. *The Journal of Chemical Physics* **73**, 1777–1788 (Aug. 1980).
122. Høyvik, I.-M., Jansik, B. & Jørgensen, P. Orbital localization using fourth central moment minimization. *The Journal of Chemical Physics* **137**, 224114 (Dec. 2012).
123. Lehtola, S. & Jónsson, H. Pipek–Mezey Orbital Localization Using Various Partial Charge Estimates. *Journal of Chemical Theory and Computation* **10**, 642–649 (Jan. 2014).
124. Marzari, N. & Vanderbilt, D. Maximally localized generalized Wannier functions for composite energy bands. *Phys. Rev. B* **56**, 12847–12865 (20 1997).
125. Pizzi, G. *et al.* Wannier90 as a community code: new features and applications. *Journal of Physics: Condensed Matter* **32**, 165902 (Jan. 2020).
126. Witten, I. H., Frank, E., Hall, M. A. & Pal, C. J. *Data mining : practical machine learning tools and techniques* (Morgan Kaufmann, Amsterdam; London, 2017).

127. Devroye, L., Györfi, L. & Lugosi, G. *A Probabilistic Theory of Pattern Recognition* 1–638 (Springer, 1996).
128. Bishop, C. M. *Pattern Recognition and Machine Learning* (Springer, 2006).
129. Steele, B. M., Chandler, J. & Reddy, S. *Algorithms for Data Science* 1–430 (Springer, 2016).
130. Chollet, F. *Deep Learning with Python* (Manning, Nov. 2017).
131. Mitchell, T. M. *Machine learning* (McGraw-Hill, New York, NY, 2010).
132. Silver, D. *et al.* Mastering the game of Go with deep neural networks and tree search. *Nature* **529**, 484–489 (Jan. 2016).
133. Mnih, V. *et al.* Human-level control through deep reinforcement learning. *Nature* **518**, 529–533 (Feb. 2015).
134. Pedregosa, F. *et al.* Scikit-learn: Machine Learning in Python. *Journal of Machine Learning Research* **12**, 2825–2830 (2011).
135. Paszke, A. *et al.* in *Advances in Neural Information Processing Systems 32* (eds Wallach, H. *et al.*) 8024–8035 (Curran Associates, Inc., 2019).
136. Abadi, M. *et al.* *TensorFlow: Large-Scale Machine Learning on Heterogeneous Systems* Software available from tensorflow.org. 2015.
137. McCulloch, W. S. & Pitts, W. A logical calculus of the ideas immanent in nervous activity. *The Bulletin of Mathematical Biophysics* **5**, 115–133 (1943).
138. Gurney, K. *An Introduction to Neural Networks* (Taylor & Francis, Inc., USA, 1997).
139. Rosenblatt, F. The perceptron: A probabilistic model for information storage and organization in the brain. *Psychological Review* **65**, 386–408 (1958).
140. Minsky, M. & Papert, S. *Perceptrons; an Introduction to Computational Geometry* (MIT Press, 1969).
141. Rumelhart, D. E., Hinton, G. E. & Williams, R. J. Learning representations by back-propagating errors. *Nature* **323**, 533–536 (Oct. 1986).
142. Hornik, K. Approximation capabilities of multilayer feedforward networks. *Neural Networks* **4**, 251–257 (1991).
143. Silver, D. *et al.* Mastering Chess and Shogi by Self-Play with a General Reinforcement Learning Algorithm. *CoRR* **abs/1712.01815** (2017).
144. Senior, A. W. *et al.* Improved protein structure prediction using potentials from deep learning. *Nature* **577**, 706–710 (Jan. 2020).
145. Callaway, E. ‘It will change everything’: DeepMind’s AI makes gigantic leap in solving protein structures. *Nature* **588**, 203–204 (Nov. 2020).
146. Elsken, T., Metzen, J. H. & Hutter, F. Neural Architecture Search: A Survey. *Journal of Machine Learning Research* **20**, 1–21 (2019).

147. Pham, H., Guan, M. Y., Zoph, B., Le, Q. V. & Dean, J. Efficient Neural Architecture Search via Parameter Sharing. *CoRR* **abs/1802.03268** (2018).
148. Kandasamy, K., Neiswanger, W., Schneider, J., Póczos, B. & Xing, E. P. Neural Architecture Search with Bayesian Optimisation and Optimal Transport. *CoRR* **abs/1802.07191** (2018).
149. Liu, H., Simonyan, K., Vinyals, O., Fernando, C. & Kavukcuoglu, K. Hierarchical Representations for Efficient Architecture Search. *CoRR* **abs/1711.00436** (2017).
150. Glorot, X. & Bengio, Y. *Understanding the difficulty of training deep feedforward neural networks.* in *AISTATS* (eds Teh, Y. W. & Titterington, D. M.) **9** (JMLR.org, 2010), 249–256.
151. Ioffe, S. & Szegedy, C. *Batch Normalization: Accelerating Deep Network Training by Reducing Internal Covariate Shift* 2015.
152. Ruder, S. An overview of gradient descent optimization algorithms. *CoRR* **abs/1609.04747** (2016).
153. Tibshirani, R. Regression Shrinkage and Selection Via the Lasso. *Journal of the Royal Statistical Society: Series B (Methodological)* **58**, 267–288 (Jan. 1996).
154. Hilt, D. E., Seegräst, D. W. & and. *Ridge, a computer program for calculating ridge regression estimates* doi:10.5962/bhl.title.68934 (Dept. of Agriculture, Forest Service, Northeastern Forest Experiment Station, 1977).
155. Srivastava, N., Hinton, G., Krizhevsky, A., Sutskever, I. & Salakhutdinov, R. Dropout: A Simple Way to Prevent Neural Networks from Overfitting. *Journal of Machine Learning Research* **15**, 1929–1958 (2014).
156. Shorten, C. & Khoshgoftaar, T. M. A survey on Image Data Augmentation for Deep Learning. *Journal of Big Data* **6**. doi:10.1186/s40537-019-0197-0 (July 2019).
157. Grisafi, A., Wilkins, D. M., Csányi, G. & Ceriotti, M. Symmetry-Adapted Machine Learning for Tensorial Properties of Atomistic Systems. *Phys. Rev. Lett.* **120**, 036002 (3 2018).
158. Bartók, A. P., Kondor, R. & Csányi, G. On representing chemical environments. *Phys. Rev. B* **87**, 184115 (18 2013).
159. Musil, F. *et al.* Efficient implementation of atom-density representations. *The Journal of Chemical Physics* **154**, 114109 (Mar. 2021).
160. LeCun, Y., Bengio, Y. & Hinton, G. Deep learning. *Nature* **521**, 436–444 (May 2015).
161. He, K., Zhang, X., Ren, S. & Sun, J. Deep Residual Learning for Image Recognition. *CoRR* **abs/1512.03385** (2015).
162. RUMELHART, D., HINTON, G. & WILLIAMS, R. in *Readings in Cognitive Science* 399–421 (Elsevier, 1988). doi:10.1016/b978-1-4832-1446-7.50035-2.

163. Sherstinsky, A. Fundamentals of Recurrent Neural Network (RNN) and Long Short-Term Memory (LSTM) network. *Physica D: Nonlinear Phenomena* **404**, 132306 (Mar. 2020).
164. LeCun, Y. *et al.* Backpropagation Applied to Handwritten Zip Code Recognition. *Neural Computation* **1**, 541–551 (1989).
165. Szegedy, C. *et al.* *Going Deeper with Convolutions* 2014.
166. Krizhevsky, A., Sutskever, I. & Hinton, G. E. *ImageNet Classification with Deep Convolutional Neural Networks* in *Advances in Neural Information Processing Systems* (eds Pereira, F., Burges, C. J. C., Bottou, L. & Weinberger, K. Q.) **25** (Curran Associates, Inc., 2012).
167. Hashemi, M. Enlarging smaller images before inputting into convolutional neural network: zero-padding vs. interpolation. *Journal of Big Data* **6**. doi:10.1186/s40537-019-0263-7 (Nov. 2019).
168. Gholamalinezhad, H. & Khosravi, H. *Pooling Methods in Deep Neural Networks, a Review* 2020.
169. Rasmussen, C. E. & Williams, C. K. I. *Gaussian processes for machine learning* OCLC: ocm61285753 (MIT Press, Cambridge, Mass, 2006).
170. Williams, C. K. I. & Rasmussen, C. E. *Gaussian Processes for Regression* in *Advances in Neural Information Processing Systems 8* (MIT press, 1996), 514–520.
171. Shi, Y. Gaussian Processes, not quite for dummies. *The Gradient* (2019).
172. Görtler, J., Kehlbeck, R. & Deussen, O. A Visual Exploration of Gaussian Processes. *Distill.* <https://distill.pub/2019/visual-exploration-gaussian-processes>. doi:10.23915/distill.00017 (2019).
173. A. Papoulis. *Probability, random variables, and stochastic processes* (McGraw-Hill, 1991).
174. Press, W. *Numerical recipes in C : the art of scientific computing* (Cambridge University Press, Cambridge Cambridgeshire New York, 1992).
175. Vapnik, V. N. *The Nature of Statistical Learning Theory* doi:10.1007/978-1-4757-3264-1 (Springer New York, 2000).
176. SCHLKOPF, B. *LEARNING WITH KERNELS : support vector machines, regularization, optimization, and beyond* (MIT Press, Place of publication not identified, 2018).
177. Shawe-Taylor, J. & Cristianini, N. *Kernel Methods for Pattern Analysis* doi:10.1017/CBO9780511809682 (Cambridge University Press, 2004).
178. Duvenaud, D. Automatic model construction with Gaussian processes. en. doi:10.17863/CAM.14087 (2014).
179. Neal, R. M. *Bayesian Learning for Neural Networks* (Springer-Verlag, Berlin, Heidelberg, 1996).
180. Schattauer, C. *et al.* Graphene quantum dot states near defects. *Phys. Rev. B* **102**, 155430 (15 2020).

181. Novoselov, K. S. *et al.* A roadmap for graphene. *Nature* **490**, 192–200 (Oct. 2012).
182. Abergel, D., Apalkov, V., Berashevich, J., Ziegler, K. & Chakraborty, T. Properties of graphene: a theoretical perspective. *Advances in Physics* **59**, 261–482 (July 2010).
183. Hanson, R., Kouwenhoven, L. P., Petta, J. R., Tarucha, S. & Vanderbilt, L. M. K. Spins in few-electron quantum dots. *Rev. Mod. Phys.* **79**, 1217–1265 (4 2007).
184. Trauzettel, B., Bulaev, D. V., Loss, D. & Burkard, G. Spin qubits in graphene quantum dots. *Nature Physics* **3**, 192–196 (Feb. 2007).
185. Recher, P., Sukhorukov, E. V. & Loss, D. Quantum Dot as Spin Filter and Spin Memory. *Phys. Rev. Lett.* **85**, 1962–1965 (9 2000).
186. Recher, P. & Trauzettel, B. Quantum dots and spin qubits in graphene. *Nanotechnology* **21**, 302001 (July 2010).
187. Schaibley, J. R. *et al.* Valleytronics in 2D materials. *Nature Reviews Materials* **1** (Aug. 2016).
188. Pacchioni, G. Valleytronics with a twist. *Nature Reviews Materials* **5**, 480–480 (June 2020).
189. Bischoff, D., Eich, M., Libisch, F., Ihn, T. & Ensslin, K. Graphene nanoribbons with wings. *Applied Physics Letters* **107**, 203107 (Nov. 2015).
190. Terrés, B. *et al.* Size quantization of Dirac fermions in graphene constrictions. *Nature Communications* **7** (May 2016).
191. Freitag, N. M. *et al.* Large tunable valley splitting in edge-free graphene quantum dots on boron nitride. *Nature Nanotechnology* **13**, 392–397 (2018).
192. Subramaniam, D. *et al.* Wave-Function Mapping of Graphene Quantum Dots with Soft Confinement. *Phys. Rev. Lett.* **108**, 046801 (4 2012).
193. Chen, H.-Y., Apalkov, V. & Chakraborty, T. Fock-Darwin States of Dirac Electrons in Graphene-Based Artificial Atoms. *Phys. Rev. Lett.* **98**, 186803 (18 2007).
194. Giavaras, G. & Nori, F. Tunable quantum dots in monolayer graphene. *Phys. Rev. B* **85**, 165446 (16 2012).
195. Giavaras, G., Maksym, P. & Roy, M. Magnetic field induced confinement-deconfinement transition in graphene quantum dots. *Journal of Physics Condensed Matter* **21** (May 2008).
196. Morgenstern, M., Freitag, N., Nent, A., Nemes-Incze, P. & Liebmam, M. Graphene Quantum Dots Probed by Scanning Tunneling Microscopy. *Annalen der Physik* **529**, 1700018 (July 2017).
197. Lemme, M. C. *et al.* Etching of Graphene Devices with a Helium Ion Beam. *ACS Nano* **3**, 2674–2676 (2009).

198. Kalhor, N., Boden, S. A. & Mizuta, H. Sub-10nm patterning by focused He-ion beam milling for fabrication of downscaled graphene nano devices. *Microelectronic Engineering* **114**, 70–77 (Feb. 2014).
199. Sanvito, S., Lambert, C. J., Jefferson, J. H. & Bratkovsky, A. M. General Green's-function formalism for transport calculations with spd Hamiltonians and giant magnetoresistance in Co- and Ni-based magnetic multilayers. *Phys. Rev. B* **59**, 11936–11948 (18 1999).
200. Papior, N. *Computational Tools and Studies of Graphene Nanostructures* PhD thesis (2016).
201. Maksym, P. A. *et al.* Proposal for a magnetic field induced graphene dot. *Journal of Physics: Conference Series* **245**, 012030 (Sept. 2010).
202. in. *ARPACK Users Guide* 1–7 (Society for Industrial and Applied Mathematics, Jan. 1998). doi:10.1137/1.9780898719628.ch1.
203. Schnez, S., Ensslin, K., Sigrist, M. & Ihn, T. Analytic model of the energy spectrum of a graphene quantum dot in a perpendicular magnetic field. *Phys. Rev. B* **78**, 195427 (19 2008).
204. Recher, P., Nilsson, J., Burkard, G. & Trauzettel, B. Bound states and magnetic field induced valley splitting in gate-tunable graphene quantum dots. *Phys. Rev. B* **79**, 085407 (8 2009).
205. Kresse, G. & Furthmüller, J. Efficient iterative schemes for ab initio total-energy calculations using a plane-wave basis set. *Phys. Rev. B* **54**, 11169–11186 (16 1996).
206. Kresse, G. & Furthmüller, J. Efficiency of ab-initio total energy calculations for metals and semiconductors using a plane-wave basis set. *Computational Materials Science* **6**, 15–50 (July 1996).
207. Kresse, G. & Hafner, J. Ab initio molecular dynamics for liquid metals. *Phys. Rev. B* **47**, 558–561 (1 1993).
208. Kresse, G. & Hafner, J. Ab initio molecular-dynamics simulation of the liquid-metal-amorphous-semiconductor transition in germanium. *Phys. Rev. B* **49**, 14251–14269 (20 1994).
209. Linhart, L., Burgdörfer, J. & Libisch, F. Accurate modeling of defects in graphene transport calculations. *Phys. Rev. B* **97** (2018).
210. Koshino, M. Interlayer interaction in general incommensurate atomic layers. *New Journal of Physics* **17**, 015014 (2015).
211. Slater, J. C. & Koster, G. F. Simplified LCAO Method for the Periodic Potential Problem. *Phys. Rev.* **94**, 1498–1524 (6 1954).
212. Marzari, N. & Vanderbilt, D. Maximally localized generalized Wannier functions for composite energy bands. *Phys. Rev. B* **56**, 12847–12865 (20 1997).
213. Mostofi, A. A. *et al.* An updated version of wannier90: A tool for obtaining maximally-localised Wannier functions. *Computer Physics Communications* **185**, 2309–2310 (Aug. 2014).

214. Souza, I., Marzari, N. & Vanderbilt, D. Maximally localized Wannier functions for entangled energy bands. *Phys. Rev. B* **65**, 035109 (3 2001).
215. Björkman, T. *et al.* Defects in bilayer silica and graphene: common trends in diverse hexagonal two-dimensional systems. *Scientific Reports* **3** (Dec. 2013).
216. Cockayne, E. *et al.* Grain boundary loops in graphene. *Phys. Rev. B* **83** (May 2011).
217. Inani, H. *et al.* Silicon Substitution in Nanotubes and Graphene via Intermittent Vacancies. *The Journal of Physical Chemistry C* (May 2019).
218. Manfrinato, V. R. *et al.* Resolution Limits of Electron-Beam Lithography toward the Atomic Scale. *Nano Letters* **13**, 1555–1558 (Mar. 2013).
219. Wittig, C. The Landau Zener Formula. *The Journal of Physical Chemistry B* **109**, 8428–8430 (2005).
220. Zener, C. Non-adiabatic crossing of energy levels. *Proceedings of the Royal Society of London. Series A, Containing Papers of a Mathematical and Physical Character* **137**, 696–702 (Sept. 1932).
221. Jawecki, T., Auzinger, W. & Koch, O. Computable upper error bounds for Krylov approximations to matrix exponentials and associated ϕ -functions. *BIT Numerical Mathematics*. doi:10.1007/s10543-019-00771-6 (2019).
222. Auzinger, W., Hofstätter, H., Koch, O., Quell, M. & Thalhammer, M. A posteriori error estimation for Magnustype integrators. *M2AN - Math. Model. Numer. Anal.* **53**, 197–218 (2019).
223. Kranz, J. J., Kubillus, M., Ramakrishnan, R., von Lilienfeld, O. A. & Elstner, M. Generalized Density-Functional Tight-Binding Repulsive Potentials from Unsupervised Machine Learning. *Journal of Chemical Theory and Computation* **14**, 2341–2352 (Mar. 2018).
224. Himanen, L., Geurts, A., Foster, A. S. & Rinke, P. Data-Driven Materials Science: Status, Challenges, and Perspectives. *Adv. Sci.* **6**, 1900808 (2019).
225. Nakhaee, M., Ketabi, S. A. & Peeters, F. M. Tight-Binding Studio: A technical software package to find the parameters of tight-binding Hamiltonian. *Computer Physics Communications* **254**, 107379 (Sept. 2020).
226. Peano, V., Sapper, F. & Marquardt, F. *Rapid Exploration of Topological Band Structures using Deep Learning* 2021.
227. Panosetti, C., Anniés, S. B., Grosu, C., Seidlmayer, S. & Scheurer, C. DFTB Modeling of Lithium-Intercalated Graphite with Machine-Learned Repulsive Potential. *The Journal of Physical Chemistry A* **125**, 691–699 (Jan. 2021).

228. Drautz, R., Hammerschmidt, T., Čák, M. & Pettifor, D. G. Bond-order potentials: derivation and parameterization for refractory elements. *Modelling and Simulation in Materials Science and Engineering* **23**, 074004 (Sept. 2015).
229. Ladines, A., Hammerschmidt, T. & Drautz, R. BOPcat software package for the construction and testing of tight-binding models and bond-order potentials. *Computational Materials Science* **173**, 109455 (Feb. 2020).
230. Ghosh, K. *et al.* Deep Learning Spectroscopy: Neural Networks for Molecular Excitation Spectra. *Adv. Sci.* **6**, 1801367 (2019).
231. Hammerschmidt, T., Drautz, R. & Pettifor, D. G. Atomistic modelling of materials with bond-order potentials. *International Journal of Materials Research* **100**, 1479–1487 (Nov. 2009).
232. Westermayr, J. & Maurer, R. J. Physically inspired deep learning of molecular excitations and photoemission spectra. *Chemical Science* **12**, 10755–10764 (2021).
233. Chmiela, S. *et al.* Machine learning of accurate energy-conserving molecular force fields. *Science Advances* **3**. doi:10.1126/sciadv.1603015 (May 2017).
234. Nakhaee, M., Ketabi, S. A. & Peeters, F. M. Machine learning approach to constructing tight binding models for solids with application to BiTeCl. *Journal of Applied Physics* **128**, 215107 (Dec. 2020).
235. García-Risueño, P. & Echenique, P. Linearly scaling direct method for accurately inverting sparse banded matrices. *Journal of Physics A: Mathematical and Theoretical* **45**, 065204 (Jan. 2012).
236. Koshino, M. Interlayer interaction in general incommensurate atomic layers. *New Journal of Physics* **17**, 015014 (2015).
237. Slater, J. C. & Koster, G. F. Simplified LCAO Method for the Periodic Potential Problem. *Phys. Rev.* **94**, 1498–1524 (6 1954).
238. Papaconstantopoulos, D. A. & Mehl, M. J. The Slater Koster tight-binding method: a computationally efficient and accurate approach. *Journal of Physics: Condensed Matter* **15**, R413–R440 (Mar. 2003).
239. Souza, I., Marzari, N. & Vanderbilt, D. Maximally localized Wannier functions for entangled energy bands. *Phys. Rev. B* **65**, 035109 (3 2001).
240. Mostofi, A. A. *et al.* An updated version of wannier90: A tool for obtaining maximally-localised Wannier functions. *Computer Physics Communications* **185**, 2309–2310 (Aug. 2014).
241. Marzari, N., Mostofi, A. A., Yates, J. R., Souza, I. & Vanderbilt, D. Maximally localized Wannier functions: Theory and applications. *Reviews of Modern Physics* **84**, 1419–1475 (Oct. 2012).
242. Marzari, N., Mostofi, A. A., Yates, J. R., Souza, I. & Vanderbilt, D. Maximally localized Wannier functions: Theory and applications. *Reviews of Modern Physics* **84**, 1419–1475 (Oct. 2012).

243. Wang, Z. *et al.* Machine learning method for tight-binding Hamiltonian parameterization from ab-initio band structure. *npj Computational Materials* **7**. doi:10.1038/s41524-020-00490-5 (Jan. 2021).
244. Papaconstantopoulos, D. A. & Mehl, M. J. The Slater Koster tight-binding method: a computationally efficient and accurate approach. *Journal of Physics: Condensed Matter* **15**, R413–R440 (Mar. 2003).
245. Nesterov, Y. & Spokoiny, V. Random Gradient-Free Minimization of Convex Functions. *Foundations of Computational Mathematics* **17**, 527–566 (Nov. 2015).
246. Golovin, D. *et al.* *Gradientless Descent: High-Dimensional Zeroth-Order Optimization* 2020.
247. Rotter, S., Tang, J.-Z., Wirtz, L., Trost, J. & Burgdörfer, J. Modular recursive Green's function method for ballistic quantum transport. *Phys. Rev. B* **62**, 1950–1960 (3 2000).
248. Lekka, C., Papanicolaou, N., Evangelakis, G. & Papaconstantopoulos, D. Transferability of Slater-Koster parameters. *Journal of Physics and Chemistry of Solids* **62**, 753–760 (2001).
249. Silva-Guillén, J., San-Jose, P. & Roldán, R. Electronic Band Structure of Transition Metal Dichalcogenides from Ab Initio and Slater–Koster Tight-Binding Model. *Applied Sciences* **6**, 284 (Oct. 2016).
250. McSloy, A. *et al.* TBMLT, a flexible toolkit for combining tight-binding and machine learning. *The Journal of Chemical Physics* **158**, 034801 (Jan. 2023).
251. Johnston, S., Khatami, E. & Scalettar, R. A perspective on machine learning and data science for strongly correlated electron problems. *Carbon Trends* **9**, 100231 (Oct. 2022).
252. Banszerus, L. *et al.* Observation of the Spin-Orbit Gap in Bilayer Graphene by One-Dimensional Ballistic Transport. *Phys. Rev. Lett.* **124**, 177701 (17 2020).
253. Tong, C. *et al.* Tunable Valley Splitting and Bipolar Operation in Graphene Quantum Dots. *Nano Letters* **21**, 1068–1073 (Jan. 2021).
254. Eich, M. *et al.* Spin and Valley States in Gate-Defined Bilayer Graphene Quantum Dots. *Phys. Rev. X* **8**, 031023 (3 2018).
255. Banszerus, L. *et al.* Electron–Hole Crossover in Gate-Controlled Bilayer Graphene Quantum Dots. *Nano Letters* **20**, 7709–7715 (Sept. 2020).
256. Medford, J. *et al.* Quantum-Dot-Based Resonant Exchange Qubit. *Phys. Rev. Lett.* **111**, 050501 (5 2013).
257. Mermin, N. *Quantum computer science : an introduction* (Cambridge University Press, Cambridge, UK New York, 2007).
258. Da Costa, D., Zarenia, M., Chaves, A., Farias, G. & Peeters, F. Analytical study of the energy levels in bilayer graphene quantum dots. *Carbon* **78**, 392–400 (Nov. 2014).

259. Nielsen, H. & Ninomiya, M. Absence of neutrinos on a lattice. *Nuclear Physics B* **185**, 20–40 (July 1981).
260. Nielsen, H. & Ninomiya, M. A no-go theorem for regularizing chiral fermions. *Physics Letters B* **105**, 219–223 (Oct. 1981).
261. Brey, L. & Fertig, H. A. Electronic states of graphene nanoribbons studied with the Dirac equation. *Phys. Rev. B* **73**, 235411 (23 2006).
262. Tworzydło, J., Groth, C. W. & Beenakker, C. W. J. Finite difference method for transport properties of massless Dirac fermions. *Phys. Rev. B* **78**, 235438 (23 2008).
263. Hernández, A. R. & Lewenkopf, C. H. Finite-difference method for transport of two-dimensional massless Dirac fermions in a ribbon geometry. *Phys. Rev. B* **86**, 155439 (15 2012).
264. Wilson, K. G. Confinement of quarks. *Phys. Rev. D* **10**, 2445–2459 (8 1974).
265. Kogut, J. & Susskind, L. Hamiltonian formulation of Wilson's lattice gauge theories. *Phys. Rev. D* **11**, 395–408 (2 1975).
266. Susskind, L. Lattice fermions. *Phys. Rev. D* **16**, 3031–3039 (10 1977).
267. Stacey, R. Eliminating lattice fermion doubling. *Phys. Rev. D* **26**, 468–472 (2 1982).
268. Da Costa, D. R., Zarenia, M., Chaves, A., Farias, G. A. & Peeters, F. M. Magnetic field dependence of energy levels in biased bilayer graphene quantum dots. *Phys. Rev. B* **93**, 085401 (8 2016).
269. Inc., W. R. *Mathematica, Version 13.0.0* Champaign, IL, 2021.
270. Zarenia, M., Partoens, B., Chakraborty, T. & Peeters, F. M. Electron-electron interactions in bilayer graphene quantum dots. *Phys. Rev. B* **88**, 245432 (24 2013).
271. Cohl, H. S. *et al.* Useful alternative to the multipole expansion of $1/r$ potentials. *Phys. Rev. A* **64**, 052509 (5 2001).
272. Bateman, H. *Partial Differential Equations of Mathematical Physics* - (Cambridge University Press, Cambridge, 1932).
273. Knothe, A., Glazman, L. I. & Fal'ko, V. I. *Theory of tunneling spectra for a few-electron bilayer graphene quantum dot* 2021.
274. López, P. H. *et al.* Strain control of hybridization between dark and localized excitons in a 2D semiconductor. *Nature Communications* **13**. doi:10.1038/s41467-022-35352-9 (Dec. 2022).
275. Mak, K. F., Lee, C., Hone, J., Shan, J. & Heinz, T. F. Atomically Thin MoS₂: A New Direct-Gap Semiconductor. *Physical Review Letters* **105**, 136805 (2010).
276. Wang, G. *et al.* Colloquium: Excitons in atomically thin transition metal dichalcogenides. *Reviews of Modern Physics* **90**, 021001 (2018).
277. Wang, Q. H., Kalantar-Zadeh, K., Kis, A., Coleman, J. N. & Strano, M. S. Electronics and optoelectronics of two-dimensional transition metal dichalcogenides. *Nature Nanotechnology* **7**, 699–712 (2012).

278. Manzeli, S., Ovchinnikov, D., Pasquier, D., Yazyev, O. V. & Kis, A. 2D transition metal dichalcogenides. *Nature Reviews Materials* **2**, doi:10.1038/natrevmats.2017.33 (2017).
279. Schaibley, J. R. *et al.* Valleytronics in 2D materials. *Nature Reviews Materials* **1**. doi:10.1038/natrevmats.2016.55 (2016).
280. Wang, Z. *et al.* Evidence of high-temperature exciton condensation in two-dimensional atomic double layers. *Nature* **574**, 76–80 (2019).
281. Andrei, E. Y. *et al.* The marvels of moiré materials. *Nature Reviews Materials* **6**, 201–206 (2021).
282. Zhang, X.-X., You, Y., Zhao, S. Y. F. & Heinz, T. F. Experimental Evidence for Dark Excitons in Monolayer WSe₂. *Physical Review Letters* **115**, 257403 (2015).
283. Malic, E. *et al.* Dark excitons in transition metal dichalcogenides. *Physical Review Materials* **2**, 014002 (2018).
284. Zhou, Y. *et al.* Probing dark excitons in atomically thin semiconductors via near-field coupling to surface plasmon polaritons. *Nature Nanotechnology* **12**, 856–860 (2017).
285. Li, Z. *et al.* Direct Observation of Gate-Tunable Dark Triions in Monolayer WSe₂. *Nano Letters* **19**, 6886–6893 (2019).
286. Zhang, X.-X. *et al.* Magnetic brightening and control of dark excitons in monolayer WSe₂. *Nature Nanotechnology* **12**, 883–888 (2017).
287. Robert, C. *et al.* Fine structure and lifetime of dark excitons in transition metal dichalcogenide monolayers. *Physical Review B* **96**, 155423 (2017).
288. Erkensten, D. *et al.* Dark exciton-exciton annihilation in monolayer WSe₂. *Physical Review B* **104**, l241406 (2021).
289. Tang, Y., Mak, K. F. & Shan, J. Long valley lifetime of dark excitons in single-layer WSe₂. *Nature Communications* **10**. doi:10.1038/s41467-019-12129-1 (2019).
290. Mapara, V. *et al.* Bright and Dark Exciton Coherent Coupling and Hybridization Enabled by External Magnetic Fields. *Nano Letters* **22**, 1680–1687 (2022).
291. Wu, Z. & Ni, Z. Spectroscopic investigation of defects in two-dimensional materials. *Nanophotonics* **6**, 1219–1237 (2017).
292. Toth, M. & Aharonovich, I. Single Photon Sources in Atomically Thin Materials. *Annual Review of Physical Chemistry* **70**, 123–142 (2019).
293. Wehner, S., Elkouss, D. & Hanson, R. Quantum internet: A vision for the road ahead. *Science* **362**. doi:10.1126/science.aam9288 (2018).
294. Atatüre, M., Englund, D., Vamivakas, N., Lee, S.-Y. & Wrachtrup, J. Material platforms for spin-based photonic quantum technologies. *Nature Reviews Materials* **3**, 38–51 (2018).
295. Baek, H. *et al.* Highly energy-tunable quantum light from moiré-trapped excitons. *Science Advances* **6**. doi:10.1126/sciadv.aba8526 (2020).

296. Turunen, M. *et al.* Quantum photonics with layered 2D materials. *Nature Reviews Physics* **4**, 219–236 (2022).
297. Dastidar, M. G., Thekkooden, I., Nayak, P. K. & Bhallamudi, V. P. Quantum emitters and detectors based on 2D van der Waals materials. *Nanoscale* **14**, 5289–5313 (2022).
298. Zhang, C. *et al.* Probing Critical Point Energies of Transition Metal Dichalcogenides: Surprising Indirect Gap of Single Layer WSe₂. *Nano Letters* **15**, 6494–6500 (2015).
299. Aslan, O. B., Deng, M. & Heinz, T. F. Strain tuning of excitons in monolayer WSe₂. *Physical Review B* **98**, 115308 (2018).
300. Lloyd, D. *et al.* Band Gap Engineering with Ultralarge Biaxial Strains in Suspended Monolayer MoS₂. *Nano Letters* **16**, 5836–5841 (2016).
301. Deilmann, T. & Thygesen, K. S. Finite-momentum exciton landscape in mono- and bilayer transition metal dichalcogenides. *2D Materials* **6**, 035003 (2019).
302. Shi, H., Pan, H., Zhang, Y.-W. & Yakobson, B. I. Quasiparticle band structures and optical properties of strained monolayer MoS₂ and WS₂. *Phys. Rev. B* **87**, 155304 (15 2013).
303. Khatibi, Z. *et al.* Impact of strain on the excitonic linewidth in transition metal dichalcogenides. *2D Materials* **6**, 015015 (2018).
304. Linhart, L. *et al.* Localized Intervalley Defect Excitons as Single-Photon Emitters in WSe₂. *Phys. Rev. Lett.* **123**, 146401 (14 2019).
305. Yang, D., Fan, X., Zhang, F., Hu, Y. & Luo, Z. Electronic and Magnetic Properties of Defected Monolayer WSe₂ with Vacancies. *Nanoscale Research Letters* **14**. doi:10.1186/s11671-019-3002-2 (2019).
306. Yang, S., Chen, Y. & Jiang, C. Strain engineering of two-dimensional materials: Methods, properties, and applications. *InfoMat* **3**, 397–420 (2021).
307. He, K., Poole, C., Mak, K. F. & Shan, J. Experimental Demonstration of Continuous Electronic Structure Tuning via Strain in Atomically Thin MoS₂. *Nano Letters* **13**, 2931–2936 (2013).
308. Kovalchuk, S. *et al.* Neutral and charged excitons interplay in non-uniformly strain-engineered WS₂. *2D Materials* **7**, 035024 (2020).
309. Harats, M. G., Kirchhof, J. N., Qiao, M., Greben, K. & Bolotin, K. I. Dynamics and efficient conversion of excitons to trions in non-uniformly strained monolayer WS₂. *Nature Photonics* **14**, 324–329 (2020).
310. Lee, J.-K. *et al.* Modification of Electrical Properties of Graphene by Substrate-Induced Nanomodulation. *Nano Letters* **13**, 3494–3500 (2013).
311. Gill, S. T. *et al.* Mechanical Control of Graphene on Engineered Pyramidal Strain Arrays. *ACS Nano* **9**, 5799–5806 (2015).

312. Khestanova, E., Guinea, F., Fumagalli, L., Geim, A. K. & Grigorieva, I. V. Universal shape and pressure inside bubbles appearing in van der Waals heterostructures. *Nature Communications* **7**. doi:10.1038/ncomms12587 (2016).
313. Branny, A., Kumar, S., Proux, R. & Gerardot, B. D. Deterministic strain-induced arrays of quantum emitters in a two-dimensional semiconductor. *Nature Communications* **8**. doi:10.1038/ncomms15053 (2017).
314. Parto, K., Azzam, S. I., Banerjee, K. & Moody, G. Defect and strain engineering of monolayer WSe₂ enables site-controlled single-photon emission up to 150 K. *Nature Communications* **12**. doi:10.1038/s41467-021-23709-5 (2021).
315. Rivera, P. *et al.* Intrinsic donor-bound excitons in ultraclean monolayer semiconductors. *Nature Communications* **12**. doi:10.1038/s41467-021-21158-8 (2021).
316. He, M. *et al.* Valley phonons and exciton complexes in a monolayer semiconductor. *Nature Communications* **11**. doi:10.1038/s41467-020-14472-0 (2020).
317. Liu, E. *et al.* Multipath Optical Recombination of Intervalley Dark Excitons and Trions in Monolayer WSe₂. *Physical Review Letters* **124**, 196802 (2020).
318. Kirchhof, J. N. *et al.* Nanomechanical Spectroscopy of 2D Materials. *Nano Letters*. doi:10.1021/acs.nanolett.2c01289 (2022).
319. Aslan, B. *et al.* Excitons in strained and suspended monolayer WSe₂. *2D Materials* **9**, 015002 (2021).
320. Liu, E. *et al.* Gate Tunable Dark Trions in Monolayer WSe₂. *Physical Review Letters* **123**, 027401 (2019).
321. Conley, H. J. *et al.* Bandgap Engineering of Strained Monolayer and Bilayer MoS₂. *Nano Letters* **13**, 3626–3630 (2013).
322. Frisenda, R. *et al.* Biaxial strain tuning of the optical properties of single-layer transition metal dichalcogenides. *npj 2D Materials and Applications* **1**. doi:10.1038/s41699-017-0013-7 (2017).
323. Noori, K., Cheng, N. L. Q., Xuan, F. & Quek, S. Y. Dielectric screening by 2D substrates. *2D Materials* **6**, 035036 (2019).
324. Schmidt, T., Lischka, K. & Zulehner, W. Excitation-power dependence of the near-band-edge photoluminescence of semiconductors. *Physical Review B* **45**, 8989–8994 (1992).
325. Barbone, M. *et al.* Charge-tuneable biexciton complexes in monolayer WSe₂. *Nature Communications* **9**. doi:10.1038/s41467-018-05632-4 (2018).
326. Molina-Sánchez, A., Sangalli, D., Hummer, K., Marini, A. & Wirtz, L. Effect of spin-orbit interaction on the optical spectra of single-layer, double-layer, and bulk MoS₂. *Physical Review B* **88**. doi:10.1103/physrevb.88.045412 (July 2013).

327. Onida, G., Reining, L. & Rubio, A. Electronic excitations: density-functional versus many-body Green's-function approaches. *Rev. Mod. Phys.* **74**, 601–659 (2 2002).
328. Golze, D., Dvorak, M. & Rinke, P. The GW Compendium: A Practical Guide to Theoretical Photoemission Spectroscopy. *Frontiers in Chemistry* **7**. doi:10.3389/fchem.2019.00377 (July 2019).
329. Plechinger, G. *et al.* Identification of excitons, trions and biexcitons in single-layer WS₂. *physica status solidi (RRL) - Rapid Research Letters* **9**, 457–461 (2015).
330. Li, Y. *et al.* Measurement of the optical dielectric function of monolayer transition-metal dichalcogenides: MoS₂, MoSe₂, WS₂, and WSe₂. *Physical Review B* **90**, 205422 (2014).
331. Morell, N. *et al.* High Quality Factor Mechanical Resonators Based on WSe₂ Monolayers. *Nano Letters* **16**, 5102–5108 (2016).
332. Nicholl, R. J. *et al.* The effect of intrinsic crumpling on the mechanics of free-standing graphene. *Nature Communications* **6**. doi:10.1038/ncomms9789 (2015).
333. Huang, J., Hoang, T. B. & Mikkelsen, M. H. Probing the origin of excitonic states in monolayer WSe₂. *Scientific Reports* **6**. doi:10.1038/srep22414 (2016).
334. Arora, A. *et al.* Dark trions govern the temperature-dependent optical absorption and emission of doped atomically thin semiconductors. *Physical Review B* **101**, 241413 (2020).
335. Shinokita, K. *et al.* Continuous Control and Enhancement of Excitonic Valley Polarization in Monolayer WSe₂ by Electrostatic Doping. *Advanced Functional Materials* **29**, 1900260 (2019).
336. Ye, T. *et al.* Room-Temperature Exciton-Based Optoelectronic Switch. *Small* **17**, 2005918 (2021).
337. Allain, A. & Kis, A. Electron and Hole Mobilities in Single-Layer WSe₂. *ACS Nano* **8**, 7180–7185 (2014).
338. Echeverry, J. P., Urbaszek, B., Amand, T., Marie, X. & Gerber, I. C. Splitting between bright and dark excitons in transition metal dichalcogenide monolayers. *Physical Review B* **93**, 121107 (2016).
339. Abramov, A. N. *et al.* Photoluminescence imaging of single photon emitters within nanoscale strain profiles in monolayer WSe₂ 2023. doi:10.48550/ARXIV.2301.09478.
340. Chodos, A., Jaffe, R. L., Johnson, K., Thorn, C. B. & Weisskopf, V. F. New extended model of hadrons. *Phys. Rev. D* **9**, 3471–3495 (12 1974).
341. Carlsson, J. M., Ghiringhelli, L. M. & Fasolino, A. Theory and hierarchical calculations of the structure and energetics of [0001] tilt grain boundaries in graphene. *Phys. Rev. B* **84**, 165423 (16 2011).
342. Sutton, A. P. & Balluffi, R. W. *Interfaces in Crystalline Materials* (Oxford University Press, London, England, Dec. 2006).

343. Datta, S. *Cambridge studies in semiconductor physics and microelectronic engineering: Electronic transport in mesoscopic systems series number 3* (Cambridge University Press, Cambridge, England, June 2013).
344. Rotter, S. *Ballistic quantum transport at high energies and high magnetic fields* PhD thesis (Technological University of Vienna, 2004).
345. Rungger, I. & Sanvito, S. Algorithm for the construction of self-energies for electronic transport calculations based on singularity elimination and singular value decomposition. *Phys. Rev. B* **78**, 035407 (3 2008).
346. Graf, G. M. & Porta, M. Bulk-Edge Correspondence for Two-Dimensional Topological Insulators. *Communications in Mathematical Physics* **324**, 851–895 (Oct. 2013).
347. Hatsugai, Y. Chern number and edge states in the integer quantum Hall effect. *Phys. Rev. Lett.* **71**, 3697–3700 (22 1993).
348. Halperin, B. I. Quantized Hall conductance, current-carrying edge states, and the existence of extended states in a two-dimensional disordered potential. *Phys. Rev. B* **25**, 2185–2190 (4 1982).
349. Chklovskii, D. B., Shklovskii, B. I. & Glazman, L. I. Electrostatics of edge channels. *Phys. Rev. B* **46**, 4026–4034 (7 1992).
350. Lier, K. & Gerhardts, R. R. Self-consistent calculations of edge channels in laterally confined two-dimensional electron systems. *Phys. Rev. B* **50**, 7757–7767 (11 1994).
351. Khanna, U., Goldstein, M. & Gefen, Y. Fractional edge reconstruction in integer quantum Hall phases. *Phys. Rev. B* **103**, L121302 (12 2021).
352. Venkatachalam, V., Hart, S., Pfeiffer, L., West, K. & Yacoby, A. Local thermometry of neutral modes on the quantum Hall edge. *Nature Physics* **8**, 676–681 (Aug. 2012).
353. Bhattacharyya, R., Banerjee, M., Heiblum, M., Mahalu, D. & Umansky, V. Melting of Interference in the Fractional Quantum Hall Effect: Appearance of Neutral Modes. *Phys. Rev. Lett.* **122**, 246801 (24 2019).
354. MacDonald, A. H. Edge states in the fractional-quantum-Hall-effect regime. *Phys. Rev. Lett.* **64**, 220–223 (2 1990).
355. Kane, C. L., Fisher, M. P. A. & Polchinski, J. Randomness at the edge: Theory of quantum Hall transport at filling $\nu=2/3$. *Phys. Rev. Lett.* **72**, 4129–4132 (26 1994).
356. Wan, X., Rezayi, E. H. & Yang, K. Edge reconstruction in the fractional quantum Hall regime. *Phys. Rev. B* **68**, 125307 (12 2003).
357. Wang, J., Meir, Y. & Gefen, Y. Edge Reconstruction in the $\nu=2/3$ Fractional Quantum Hall State. *Phys. Rev. Lett.* **111**, 246803 (24 2013).
358. Bid, A. *et al.* Observation of neutral modes in the fractional quantum Hall regime. *Nature* **466**, 585–590 (July 2010).

359. Sabo, R. *et al.* Edge reconstruction in fractional quantum Hall states. *Nature Physics* **13**, 491–496 (Jan. 2017).
360. Yacoby, A., Hess, H., Fulton, T., Pfeiffer, L. & West, K. Electrical imaging of the quantum Hall state. *Solid State Communications* **111**, 1–13 (June 1999).
361. McCormick, K. L. *et al.* Scanned potential microscopy of edge and bulk currents in the quantum Hall regime. *Phys. Rev. B* **59**, 4654–4657 (7 1999).
362. Weitz, P., Ahlsweide, E., Weis, J., Klitzing, K. & Eberl, K. Hall-potential investigations under quantum Hall conditions using scanning force microscopy. *Physica E: Low-dimensional Systems and Nanostructures* **6**, 247–250 (Feb. 2000).
363. Weis, J. & von Klitzing, K. Metrology and microscopic picture of the integer quantum Hall effect. *Philosophical Transactions of the Royal Society A: Mathematical, Physical and Engineering Sciences* **369**, 3954–3974 (Oct. 2011).
364. Aoki, N., da Cunha, C. R., Akis, R., Ferry, D. K. & Ochiai, Y. Imaging of integer quantum Hall edge state in a quantum point contact via scanning gate microscopy. *Phys. Rev. B* **72**, 155327 (15 2005).
365. Paradiso, N. *et al.* Imaging Fractional Incompressible Stripes in Integer Quantum Hall Systems. *Phys. Rev. Lett.* **108**, 246801 (24 2012).
366. Pascher, N. *et al.* Imaging the Conductance of Integer and Fractional Quantum Hall Edge States. *Phys. Rev. X* **4**, 011014 (1 2014).
367. Suddards, M. E., Baumgartner, A., Henini, M. & Mellor, C. J. Scanning capacitance imaging of compressible and incompressible quantum Hall effect edge strips. *New Journal of Physics* **14**, 083015 (Aug. 2012).
368. Lai, K. *et al.* Imaging of Coulomb-Driven Quantum Hall Edge States. *Phys. Rev. Lett.* **107**, 176809 (17 2011).
369. Uri, A. *et al.* Nanoscale imaging of equilibrium quantum Hall edge currents and of the magnetic monopole response in graphene. *Nature Physics* **16**, 164–170 (Dec. 2019).
370. Li, G., Luican-Mayer, A., Abanin, D., Levitov, L. & Andrei, E. Y. Evolution of Landau levels into edge states in graphene. *Nature Communications* **4**. doi:10.1038/ncomms2767 (Apr. 2013).
371. Coissard, A. *et al.* Absence of edge reconstruction for quantum Hall edge channels in graphene devices. *arXiv*, 2210.08152 (2022).
372. Mashoff, T., Pratzer, M. & Morgenstern, M. A low-temperature high resolution scanning tunneling microscope with a three-dimensional magnetic vector field operating in ultrahigh vacuum. *Review of Scientific Instruments* **80**, 053702 (May 2009).
373. Dombrowski, R., Steinebach, C., Wittneven, C., Morgenstern, M. & Wiesendanger, R. Tip-induced band bending by scanning tunneling spectroscopy of the states of the tip-induced quantum dot on InAs(110). *Phys. Rev. B* **59**, 8043–8048 (12 1999).

374. Jung, S. *et al.* Evolution of microscopic localization in graphene in a magnetic field from scattering resonances to quantum dots. *Nature Physics* **7**, 245–251 (Jan. 2011).
375. Chae, J. *et al.* Renormalization of the Graphene Dispersion Velocity Determined from Scanning Tunneling Spectroscopy. *Phys. Rev. Lett.* **109**, 116802 (11 2012).
376. Luican, A., Li, G. & Andrei, E. Y. Quantized Landau level spectrum and its density dependence in graphene. *Phys. Rev. B* **83**, 041405 (4 2011).
377. Walkup, D. *et al.* Tuning single-electron charging and interactions between compressible Landau level islands in graphene. *Phys. Rev. B* **101**, 035428 (3 2020).
378. Liu, M.-H. *et al.* Scalable Tight-Binding Model for Graphene. *Phys. Rev. Lett.* **114**, 036601 (3 2015).
379. Schnez, S., Ensslin, K., Sigrist, M. & Ihn, T. Analytic model of the energy spectrum of a graphene quantum dot in a perpendicular magnetic field. *Phys. Rev. B* **78**, 195427 (Nov. 2008).
380. Gutiérrez, C. *et al.* Interaction-driven quantum Hall wedding cake like structures in graphene quantum dots. *Science* **361**, 789–794 (Aug. 2018).
381. Chklovskii, D. B., Shklovskii, B. I. & Glazman, L. I. Electrostatics of edge channels. *Phys. Rev. B* **46**, 4026–4034 (Aug. 1992).
382. Morgenstern, M. *et al.* Low temperature scanning tunneling spectroscopy on InAs(110). *J. Electr. Spectr. Rel. Phen.* **109**, 127–145 (Aug. 2000).
383. Joynt, R. & Prange, R. E. Conditions for the quantum Hall effect. *Phys. Rev. B* **29**, 3303–3317 (Mar. 1984).
384. Ando, T. Electron Localization in a Two-Dimensional System in Strong Magnetic Fields. II. Long-Range Scatterers and Response Functions. *J. Phys. Soc. Jp.* **53**, 3101–3111 (Sept. 1984).
385. Thomas Ihn. *Semiconductor Nanostructures* (Oxford University Press, 2010).
386. Morgenstern, M. *et al.* Origin of Landau oscillations observed in scanning tunneling spectroscopy on InAs(110). *Phys. Rev. B* **62**, 7257–7263 (Sept. 2000).
387. Teichmann, K. *et al.* Controlled Charge Switching on a Single Donor with a Scanning Tunneling Microscope. *Phys. Rev. Lett.* **101**, 076103 (Aug. 2008).
388. Wang, Z., Luitz, D. J. & Villadiego, I. S. Quantum Monte Carlo at the graphene quantum Hall edge. *Phys. Rev. B* **106**, 125150 (Sept. 2022).
389. Schöberl, J. NETGEN An advancing front 2D/3D-mesh generator based on abstract rules. *Computing and Visualization in Science* **1**, 41–52 (July 1997).

390. Sachs, B., Wehling, T. O., Katsnelson, M. I. & Lichtenstein, A. I. Adhesion and electronic structure of graphene on hexagonal boron nitride substrates. *Phys. Rev. B* **84**, 195414 (19 2011).
391. Jung, J. *et al.* Moiré band model and band gaps of graphene on hexagonal boron nitride. *Phys. Rev. B* **96**, 085442 (8 2017).
392. Kim, H. *et al.* Accurate Gap Determination in Monolayer and Bilayer Graphene/BN Moiré Superlattices. *Nano Letters* **18**, 7732–7741 (Nov. 2018).
393. Jung, J., DaSilva, A. M., MacDonald, A. H. & Adam, S. Origin of band gaps in graphene on hexagonal boron nitride. *Nature Communications* **6**. doi:10.1038/ncomms7308 (Feb. 2015).
394. Nam, N. N. T. & Koshino, M. Lattice relaxation and energy band modulation in twisted bilayer graphene. *Phys. Rev. B* **96**, 075311 (7 2017).
395. Zakharchenko, K. V., Katsnelson, M. I. & Fasolino, A. Finite Temperature Lattice Properties of Graphene beyond the Quasiharmonic Approximation. *Phys. Rev. Lett.* **102**, 046808 (4 2009).
396. Lanczos, C. An iteration method for the solution of the eigenvalue problem of linear differential and integral operators. *Journal of Research of the National Bureau of Standards* **45**, 255 (Oct. 1950).
397. Hall, E. H. On a New Action of the Magnet on Electric Currents. *American Journal of Mathematics* **2**, 287 (Sept. 1879).
398. Von Klitzing, K. The quantized Hall effect. *Rev. Mod. Phys.* **58**, 519–531 (3 1986).
399. Zhang, Y., Tan, Y.-W., Stormer, H. L. & Kim, P. Experimental observation of the quantum Hall effect and Berry's phase in graphene. *Nature* **438**, 201–204 (Nov. 2005).
400. Thouless, D. J., Kohmoto, M., Nightingale, M. P. & den Nijs, M. Quantized Hall Conductance in a Two-Dimensional Periodic Potential. *Phys. Rev. Lett.* **49**, 405–408 (6 1982).
401. Kohmoto, M. Topological invariant and the quantization of the Hall conductance. *Annals of Physics* **160**, 343–354 (Apr. 1985).
402. Koshino, M. & Ando, T. Hall plateau diagram for the Hofstadter butterfly energy spectrum. *Phys. Rev. B* **73**, 155304 (15 2006).
403. Kubo, R. Statistical-Mechanical Theory of Irreversible Processes. I. General Theory and Simple Applications to Magnetic and Conduction Problems. *Journal of the Physical Society of Japan* **12**, 570–586 (June 1957).
404. Kubo, R., Yokota, M. & Nakajima, S. Statistical-Mechanical Theory of Irreversible Processes. II. Response to Thermal Disturbance. *Journal of the Physical Society of Japan* **12**, 1203–1211 (Nov. 1957).
405. *Theoretische Festkörperphysik* doi:10.1007/978-3-540-74790-1 (Springer Berlin Heidelberg, 2008).

406. Streda, P. Theory of quantised Hall conductivity in two dimensions. *Journal of Physics C: Solid State Physics* **15**, L717–L721 (Aug. 1982).
407. Moon, P. & Koshino, M. Energy spectrum and quantum Hall effect in twisted bilayer graphene. *Phys. Rev. B* **85**, 195458 (19 2012).
408. Entin-Wohlman, O., Hartzstein, C. & Imry, Y. Quantum oscillations in the magnetotransport of a finite two-dimensional Anderson model. *Phys. Rev. B* **34**, 921–926 (2 1986).
409. Geim, A. K. & Grigorieva, I. V. Van der Waals heterostructures. *Nature* **499**, 419–425 (2013).
410. Lu, X. *et al.* Superconductors, orbital magnets and correlated states in magic-angle bilayer graphene. *Nature* **574**, 653–657 (Oct. 2019).
411. Yankowitz, M. *et al.* Tuning superconductivity in twisted bilayer graphene. *Science* **363**, 1059–1064 (Mar. 2019).
412. Stepanov, P. *et al.* Untying the insulating and superconducting orders in magic-angle graphene. *Nature* **583**, 375–378 (July 2020).
413. Saito, Y., Ge, J., Watanabe, K., Taniguchi, T. & Young, A. F. Independent superconductors and correlated insulators in twisted bilayer graphene. *Nat. Phys.* **16**, 926–930 (Sept. 2020).
414. Cao, Y. *et al.* Correlated insulator behaviour at half-filling in magic-angle graphene superlattices - Nature. *Nature* **556**, 80–84 (2018).
415. Zondiner, U. *et al.* Cascade of phase transitions and Dirac revivals in magic-angle graphene. *Nature* **582**, 203–208 (June 2020).
416. Wong, D. *et al.* Cascade of electronic transitions in magic-angle twisted bilayer graphene. *Nature* **582**, 198–202 (June 2020).
417. Sharpe, A. L. *et al.* Emergent ferromagnetism near three-quarters filling in twisted bilayer graphene. *Science* **365**, 605–608 (Aug. 2019).
418. Sharpe, A. L. *et al.* Evidence of Orbital Ferromagnetism in Twisted Bilayer Graphene Aligned to Hexagonal Boron Nitride. *Nano Lett.* **21**, 4299–4304 (May 2021).
419. Serlin, M. *et al.* Intrinsic quantized anomalous Hall effect in a moiré heterostructure. *Science* **367**, 900–903 (Feb. 2020).
420. Zhang, Y.-H., Mao, D. & Senthil, T. Twisted bilayer graphene aligned with hexagonal boron nitride: Anomalous Hall effect and a lattice model. *Phys. Rev. Res.* **1**, 033126 (Nov. 2019).
421. Bultinck, N., Chatterjee, S. & Zaletel, M. P. Mechanism for Anomalous Hall Ferromagnetism in Twisted Bilayer Graphene. *Phys. Rev. Lett.* **124**, 166601 (Apr. 2020).
422. Wang, Z. *et al.* Composite super-moiré lattices in double-aligned graphene heterostructures. *Science Advances* **5**. doi:10.1126/sciadv.aay8897 (Dec. 2019).
423. Chizhova, L. A., Libisch, F. & Burgdörfer, J. Graphene quantum dot on boron nitride: Dirac cone replica and Hofstadter butterfly. *Phys. Rev. B* **90**, 165404 (16 2014).

424. Martinez-Gordillo, R., Roche, S., Ortmann, F. & Pruneda, M. Transport fingerprints at graphene superlattice Dirac points induced by a boron nitride substrate. *Phys. Rev. B* **89**, 161401 (16 2014).
425. Yankowitz, M. *et al.* Emergence of superlattice Dirac points in graphene on hexagonal boron nitride. *Nature Physics* **8**, 382–386 (Mar. 2012).
426. Lopes dos Santos, J. M. B., Peres, N. M. R. & Castro Neto, A. H. Graphene Bilayer with a Twist: Electronic Structure. *Phys. Rev. Lett.* **99**, 256802 (25 2007).
427. Ribeiro-Palau, R. *et al.* Twistable electronics with dynamically rotatable heterostructures. *Science* **361**, 690–693 (Aug. 2018).
428. Jung, J., Raoux, A., Qiao, Z. & MacDonald, A. H. Ab initio theory of moiré superlattice bands in layered two-dimensional materials. *Phys. Rev. B* **89**, 205414 (20 2014).
429. Chen, S.-C., Kraft, R., Danneau, R., Richter, K. & Liu, M.-H. Electrostatic superlattices on scaled graphene lattices. *Communications Physics* **3**. doi:10.1038/s42005-020-0335-1 (Apr. 2020).
430. Park, J. M., Cao, Y., Watanabe, K., Taniguchi, T. & Jarillo-Herrero, P. Flavour Hund's coupling, Chern gaps and charge diffusivity in moiré graphene. *Nature* **592**, 43–48 (Apr. 2021).
431. Wang, L. *et al.* One-Dimensional Electrical Contact to a Two-Dimensional Material. *Science* **342**, 614–617 (Nov. 2013).
432. Codecido, E. *et al.* Correlated insulating and superconducting states in twisted bilayer graphene below the magic angle. *Sci. Adv.* **5**, eaaw9770 (Sept. 2019).
433. Castellanos-Gomez, A. *et al.* Deterministic transfer of two-dimensional materials by all-dry viscoelastic stamping. *2D Materials* **1**, 011002 (2014).
434. Greben, K., Arora, S., Harats, M. G. & Bolotin, K. I. Intrinsic and Extrinsic Defect-Related Excitons in TMDCs. *Nano Letters* **20**, 2544–2550 (2020).
435. Li, Z. *et al.* Momentum-Dark Intervalley Exciton in Monolayer Tungsten Diselenide Brightened via Chiral Phonon. *ACS Nano* **13**, 14107–14113 (2019).
436. Liu, E. *et al.* Valley-selective chiral phonon replicas of dark excitons and trions in monolayer WSe₂. *Physical Review Research* **1**, 032007 (2019).
437. Merle, B. *Mechanical Properties of Thin Films Studied by Bulge Testing* PhD thesis (2013), 159.
438. Kang, J., Tongay, S., Zhou, J., Li, J. & Wu, J. Band offsets and heterostructures of two-dimensional semiconductors. *Applied Physics Letters* **102**, 012111 (2013).
439. HUSIMI, K. Some Formal Properties of the Density Matrix. *Proceedings of the Physico-Mathematical Society of Japan. 3rd Series* **22**, 264–314 (1940).

440. Datseris, G. & Fleischmann, R. *Husimi function for electrons moving in magnetic fields* 2019. doi:10.48550/ARXIV.1912.04622.
441. Datseris, G. & Fleischmann, R. Phase space analysis of quantum transport in electronic nanodevices. *Journal of Physics Communications* **4**, 075006 (July 2020).
442. Couto, N. J. *et al.* Random Strain Fluctuations as Dominant Disorder Source for High-Quality On-Substrate Graphene Devices. *Phys. Rev. X* **4**, 041019 (Oct. 2014).
443. Neumann, C. *et al.* Raman spectroscopy as probe of nanometre-scale strain variations in graphene. *Nat. Commun.* **6**, 8429 (Sept. 2015).
444. Guinea, F., Katsnelson, M. I. & Geim, A. K. Energy gaps and a zero-field quantum Hall effect in graphene by strain engineering. *Nat. Phys.* **6**, 30–33 (Sept. 2009).
445. Georgi, A. *et al.* Tuning the Pseudospin Polarization of Graphene by a Pseudomagnetic Field. *Nano Lett.* **17**, 2240–2245 (Mar. 2017).
446. Pierret, A. *et al.* Dielectric permittivity, conductivity and breakdown field of hexagonal boron nitride. *Mater. Res. Express* **9**, 065901 (June 2022).
447. Laturia, A., Van de Put, M. L. & Vandenberghe, W. G. Dielectric properties of hexagonal boron nitride and transition metal dichalcogenides: from monolayer to bulk. *npj 2D Mater. Appl.* **2**, 1–7 (Mar. 2018).